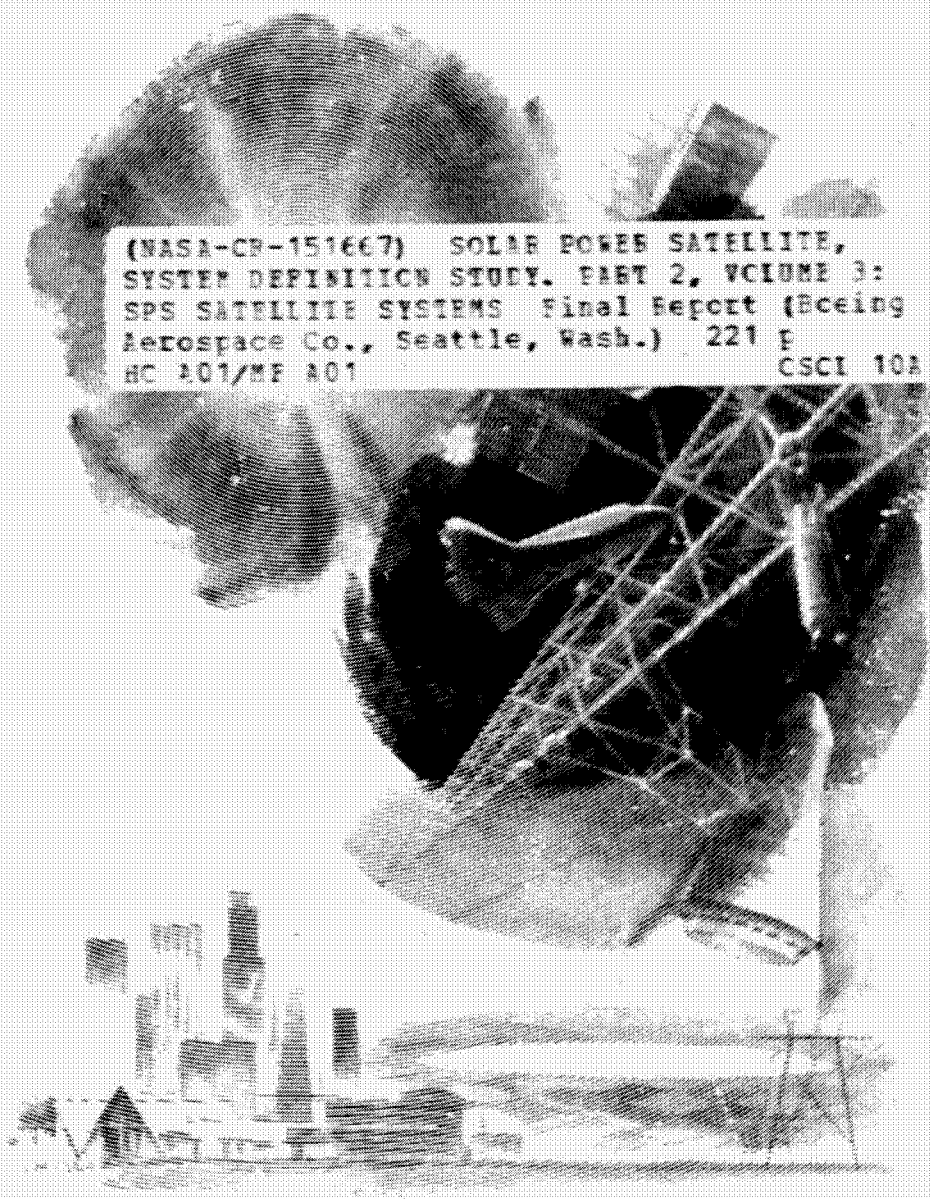


**BOEING**

~~SECRET~~  
CR-151667  
D180-22876-3

NAS9 15196  
DRL T-1346  
DRD MA-664T  
LINE ITEM 3

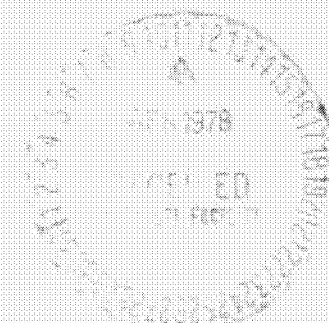
**Volume III  
SPS Satellite Systems**



(NASA-CR-151667) SOLAR POWER SATELLITE,  
SYSTEM DEFINITION STUDY. PART 2, VOLUME 3:  
SPS SATELLITE SYSTEMS Final Report (Boeing  
Aerospace Co., Seattle, Wash.) 221 p  
HC 201/MF A01

N78-20157

Unclass  
CSCI 10A G3/15 09494



# Solar Power Satellite

SYSTEM DEFINITION STUDY  
PART II

D180-22876-3

CONTRACT NAS9-15196  
DRL T-1346  
DRD MA-66-7  
LINE ITEM 3

# Solar Power Satellite

## SYSTEM DEFINITION STUDY PART II

VOLUME III  
SPS SATELLITE SYSTEMS  
D180-22876-3  
DECEMBER 1977

Submitted To  
The National Aeronautics and Space Administration  
Lyndon B. Johnson Space Center  
in Fulfillment of the Requirements  
of Contract NAS9-15196

Supervised By:

  
D. L. Gregory

Approved:

  
G. R. Woodcock  
Study Manager

BOEING AEROSPACE COMPANY  
MISSILES AND SPACE GROUP-SPACE DIVISION  
P.O. BOX 3999  
SEATTLE, WASHINGTON

**FOREWORD**

The SPS system definition study was initiated in December 1976. Part I was completed on May 1, 1977. Part II technical work was completed October 31, 1977.

The study was managed by the Lyndon B. Johnson Space Center (JSC) of the National Aeronautics and Space Administration (NASA). The Contracting Officer's Representative (COR) was Clarke Covington of JSC. JSC study management team members included:

Dickey Arndt	Microwave System Analysis	Andrei Konradi	Space Radiation Environment
Harold Benson	Cost Analysis	Jim Kelley	Microwave Antenna
Bob Bond	Man-Machine Interface	Don Kessler	Collision Probability
Jim Cioni	Photovoltaic Systems	Lou Leopold	Microwave Generators
Hu Davis	Transportation Systems	Lou Livingston	System Engineering and
R. H. Dietz	Microwave Transmitter and Rectenna	Jim Meany	MPTS Computer Program
Bill Dusenbury	Energy Conversion	Stu Nachtwey	Microwave Biological Effects
Bob Gundersen	Man-Machine Interface	Sam Nassiff	Construction Base
Alva Hardy	Radiation Shielding	Bob Ried	Structure and Thermal Analysis
Buddy Heineman	Mass Properties	Jack Seyl	Phase Control
Lyle Jenkins	Space Construction	Bill Simon	Thermal Cycle Systems
Jim Jones	Design	Fred Stebbins	Structural Analysis
Dick Kennedy	Power Distribution		

The study was performed by the Boeing Aerospace Company. The Boeing study manager was Gordon Woodcock. Boeing Commercial Airplane Company assisted in the analysis of launch vehicle noise and overpressures. Boeing technical leaders were:

Ottis Bullock	Structural Design	Don Grim	Electrical Propulsion
Vince Caluori	Photovoltaic SPS's	Henry Hillbrath	Propulsion
Bob Conrad	Mass Properties	Dr. Ted Kramer	Thermal Analysis and Optics
Eldon Davis	Construction and Orbit-to-Orbit Transportation	Frank Kilburg	Alternate Antenna Concepts
Rod Darrow	Operations	Walt Lund	Microwave Antenna
Owen Denman	Microwave Design Integration	Keith Miller	Human Factors and Construction Operations
Hal DiRamio	Earth-to-Orbit Transportation	Dr. Ervin Nalos	Microwave Subsystem
Bill Emsley	Flight Control	Jack Olson	Configuration Design
Dr. Joe Gauger	Cost	Dr. Henry Oman	Photovoltaics
Jack Gewin	Power Distribution	John Perry	Structures
Dan Gregory	Thermal Engine SPS's	Scott Rathjen	MPTS Computer Program Development

The General Electric Company Space Division was the major subcontractor for the study. Their contributions included Rankine cycle power generation, power processing and switchgear, microwave transmitter phase control and alternative transmitter configurations, remote manipulators, and thin-film silicon photovoltaics.

Other subcontractors were Hughes Research Center--gallium arsenide photovoltaics; Varian--klystrons and klystron production; SPIRE--silicon solar cell directed energy annealing.

**D180-22876-3**

**This report was prepared in 8 volumes as follows:**

- |            |   |             |   |
|------------|---|-------------|---|
| <b>I</b>   | <b>– Executive Summary</b>                    | <b>V</b>    | <b>– Space Operations</b>   |
| <b>II</b>  | <b>– Technical Summary</b>                    | <b>VI</b>   | <b>– Evaluation Data Book</b>   |
| <b>III</b> | <b>– SPS Satellite Systems</b>                | <b>VII</b>  | <b>– Study Part II Final Briefing Book</b>  |
| <b>IV</b>  | <b>– Microwave Power Transmission Systems</b> | <b>VIII</b> | <b>– SPS Launch Vehicle Ascent and Entry Sonic Overpressure and Noise Effects</b> |



## **D180-22876-3**

### **CONTENTS**

<b>Section</b>	<b>Title</b>	<b>Page</b>
<b>1.0</b>	<b>INTRODUCTION</b>	<b>1</b>
<b>2.0</b>	<b>REQUIREMENTS</b>	<b>3</b>
2.1	Programmatic Requirements	3
2.2	Specific Requirements	3
<b>3.0</b>	<b>ENVIRONMENT</b>	<b>7</b>
3.1	Meteoroids	7
3.1.1	Flux-Mass Model	7
3.1.2	Man-Made Objects	8
3.2	Radiation	8
3.2.1	Ionizing Radiation	8
3.2.2	Radiation Cycle Prediction	9
<b>4.0</b>	<b>PRIMARY SUBSYSTEMS</b>	<b>13</b>
4.1	Materials	13
4.1.1	Provisional Material Availability Requirements	13
4.1.2	Thermal Engine Satellite Materials	13
4.1.3	Thermal Engine SPS Material Selection	16
4.1.4	Photovoltaic Satellite Cell Material Selection	16
4.2	Solar Concentrators	17
4.2.1	Photovoltaic Application	17
4.3	Solar Concentration for Thermal Engines	17
4.4	Solar Cells	17
4.4.1	Silicon Single Crystal Solar Cells	20
4.4.2	Gallium Arsenide Solar Cells	23
4.4.3	Other Thin Solar Cells	25
4.4.4	Metal-Insulation Semiconductor Cells	27
4.4.5	Other Solar Cell Development	30
4.4.6	Conclusions	30
4.5	Turbogenerator Systems	32
4.5.1	Potassium Rankine Systems	32
4.5.2	Generators	37
4.5.3	Potassium Boilers	37
4.5.4	Pumps	37
4.5.5	Radiators	41
4.6	Power Distribution and Control	42
4.6.1	Type Section	45
4.6.2	Rotary Joint	59
4.7	Photovoltaic Reference Attitude Control	72

## **D180-22876-3**

### **CONTENTS**

<b>Section</b>	<b>Title</b>	<b>Page</b>
4.8	Interface to Transportation System .....	72
4.8.1	Photovoltaic SPS .....	72
4.9	Annealing .....	75
5.0	CONFIGURATION SELECTION .....	79
5.1	Configuration Selection Trades .....	79
5.1.1	Silicon Photovoltaic .....	79
5.1.2	Rankine Thermal Engine .....	91
5.2	Other SPS Options .....	107
5.2.1	Gallium Arsenide Photovoltaic Alternate .....	108
5.2.2	Brayton Thermal Engine .....	116
6.0	SATELLITE CONFIGURATION DEFINITION .....	121
6.1	Configuration .....	121
6.1.1	Silicon Photovoltaic .....	121
6.1.2	Rankine Thermal Engine .....	145
6.2	Mass Summary .....	169
6.2.1	Silicon Photovoltaic Mass Summary .....	169
6.2.2	Rankine Thermal Engine Mass Summary .....	169
6.3	Cost Summaries .....	173
6.3.1	Silicon Photovoltaic Cost Summary .....	173
6.3.2	Potassium Rankine Cost Summary .....	173

### **APPENDICES**

<b>Appendix</b>	<b>Page</b>
A Rotary Joint Analysis General Electric Space Division .....	177
B Analysis and Comparison of Alternate Structural Approaches .....	183

## LIST OF FIGURES

Figure	Title	Page
3-1	Meteoroid Flux-Mass Model (Omnidirectional).....	7
3.2-1	Predictions for Solar Cycle 21.....	10
3.2-2	Damage Coefficient Comparison.....	11
3.2-3	Spectrum of Protons Incident on Solar Cells of Solar Power Satellite.....	11
3.2-4	Spectrum of Electrons Incident on Solar Cells of Solar Power Satellite.....	12
4-1	Extrapolated Strengths for 1% Creep in 30 Years at Temperature Indicated.....	14
4-2	Thermal Engine SPS Material Availability.....	15
4.2-1	Concentration Ratio "2".....	18
4.2-2	Concentration Ratio "3".....	18
4.2-3	Cylindrical CPC (2-Dimensional).....	18
4.2-4	Conic CPC (3-Dimensional).....	19
4.2-5	CPC Surface Generation (3 Dimensional).....	19
4.4-1	Solarex 50 $\mu$ m Thick Solar Cell Develops 60 mW With 11 Percent Efficiency.....	21
4.4-2	Fluence of $10^{15}$ One-MeV Electrons Produces Only an 8 Percent Loss of Output in 50 $\mu$ m Thick Cell.....	22
4.4-3	Thinner Silicon Solar Cells Lose Less of Their Output When Irradiated Thickness of Gallium Arsenide, $\mu$ m.....	22
4.4-4	Gallium Required for Solar Power Satellite.....	24
4.4-5	The Effect of Grain Size on AM1 Efficiency of 2 $\mu$ m Thick GaAs and InP Cells and 10 $\mu$ m Thick (Solid Lines) and 25 $\mu$ m Thick Si Cells.....	28
4.4-6	The Effect of Grain Size on the AM1 Efficiency of 2 $\mu$ m Thick GaAs and 10 and 25 $\mu$ m Thick Si MOS Schottky Barrier Cells.....	28
4.4-7	MIS Solar Cell Development in France Has 11.7 Percent Efficiency.....	29
4.4-8	Grooves in Cell Cover Refract Sunlight.....	31
4.5-1	Cycle Temperature Influence on Brayton and Rankine Cycles.....	34
4.5-2	National Alkali Metal Data Base.....	34
4.5-3	Potassium Turbine Testing.....	36
4.5-4	Moisture Extraction Effectiveness Determined.....	38
4.5-5	Electromagnetic Pumps.....	40
4.5-6	Manifold Arrangement Options.....	43
4.6-1	Thermal Engine SPS Power Distribution.....	44
4.6-2	Refrigerated Conductor Parameters.....	47
4.6-3	Coaxial Superconducting Power Transmission Cable.....	49
4.6-4	SPS Superconductor Analysis Summary.....	51
4.6-5	Cryoresistive Cooling of Conductors.....	54
4.6-6	Electrical Schematic--Power Generator.....	55
4.6-7	Electrical Schematic--Photovoltaic.....	57

## LIST OF FIGURES (Continued)

Figure	Title	Page
4.6-8	Photovoltaic Reference Power Collection .....	60
4.6-9	Electrical "Slip-Ring" Assembly .....	67
4.6-10	Silver Slip-Ring Grade 26 Brush 85 Ag 3 Gr 12 MoS <sub>2</sub> .....	69
4.6-11	Slip Ring Temperatures .....	70
4.6-12	Gimbal Assembly Feeder Conductor Temperatures .....	70
4.6-13	Slip Ring Feeders .....	71
4.6-14	Conductor Temperatures .....	73
4.6-15	Rotary Ball Joint Temperatures .....	73
4.6-16	Ring Feeder Induced Forces in Newtons/Meter of Depth .....	74
4.8-1	Component Packaging Characteristics .....	76
4.8-2	Component Mix Per Delivery Flight .....	77
5.1-1	Part II Midterm Photovoltaic Reference Configuration .....	85
5.1-2	Thin Cells Exhibit Lower Radiation Degradation .....	87
5.1-3	Thin Cells Exhibit Lower Degradation .....	87
5.1-4	Reflector Radiation Degradation .....	88
5.1-5	Shadowing Affects String Output .....	88
5.1-6	Photovoltaic Reference 20 Meter Beam Structure .....	90
5.1-7	Potassium Vapor Pressure vs Temperature .....	92
5.1-8	High and Low Pressure Turbines .....	93
5.1-9	Extrapolation of Turbine Weights .....	94
5.1-10	Cycle Temperature Ratio Selection .....	96
5.1-11	Candidate Heat Pipe Working Fluids .....	97
5.1-12	Influence of Heat Spacing on Emissivity .....	98
5.1-13	Steerable Facet (Heliostat) .....	101
5.1-14	Pointing the Facets .....	102
5.1-15	Facet Hub .....	103
5.1-16	Definition of Angles and Axes .....	104
5.1-17	Attitude Control Propellant-Photovoltaic POP .....	106
5.1-18	Perpendicular-to-Ecliptic Plane Orientation .....	107
5.2-1	GaAs Satellite, CR2 vs CR1 .....	109
5.2-2	GaAs Satellite, Sensitivity to Cell Performance .....	109
5.2-3	Sensitivity of Satellite Mass and Cost to GaAs Solar Cell Thickness .....	110
5.2-4	CPC Operation .....	110
5.2-5	GaAs, CR>2, Options .....	113
5.2-6	Passive Thermal Control for GaAs Options .....	113
5.2-7	System Mass Characteristics for CR>2 Options .....	114
5.2-8	GaAs Requirements for CR>2 Options .....	114

## LIST OF FIGURES (Continued)

Figure	Title	Page
5.2-9	Reduction in Gallium Required for CR>2 System .....	117
5.2-10	Solar Brayton Cycle .....	117
5.2-11	Insulated Helium Ducts Reduce Mass .....	118
5.2-12	One Module, Brayton SPS .....	119
5.2-13	Brayton SPS Configuration .....	120
5.2-14	Brayton SPS Mass Statement .....	120
6.1-1	Photovoltaic Reference Configuration .....	124
6.1-2	Low Cost Annealable Blanket Structure .....	124
6.1-3	Photovoltaic Reference Configuration Solar Array Fundamental Element "Blanket Panel" .....	126
6.1-4	Photovoltaic Panel to Array Assembly .....	126
6.1-5	Joint Tape Configuration .....	128
6.1-6	Photovoltaic Reference Solar Array Arrangement and Attachment .....	129
6.1-7	Loads Analysis and Loads/Sizing Summary for Critical Beam in Upper Surface .....	131
6.1-8	Reference Length of 20M Beams .....	131
6.1-9	Photovoltaic Satellite Structural Details .....	132
6.1-10	680 Meter Beam Cost and Weight Size Selection .....	133
6.1-11	Array Edge Loading .....	133
6.1-12	Sizing Data for a 20 Meter Long Tapered Tube of Graphite Epoxy .....	135
6.1-13	Antenna Support .....	137
6.1-14	Circular Ring Beam Geometry .....	137
6.1-15	Drive Ring and Roller Assembly Location Relative to Outer Base Chords of Circular Ring Beams .....	138
6.1-16	Summer Solstice .....	143
6.1-17	Autumnal Equinox .....	143
6.1-18	Winter Solstice .....	143
6.1-19	Spring Equinox .....	143
6.1-20	Annual Power Variation .....	144
6.1-21	Cavity Absorber and Compound Parabolic Concentrator .....	147
6.1-22	General Arrangement—Rankine Cycle SPS .....	149
6.1-23	General Arrangement—Rankine Module, SPS .....	150
6.1-24	Modules Consist of Concentrator and Focal Point Assembly .....	153
6.1-25	Facet Support Structure .....	155
6.1-26	Alternate Structure Approach .....	155
6.1-27	Reflector Facet .....	156
6.1-28	CPC Aperture Door Assembly .....	158

**D180-22876-3**

**LIST OF FIGURES (Continued)**

<b>Figure</b>	<b>Title</b>	<b>Page</b>
6.1-29	Turbogenerator Pallet . . . . .	158
6.1-30	Alkali Metal Vapor Turbine. . . . .	159
6.1-31	Droplet Impact Damage . . . . .	161
6.1-32	Turbine Size is Within National Capability . . . . .	163
6.1-33	Generator . . . . .	165
6.1-34	Primary Radiator System . . . . .	165
6.1-35	Radiator Mass Summary . . . . .	167
6.1-36	Attitude Control System. . . . .	168
6.2-1	Mass/Size Uncertainty Analysis Results. . . . .	172
6.2-2	Potassium Rankine SPS Mass Statement . . . . .	172

**D180-22876-3**

**LIST OF TABLES**

<b>Table</b>	<b>Title</b>	<b>Page</b>
3.2-1	Solar Proton Fluence. . . . .	10
4.4-1	Solar Cell Development Status October, 1977, For Cell Types Pertinent to the Solar Power Satellite . . . . .	26
4.6-1	Superconductive Cable Mass Summary . . . . .	51
4.6-2	Superconductor Power Distribution Summary . . . . .	52
4.6-3	Photovoltaic SPS Power Sector Summary . . . . .	61
4.6-4	Photovoltaic SPS Power Sector Summary . . . . .	64
4.6-5	Photovoltaic SPS Power Sector Summary . . . . .	64
4.6-6	Thermal Engine Satellite Power Distribution Summary. . . . .	65
4.6-7	Satellite Power Distribution System Comparisons. . . . .	65
4.6-8	COMSAT Selected Brush/Slip Ring Materials for Space Applications . . . . .	69
4.7-1	Photovoltaic Reference Attitude Control Summary . . . . .	74
5.1-1	Photovoltaic Energy Conversion Comparisons. . . . .	81
5.1-2	Part I Nominal Mass Summary Weight in Metric Tons. . . . .	83
5.1-3	Part II Midterm Nominal Mass Summary Weight in Metric Tons. . . . .	85
5.1-4	Solar Cell Selection . . . . .	89
5.2-1	CPC Characteristics. . . . .	111
5.2-2	Mass Assumptions for CR>2 Options . . . . .	115
6.1-1	Part II Reference System Energy Conversion/Sizing . . . . .	122
6.1-2	Photovoltaic Blanket Weight Buildups. . . . .	130
6.1-3	Loads/Sizing Summary for Critical Beam in Upper Surface. . . . .	134
6.1-4	Mass Definition for 20M Beam Section (Upper Surface Beams) . . . . .	134
6.1-5	Photovoltaic Reference Attitude Control . . . . .	140
6.1-6	Photovoltaic Satellite Instrumentation and Control . . . . .	141
6.2-1	Reference Photovoltaic Final Mass Summary . . . . .	170
6.2-2	Photovoltaic Reference Configuration Nominal Mass Summary Weight in Metric Tons. . . . .	171
6.3-1	Reference Photovoltaic Final Cost Summary . . . . .	174
6.3-2	Capital Cost Summary – Thermal Engine SPS (Rankine) Dollars in Millions. . . . .	175

## **1.0 INTRODUCTION**

This is Volume III of a set of 8 which comprises the final report of a study of Solar Power Satellites (SPS) conducted for the National Aeronautics and Space Administration's Johnson Space Flight Center under Contract NAS9-15196. These volumes are:

- I**    Executive Summary
- II**   Technical Summary
- III**   SPS Satellite Systems
- IV**   Microwave Power Transmission System
- V**    Space Operations
- VI**   Evaluation Data Book
- VII**  Study Part II Final Briefing
- VIII** SPS Launch Vehicle Ascent and Entry Sonic Overpressure and Noise Effects

The study was divided into two parts of approximately equal duration. This documentation summarizes the Part 1 results and details the Part 2 activities and results.

This volume concentrates upon the power generation portion of the SPS. The transmitter systems are not covered, although their masses are included in the overall mass statement.

Two generic types of power generation systems were investigated. These were the photovoltaic (solar cell) and thermal engine systems; both convert solar energy to the electrical power required by the transmitter systems.

The two systems are fundamentally different in their approach to energy conversion. Solar cells are passive "no moving part" devices which effect direct conversion of solar energy to a direct current output. The thermal engine concept employs generators turned by turbines energized by a heated working fluid. Concentrated solar energy heats this working fluid; excess heat is rejected to space by a radiator.

The two systems were found to be approximately equal in mass; however, in-space construction of the thermal engine system is more complex and involves a more expensive construction station and higher "front-end" cost.

Parts 2.0 and 3.0 of this volume give system requirements and a definition of the operational environment. Section 4.0 gives a brief description of the primary SPS subsystems and explains why specific subsystem types were selected, for example, why the Rankine cycle was selected over the Brayton for thermal engine energy conversion. Section 5.0 explains trades leading to exact configuration selection, for example, selection of the Rankine cycle operating temperatures. Section 6.0 gives a detailed description of the two satellite configurations.



## 2.0 REQUIREMENTS

### 2.1 PROGRAMMATIC REQUIREMENTS

Primary overall requirements of a programmatic nature are given in Volume II of this document set. More specific requirements influencing the actual satellite configurations are given in the following section.

### 2.2 SPECIFIC REQUIREMENTS

These requirements apply to the power generation system (non-transmitter) portion of the SPS.

- (1) The operational location for the satellites shall be geosynchronous orbit.
- (2) Nominal life shall be 30 years (indefinite with appropriate refurbishment).
- (3) System sizing shall be such as to deliver a minimum of 8.215 MW to each of two microwave transmitters per satellite, over the course of a year, excepting occultation periods and five minutes before and after occultation.
- (4) Station keeping systems shall be provided such that perturbing effects do not reduce inter-satellite spacings below 50 km for a nominal spacing of 75 km. Nominal orbit error allocations are: out-of-plane  $2.2^\circ$ , equivalent to 15.5 km longitude error; eccentricity 0.0004, equivalent to 16.87 km longitude error; long-period drift, 10 km.

The RSS of these three parameters is 25 km total random error. If the satellites can be shifted as a group, the group may exceed 25 km from the assigned locations.

- (5) The satellites shall have attitude control capability and structural integrity to recover from a gravity gradient stable attitude to a nominal flight attitude (in geosynchronous orbit).
- (6) The power generating system shall be designed to degrade (include random malfunctions) by no more than 2% in the course of one year. Degradation of solar arrays below this quantity shall be correctable (for example, by annealing) within a period of 60 days.
- (7) In addition to the capability of handling start-up and shut down power ramps, the power generation system shall be capable of operating at power levels between 50% and 100% of nominal (for load following).
- (8) Partial shadowing by other SPS's shall not cause total disruption of operation or damage. Loss of output proportionate to the shadowing is acceptable.

**D180-22876-3**

- ( 9) Each SPS shall have provisions for the storage of consumables for one year of operation.**
- (10) Satellites shall be designed for construction in space from prefabricated elements and other materials delivered to space construction site(s) from Earth by a space transportation system.**
- (11) Energy Collection and Concentration Subsystem (if used; the "CR=1" photovoltaic satellite has none):**
  - (a) The energy collection subsystem shall be designed to avoid variation in concentrated sunlight intensity that would damage or seriously interfere with operation of the energy conversion subsystem.**
  - (b) The energy collection subsystem shall actively or passively compensate for variations in sun elevation due to satellite attitude. The energy collection subsystem shall also compensate for expected structural deformations in the SPS due to space environment and other operational factors, and for attitude variations due to normal operation of the attitude control system.**
  - (c) The energy collection subsystem shall be designed to preclude arcing and/or other potentially damaging effects associated with electrostatic charge build-up due to the geosynchronous orbit natural or induced environments.**
- (12) Energy Conversion Subsystem (Photovoltaic):**
  - (a) The photovoltaic system shall be modularized into space installable blankets ("strings") of approximately 80,000 KWe nominal generating capacity each at beginning of life under nominal operating conditions including applicable sunlight concentration. The nominal voltage output of each module shall be 44,000 volts.**
  - (b) The photovoltaic system shall employ radiation shielding and/or annealing as appropriate for minimum power cost.**
  - (c) Individual converters (cells) shall be wired into the blanket array such that either open or short-circuit failures of individual converters do not cause 1) loss of array output disproportionate to the loss of the individual converter's contribution, or 2) arcing.**
  - (d) The photovoltaic system shall be designed such that a blanket module and/or its switch-gear can be isolated from the operating onboard electric power distribution system, and its generated electrical potential reduced to safe levels, so that it may be serviced without shutdown of the entire energy conversion subsystem.**

**D180-22876-3**

**(13) Energy Conversion Subsystem (Thermal Engine):**

- (a) The thermal engine systems shall be modularized into space installable elements, with a nominal generating capacity per machine set of 32,000 KWe. The nominal DC voltage output of each machine set shall be controllable within the range 40,000 to 45,000 volts at rated power output.
- (b) Individual generators shall be provided with controls and connected to the onboard power distribution system such that planned shutdown of an individual generator does not impair operations of the SPS except for loss of the output contributed by that generator.
- (c) Individual engine generators shall be designed to allow service, including entry to fluid systems, without shutdown of other, functioning, engine-generators, except in the case where access to the interior of the cavity absorber may be required.
- (d) Fluid systems shall include scavenging and/or inventory control such that intentional or unintentional breaches of fluid system integrity will not cause excessive loss of fluid.
- (e) The thermal engine energy conversion system shall be capable of surviving without damage a maximum-duration geosynchronous occultation (72 minutes) when entering the shadow cold, i.e., after an extended shutdown period, and then reaching full power within one hour.
- (f) Normal restart after occultation, i.e., upon entering the shadow hot, shall reach full power within five minutes after leaving the shadow.
- (g) The axes of rotation of the turbogenerators shall be parallel. One half of the machines shall rotate in one direction, the other half in the other, to minimize the net angular momentum.

**(14) Power Distribution System:**

- (a) The power distribution system shall conduct DC electrical power from the energy conversion system interfaces to the transmitter rotary joint interfaces. (It is assumed that there are two 5-GW ground output antennas and associated rotary joints per SPS.) The distribution system shall supply the following nominal voltages and currents to the rotary joint interface.

Bus A 40,800 volts at 138,600 amps (5.65 GW)

Bus B 38,700 volts at 59,400 amps (2.30 GW)

A common return for these two supplies shall be provided.

### **D180-22876-3**

This requirement is based on estimated Klystron characteristics described in the following, and is subject to revision:

#### **Supporting Rationale Reference Klystron Parameters**

The following are the parameters for the reference DC to RF converter:

Tube Type: Klystron-Depressed Collector  
RF Power Output: 70.66 KW  
Efficiency: 0.851  
Number of Depressed Collectors: 5  
Modulating Anode Voltage: 21,050  $\pm$ 0.5%  
Body Anode Voltage: 21,050  $\pm$ 0.5%  
Body Anode Current: 0.088 Amperes  
Beam Current: 2.20 Amperes

#### **KLYSTRON TUBE ELEMENT REQUIREMENTS**

<b>ELEMENT</b>	<b>VOLTS D.C.</b>	<b>CURRENT (AMPS)</b>	<b>POWER (WATTS)</b>
Modulating Anode	21,050	0.088	1,852.4
Body Anode	21,050	0.088	1,852.4
Spike Electrode 0	0	0.044	—
Collector #1	21,050	0.044	926.4
Collector #2	25,160	0.088	2,214.1
Collector #3	29,470	0.154	4,538.4
Collector #4	37,890	0.330	12,503.7
Collector #5	40,000	1.452	58,080.0
Cathode	TBD	TBD	50.0
Solenoid	TBD	TBD	1,000.0
<b>TOTAL POWER</b>			<b>83,017.4</b>
<b>PROCESSED POWER</b>			<b>12,433.7</b>
<b>EFFICIENCY</b>			<b>85.1%</b>

- (b) The power distribution system shall employ dedicated aluminum conductors (not part of main structure) which are passively cooled by radiation to free space.
  - (c) The power distribution system shall have switching and control equipment as necessary to isolate the rotary joint and power transmission system from energy conversion system startup and shutdown transients. This requirement may be in part met by delayed activation of power distribution provided that the delay is not greater than five minutes.
- (15) The SPS shall be designed to the ionizing radiation environment given in the "Environment" portion of this document (Section 3.2.1).

### 3.0 ENVIRONMENT

This section specifies the environmental factors assumed, for this study, to prevail in the geosynchronous operational orbit. Also provided are some factors associated with low orbit locations used for assembly and the intermediate regions used for transfer from low to high orbit.

#### 3.1 METEOROIDS

##### 3.1.1 Flux-Mass Model

The average total meteoroid environment was based upon the model given in Reference (1). The flux-mass model is shown in Figure 3-1. The meaning of this flux-mass model is that for a given area, say one square meter, in free space particles will pass through in all directions (including "both sides" of the area) at the average rates specified. Models such as this are derived from observations of meteors in our atmosphere and from limited space flight data.

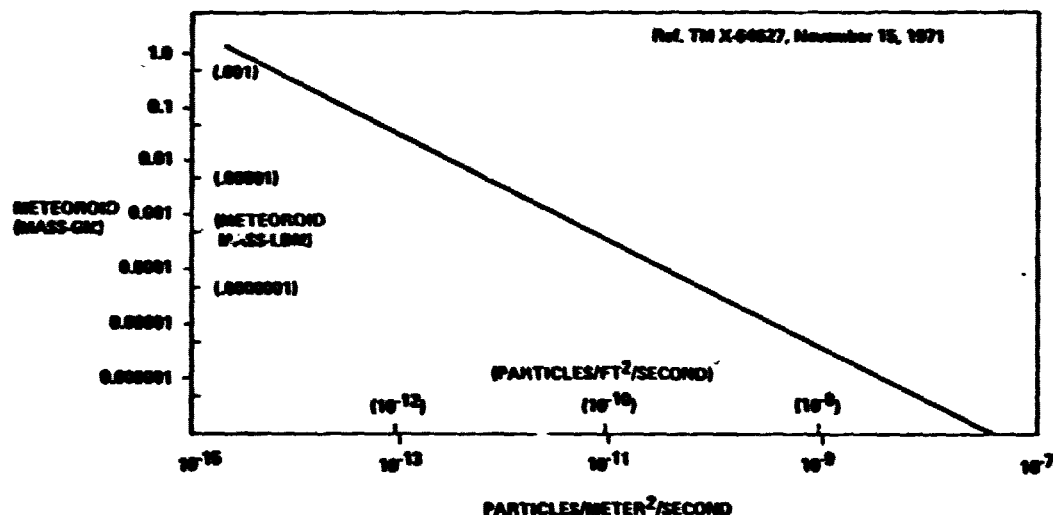


Figure 3-1 Meteoroid Flux-Mass Model (Omnidirectional)

Most meteoroids are apparently in elliptical orbits about the sun and the orbits are of relatively low inclination to the ecliptic. The orbital motion of the Earth (and of objects in orbit about the Earth), coupled with this low inclination of the meteoroids' orbit, causes a significant directional effect. Planar objects, such as the thermal engine SPS radiators, are thus advantageously flown "edge on" to the prevalent meteoroid stream. Using such an orientation, a previous study (Reference (2)) has determined that the number of hits per unit (projected) area per second, will be approximately 40% of that indicated by the omnidirectional flux-mass model. Thus the "particles/meter<sup>2</sup>/second" quantities of Figure 3-1 can be multiplied by 0.4 for radiators mounted perpendicular to the north-south axis of the SPS.

## **D180-22876-3**

### **3.1.2 Man-Made Objects**

The probable incidence of man-made objects such as satellites or satellite parts is discussed in Volume VI of this document set.

## **3.2 RADIATION**

### **3.2.1 Ionizing Radiation**

The SPS shall be designed to the following ionizing radiation environments:

#### **High Energy Particles**

For high energy trapped electrons and protons, the electron flux maps AE-4<sup>(2)</sup> and AE-6<sup>(3)</sup> and the proton flux maps AP-5<sup>(4)</sup>, AP-6<sup>(5)</sup>, and AP-7<sup>(6)</sup> shall be used. The anticipated AP-8 proton flux map shall be used when it becomes available. These flux maps, described in a series of publications by J. Vette and co-workers at the National Space Science Data Center, are the standard high energy trapped particle data source.

The solar proton environment model of J. King<sup>(7)</sup>, and the survey and predictions of W. R. Webber<sup>(8)</sup>,<sup>(9)</sup> be used to define both an expected and a worst case solar proton environment.

#### **Low Energy Particles**

Electrons of energy less than 250 keV, and protons below 0.5 MeV are not treated in the trapped particle flux maps and must be defined from the research literature. The S/C charging article by DeForrest<sup>(10)</sup> is typical of the data available in this area that shall be used.

#### **Ionosphere and Space Radiation Environment Definition**

The NASA Space Vehicle Design Handbook ionosphere environment shall be used.

#### **References:**

- (1) NASA TMS-64627 "Space and Planetary Environmental Guidelines for Use in Space Vehicle Development," Nov. 15, 1971.
- (2) D. Gregory "Final Technical Report, Systems Definition, Space-Based Power Conversion Systems," NAS8-31628, Boeing Aerospace Company Document D180-20309-2.
- (3) G. Singley and J. Vette, A Model Environment for Outer Zone Electrons, NSSDC-72-13, 1972.
- (4) M. Teague, K. Chan, J. Vette, "AE6: A Model Environment of Trapped Electrons for Solar Maximum," NSSDC 76-04, May, 1976.

### **D180-22876-3**

- ( 5) J. King, "Models of the Trapped Radiation Environment, Vol. IV, Low Energy Protons," NASA SP-3024, 1970.
- ( 6) J. Larine and J. Vette, Models of the Trapped Radiation Environment, Vol. V, Inner Belt Protons, NASA SP-3024, 1970.
- ( 7) J. Larine and J. Vette, Models of the Trapped Radiation Environment. Vol. VI, High Energy Protons, NASA SP-3024, 1970.
- ( 8) J. King, "Solar Proton Fluences as Observed During 1966-1972 and as Predicted for 1977-1983 Space Missions," NASA Goddard X-601-73-324, 1973.
- ( 9) W. R. Webber, "An Evaluation of the Radiation Hazard Due to Solar Particle Events," Boeing Document D2-90469, 1963.
- (10) W. R. Webber, "An Evaluation of Solar Cosmic Ray Events During Solar Minimum," Boeing Document D2-84274-1, 1966.
- (11) S. DeForrest, "Spacecraft Charging at Synchronous Orbit," J. Geophys. Res. 77, 651, 1972.

#### **3.2.2 Radiation Cycle Prediction**

Predictions of the sunspot number for the coming Cycle 21 are compared in Figure 3.2-1. F. M. Smith bases his prediction on two non-synchronous components related to planet-caused tidal variations on the sun. W. Gliessberg of the Astronomical Institute in West Germany bases his predictions on 80-year repeatability of sunspot phenomena. Ted Cohen and Paul Lintz base their prediction on a periodicity of 179 years obtained from a maximum entropy analysis.

A solar power satellite launched in 1990 will experience Cycles 22, 23 and 24 for which no predictions have yet been made. We therefore used data averaged for us by Professor W. R. Webber, University of New Hampshire, who is our consultant on solar activity.

The average expected solar proton fluence ( $>10$  MeV), and a 90% value, are shown in Table 3.2-1). An equivalent 1-MeV electron damage fluence for a 6 mil 10 ohm-cm n/p solar cell with 6 mil cover slip and 3 mils of equivalent back side Kapton, adhesive and mylar shielding is also given. The proton damage coefficient used is shown in Figure 3.2-2 as "1/E." The electron damage coefficient is taken from the TRW Solar Cell Handbook. The incident proton spectral shape is shown in Figure 3.2-3, while the trapped electron spectrum is shown in Figure 3.2-4.

D180-22876-3

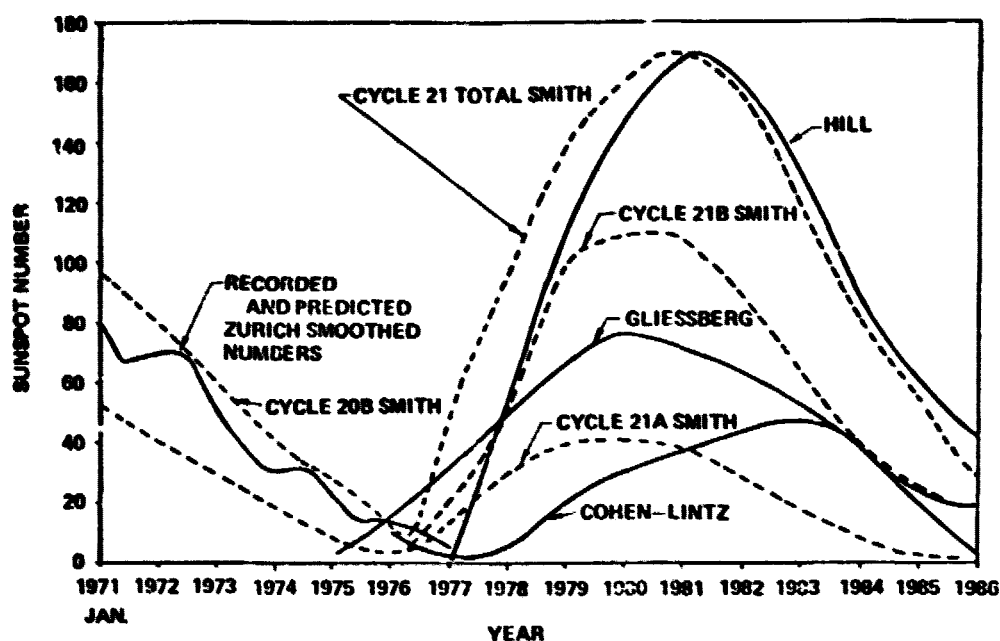


Figure 3.2-1 Predictions For Solar Cycle 21

Table 3.2-1 Solar Proton Fluence

	AVERAGE FLUENCE	90% FLUENCE
<b>SOLAR CYCLE 21</b>		
$Q_p (> 10 \text{ MeV})/\text{CM}^2$	$3.28 \times 10^{10}$	$10^{11}$
1-MeV DENI ELECTRONS	$2.3 \times 10^{14}$	$6.98 \times 10^{14}$
<b>SOLAR CYCLE 21, 22, &amp; 23</b>		
$Q_p (> 10 \text{ MeV})/\text{CM}^2$	$1.1 \times 10^{11}$	$2.25 \times 10^{11}$
1-MeV DENI ELECTRONS	$7.7 \times 10^{14}$	$1.6 \times 10^{15}$
<b>TRAPPED ELECTRON FLUENCE</b>		
YEARLY FLUENCE ( $> 0.25 \text{ MeV}$ )	$3 \times 10^{14} \text{ e/cm}^2$	
YEARLY 1-MeV DENI FLUENCE (6 MIL COVER SLIPS, 10 OHM-CM, n/p)	$2 \times 10^{13} \text{ 1-MeV e/cm}^2 \cdot \text{YEAR}$	



D180-22876-3

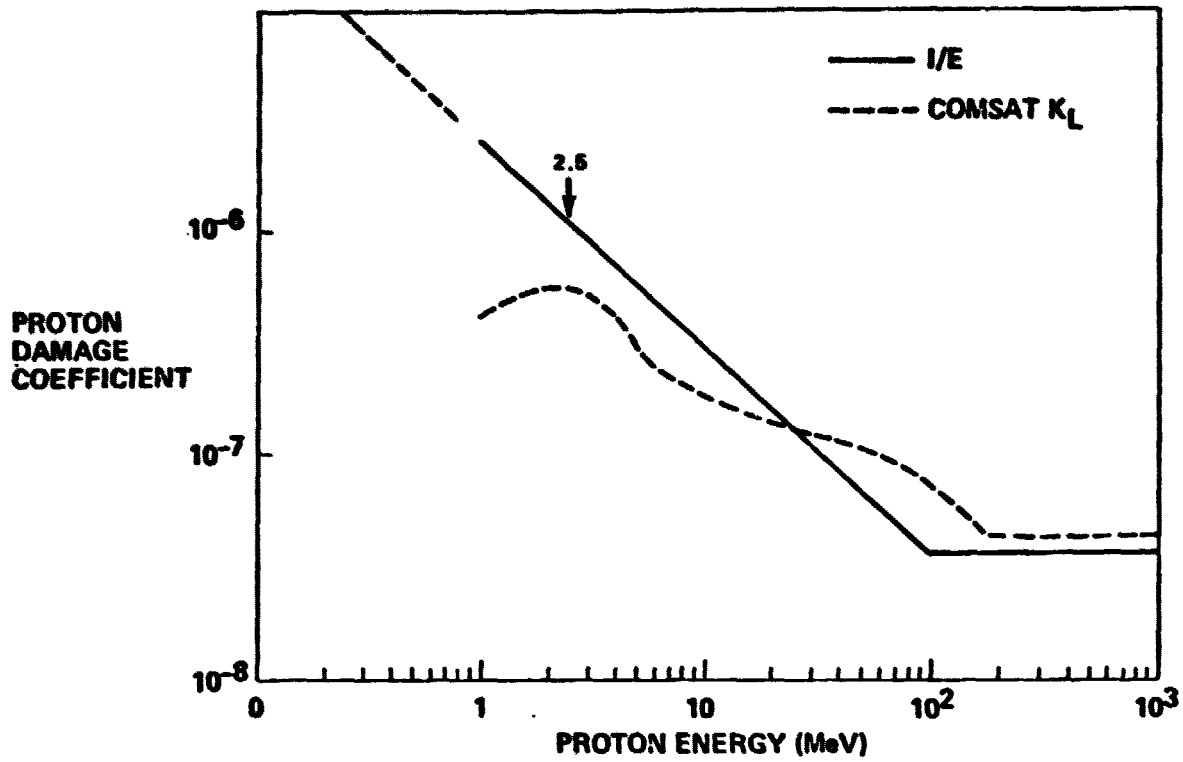


Figure 3.2-2 Damage Coefficient Comparison

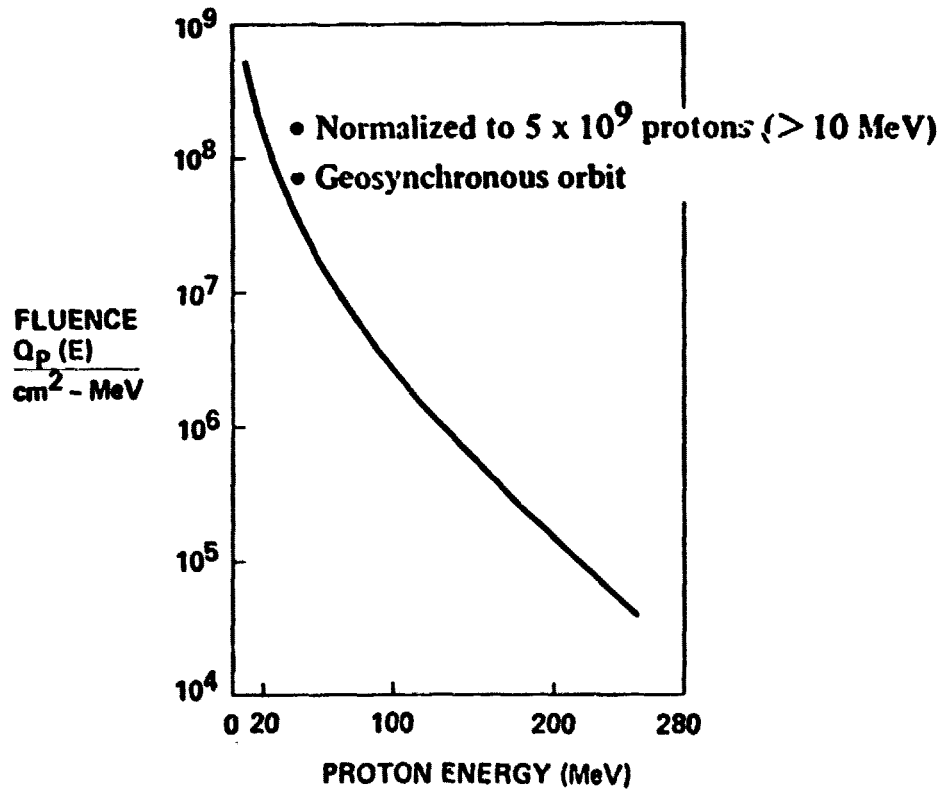


Figure 3.2-3 Spectrum of Protons Incident on Solar Cells on Solar Power Satellite

D180-22876-3

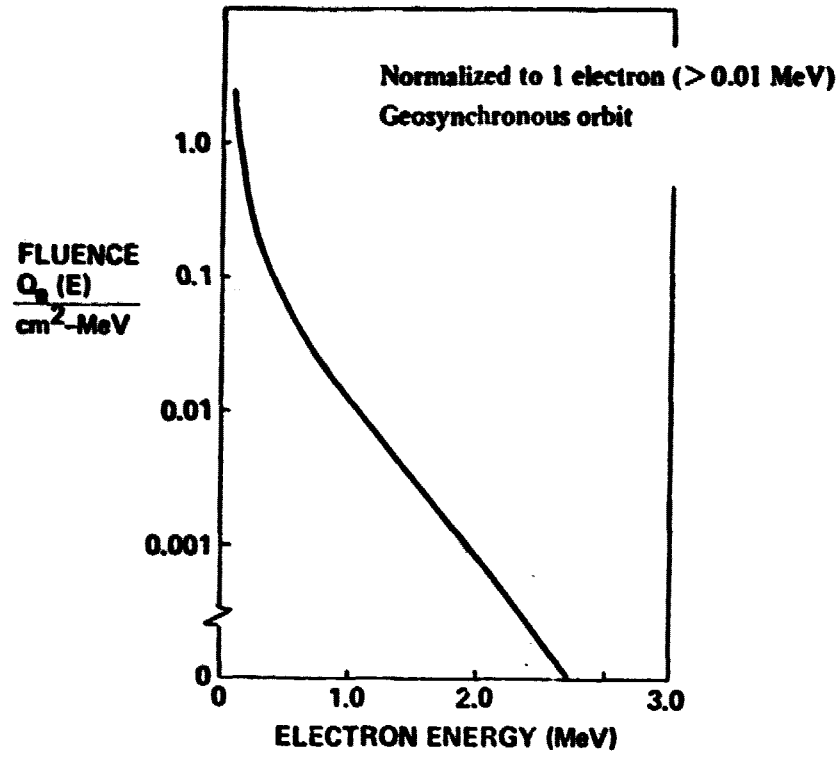


Figure 3.2-4 Spectrum of Electrons Incident on Solar Cells of Solar Power Satellite

## **4.0 PRIMARY SUBSYSTEMS**

This section describes individual subsystems and the decision processes involved in design selections affecting them.

### **4.1 MATERIALS**

If solar power satellites become a "national energy solution," 100 or more units could be required for the United States alone. As a global solution, literally thousands of satellites might be required. Therefore, careful attention should be given the abundances of materials considered for power satellite use. Not only should the material be adequate for the application in the engineering sense (strength, temperature capability, etc.) but resources must be adequate for the expected need.

#### **4.1.1 Provisional Material Availability Requirements**

As a general rule, the following requirements were used in this study:

- (1) Materials used must be probably "sufficiently abundant" in the year 2020. It is illogical to baseline materials for SPS which will be in short supply by the time of SPS incorporation.
- (2) A program of 112 SPS units ( $10^{10}$  watts output each) should not use more than 5% of the currently known world resources of any material.
- (3) The current world production rate of any material should be adequate for the production of one SPS per year. Implementation of this requirement tends to insure that the "industrialization" required for SPS will be able to successfully occur.

#### **4.1.2 Thermal Engine Satellite Materials**

The thermal engine satellite must have high temperature assemblies in order to operate efficiently. These include the cavity absorber, boiler, turbines and radiators. The last three of these are pressure vessels, exposed to hoop stress for the 30 year (260,000 hour) design life of the SPS. Coupon tests of candidate materials are, in general, for no more than 10,000 hours so that considerable extrapolation is required.

Figure 4-1 contains probably the best data available for potential thermal engine materials. Shown is the one percent creep stress (the stress to obtain a one percent elongation) versus temperature for an accumulated exposure of 30 years.

These allowable design stresses for weldable containment alloys have been reduced from previous estimates to reflect more conservative values, based on long term creep tests sponsored by the NASA-Lewis Research Center.

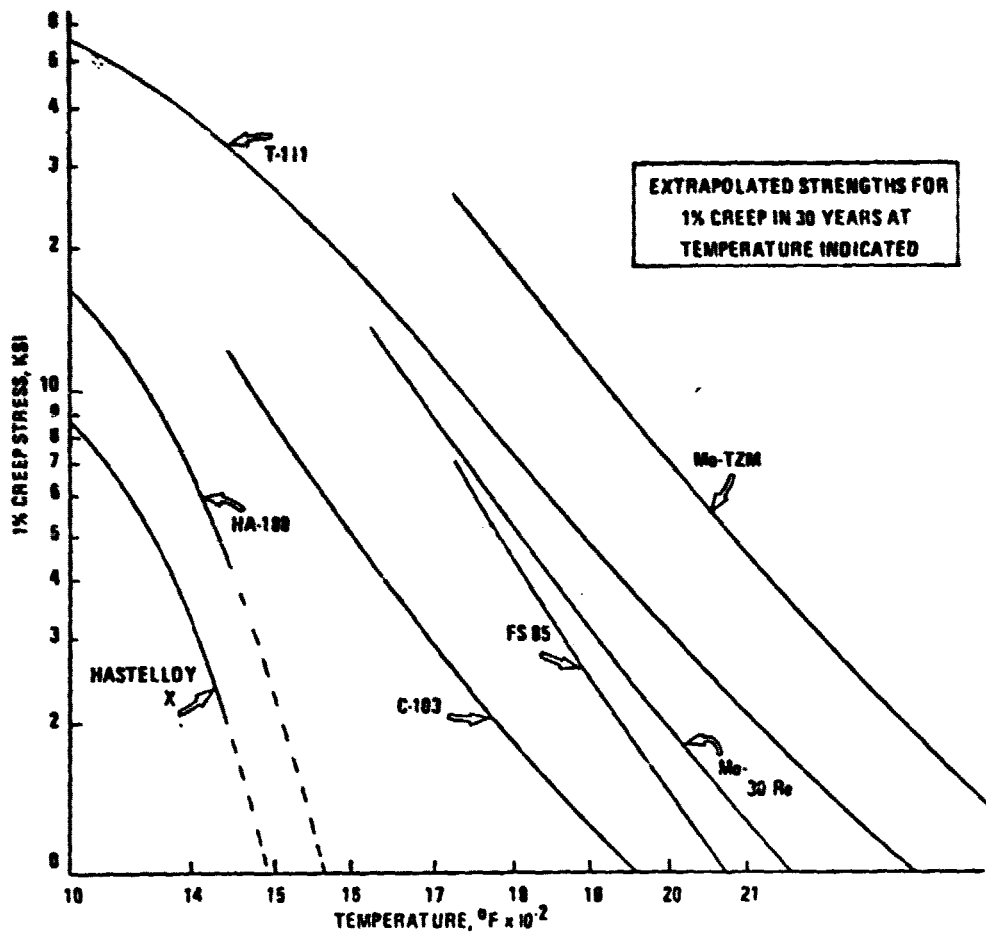


Figure 4-1 Extrapolated Strengths for 1% Creep in 30 Years at Temperature Indicated

Molybdenum TZM alloy is included as a non-weldable, very high strength alloy which would be used for highly stressed rotating parts such as turbine discs and blades; the alloy has well documented high temperature strength, is readily available and its metal processing, machining and fabrication technology is well established.

High strength weldable columbium base alloys such as FS-85 contain tungsten and zirconium which, jointly, produce grain boundary embrittlement when operating in the 1006-1283K (1350-1850 $^\circ\text{F}$ ) temperature range for long periods of time. Only the resolution strengthened alloys, such as C-103 (Cb-10 Hf-Ti), or the weaker Cb-1 Zr, have strengths superior to the nickel and cobalt base superalloys and possess good weldability and long-term thermal stability; while weldable superalloys, such as the nickel base alloys, Hastelloy X and Inconel 617, and the cobalt base alloy, HA-188 are

available and have good high temperature strength characteristics, they will not serve in the very hottest portions of the system. Therefore, the weldable columbium alloy, C-103, appears to be the most promising material for use in the highest temperature boiler, duct and turbine containment components and the non-weldable molybdenum alloy TZM appears most suited for the hottest turbine rotating components.

Figure 4-2 shows material availability data pertinent to the thermal engine SPS. Most of the data was drawn from "United States Mineral Resources," Paper 820, U.S. Dept. of Interior, 1973.

SPS-1148

- GENERAL RULES: 1) MATERIAL TO BE PREDICTED TO BE "SUFFICIENTLY ABUNDANT" IN 2020.  
2) SPS TO NOT USE OVER 5% OF WORLD RESOURCES OF ANY MATERIAL  
3) CURRENT WORLD PRODUCTION RATE ADEQUATE FOR ONE SPS/YEAR

● TURBINE WHEEL/BLADE MATERIAL (NEED ~ 6000 MT/SPS)  
(WROUGHT MATERIAL)

<u>MATERIAL</u>	<u>STATE OF ART</u>	<u>WORLD RESOURCES (MT)</u>	<u>PRODUCTION RATE (MT/YR)</u>
MOLYBDENUM (TZM)	DEVELOPED	29,000,000	91,000
SILICON CARBIDE	EARLY TEST	VERY ABUNDANT	VERY SMALL

● TURBINE HOUSING MATERIAL/BOILER TUBES (NEED 4000 TO 7000 MT/SPS)  
(WELDABLE DUCTILE MATERIAL)

<u>MATERIAL</u>	<u>STATE OF ART</u>	<u>WORLD RESOURCES (MT)</u>	<u>PRODUCTION RATE (MT/YR)</u>
TANTALLUM (T111)	DEVELOPED	100,000	PERHAPS 1,000
NIUBIUM (C103)	DEVELOPED	17,000,000	ABOUT 20,000
SILICON CARBIDE	EARLY TEST	VERY ABUNDANT	VERY SMALL

● RANKINE CYCLE WORKING FLUID

<u>MATERIAL</u>	<u>STATE OF ART</u>	<u>WORLD RESOURCES (MT)</u>	<u>PRODUCTION RATE (MT/YR)</u>
CESIUM	DEVELOPED	100,000	~8
POTASSIUM	DEVELOPED	> 10 <sup>9</sup>	10,000,000

\*MT - METRIC TON/SPS

Figure 4-2 Thermal Engine SPS Material Availability

Turbine wheel and blade materials require a material capable of taking the required stress for the baselined 30-year life of the system. These materials may be wrought, that is high ductility is not required; a molybdenum alloy has been selected. Turbine housings, however, require a weldable, ductile material. Tantalum would be ideal and would permit a very high turbine inlet temperature. However, it is in relatively short supply; therefore, niobium (also called columbium) has been selected. Silicon carbide is truly the ultimate material for this utilization. Early test results are quite promising, however, it is not felt appropriate to baseline it.

#### **4.1.3 Thermal Engine SPS Material Selection**

The relatively large turbine sizes and weights of the potassium turbines scaled from prior land-based power conversion system studies suggests the possibility of considering the use of cesium as a working fluid to reduce turbine size. In prior space power studies the relatively low power levels required and small turbine sizes occasioned by the use of cesium as a working fluid would have resulted in small first stage turbines, very short first stage turbine blades and significant first stage tip losses. These effects are of less consequence in the larger power level turbines now being considered.

The physical and thermodynamic properties of cesium result in smaller diameter turbines with fewer stages. As a result of the reduced number of stages turbine disk temperatures are lower than for equivalent potassium systems; furthermore, the reduced expansion ratio of cesium vapor turbines should limit the growth of scroll weights and sizes in the latter stages.

Prior comparative studies of potassium and cesium turbines over a more limited temperature range indicate cesium turbines could weigh less than half that of similar potassium turbines. Specific preliminary design effort is necessary to determine the effectiveness of such potential weight reductions.

So cesium seems to have significant advantages, but is in relatively short supply. Our current fluid inventory for the 10 GW (ground output) SPS is about 6000 metric tons of potassium, over half of which is in the radiator. An "all-cesium" SPS would have roughly the same fluid mass, which is high relative to the world resources (100,000 metric tons). A cascaded system could greatly reduce the amount of cesium required: the cesium loop consists only of the boiler, turbine, pumps, contact heaters and a cesium-to-water heat exchanger. The radiator loop employs water. So at the expense of the additional elements of the two liquid system, cesium may be proved to be sufficiently abundant (if the use per SPS is only a few hundred metric tons).

Due to the complexity of the cascaded system, and the relatively large radiator required (from the low heat rejection temperature) it was decided to baseline the relatively simple, single loop, potassium system.

#### **4.1.4 Photovoltaic Satellite Cell Material Selection**

The primary materials evaluated were silicon and gallium-aluminum-arsenide/gallium arsenide (multijunction). Trades leading to selection of a baseline and a discussion of gallium availability are described in Section 4.4, "Solar Cells."

## **4.2 SOLAR CONCENTRATORS**

### **4.2.1 Photovoltaic Application**

Concentration of sunlight on solar cells has some advantages but also creates some deleterious effects. The obvious advantages are reduction in the actual solar cell material requirements, and the possibility of lower system mass if the reflecting material is significantly less massive, per unit of area projected, than the solar cell blankets.

Some of the disadvantages of concentrated systems are higher operating temperatures causing lower cell efficiencies, problems associated with uneven illumination as discussed in the Part I Final Report and updated in Section 5.1.1.4, and a higher degree of complexity in system construction and maintenance.

Both the advantages and disadvantages of concentrated systems are partially dependent on the type and degree of concentration, as well as on the type of solar cell used. Figures 4.2-1 and 4.2-2 show planar concentrators for concentration ratios of two and three, respectively. The effective limit of concentration ratio for planar concentrators is three. For higher concentration ratios Compound Parabolic Concentrators (CPC's) may be used. CPC's may be either two-dimensional, cylindrical (Fig. 4.2-3) or three-dimensional, conic (Fig. 4.2-4). The generation of a three-dimensional CPC surface is illustrated as Figure 4.2-5.

The use of concentrators was investigated in Part I of this study and are briefly revisited in Section 5 including pertinent updates.

## **4.3 SOLAR CONCENTRATION FOR THERMAL ENGINES**

The use of curved reflector surfaces and secondary concentrators allows high (over 1000) concentration ratios to be obtained for thermal engine use. Section 6.1.2.4 explains how multiple facets are used to form the curved reflectors.

## **4.4 SOLAR CELLS**

Significant advances have been made during the Part 2 study period by ERDA contractors who are developing silicon and gallium arsenide solar cells. Metal-insulation-semiconductor structure for thin-film solar cells has produced 11.7 percent efficiency, and a 21 percent limit is now predicted. Progress in solar cells based on other polycrystal and other thin-film materials has been slower. Solar cell developments occurring during the Part 2 study period are described in the paragraphs that follow.

D180-22876-3

ORIGINAL PAGE 1  
OF POOR QUALITY

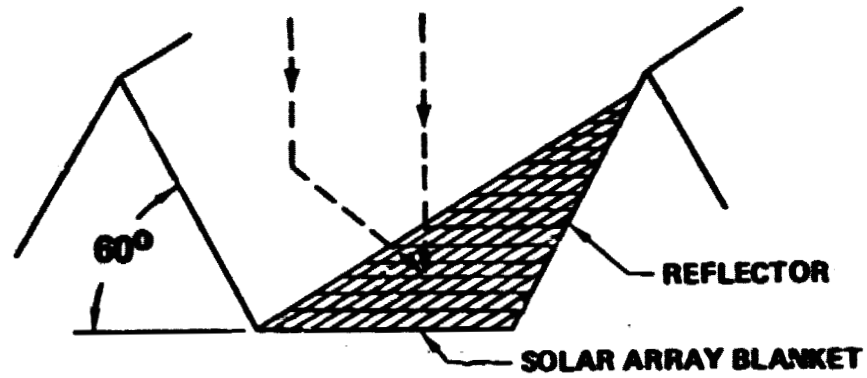


Figure 4.2-1 Concentration Ratio "2"

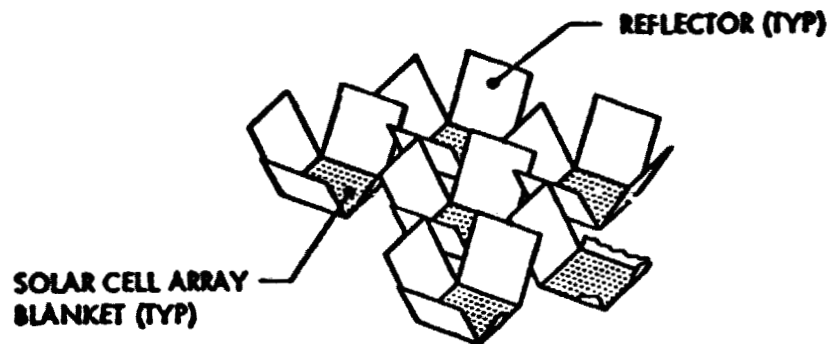


Figure 4.2-2 Concentration Ratio "3"

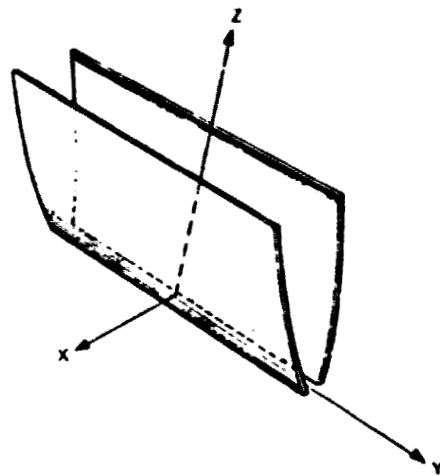


Figure 4.2-3 Cylindrical CPC (2-Dimensional)



D180-22876-3

ORIGINAL PAGE IS  
OF POOR QUALITY

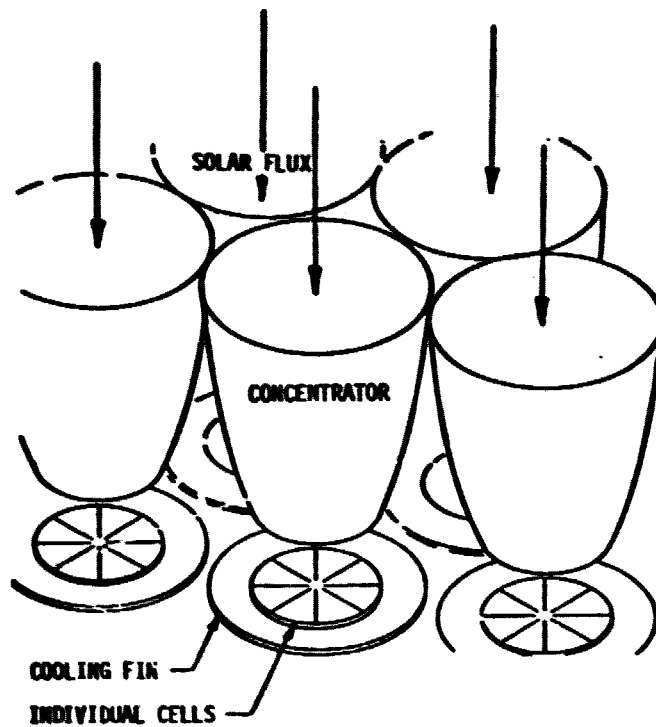


Figure 4.2-4 Conic CPC (3-Dimensional)

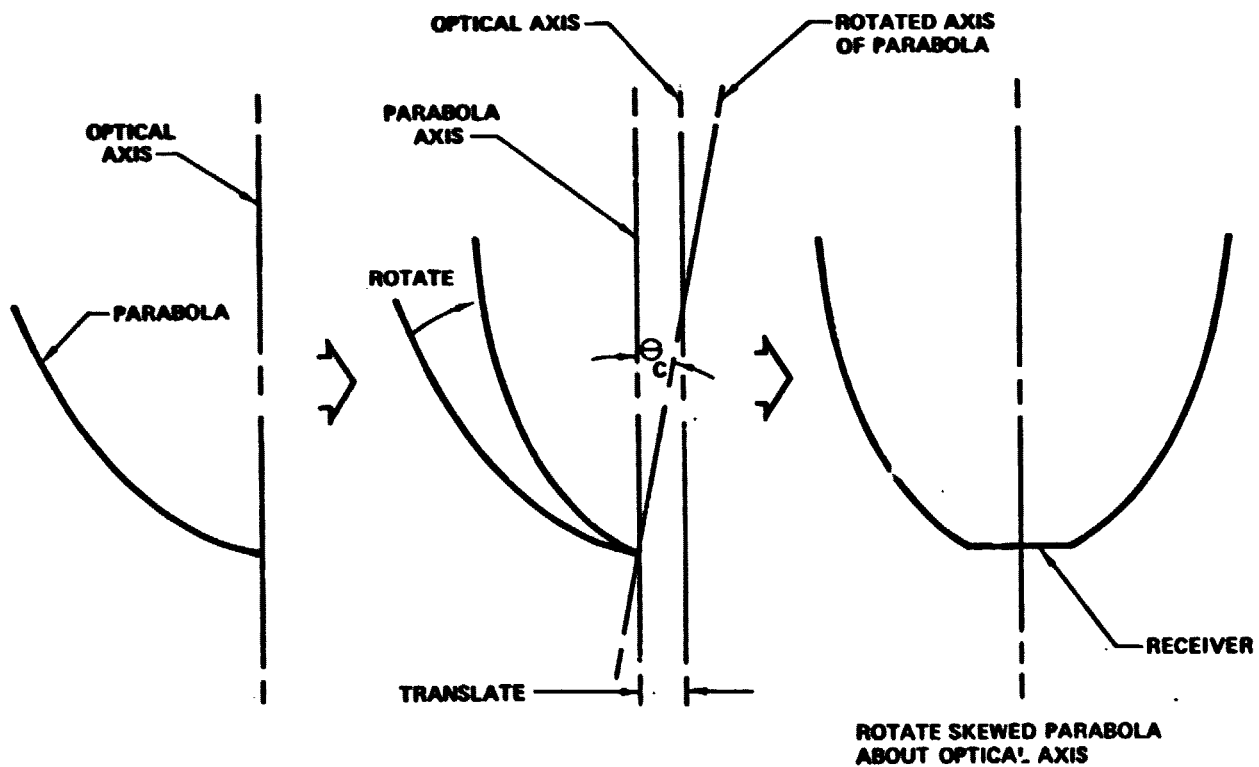


Figure 4.2-5 CPC Surface Generation (3-Dimensional)

#### 4.4.1 Silicon Single Crystal Solar Cells

Solarex Corporation, a JPL contractor developing thin single-crystal silicon solar cells, has produced over 3000 cells that are only 50  $\mu\text{m}$  (2 mils) thick (Ref. 4.4-1). The pilot line making the cells was constructed in 2.5 months, and one month later (June 1977), it had produced 2000 cells, each 4  $\text{cm}^2$  in area, for delivery to Jet Propulsion Laboratory. NASA has contracted with Solarex to keep this pilot line in production.

Cell yields improved from 0 to 61 percent during the fabrication of the 50  $\mu\text{m}$  cells. A total of 5173 cells was started, with 2049 passing final inspection. Front contact failure and breakage were the most common causes for rejection. Acceptable output of the 4  $\text{cm}^2$  cell without cover was 55 mW at 25°C when illuminated with 135.6 mW/ $\text{cm}^2$  of simulated sunlight having an air-mass-zero (AMO) spectrum. This cell output corresponds to 10.1 percent efficiency. The current-voltage curve of an 11 percent cell is shown in Figure 4.4-1. Laboratory cells have had 12.5 percent efficiency, and 75  $\mu\text{m}$  cells have been better than 13 percent efficient. One 30  $\mu\text{m}$  cell had 11 percent efficiency.

The solarex cells are sawed to a thickness of around 300  $\mu\text{m}$  from Czochralski grown single silicon crystal, and then etched to 50  $\mu\text{m}$  thickness in a 40 percent NaOH solution at 373K (212°F). The yield of the etching process has reached 90 percent. The wafers are then phosphorous diffused at 1138K (1588°F) for 15 minutes, and the 500 Å thick  $\text{P}^+$  back-surface field is generated by diffusing vacuum-deposited aluminum at 1073K (1471°F) for 10 minutes. Photolithography is used in defining the front-surface contact fingers and bus, which are layers of titanium, palladium and silver, vacuum deposited and subsequently sintered. Application of a tantalum oxide anti-reflection coating requires a temperature of 673K (751°F) for one minute. This coating might not be suitable for the solar power satellite, where we anticipate thermal annealing temperatures as high as 773K (931°F). Heliotek's 50  $\mu\text{m}$  cells, which have a textured surface to reduce reflectance, would not need an anti-reflection coating. Heliotek's cells have generated 67 mW output under 135.6 mW/ $\text{cm}^2$  of simulated AMO sunlight. This corresponds to 12.35 percent efficiency. However, Heliotek has not been able to match Solarex's cell production rate.

Four operators manned the Solarex pilot line which produced 2000 cells in one month. To build a production line making 50,000 cells a month Solarex needs \$800,000 and six months time. Such a line would produce 4  $\text{cm}^2$  cells for \$5.00 each. Solarex has also made 39  $\text{cm}^2$  hexagonal cells and 5 by 5 cm square cells from 50  $\mu\text{m}$  thick silicon.

Radiation resistance is the most surprising characteristics of the 50  $\mu\text{m}$  cells. Figure 4.4-2, published by Solarex, shows that after absorbing a fluence of  $10^{15}$  one-MeV electrons, the thin cell can still produce 92 percent of its initial output. This radiation resistance is also apparent in a cross-plot of data from JPL's "Solar Array Design Handbook" (Fig. 4.4-3). The durability of the 50  $\mu\text{m}$  cells in a solar-flare proton environment in geosynchronous orbit has not yet been established. Some insight will come when Boeing irradiates with protons the ten cells that were sent to SPIRE Corporation for electrostatic bonding to borosilicate glass covers. After the cells are irradiated, SPIRE will attempt to anneal out the radiation damage by heating with a controlled laser beam.

D180-22876-3

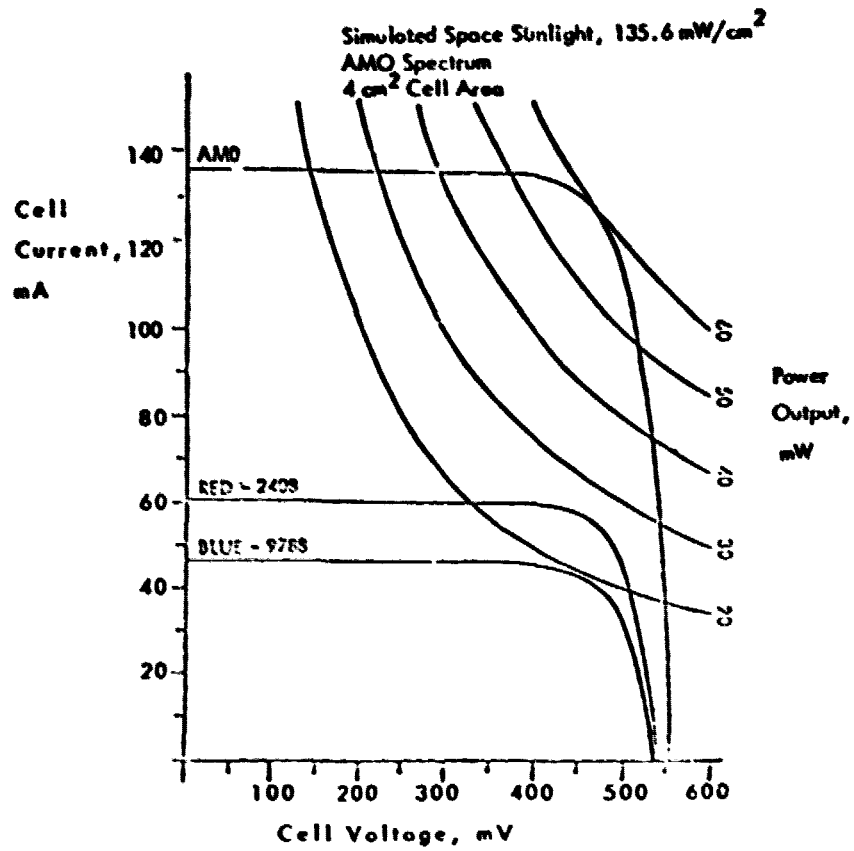


Figure 4.4-1 Solarex 50  $\mu$ m Thick Solar Cell Develops 60 mW With 11 Percent Efficiency

D180-22876-3

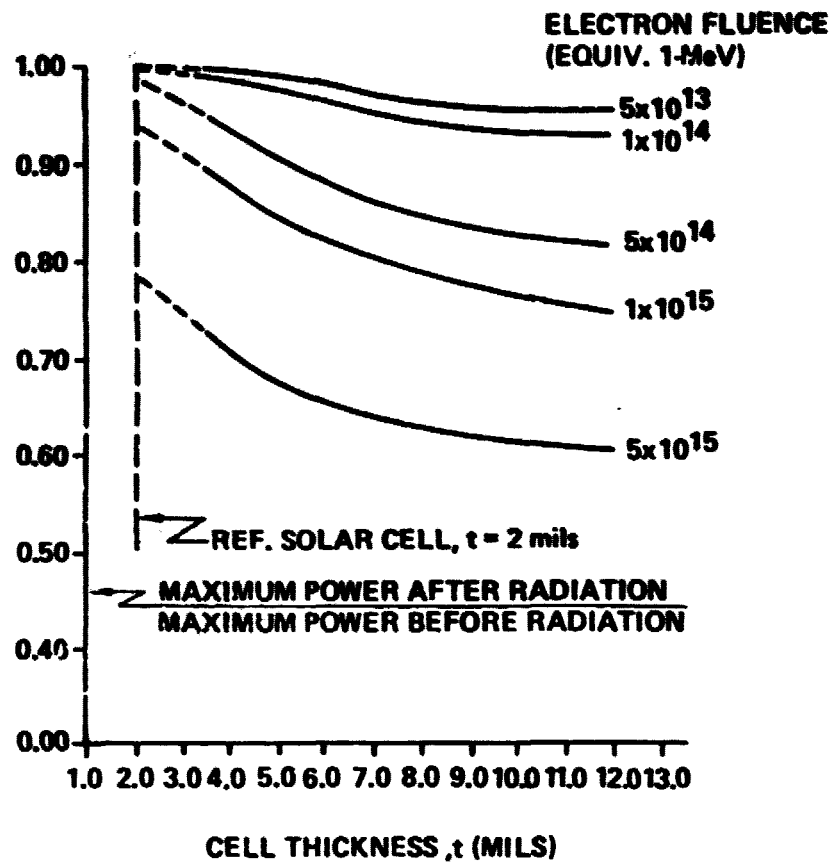


Figure 4.4-2 Fluence of  $10^{15}$  One-MeV Electrons Produces Only an 8 Percent Loss of Output In 50  $\mu$ m Thick Cell

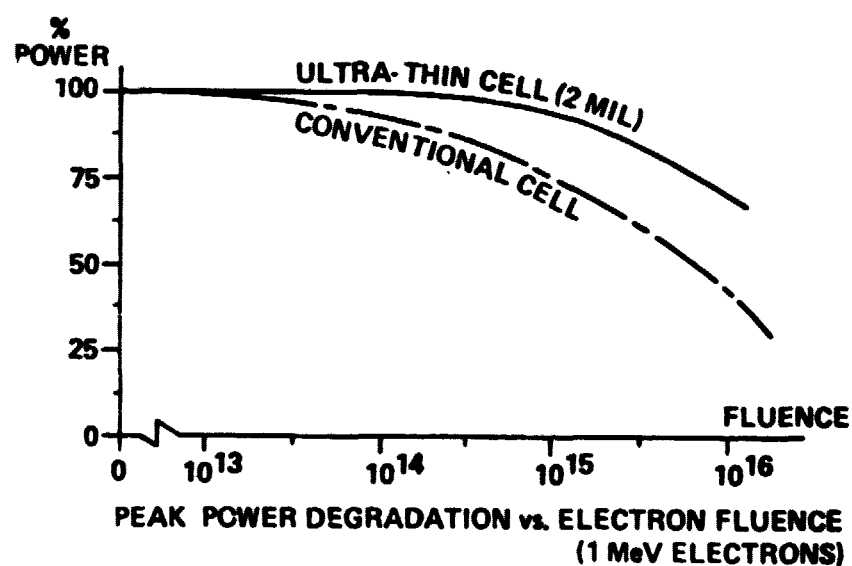


Figure 4.4-3 Thinner Silicon Solar Cells Lose Less of Their Output When Irradiated Thickness of Gallium Arsenide,  $\mu$ m

### **D180-22876-3**

Engineers at COMSAT Laboratories say that the radiation resistance and light weight of a 50  $\mu\text{m}$  cell give it a clear advantage over conventional cells for geosynchronous-orbit communication satellites. The radiation resistance also permits the use of thin substrates. Previously thin substrates were not practical for synchronous-orbit satellites because the differential contraction between the silicon in the cells and the aluminum in the substrate stressed the cell-to-cell interconnections during the long eclipses. The thermal mass of a heavy substrate was used to limit the temperature excursions to values that would permit reasonable cycle life for the panels. Now COMSAT has sponsored the development by MBB and Telefunken in Germany of a graphite epoxy substrate that weighs only 63 grams per  $\text{m}^2$ . The matrix of graphite is so arranged that the coefficient of thermal expansion of the resulting sheet matches precisely the coefficient of thermal expansion of the silicon in the cells. Tests at COMSAT Labs have shown that with this new substrate, thermal cycling in geosynchronous orbit will no longer be a serious life-limiting problem.

COMSAT Labs, with the assistance of the NASA Lewis Research Center, had tested lightweight substrates for their ability to dissipate spacecraft charging in geosynchronous orbit. The conductivity of the carbon in the graphite substrate was sufficient to limit charging in a 63 grams per  $\text{m}^2$  substrate to one kV. However, during the tests the investigators discovered that a light coating of soot on the back of any insulated panel will limit the spacecraft charging voltage to less than 100 volts. Soot, suitably applied and covered with a protective coating, will probably solve the charging problem for insulated solar panels.

#### **4.4.2 Gallium Arsenide Solar Cells**

Previous contract reports showed that the nation's potential gallium resources could not support a program of one or more solar power satellites per year if single-crystal 125- $\mu\text{m}$  (5 mil) thick cells are used. Figure 4.4-4, reproduced from previous work, shows the gap between gallium availability and requirements for the solar power satellite program.

Availability of gallium and other photovoltaic materials is being investigated by Batelle Northwest Laboratories, with ERDA funding the work. ERDA has not yet released the first report, which will include a comprehensive picture of gallium availability. The report will probably state that no significant sources of gallium other than bauxite, zinc ore, and fly ash have been identified. However, it will note that ALCOA has determined that the recovery of gallium from bauxite can easily be as high as 80 percent, rather than the 10 percent previously assumed. It will also stress that gallium is a by-product, and that expanding the production of the basic metals just to increase gallium output will probably not be practical. By 1990 the U.S. could be producing  $2.5 \times 10^6$  kg per year of gallium as a by-product from zinc and aluminum refining.

On the other hand, the thin-film high-efficiency gallium-arsenide solar cell may not be far away. Such a cell would be made by depositing on a suitable substrate, by evaporation or by chemical means, a layer of gallium arsenide which is between 4 and 10  $\mu\text{m}$  thick. The crystallites on the film would then be consolidated to a diameter of perhaps 15  $\mu\text{m}$ , and junctions would be formed on them. Suitably large crystallites have now been grown at several institutions. At MIT's Lincoln Labs, for example, 25  $\mu\text{m}$  crystallites have been grown on films 2  $\mu\text{m}$  thick by heating with a laser beam.

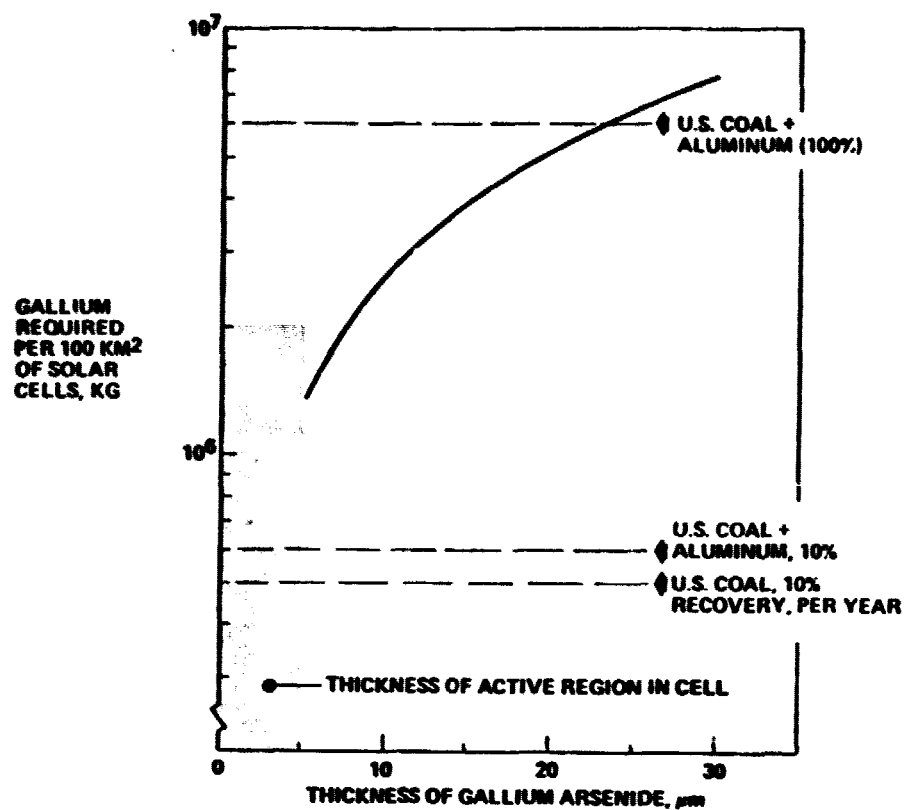


Figure 4.4-4. Gallium Required for Solar Power Satellite

### D180-22876-3

Perhaps the most important breakthrough has been the formation of a gallium arsenide homojunction cell by John C. Fan of MIT's Lincoln Labs. Previous high-efficiency gallium arsenide solar cells have had a heterojunction formed with gallium-aluminum arsenide. Fan's cell, which has a very thin degenerate  $N^+$  layer on p-type single-crystal gallium arsenide, had a 20.5 percent efficiency in air-mass-one sunlight. The 500 Å  $N^+$  layer provides high conductivity with low light absorption, and anodizing reduces surface recombination velocity. No vacuum processes are involved in making the cell. The next step for Fan is to generate homojunctions on his thin-film gallium arsenide with 25 μm crystallites.

Another approach to thin-film gallium arsenide cells is JPL's AMOS concept in which 16.2 percent efficiency has been demonstrated, but using sliced polycrystalline gallium arsenide rather than thin deposited films of gallium arsenide. The AMOS development is now funded with \$363K from ERDA.

In general, the thin-film gallium arsenide work looks good with large grain sizes grown, and with short-circuit currents approaching those of single-crystal cells. Achieving good contacts seems to be the most important remaining problem. Gold and palladium make good contacts, but are too costly.

#### 4.4.3 Other Thin Solar Cells

The status of other thin-film solar cells is summarized in Table 4.4-1. The changes during the past year in achieved efficiency of cells other than silicon and gallium arsenide has not been significant. Very few materials have produced stable conversion efficiencies above 10 percent.

Dr. Morton Prince, at ERDA's review of its contracted solar cell development, summarized the status of thin-film p-n junction silicon solar cells as follows: The key problem with these cells is the substrate. If the low-cost silicon solar cell program achieves its objectives, then the lowest cost substrate for thin-film cells may well be single-crystal silicon! Grain-boundary recombination limits the performance of junction-type thin-film silicon concepts, which are based on polycrystalline silicon. Graphite could be a low-cost substrate for amorphous silicon. Hole traps, which collapse the depletion region and reduce the diffusion length of holes, are the most significant problem in amorphous silicon. RCA workers have obtained 6 percent efficiency from thin-film amorphous-silicon cells produced by plasma deposition from silane gas. Higher efficiency could be had if hole diffusion length could be increased.

Recrystallization of polycrystal and amorphous films of silicon is a tough problem, according to Dr. Allan Kirkpatrick of SPIRE. No one has been able to do it yet.

D180-22876-3

Table 4.4-1 Solar Cell Development Status in October, 1977, for Cell Types Pertinent  
To The Solar Power Satellite

SPG 26

AIR-MASS-ZERO CONVERSION EFFICIENCY, PERCENT

CELL	TYPE	PRODUCTION CELLS 1977	RESEARCH CELLS		PROBABLE 1987	THEORETICAL LIMIT	NOTES
			BEST ACHIEVED	1978			
GALLIUM ARSENIDE	SINGLE CRYSTAL	17	18.5	21	22	25	HUGHES ACHIEVED 17.5% IN 2x2cm SPACE CELLS. BEING DEVELOPED BY JPL, VARIAN, SMU, MIT LINCOLN LABS FOR ERDA
	THIN FILM		12	15	17	25	
SILICON	SINGLE CRYSTAL	14.6	15.6	18	19	22	WOLF GIVES 19% GOAL  { CLAIMED TO BE RADIATION RESISTANT
	POLYCRYSTAL		12.0	14	16	22	
	THIN FILM		7.2	12	13	22	
	METALLURGICAL		6.0	10	12	22	
	VERTICAL JUNCTION		13	15	18	22	
CADMIUM SULFIDE			8.5	10	10		
InPCdS	SINGLE CRYSTAL		15	17			(?) IN RESOURCES
	THIN FILM		5.7	10			
InP/InSnO	SINGLE CRYSTAL		15		17		{ SPLUTTERED, SCHOTTKY BARRIER, BELL LABS BEING DEVELOPED AT BOEING
CuInSe	THIN FILM		3			17	
Cd/CuInSe	THIN FILM		6.2			17	
Si/GaAs	TANDEM JUNCTION					34	



#### 4.4.4 Metal-Insulation-Semiconductor Cells

Development of Schottky-barrier diodes inspired the development of solar cells incorporating Schottky barriers rather than a simple P-N junction. Schottky barriers are potentially advantageous in that the bulk material in the solar cell need not be single-crystal, nor need it be very thick. One approach being developed by RCA Laboratories applies 1- $\mu\text{m}$  thick films on amorphous silicon, with platinum Schottky barriers and zirconium dioxide antireflection coatings to achieve 5.5 percent conversion efficiency (Ref. 4.4-2). Amorphous silicon, being highly absorptive, need be only one  $\mu\text{m}$  thick, and the substrate can be steel or glass. Open-circuit voltages are highest with the most expensive metals. A platinum barrier produced 800 mV, whereas nickel, chromium and aluminum gave voltages below 300 mV. Of course the value of the metal used is trivial, the Schottky barrier metallization being only 50 to 100  $\text{\AA}$  thick.

Estimates had been made of the efficiency versus grain size for polycrystalline p-n junction solar cells of silicon and gallium arsenide. These estimates used one and two-dimensional analyses to simplify the mathematics. Lanza and Hovel of IBM, using a sophisticated analysis in which the three-dimensional nature of the grains in polycrystalline cells is taken into account, determined that silicon cells 10  $\mu\text{m}$  thick will be at best 8 percent efficient for 100  $\mu\text{m}$  grain sizes and 10 percent efficient if 25  $\mu\text{m}$  thick. (See Reference 4.4-3). They found that gallium arsenide 2  $\mu\text{m}$  thick cells can be 12 percent efficient if the grain size is 3  $\mu\text{m}$  or greater. Figures 4.4-5 and 4.4-6 summarize their conclusions.

The metal-insulation-semiconductor (MIS) cell does not have the limitations cited by Lanza and Hovel. The interfacial insulating layer or oxide between the metal and semiconductor of the Schottky barrier increases conversion efficiency considerably. For example, Stirn and Yeh report that they obtained 16.2 percent efficiency in JPL's AMOS gallium arsenide cell. In fact, Lofersky, et al predict that the theoretical maximum efficiency of these cells can be 21 percent under Earth-surface illumination with high substrate doping, low metal work function, and low interface defect density. (See Reference 4.4-4). The MIS cell, also called a metal-oxide-semiconductor (MOS) cell because the insulation is usually silicon oxide, typically consists of a p-type layer of silicon, doped to 0.1  $\Omega\text{cm}$  resistivity, onto which an oxide layer generated by hot nitric acid, anodic oxidation, or boiling de-ionized water. The oxide layer is usually less than 60  $\text{\AA}$  thick. The metal, for example titanium, is evaporated onto a thickness of 50  $\text{\AA}$ , making its resistance about 800 ohms per square. Its transmission may be only 60 percent. Contact to the metal is then made with a silver grid.

The best performance of a MIS cell was reported by Fabre et al from the Laboratoires d'Electronique et de Physique Appliquee in France (Ref. 4.4-5). They obtained an efficiency of 11.7 percent with a 2.6  $\text{cm}^2$  cell (Fig. 4.4-7).

Professor Loferski thought that the MIS was the most likely configuration to be used on the solar power satellite.

D180-22876-3

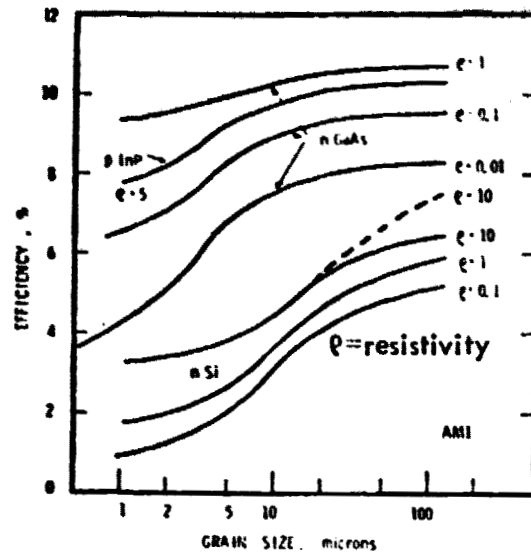


**Figure 4.4-5** The effect of grain size on AM1 efficiency of 2  $\mu\text{m}$  thick GaAs and InP cells and 10  $\mu\text{m}$  thick (solid lines) and 25  $\mu\text{m}$  thick (dotted lines) Si cells. The "classical" Schottky barrier dark current is used, and the metal transparency is 100%.

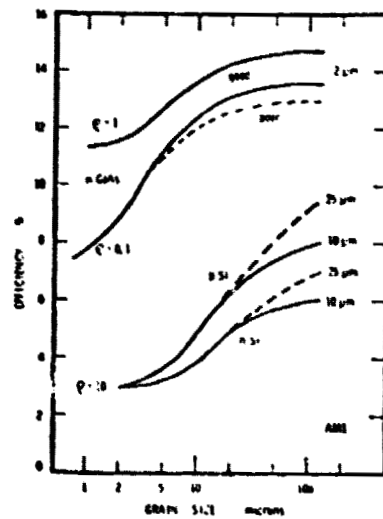


**Figure 4.4-6** The effect of grain size on the AM1 efficiency of 2  $\mu\text{m}$  thick GaAs and 10 and 25  $\mu\text{m}$  thick Si MOS Schottky barrier cells. The transmittance of 75Å of Au covered by an AR coating was used.

D180-22876-3

ORIGINAL PAGE  
OF POOR QUALITY

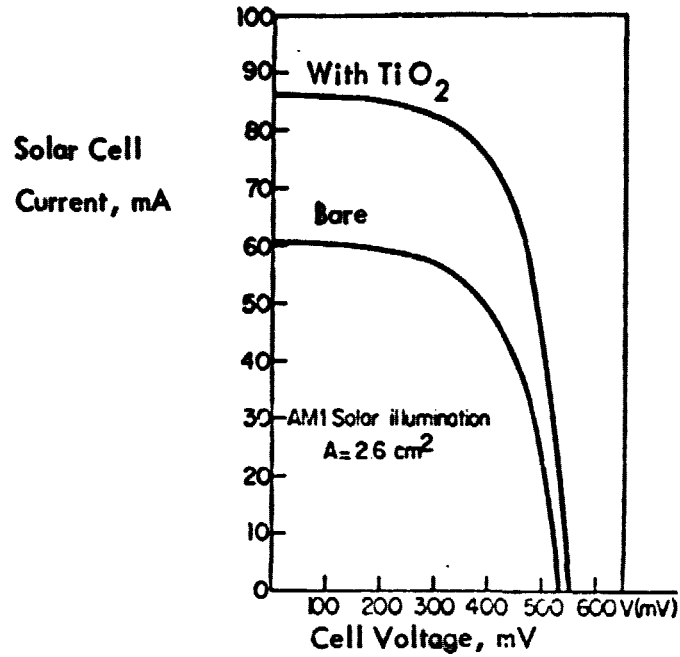


Figure 4.4-7 MIS Solar Cell Developed in France has 11.7 Percent Efficiency

#### 4.4.5 Other Solar Cell Developments

Oak Ridge National Laboratory (ORNL) has been making respectable solar cells by ion implantation and also by generating dopants by transmuting elements with neutrons. The neutrons, with a 2-meter range in silicon, transmute silicon atoms into phosphorous with a uniformity that cannot be approached by other means. However, these radiation processes severely damage the crystal structure. ONRL scientists have found that the radiation damage is better annealed out with a laser beam than with oven-heating. Apparently oven-heating causes additional diffusion to take place degrading cell performance.

A sawtooth cover invented by A. Neulenberg of COMSAT is a real breakthrough (Fig. 4.4-8). The sawtooth cover makes the grid lines invisible. Besides eliminating the reflection from the grids, the sawtooth cover makes it possible to put on enough grids to make the series resistance of the cell virtually zero. The cover can also be made a little larger than the cell to capture the light that would otherwise be trapped in the gap between cells. The new cover can increase solar cell output by as much as 12 percent.

#### 4.4.6 Conclusions

At this time 50  $\mu\text{m}$  single-crystal solar cells look best for the reference design of the solar power satellite. While today these cells do not have the desired 18 percent efficiency in standard air-mass-zero conditions, there are many approaches that have a good chance of achieving this 18 percent goal. One of the following will probably succeed.

- *Single-Crystal Silicon Cells.* The 50  $\mu\text{m}$  cells are being developed for today's space applications where the combination of 12.5 percent efficiency, low weight, and radiation resistance make these cells clearly superior to conventional cells. The program emphasis is now on production. Many opportunities for improving efficiency are available. For example, Solarex chose to throw away the power that would be available from infrared photons because texturing of the cell surface is not compatible with the Solarex photolithographic process for depositing grid lines.
- *Thin-Film Gallium Arsenide.* Invention of the homojunction gallium arsenide solar cell, together with the laser-generated 25  $\mu\text{m}$  crystallites in 2  $\mu\text{m}$  thick films of gallium arsenide, open the route to high-efficiency thin-film gallium arsenide cells. Cell thickness need by only some 2 to 8  $\mu\text{m}$ . The resulting gallium requirement for solar power satellites may become attainable with U.S. national resources.
- *Gallium Arsenide AMOS Cell.* JPL has already achieved 16.2 percent efficiency with its AMOS cell, but with sliced polycrystalline gallium arsenide. Here again only a few micrometers of gallium arsenide is required for high cell efficiency. JPL's AMOS development program is well funded.

D180-22876-3

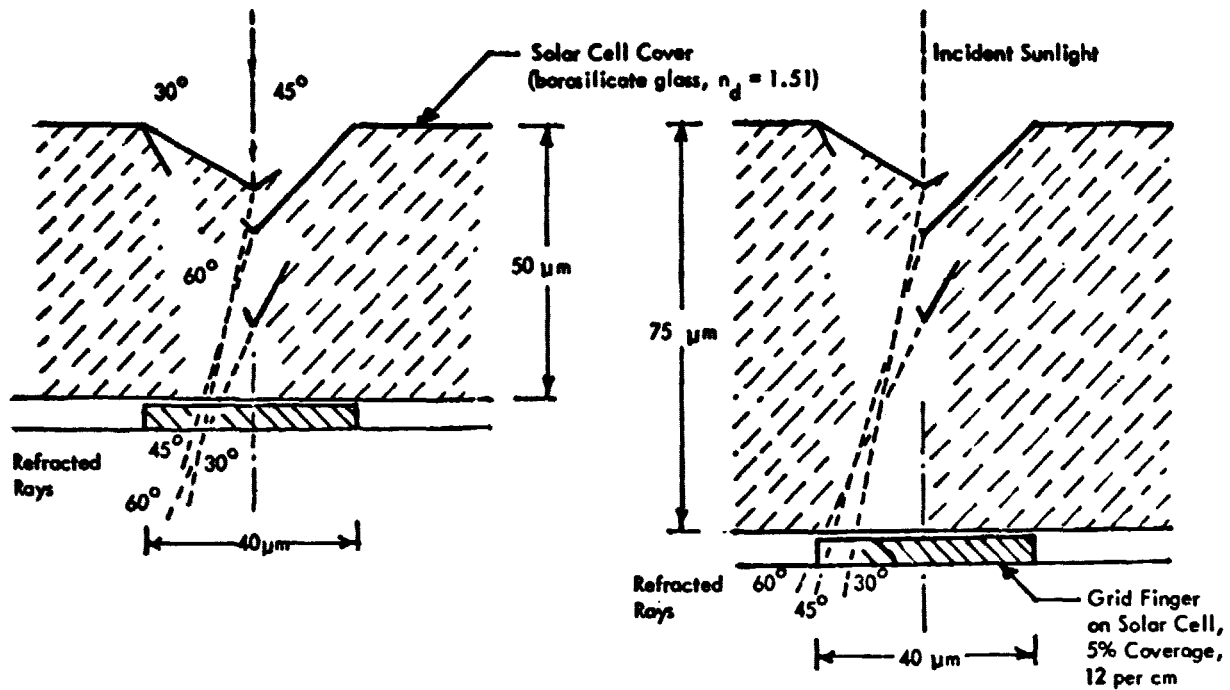


Figure 4.4-8 Grooves in Cell Cover Refract Sunlight

### **D180-22876-3**

- **Metal - Oxide - Semiconductor.** Fourteen papers at the 12th Photovoltaic Specialists Conference (November, 1976) dealt with metal-insulator-semiconductor (MIS) or its equivalent, metal oxide semiconductors (MOS) solar cells. Efficiencies up to 11.7 percent were reported. Dr. Loferski of Brown University predicts 21 percent as being achievable. Significant progress can be expected in the next ten years.

#### **References**

- 4.4-1 Lindmayer, J., "Pilot Line Report, Development of a High Efficiency Thin Solar Cell," Report SX/105PL, June, 1977. Solarex Corporation.
- 4.4-2 Carlson, D. E., Wroblewski, C. R., Triano, A. R., and Daniel, R. E., "Solar Cells Using Schottky Barriers on Amorphous Silicon," PROCEEDINGS OF THE 12th PHOTOVOLTAIC SPECIALISTS CONFERENCE, 1976
- 4.4-3 Lanze, C., and Hovel, H. J., "Efficiency Calculations for Thin Film Polycrystalline Semiconductor Schottky Barrier Solar Cells," PROCEEDINGS OF THE 12th PHOTOVOLTAIC SPECIALISTS CONFERENCE, 1976
- 4.4-4 St. Pierre, J. A., Singh, R., Shewchuk, J., and Loferski, J. J., "Solar Cells Based on Metal-Insulator-Semiconductor Structures," PROCEEDINGS OF THE 12th PHOTOVOLTAIC SPECIALISTS CONFERENCE, 1976
- 4.4-5 Fabre, E., Michel, J., and Budget, Y., "Photocurrent Analysis in MIS Solar Cells," PROCEEDINGS OF THE 12th PHOTOVOLTAIC SPECIALISTS CONFERENCE, 1976

#### **4.5 TURBOGENERATOR SYSTEMS**

##### **4.5.1 Potassium Rankine Systems**

###### **4.5.1.1 Rationale for Rankine**

Trade studies performed in Parts I & II of this study led to the selection of the Rankine cycle as the most promising "near-technology" thermal engine option. The nearest competitor, the closed cycle Brayton, is potentially relatively light only with the extremely high (1600K = 2420°F) or higher inlet temperature. The potassium Rankine SPS has approximately the mass of the silicon photovoltaic SPS when the turbine inlet temperature is only 1242K (1776°F).

### D180-22876-3

Figure 4.5-1 compares Brayton and Rankine systems at the same turbine inlet temperature (1242K = 1776 °F). The abscissa is the cycle temperature ratio, defined as the ratio of the cycle working fluid minimum and maximum temperatures. (The Brayton working fluid is helium; the Rankine fluid is potassium). Both systems in this figure produce  $10^9$  watts busbar. Note that the Brayton cycle efficiency can be quite high: 45% at a temperature ratio of 0.25; however, it falls to only 10% at a temperature ratio of 0.48. This is because compressor pumping power becomes so large as to take nearly all of the power produced by the turbine. The most significant factors in this figure are the "radiator effective temperature" and the "radiator area." Since radiator heat rejection is proportional to  $T^4$ , a high temperature radiator is very effective, even if the power to be rejected is large (due to low efficiency). The minimum Brayton radiator area of  $1.03 \text{ km}^2$  occurs at a cycle temperature ratio of 0.41 where the cycle efficiency is 21%. The Rankine radiator area of  $0.18 \text{ km}^2$  occurs at a cycle temperature ratio of 0.75 where the efficiency is 19%. At the points just mentioned, the Brayton solar collector area is  $4.6 \text{ km}^2$ ; the Rankine collector area is  $5.3 \text{ km}^2$ .

The fundamental difference in mass results from the fact that the radiator contains pressure vessels and is exposed to the meteoroid environment. Even with heat pipe radiating elements, if the working fluid loss in 30 years of operation is to be kept to a reasonable amount (say 10%), significant meteoroid armoring is required. The solar concentrator is relatively unaffected by penetrations and can be quite thin.

If a power level appropriate to a "10 GW" SPS is required (approximately 18GW busbar), then the areas in Figure 4.5-1 must be multiplied by 18. The resultant radiating areas are  $18.54 \text{ km}^2$ , Brayton and  $3.24 \text{ km}^2$ , Rankine. The corresponding radiator masses are  $92 \times 10^6 \text{ kg}$ , Brayton and  $16 \times 10^6 \text{ kg}$ , Rankine. The Brayton radiator is more massive than the entire Rankine SPS including transmitters. Lighter Brayton satellites, previously analyzed, achieved lower mass by the use of higher turbine inlet temperatures (with ceramic components).

Of course the preceding analysis is based on equal mass per unit area for the two radiator types. Our analyses indicate the Rankine radiator is actually lighter per unit area since one manifold contains vapor as opposed to the two liquid manifolds in the NaK system which is best employed in the Brayton radiator.

As a consequence, the Rankine SPS has been selected as the thermal engine baseline. Additional data relative to this selection is contained in the Part I final report for this study "Solar Power Satellite System Definition Study, Part I, Volume II, System Requirements and Energy Conversion Options, July 29, 1977" (Boeing document D180-20689-2).

#### 4.5.1.2 Data Base

A significant alkali metal data base was established in the 1960's as a result of efforts by the NASA, AEC, Air Force and their subcontractors. Figure 4.5-2 summarizes this data base.

D180-22876-3

ORIGINAL PAGE IS  
OF POOR QUALITY

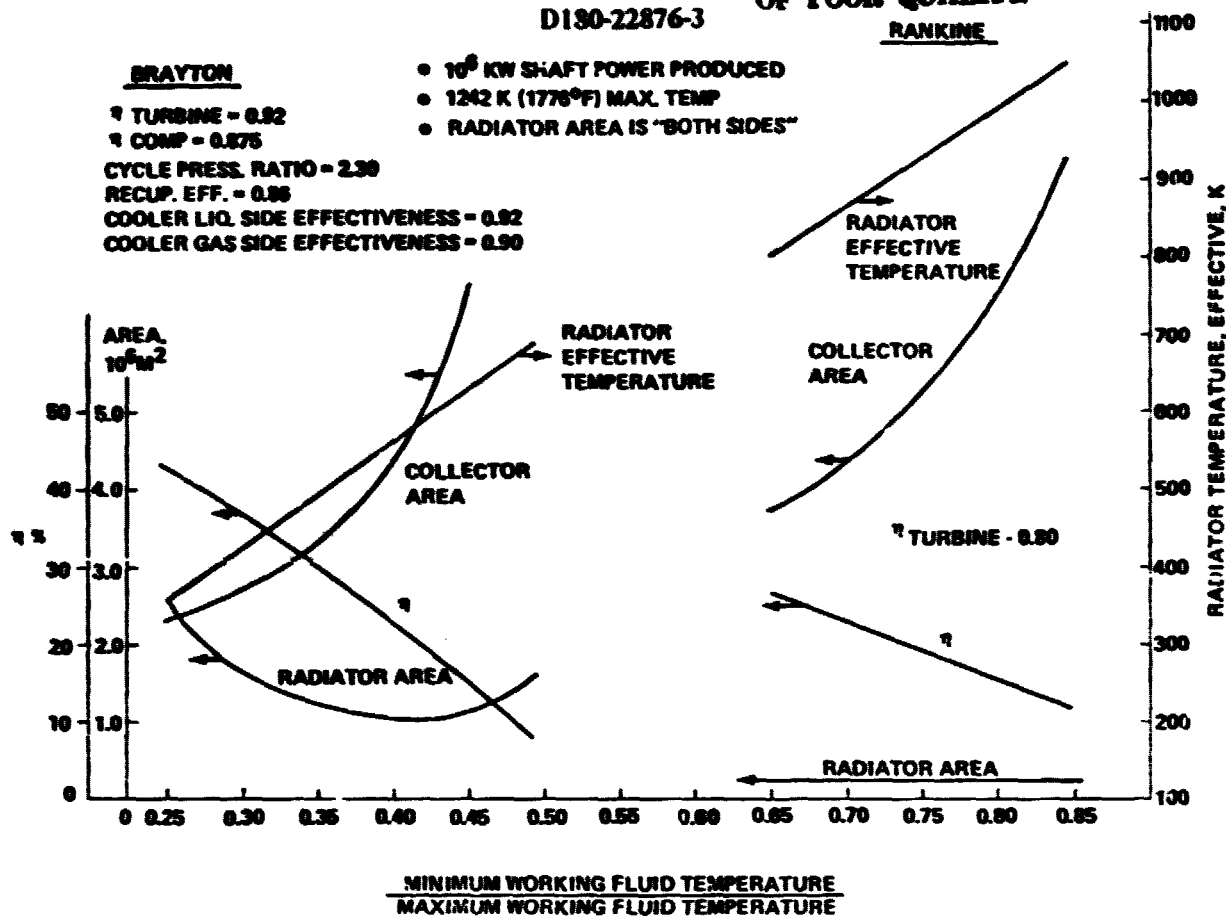


Figure 4.5-1 Cycle Temperature Influence on Brayton and Rankine Cycles

TURBINE EFFICIENCY: 80%; LeRe TESTS

EROSION CONTROL: THREE METHODS DEMONSTRATED

POTASSIUM HARDWARE:

	Potassium (800,000 hours testing)							Cesium (>23,000 hours testing)  (b)
	AirResearch	GE	JPL	NASA-Lewis	ORNL	PaW	Other <sup>a</sup>	
	Testing hours accumulated							
Corrosion test systems:								
Boiling	1300	25 500	-----	-----	62 800	12 000	-----	3500
All-liquid	-----	-----	-----	-----	-----	-----	156 000	-----
Component test systems, boiling	5900	19 600	-----	1000	2 800	4 900	300	2400
Simulated powerplant systems	-----	-----	~1000	-----	10 200	-----	-----	-----
Boilers	7200	40 100	1000	1000	75 800	16 900	300	6000
Turbines	3050	10 100	-----	-----	5 000	-----	100	-----
Boiler feed pumps:								
Electromagnetic	7200	34 600	3600	1000	26 900	4 900	3 300	5600
Turbine driven	-----	-----	-----	-----	5 000	-----	-----	-----
Other pumps	5900	18 600	3600	1600	6 100	1 300	57 600	-----
Condensers	7200	40 100	~1000	1600	75 800	16 900	300	5600
Seals	3050	10 100	-----	-----	-----	-----	-----	-----
Bearing tests	3000	-----	-----	-----	4 500	-----	1 600	-----

<sup>a</sup> Includes testing hours of Aerojet Nucleonics, Allison, Rocketdyne, United Nuclear.

<sup>b</sup> Includes testing hours of Brookhaven, Aerojet Nucleonics, Westinghouse Astronuclear.

Figure 4.5-2 National Alkali Metal Data Base (From General Electric)



### **D180-22876-3**

As a result of this effort, which was primarily directed toward small scale nuclear power applications in space, the following summary statements regarding alkali metal Rankine cycle technology status:

- (1) A 10 year \$24 M (1968\$) space power program was conducted.
- (2) 12,000 hours of potassium turbine testing was accumulated
- (3) 800,000 hours of alkali metal tests were conducted
- (4) Methods were established for refractory alloy processing, forming machining and welding.
- (5) Methods for alkali metal purification, analysis, handling and control were established.
- (6) Materials compatibility with alkali metals were determined
- (7) Alkali metal bearings were investigated
- (8) Electromagnetic boiler feed pumps were operated 10,000 hours at 1000 to 1400 °F
- (9) Dump tanks, getting systems, valves, etc., were evaluated
- (10) A 450 kWe space-type turbo-alternator went through a preliminary design cycle

Over 10,000 hours of potassium turbine testing have been conducted on two-and three-stage turbines operating in a 3000 KW AISI Type 316 stainless steel test facility. The turbines operated at temperatures up to 1117K (1550 °F) and represented the latter stages of a space power system intended for a 1422K (2100°F) turbine inlet temperature. Turbine design and performance predictions were verified. Various turbine disc, blade and casing materials were evaluated, including superalloys and molybdenum alloys. Methods of controlling moisture and blade erosion on the turbine were evaluated including droplet extraction at the turbine blade tips and in interstage swirl devices. The analysis, handling and control of potassium during system operation and explicit operating and maintenance experience was gained.

#### **4.5.1.3 Turbine Systems**

Potassium Rankine turbines are similar to the water Rankine turbines used to generate approximately 90% of our current terrestrial electrical power. Shown in Figure 4.5-3 is a two-stage turbine built by General Electric, our subcontractor in this area. Potassium vapor from a boiler is admitted to the turbine from the left. After passing through the two stators and rotors the expanded (and consequently cooler) flow is collected in the plenum at the right. The machine in the photograph had a disc diameter of approximately 0.25M (10 inches).

“Full size” turbines would have more stages (4 to 8). Also, by mounting two turbines “end-to-end,” with common shafts and housing, the axial thrusts resulting from flow through the turbines are balanced. Details of the selected turbine configuration are given in Section 5.1.2.

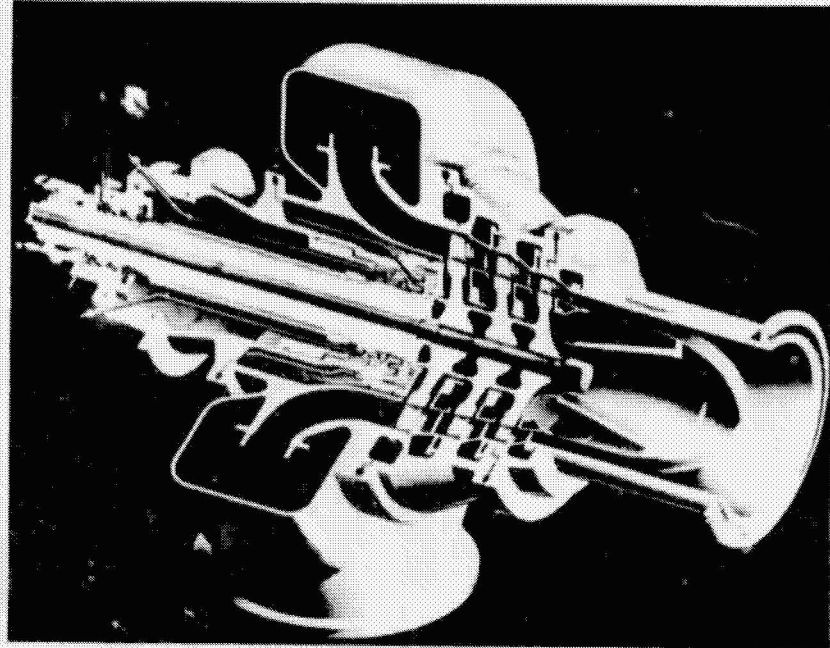
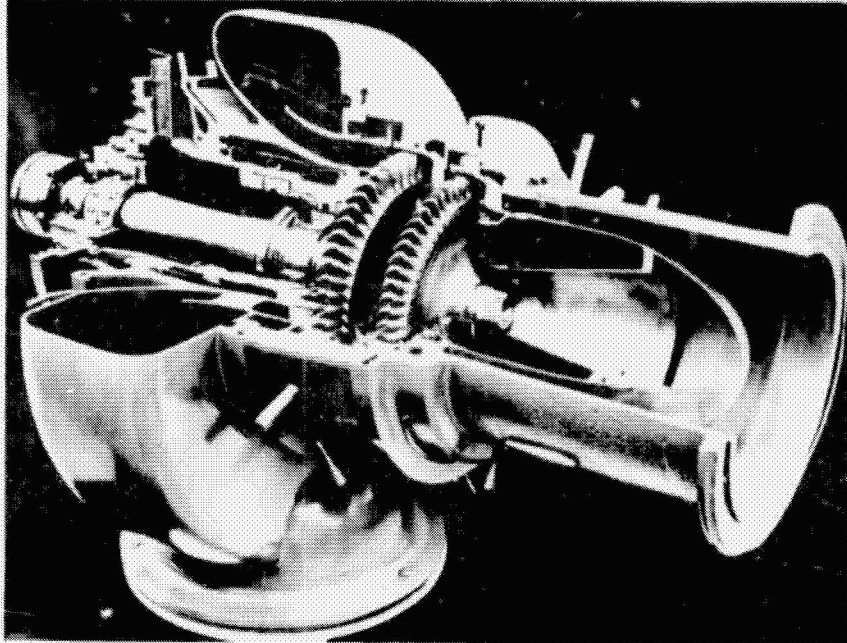


Figure 4.5-3. Potassium Turbine Testing

D180-22876-3

ORIGINAL PAGE IS  
OF POOR QUALITY

#### **4.5.2 Generators**

The microwave transmitter requires direct current at approximately 40,000 volts. The power distribution system (see section 4.6) links the generators to the microwave transmitters. The selected power distribution system is passive, i.e., it does not convert the generator output to a different form. Hence, the generators are high voltage d.c. machines. They are directly driven by the turbines, without gearing. The selected rotational speed is 7200 rpm.

Generator design is based on light weight systems currently evolving for high power airborne use. Although there is a mass advantage to cryogenic generators, this tends to be offset by the mass of the cooling system (cryostat). This offsetting effect makes refrigerated power distribution inferior to passive, radiation cooled systems (as explained in Section 4.6). It is advantageous to operate generators at relatively high temperature to minimize the mass of the associated radiators. These radiators are required since the surface area of the generators themselves is not sufficient for the required waste heat rejection.

#### **4.5.3 Potassium Boilers**

As previously explained, a significant data base exists relative to alkali metal boiling and condensation. The boilers (one per turbogenerator) are mounted inside the cavity absorber where they are exposed to the requisite thermal flux, produced by the solar concentrator system. Zero gravity conditions favor the use of once-through boiling and the delivery of dry, slightly superheated vapor.

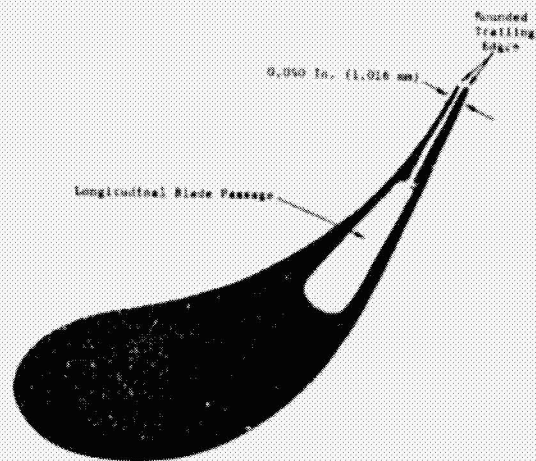
Boiling can best occur when the liquid is in contact with the tube walls. This could be "encouraged" by centrifugal force induced by causing a swirling motion in the flow.

If boiler droplet emission proves to be a problem, a separator device could be provided in the vapor duct between the boiler and the turbine inlet. Figure 4.5-4 shows such a separator (separators of this type are sometimes called "demisters"). Such separators have achieved 80% effectiveness.

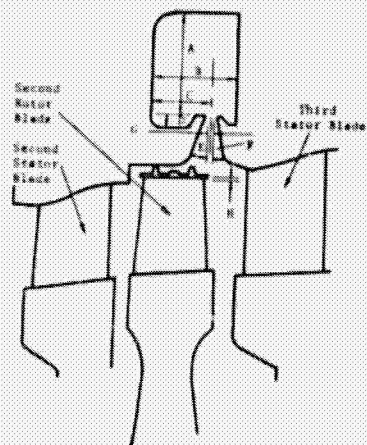
#### **4.5.4 Pumps**

Through part 1 of this study, motor driven mechanical pumps had been favored for radiator fluid pumping, since their overall efficiency of at least 80% was critical in achieving low SPS mass. This was because radiator pumping power is quite high in the Brayton systems then receiving primary emphasis. Since this pump type involves two parts (motor and pump), a rotating seal is required. This seal and the bearings were potential sources of reliability problems.

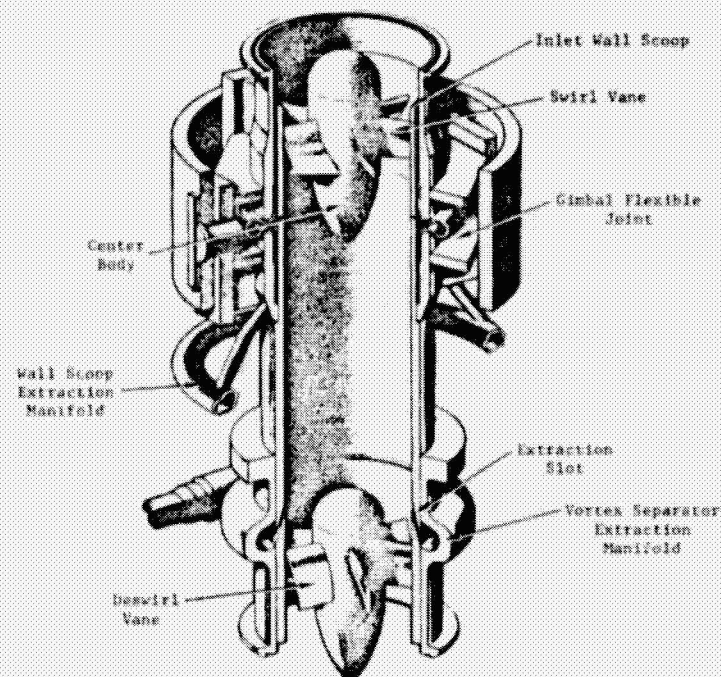
When Rankine systems were baselined for part 2 of the study, it was found that electromagnetic (EM) pumps could be effectively used despite their high specific mass and low efficiency. This is because the Rankine pumping power is relatively low.



STATOR VANE TRAILING EDGE  
DROPLET EXTRACTION



ROTOR LIQUID EXTRACTION



EXTERNAL INTERSTAGE VORTEX LIQUID SEPARATION

Figure 4.5-4. Moisture Extraction Effectiveness Determined

D180-22876-3

ORIGINAL PAGE IS  
OF POOR QUALITY

### **D180-22876-3**

**EM pumps have been used extensively in the pumping of liquid metals. They have the advantages of absence of seals and bearings, operating reliability and reduced maintenance requirements.**

**For the Rankine cycle space power program, a light weight 193Kg (425 lbs.) electromagnetic boiler feed pump, capable of operating at a liquid metal temperature up to 1033K (1400°F), was designed, built and tested for 10,000 hours. It pumped 811K (1000°F) potassium at flow rates up to 1.47kg/sec (3.25 lb/sec) at a developed head of 1650kPa (240 psi), a NPSH of 48kPa (7 psi) and an efficiency of 16.5%. The pump featured a T-111 alloy helical pump duct and a high temperature stator with a 811K (1000°F) maximum operating temperature; the stator materials consisted of Hiperc 27 magnetic laminations, 99% alumina slot insulators, type "S" glass tape interwinding insulation and nickelclad silver conductors joined by brazing in the end turns. Pump windings were cooled by liquid NaK at 775K (900°F).**

**Large size annular linear EM pumps are under development for the Liquid Metal Fast Breeder Reactor. A 680Kg/sec (1602 lb/sec) pump has been built and is awaiting test; pumps of larger sizes have been considered in the range of 1409; 3435; 3759; and 6100 Kg/sec (3108; 7573; 8289 and 13470 lb/sec). Weight and cost estimates for commercial land based versions of these pumps have been initiated. While these pumps were designed for handling sodium at about 732K (858°F), their development indicates pump scale-up experience well above that of the earlier higher temperature boiler feed pumps for Rankine space power systems.**

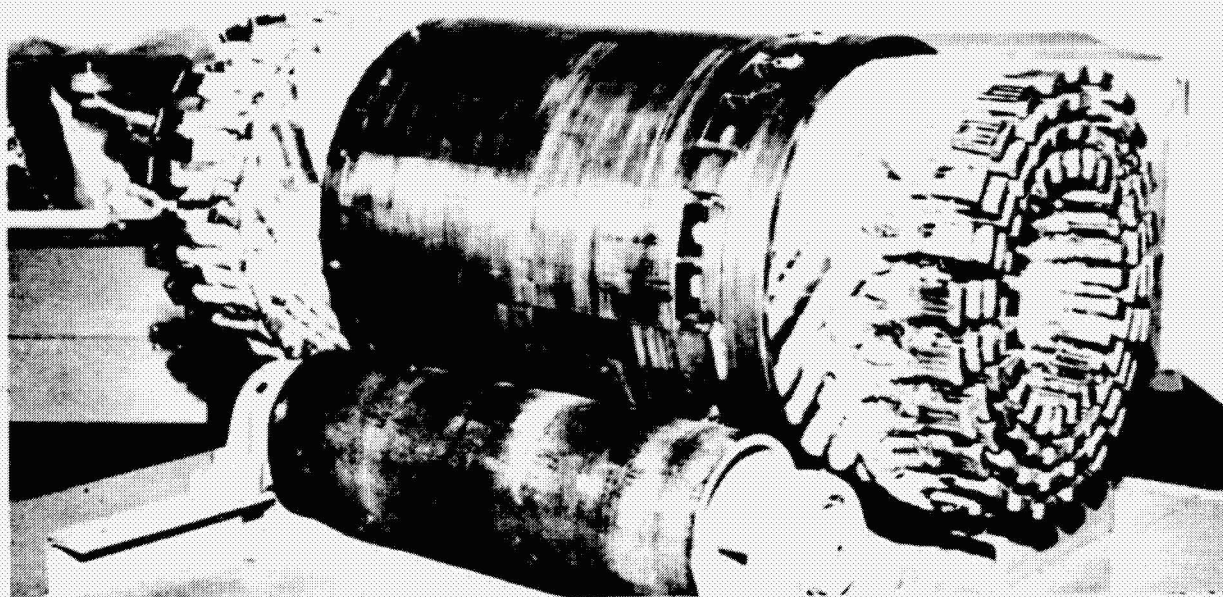
**Since the design technology for EM pumps is well-developed and relatively large pumps have been built, the design and production of pumps of the required size and operating characteristics for the SPS should be a straightforward engineering problem. The use of higher pump voltages and improved high temperature electrical insulation, magnetic and conductor materials will be required utilizing experience gained in the design and test of the 1033K (1400°F) boiler feed EM pump.**

**Pumping at low NPSH has been demonstrated and avoidance of cavitation in these pumps can be circumvented by (1) subcooling of the condensed potassium to minimize possibility of cavitation (only very low energy losses are involved), (2) minimizing condensate return line pressure losses and (3) reliance upon the dynamic pressure head of the high velocity condensing potassium vapor to help support the minimum NPSH required to prevent cavitation.**

**Figure 4.5-5 shows the EM pump (as described above) fabricated by General Electric for the space power test program.**

SPS-1232

- NO MOVING PARTS
- NO RUBBING SEALS
- RELATIVELY HEAVY (APPROXIMATELY 100 TIMES HEAVIER THAN MECHANICAL)
- RELATIVELY LOW EFFICIENCY (17% VS. 80%, MECHANICAL)
- GOOD DATA BASE



● 10,000 TEST HOURS

● 17% EFFICIENCY

● UP TO 1033 K (1400°F)

Figure 4.5-5. Electromagnetic Pumps

**4.5.5 Radiators****4.5.5.1 Temperature**

The amount of energy which must be input to a conversion system is inversely proportional to the efficiency,  $\eta$ , where  $P_{out}$  is the useful power to be rejected.

$$P_{in} = \frac{P_{out}}{\eta} \quad (1)$$

After removal of the useful power, the waste heat to be rejected is:

$$P_{rej} = P_{in} - P_{out} \quad (2)$$

$$= \frac{P_{out}}{\eta} - P_{out} \quad (3)$$

$$= P_{out} \left( \frac{1}{\eta} - 1 \right)$$

Thus, the heat to be rejected grows rapidly as the cycle efficiency ( $\eta$ ) diminishes:

$\eta$	$\frac{P_{in}}{P_{out}}$	$\frac{P_{rej}}{P_{out}}$
50%	2.0	1.0
40%	2.5	1.5
30%	3.33	2.33
20%	5.00	4.00
10%	10.0	9.00

Thermal cycle efficiencies are relatable to the ideal, or Carnot, efficiency.

$$\eta_{ideal} \propto \frac{T_{in} - T_{rej}}{T_{in}} \quad (5)$$

As will be explained in section 5.1.2, the selected Rankine cycle temperature ratio is 0.75, i.e.:

$$\frac{T_{rej}}{T_{in}} = 0.75 \quad (6)$$

Consequently  $\eta_{ideal}$  is limited to 0.25 (the actual efficiency is 0.189). However, with a turbine inlet temperature of 1231K (1776°F), the radiator temperature is close to 932K(1218°F). At this temperature, thermal radiation is quite effective, so much so that the radiator has less area than if the rejection temperature were lower (although the cycle would be more efficient, and there would be less heat to reject). Refer back to the right side of Figure 4.5-1.

#### **4.5.5.2 Radiating Elements**

Heat pipes have been selected as the radiator heat dissipation elements. For high temperature radiators, fins are a poor choice. This is because thermal conductivity through the fin material is inadequate to keep up with high temperature surface radiation (conductivity varies directly with temperature; radiation, with the fourth power of temperature). If the working fluid (potassium), is conducted directly through tubular radiating elements, these elements must be capable of isolation by valves. Without isolation, a single leak can cause loss of the entire fluid inventory.

Heat pipes can be used as radiating elements by wrapping their evaporator sections around a manifold carrying the working fluid to be cooled. Meteoroid penetration of a heat pipe makes that pipe inactive but does not cause loss of working fluid in the manifold. A derivation of the optimum spacing between heat pipes and the associated view factor effects is given in Section 5.1.2.

#### **4.5.5.3 Manifolds**

Rankine cycle radiators employ an inlet vapor duct and a liquid return duct. The radiator panels themselves incorporate "throughpipes," on which the heat pipes are mounted, which accept the flow from the inlet duct and output flow to the return duct. Two primary options exist for the arrangement of these elements, as shown in Figure 4.5-6.

### **4.6 POWER DISTRIBUTION AND CONTROL**

The function of the power distribution and control system is to acquire power from the power generation system, condition, regulate and control the quantity and quality of the electrical power, transmit the power to the MPTS antenna, provide for energy storage, and provide for fault detection and isolation. The MPTS antenna power distribution system is discussed in detail in Volume 4, MPTS. The following paragraphs report the power distribution and control system status at the end of part I of the study, refrigerated conductor system analysis, the current status of the satellite power distribution system, and rotary joint design analysis.



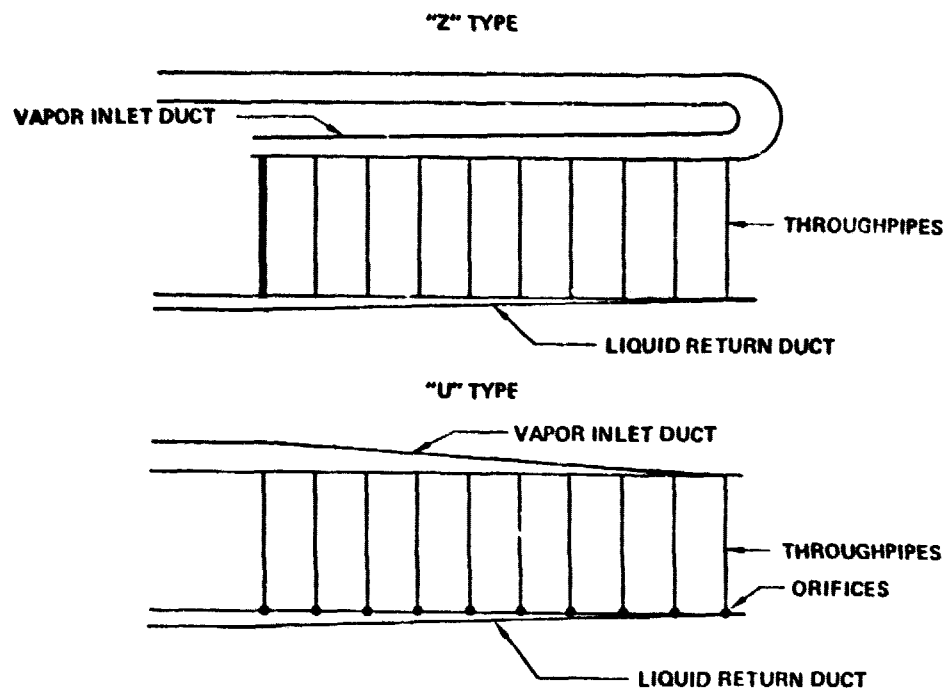
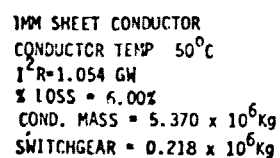


Figure 4.5-6 Manifold Arrangement Options



**Figure 4.6-1: Thermal Engine SPS Power Distribution**

#### 4.6.1 Type Section

##### 4.6.1.1 Power Distribution and Control Status—Part I Study End

The power distribution and control system status for each element at the end of the Part I study effort was as follows:

**Conductors**—The conductors for the satellite were selected to be one millimeter thick electrical conductor (EC grade aluminum sheet). Aluminum was selected as the conductor material based on the product of resistivity and density (Ref. 4.6-1). Sheet conductors were selected over other shapes because they maximize the ratio of surface area (for radiation of waste heat) to enclosed area (for current conduction). The thickness of one millimeter was selected to minimize handling damage.

**Switchgear**—The switchgear selected was the liquid metal plasma valve switch with a parallel mechanical contactor. Commutation circuitry is also required. One switchgear was required per power sector or generator. Isolation disconnects were provided.

**DC/DC Converter**—DC/DC converters had a specific mass of one kilogram per kilowatt of input. Efficiency was 0.96.

**Main Buses**—Three main buses were provided. The DC RF converter used as the baseline during Part I was a Klystron with three depressed collectors. It was determined that it was more efficient to process all power required by the Klystron (heater, solenoid, one depressed collector, and acceleration anodes), except for the two depressed collectors which intercept the majority of the beam current. This efficiency was compared with generating the required voltages on the satellite and using buses to transmit the power to the MPTS Klystrons. Thus three buses were required to deliver the two voltages (40,000 volts, collector A, and 37,900 volts, collector B) to the Klystrons.

**Power Sectors**—Power sectors are defined as that portion of the power generation equipment whose output is controlled by one switchgear unit. Power sectors for the thermal engine were straightforward. Each generator was considered a power sector. For the photovoltaic SPS the selection was more complex. Power sector size was selected based on a reliability/maintainability analysis and based on the annealing concept. The power sector size selected represented approximately 0.5% of the total satellite output (or 1% of each antenna output).

**Rotary Joint**—The rotary joint defined in the JSC baseline (Ref. 4.6-1) was used. No effort was expended on rotary joint analysis in Part I of the study effort.

**Energy Storage**—Not defined in Part I.

**Power Distribution and Control for Self-Powered Orbit Transfer**—Because of the severity of the plasma problem at LEO, power was acquired from the array at a considerably lower voltage than at GEO operations. The Part I analysis showed that it was more efficient and a lower weight system was obtained if power was processed for all ion thruster requirements. Power was acquired from the array at a higher voltage than required by the thrusters (but much lower than the GEO operating voltage) and a DC/DC converter used to provide the proper thruster voltages.

**Conductor Operating Temperature**—Conductor operating temperatures were selected during Part I. The rationale used to determine these temperatures was to minimize the total satellite mass. The sum of conductor mass and power generation system mass required to generate the conductor  $I^2R$  losses was minimized. The optimum conductor operating temperature for thermal engine SPS was determined to be 323K (121°F) and for the photovoltaic SPS, 373K (212°F).

#### 4.6.1.2 Refrigerated Power Distribution Systems

One of the areas that was investigated during the system definition study for the SPS power distribution and control system was the application of refrigerated conductor system to improve system efficiency and mass. The possibility of greatly reducing system size and mass by operating in either the superconducting or the cryoresistive (LN<sub>2</sub> temperature) regime is attractive. Both temperature regimes were investigated during the course of the analysis. The analysis was performed on the Thermal Engine SPS Configuration. (See Figure 4.6-1.)

**Superconducting Power Distribution System**—A number of superconductor materials are available for use as the superconducting medium in power transmission lines (Refs. 5-1 thru 5-6). Figure 4.6-2 shows some conductor parameters which were used to select the superconductor and stabilizing conductor for the transmission line discussed herein. Aluminum was selected as the stabilizing conductor for the superconducting cable.

Also shown in Figure 4.6-2 are several candidate superconductive materials which were considered for use in the superconducting cable. Niobium-tin was selected as the superconducting material for two primary reasons:

- (1) It has a relatively high critical temperature (the temperature at which the transition to superconduction occurs); and
- (2) Niobium-tin has been shown to be adaptable to cable fabrication. The selection of a material with a high critical temperature is extremely important in terms of total system mass and efficiency. The refrigeration system mass and power requirements are heavily dependent upon the refrigeration cycle low-end temperature. Other superconductive materials have higher critical temperatures, but have not been shown to be amenable to cable fabrication techniques.

D180-22876-3

CYTORESISTIVE - LN<sub>2</sub>  
CONDUCTOR MATERIALS (78°K)

ALUMINUM  
COPPER

RESISTIVITY  
OHM-CM  
25x10<sup>-6</sup>  
20x10<sup>-6</sup>

DENSITY  
gm/cm<sup>3</sup>  
2.70  
8.89

SUPER CONDUCTIVE

SUPERCONDUCTOR

NIOBIUM-TIN Nb<sub>3</sub>Sn  
NIOBIUM-ZIRC  
NIOBIUM TITANIUM  
NIOBIUM ALUMINUM

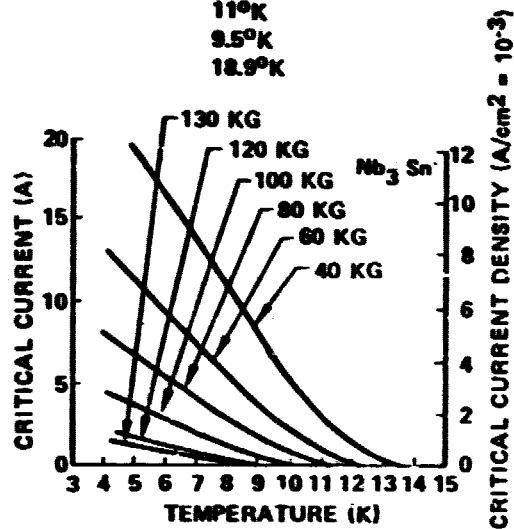
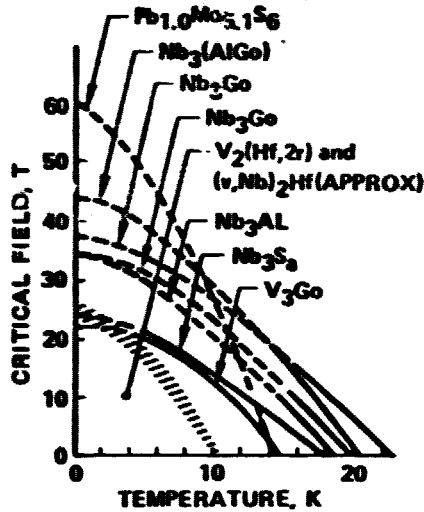
CRITICAL TEMP.

18°K

11°K

9.5°K

18.9°K



CRITICAL CURRENT DENSITY, J<sub>C</sub>  
VERSUS TEMPERATURE, T, AT  
VARIOUS MAGNETIC FIELDS  
FOR THE Nb<sub>3</sub>Sn MULTIFILAMENTARY  
WIRE.

Figure 4.6-2. Refrigerated Conductor Parameters

### **D180-22876-3**

The thermal engine satellite was used as the baseline to perform the refrigerated conductor system analysis. Figure 4.6-1 shows the thermal engine SPS with sheet conductors against which the superconductor system was compared. For the sheet conductor power distribution system, the conductor mass was 3.193 metric tons and the conductor losses were 0.715 gigawatts. Using a specific mass of 3.3 kg/kw for the thermal engine SPS, 2,360 metric tons of power generation mass are required to provide for the conductor losses. This yields a total of 5,553 metric tons of SPS mass which can be attributed to the power distribution system conductors.

Total system mass and power for the superconducting cable system was determined by designing a system with a typical run from the generators to the rotary joint as a baseline. This baseline system was then scaled to the entire satellite.

The superconductor cable designed for the SPS is shown in Figure 4.6-3. The cable is coaxial and is made up of the following elements:

- (1) An open area in the center for refrigerant flow. The diameter of this open area is 5 cm.
- (2) A spiral helix of aluminum to provide support for cable lay-up.
- (3) Layers of counterspiraled aluminum stabilizing conductor. The purpose of the counterspiraled aluminum stabilizing conductor. The purpose of the counterspiraling is to cancel out transverse magnetic fields caused by winding the conductor in a spiral.
- (4) A superconducting layer of niobium-tin.
- (5) A layer of electrical insulation made of wound polytetrafluoroethylene teflon (PTFE).
- (6) A second region of counterspiraled stabilizing aluminum conductor similar to (3) above.
- (7) A second superconductor similar to (4) above.
- (8) An open area with spaces to provide for refrigerant flow between the outer conductor and the pressure jacket (effective flow area equal to item 1).
- (9) A corrugated flexible stainless steel outer pressure jacket with a thickness of 0.030 inches.
- (10) Thermal insulation composed of 30 layers of super insulation. The thickness of the multi-layered insulation is 1 inch (2.54 cm).
- (11) An outer covering of TFE coated glass cloth.

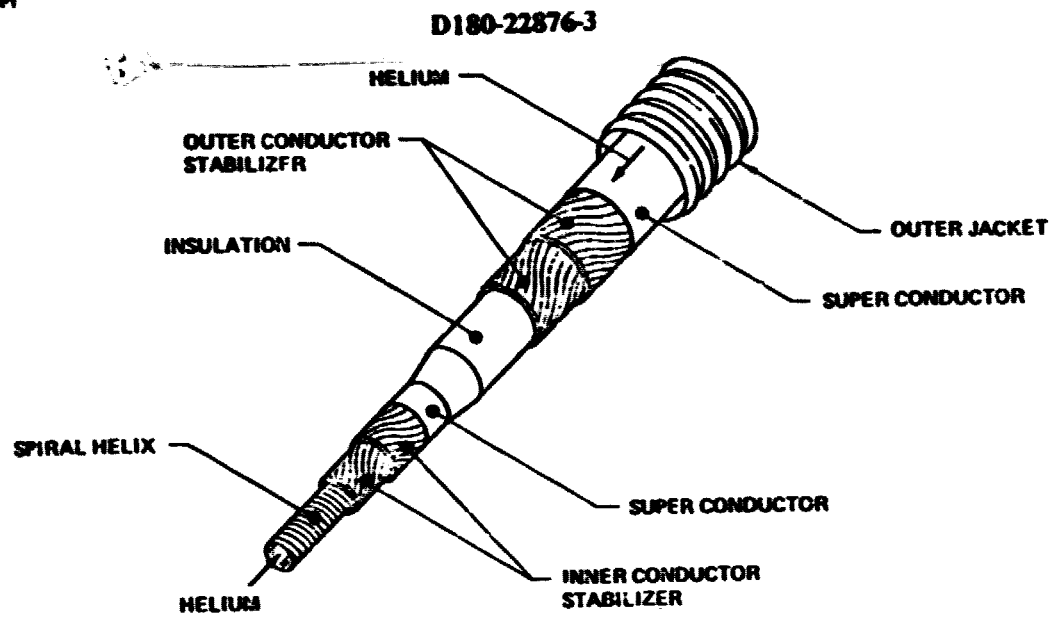


**Figure 4.6-3. Coaxial Superconducting Power Transmission Cable**

The outside diameter of the total superconducting including the thermal insulating jacket is approximately 12.4 centimeters and has a mass of 10.06 kilograms per meter of length as shown in Table 4.6-1. For the thermal engine SPS used for the study, a total length of 52,440 meters of superconductor are required. This yields a total conductor mass of 528 metric tons.

The results of the superconductor analysis are shown in Figure 4.6-A. The power required to operate the refrigerators and pumps for the liquid helium refrigeration cycle is considerably less than the sheet conductor  $I^2R$  losses even at relatively high values of super insulation thermal performance. The weight and power required by the refrigeration/radiator system is heavily dependent on the refrigeration cycle temperatures. Values of 6K (-449°F) and 8K (-446°F) were used for conductor inlet and outlet refrigerant temperatures respectively. The primary reason for selecting these values was to assure no loss of superconductivity for short periods of refrigerant plant outages. Since, with DC superconducting cables, the primary heat load to the refrigerator system is leakage through the superinsulation, a considerable reduction in refrigerator/radiator mass and power requirements could be realized by the development of a superconductor with a higher critical temperature.

As can be seen from Figure 4.6-4, the superconductive conductor system can be less massive than the equivalent sheet conductor system when the thermal performance of the super insulation is good enough. Table 4.6-2 summarizes the mass of the superconductor power distribution system for two values of thermal performance within the range of values measured on space programs. Also shown is the sheet conductor mass summary to allow for comparison.

Based on the results obtained during this study where only the conductor system was analyzed, the use of a superconductive conductor system on the SPS is not recommended at this time due to the system complexity and roughly equal mass with the aluminum sheet conductor concept. Superconductor systems should not be totally dismissed from consideration as a SPS power distribution system element, however. The development of superconductor materials with critical temperatures higher than the present liquid hydrogen temperature could swing the trade into a more favorable position. This is particularly true for the thermal engine SPS concept where the use of superconducting generators could also contribute to the mass savings. It is recommended that the SPS studies should continue to use conventional conductors, but that the superconductor technology status should be monitored for advances which would be applicable to SPS usage.

**Cryoresistive Power Distribution System**—The resistivity of aluminum decreases from approximately 3.75 micro-ohm-centimeters to 0.25 micro-ohm centimeters at LN<sub>2</sub> temperatures. This represents an improvement of about 15 times and hence a reduction of the  $I^2R$  losses to about 1/15 of the losses near 373K (212°F).

This decrease in  $I^2R$  losses must be more than the offset by the refrigeration system power requirement in order for the refrigerated conductor system to win out. Each watt of cooling requires 14 to



Table 4.6-1. Superconductive Cable Mass Summary

CABLE ELEMENT	MATERIAL	SP. GR. GM/CM <sup>3</sup>	d <sub>i</sub> CM	d <sub>o</sub> CM	Kg/M
• SPIRAL CABLE SUPPORT	AL	2.7	5.00	5.20	0.144
• STABILIZER CONDUCTOR (1.33 FILL FACTOR)	AL	2.7/1.33	5.20	5.80	2.105
• SUPERCONDUCTOR (INNER)	Nb <sub>3</sub> Sn	8.4	5.80	5.82	0.327
• INSULATION	TFE	2.2	5.82	6.82	2.184
• STABILIZER CONDUCTOR (1.33 FILL FACTOR)	AL	2.7/1.33	6.82	7.29	2.105
• SUPERCONDUCTOR (OUTER)	Nb <sub>3</sub> Sn	8.4	7.29	7.31	0.327
• SPACER	TFE	2.2	7.31	8.86	0.040
• OUTER PRESSURE VESSEL (CORRUGATED)	STAINLESS STEEL	8.0	8.86	9.86	2.535
• SUPERINSULATION	KAPTON/ MYLAR/ NET	1.9x10 <sup>-2</sup>	9.86	12.40	0.187
• OUTER COVER	TFE COATED GLASS	.274 Kg/M <sup>2</sup>	12.40	12.40+	0.107
	TOTAL				10.061

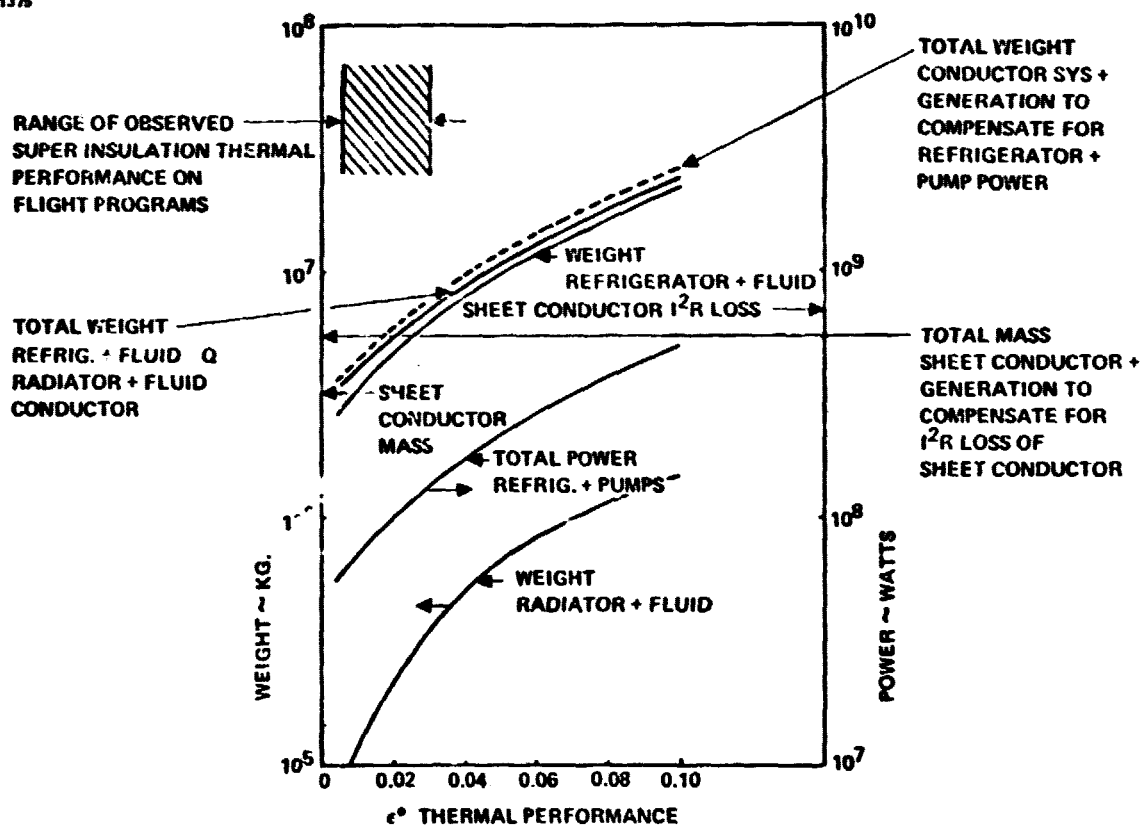


Figure 4.6-4. SPS Superconductor Analysis Summary

Table 4.6-2. Superconductive Power Distribution Summary

SYSTEM ELEMENT	SUPERCONDUCTIVE CONDUCTOR		AL SHEET CONDUCTOR
	THERM. PERF = 0.02	THERM. PERF = .01	
CONDUCTOR WT.	.528 x 10 <sup>6</sup> Kg	.528 x 10 <sup>6</sup> Kg	3.193 x 10 <sup>6</sup> Kg
REFRIGERATOR + FLUID	4.964 x 10 <sup>6</sup> Kg	3.436 x 10 <sup>6</sup> Kg	
RADIATOR + FLUID	.218 x 10 <sup>6</sup> Kg	.120 x 10 <sup>6</sup> Kg	
CABLE TERMINATIONS (22 REQ'D @ 4.0 Kg ea.)	.009 x 10 <sup>6</sup> Kg	.009 x 10 <sup>6</sup> Kg	
TOTAL CONDUCTOR SYSTEM WT	5.719 x 10 <sup>6</sup> Kg	4.093 x 10 <sup>6</sup> Kg	3.193 x 10 <sup>6</sup> Kg
CONDUCTOR POWER LOSSES	1.08 x 10 <sup>8</sup> WATTS	.756 x 10 <sup>8</sup> WATTS	7.15 x 10 <sup>8</sup> WATTS
POWER GEN. WT TO COMPENSATE FOR POWER LOSSES @ 3.3 Kg/Kw	.356 x 10 <sup>6</sup> Kg	.249 x 10 <sup>6</sup> Kg	2.360 x 10 <sup>6</sup> Kg
TOTAL WT FOR CONDUCTOR SYSTEM & LOSSES	6.075 x 10 <sup>6</sup> Kg	4.34 x 10 <sup>6</sup> Kg	5.553 x 10 <sup>6</sup> Kg

15 watts of refrigerator and pumping power at  $LN_2$  temperature. Thus the reduction in  $I^2R$  losses by operating at  $LN_2$  temperature is approximately offset by the increase in power for the refrigeration system.

The results of the study for cryoresistive conductors are summarized in Figure 4.6-5. The mass of the refrigerating system at the same current density ( $449 \text{ amp/cm}^2$ ) as the baseline thermal engine SPS shown in Figure 4.6-1 is approximately the same as the sheet conductor weight. The total power required at the same current density is also approximately equal to the  $I^2R$  losses. Thus the total system mass (conductor + refrigeration system) is approximately twice the sheet conductor mass and the power required is approximately equal to the sheet conductor  $I^2R$  losses.

The cryoresistive conductor system requires the same amount of power generation mass for an equivalent efficiency. The cryoresistive conductor system is twice as massive. Therefore, the cryoresistive conductor system should not be considered for use on the SPS.

### **SUPER CONDUCTIVITY**

#### **References**

- 4.6-1 Dean, J. W. and Laquer, H. L., "Conceptual Design of a DC Superconducting Power Transmission line," IEEE 1976 Underground Transmission and Distribution Proc.
- 4.6-2 Forsyth, F. B. et. al., "Flexible Superconducting Power Cables," IEEE Transactions PAS92,493 (1973).
- 4.6-3 Mauser, S. F. et. al., "Development of a 138-KV Superconducting Cable Termination," IEEE Transactions on Power Apparatus and Systems, Vol. PAS-95, No. 3, May-June 1976.
- 4.6-4 Haid, D. A., "Future Application of Superconducting Cables to Electric Power Transmission," A.S.M.E. Paper 74 WA/P1D-18.
- 4.6-5 Belanger, B. C., "Superconducting and Resistive Cryogenic Power Transmission Research in the U.S. An opportunity for Cryogenic Innovation," Advances in Cryogenic Engineering P.1-22, Plenum.
- 4.6-6 Dew-Hughes, D., "Superconducting Materials for Large Scale Applications," Advances in Cryogenic Engineering, P316-324, Plenum.

D180-22876-3

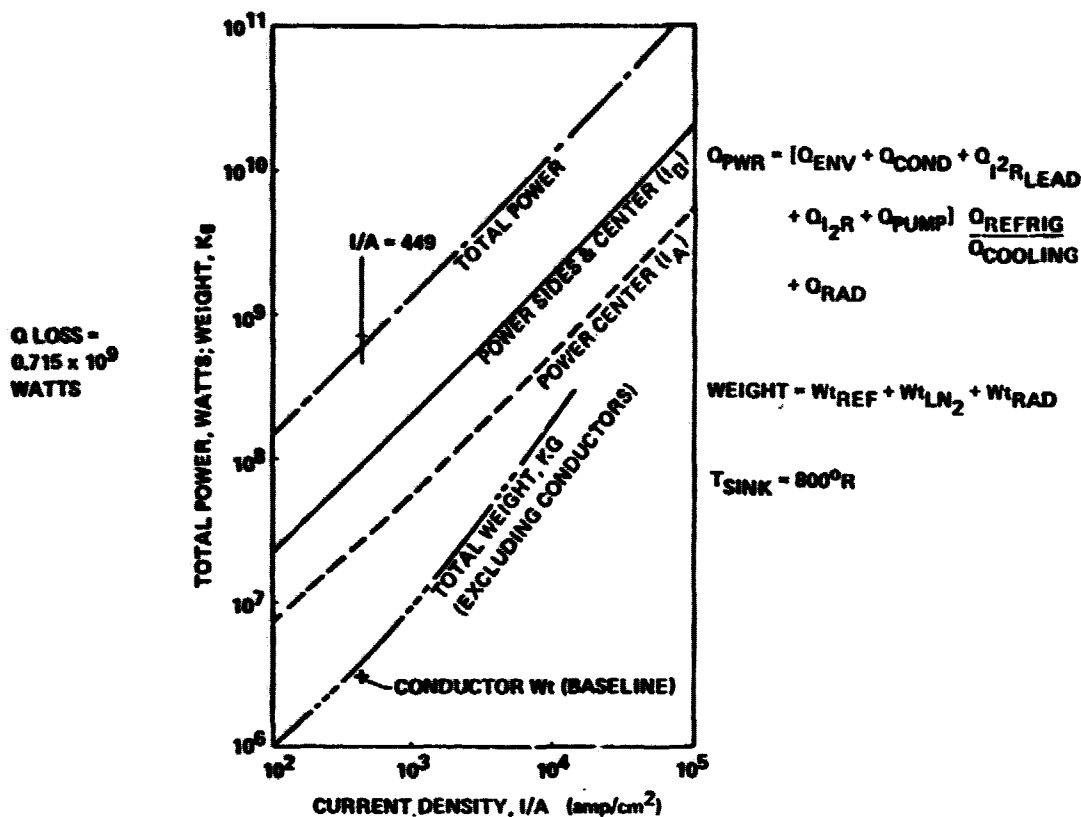


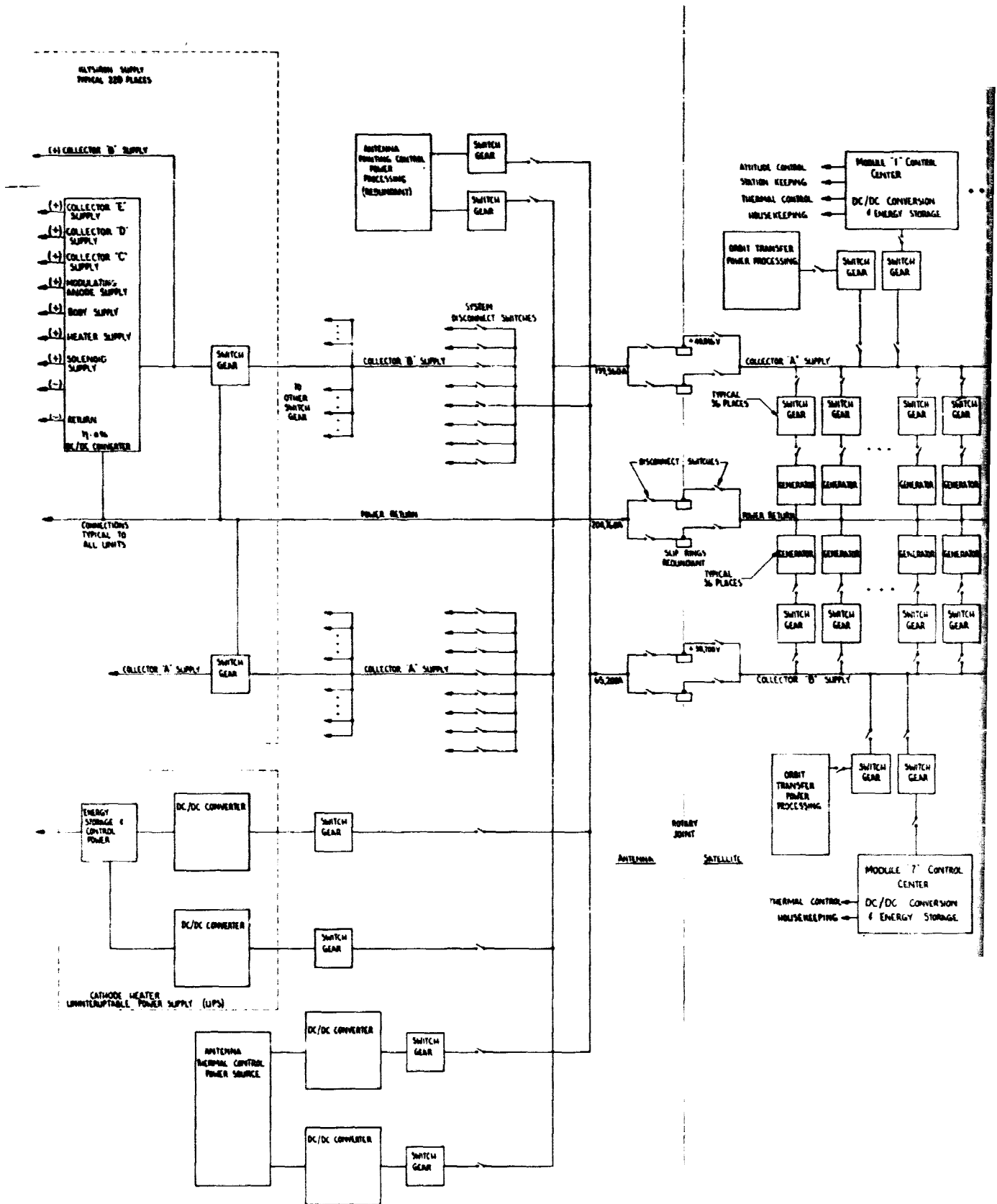
Figure 4.6-5. Cryoresistive Cooling of Conductors

#### 4.6.1.3 Power Distribution and Control Systems for Reference Solar Power Satellites

The design concepts developed during the Part I study effort on the satellite power distribution and control system remain essentially unchanged at the end of the Part II study. However, system updates were accomplished to: 1) reflect satellite configuration changes; 2) incorporate results of investigations in areas which were not covered in the Part I study effort; and 3) incorporate any changes required to establish compatibility between the MPTS antenna and the satellite power distribution and control system.

The block diagrams for the power distribution and control systems for the thermal engine and photovoltaic satellites are shown in Figures 4.6-6 and 4.6-7 respectively. The main power buses are all conductor grade aluminum sheet conductors.

ORIGINAL PAGE IS  
OF POOR QUALITY



FOLDOUT FRAME 2

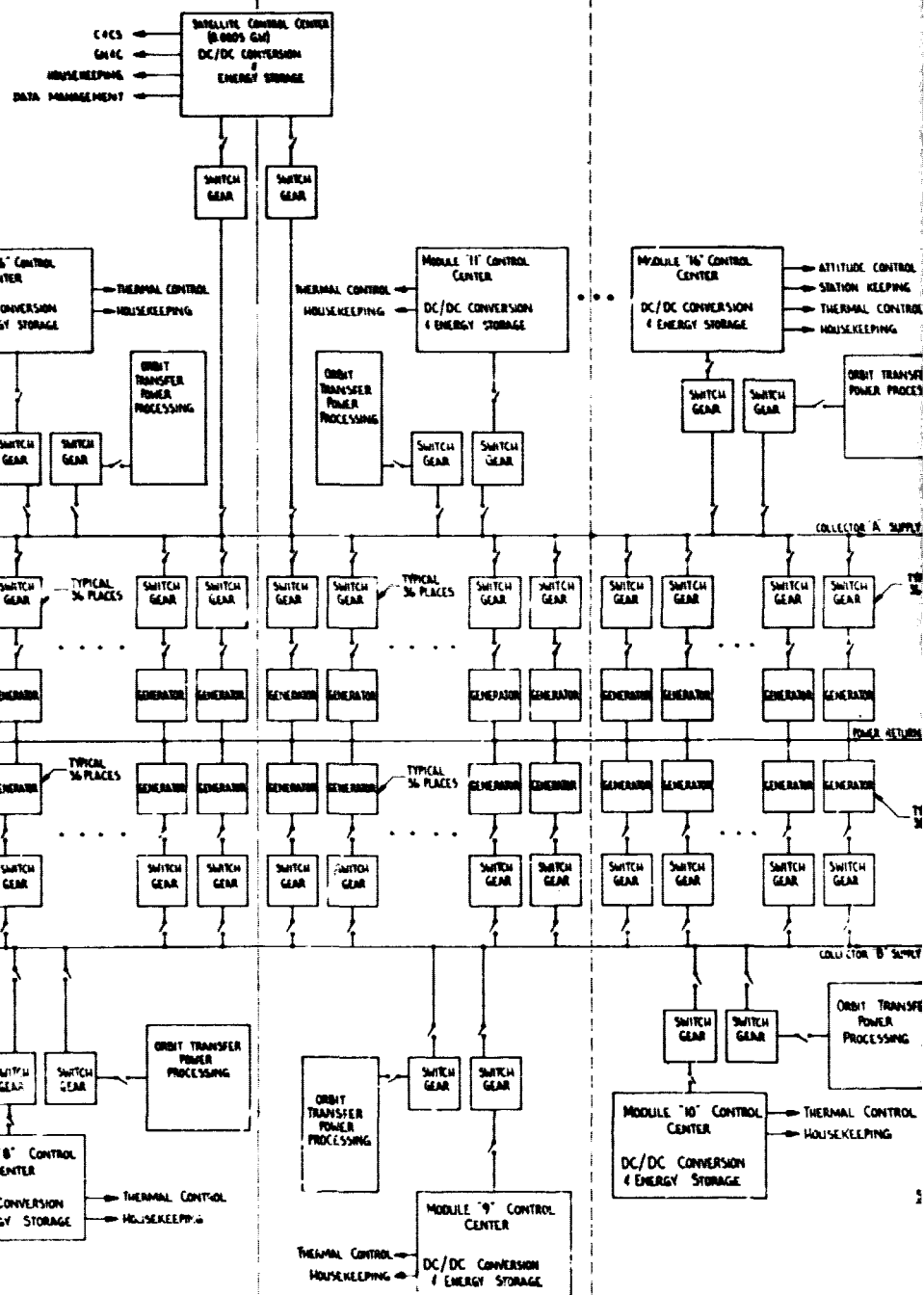


Figure 4.6-6. Electric

FOLDOUT FRAME 12

ORIGINAL PAGE IS  
OF POOR QUALITY

A REVISED 10-10-77 *h* D180-22876-3

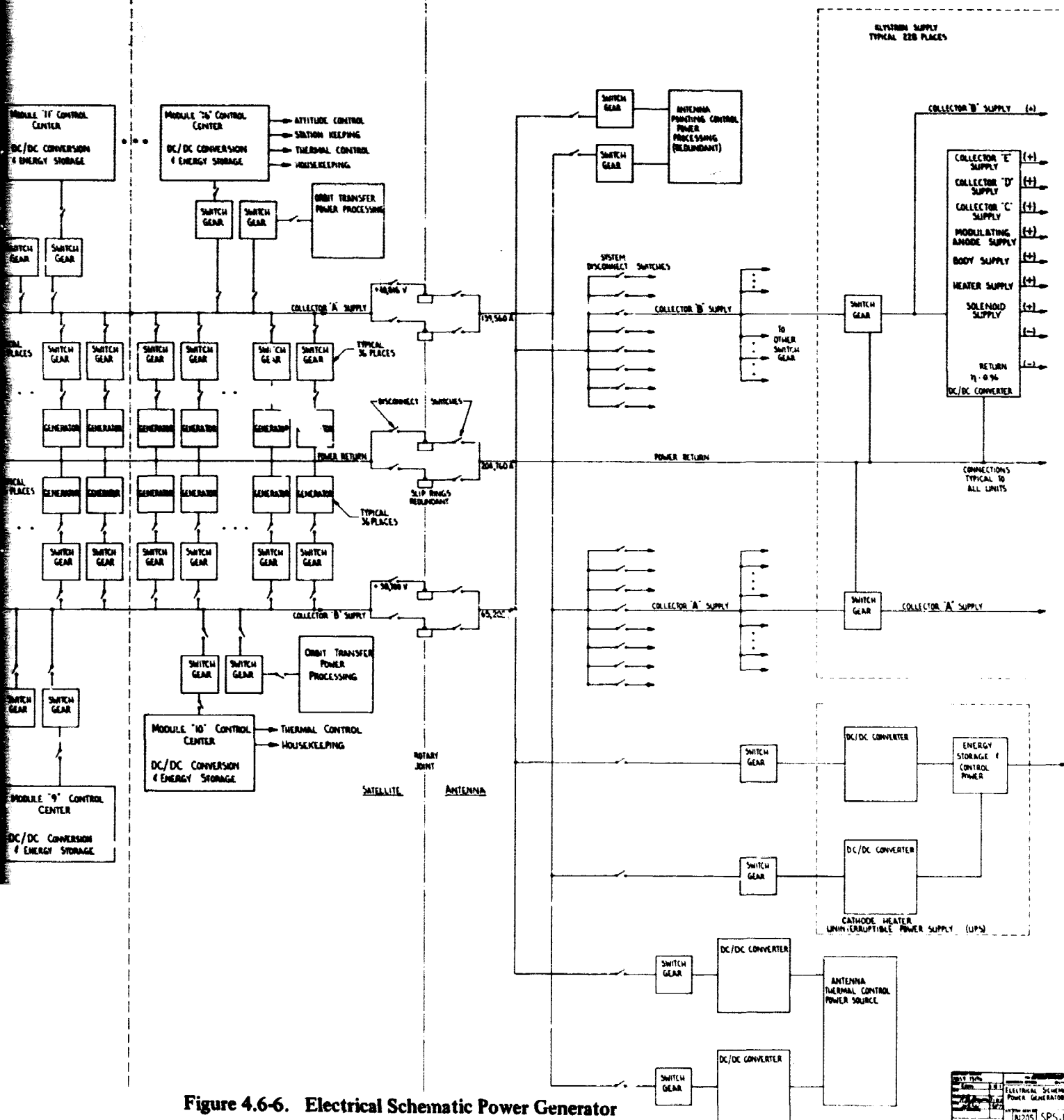
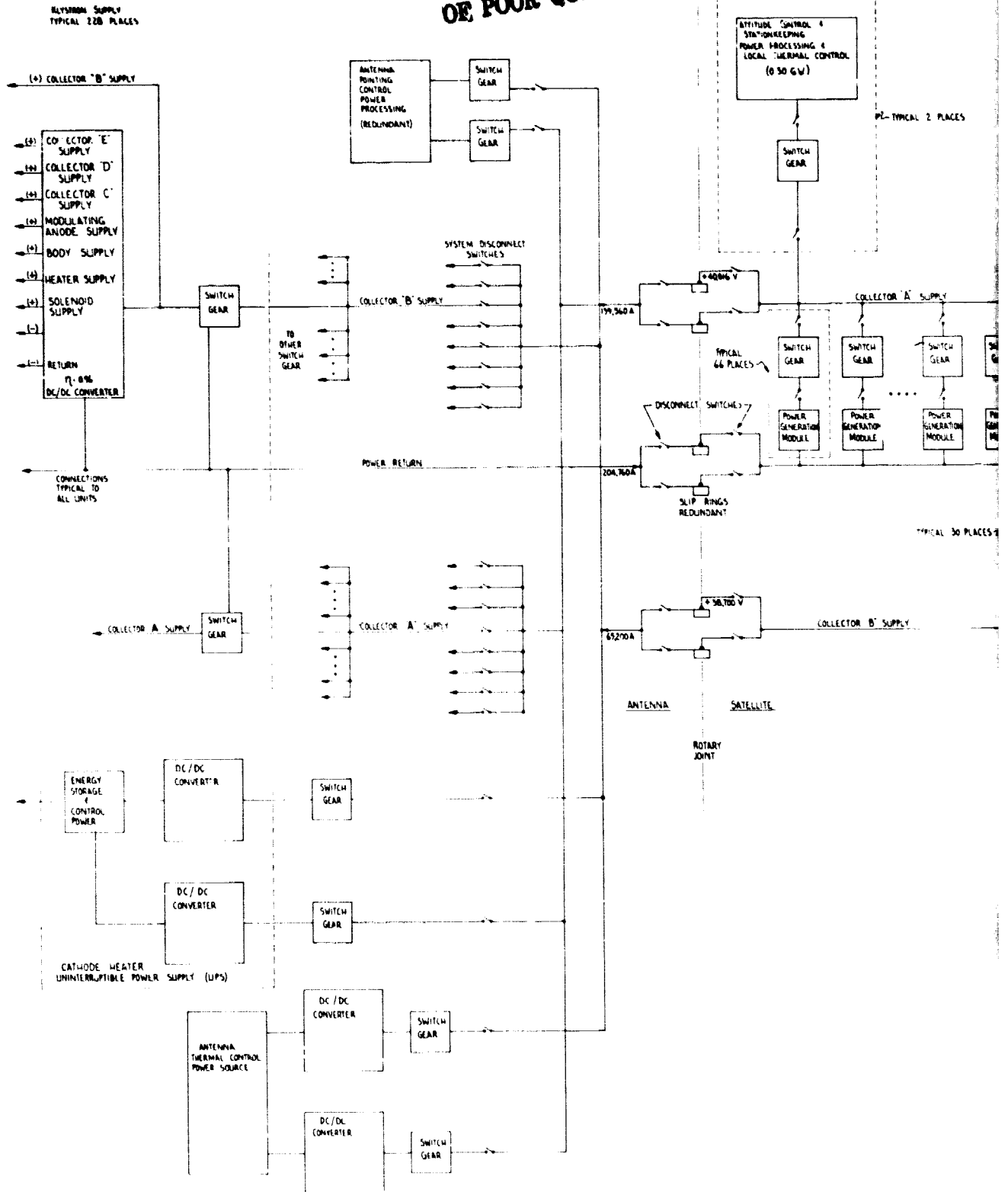


Figure 4.6-6. Electrical Schematic Power Generator

Electrical Schematic  
Power Generator  
180291 SPS-10-12

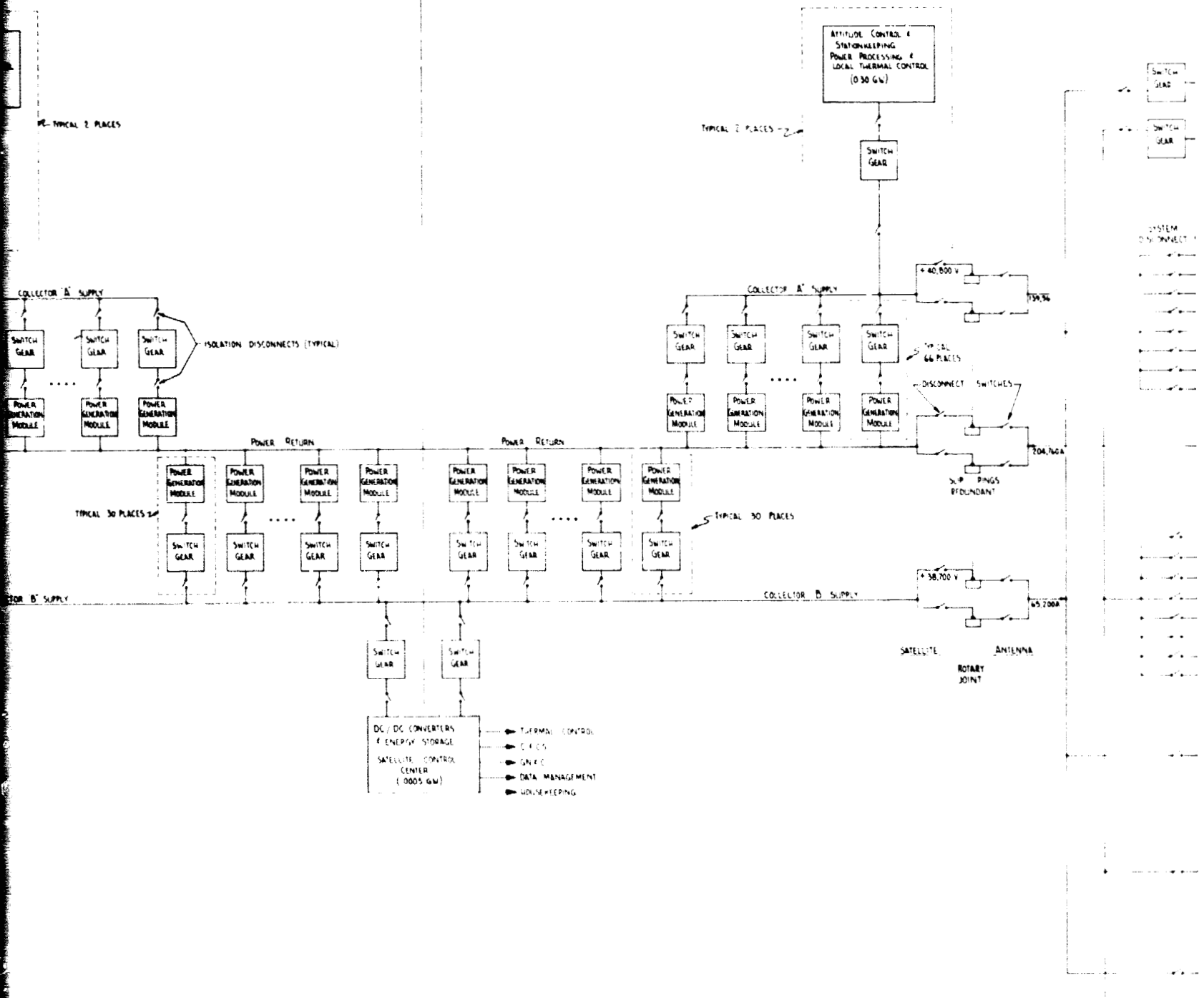
# **RELDOUT FRAME**

ORIGINAL PAGE IS  
OF POOR QUALITY





**FOLDOUT FRAME 2**



ORIGINAL PAGE IS  
OF POOR QUALITY

Figure 4.6-7. L

ORIGINAL PAGE IS  
OF POOR QUALITY



**Figure 4.6-7. Electrical Schematic Photovoltaic**

### **D180-22876-3**

The basic concept is illustrated in Figure 4.6-8. The paths for current flow through the cell strings within the power sector are as shown. Jumpers are used at the satellite edge to connect power sectors. These jumpers are included in the mass summary shown in Table 4.6-3 as acquisition buses along with the small buses used to acquire the power from the power sector prior to connecting to the switchgear shown in Figure 4.6-8.

Some of the important parameters for the photovoltaic solar power satellite are summarized in Table 4.6-4. For each power sector, the main bus voltage, sector current and the main bus power loss to transmit the sector current to the rotary joint are shown. During the conduct of the part I study effort, discussions with the NASA/JSC SPS systems definition study COR, C. Covington, led to the investigations of satellite power distribution system buses which routed power in only one direction (laterally or longitudinally dependent upon satellite configuration). The primary reason for the investigation was to attempt to take advantage of the large distance accumulated by connecting in series enough solar cells to achieve 42 to 44 kilovolts.

Discussions of the areas of switchgear, DC/DC converters, and energy storage are included in the power distribution section of Volume IV, MPTS, of this final report. Reports provided by General Electric in the area of DC/DC converters and switchgear are included in the appendices of Volume IV.

Power sector summary data for the thermal engine SPS is shown in Table 4.6-5. The mass and loss summary for the thermal engine satellite is shown in Table 4.6-6. For the thermal engine satellite, a power sector is equivalent to a satellite module.

A summary comparison of the power distribution systems for the two satellite energy conversion options (photovoltaic and thermal engine) is shown in Table 4.6-7. In general, the power distribution system for the photovoltaic SPS is lighter, less efficient, and requires less energy storage than the thermal engine SPS. The primary reason for increased energy storage required for the thermal engine satellite is for engine start-up. Energy storage is required for start-up of only one engine per cavity. All other start-up is bootstrapped to the first engine.

#### **4.6.2 Rotary Joint**

The MPTS antenna-to-spacecraft interface requires 360° rotation about the spacecraft central axis with limited motion for elevation steering while maintaining structural and electrical integrity between the satellite and the antenna. Previous designs of rotary joints (Ref: 4.6-1 and 4.6-2) were massive and mounted directly behind the center of the microwave antenna with its high thermal radiation environment. An alternate concept was developed which is lighter and is mounted between the satellite and the antenna.

D180-22876-3

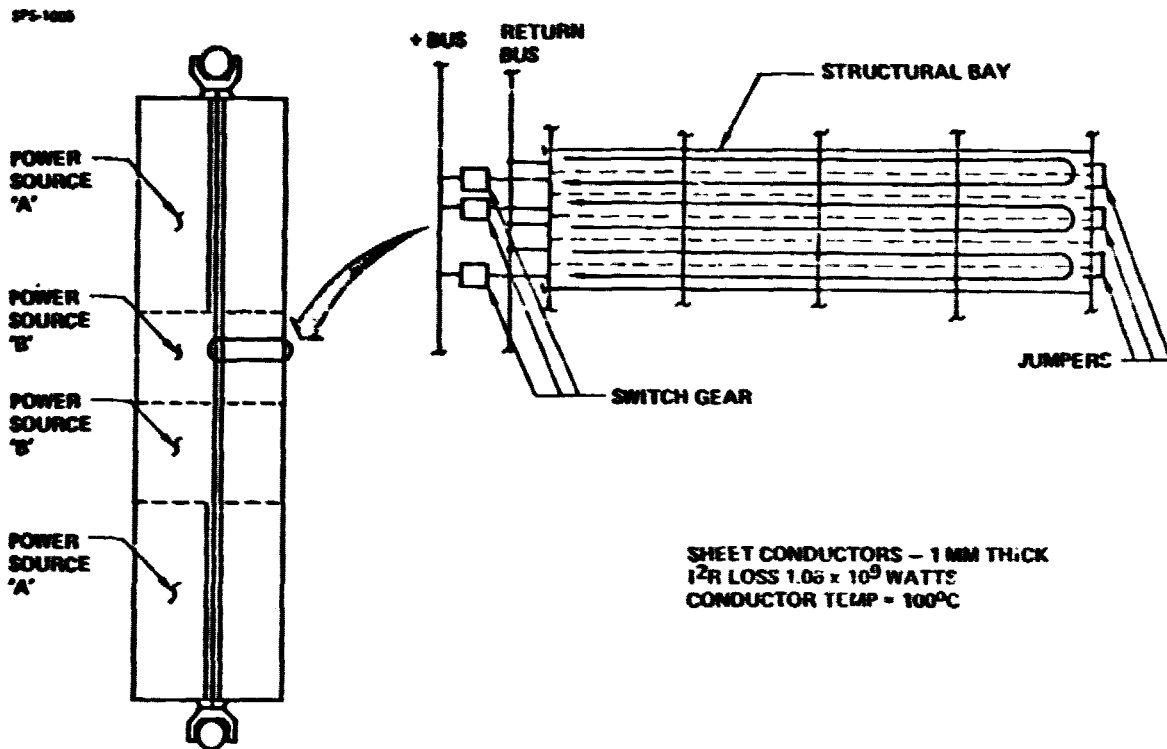


Figure 4.6-8. Photovoltaic Reference Power Collection

**D180-22876-3**

**Table 4.6- 3. Photovoltaic SPS Power Sector Summary**

<b>POWER SECTOR</b>	<b>DISTANCE TO ROTARY JOINT ~ M.</b>	<b>MAIN BUS VOLTAGE ~ VDC</b>	<b>SECTOR CURRENT = AMPS</b>	<b>MAIN BUSS I<sup>2</sup>R LOSS - WATTS</b>
A1	415.57	40,993.41	2,216.18	428,631
A2	415.57	40,993.41	2,216.18	428,631
A3	625.19	41,090.96	2,214.47	644,322
A4	625.19	41,090.96	2,214.47	644,322
A5	834.81	41,188.52	2,211.46	859,196
A6	834.81	41,188.52	2,211.46	859,196
A7	1,075.57	41,300.57	2,208.03	1,105,274
A8	1,075.57	41,300.57	2,208.03	1,105,274
A9	1,285.19	41,398.13	2,205.03	1,318,895
A10	1,285.19	41,398.13	2,205.03	1,318,895
A11	1,494.81	41,495.68	2,201.17	1,531,310
A12	1,494.81	41,495.68	2,201.17	1,531,310
A13	1,494.81	41,495.68	2,201.17	1,531,310
A13	1,735.57	41,607.73	2,197.74	1,775,181
A14	1,735.57	41,607.73	2,197.74	1,775,181
A15	1,945.19	41,705.29	2,194.10	1,986,297
A16	1,945.19	41,705.29	2,194.10	1,986,297
A17	2,154.81	41,802.85	2,190.45	2,196,693
A18	2,154.81	41,802.85	2,190.45	2,196,693
A19	2,395.57	41,914.90	2,186.16	2,437,350
A20	2,395.57	41,914.90	2,186.16	2,437,350
A21	2,605.19	42,012.46	2,181.88	2,645,442
A22	2,605.19	42,012.46	2,181.88	2,645,442
A23	2,814.81	42,110.01	2,178.23	2,853,503
A24	2,814.81	42,110.01	2,178.23	2,853,503
A25	3,075.57	42,231.37	2,172.87	3,110,181
A26	3,075.57	42,231.37	2,172.87	3,110,181
A27	3,285.19	42,328.93	2,168.37	3,315,286
A28	3,285.19	42,328.93	2,168.37	3,315,286
A29	3,494.81	42,426.48	2,162.79	3,517,745
A30	3,494.81	42,426.48	2,162.79	3,517,745
A31	3,725.57	42,533.88	2,158.29	3,742,216
A32	3,725.57	42,533.88	2,158.29	3,742,216
A33	3,935.19	42,631.44	2,154.22	3,945,325
A34	3,935.19	42,631.44	2,154.22	3,945,325

**D180-22876-3**

**Table 4.6-3 Photovoltaic SPS Power Sector Summary (Cont'd)**

<b>POWER SECTOR</b>	<b>DISTANCE TO ROTARY JOINT ~ M.</b>	<b>MAIN BUS VOLTAGE ~ VDC</b>	<b>SECTOR CURRENT = AMPS</b>	<b>MAIN BUSS I<sup>2</sup>R LOSS - WATTS</b>
A35	4,144.81	42,728.99	2,149.71	4,146,769
A36	4,144.81	42,728.99	2,149.71	4,146,769
A37	4,395.57	42,845.70	2,143.92	4,385,817
A38	4,395.57	42,845.70	2,143.92	4,385,817
A39	4,605.19	42,943.26	2,138.56	4,583,490
A40	4,605.19	42,943.26	2,138.56	4,583,490
A41	4,814.81	43,040.81	2,133.20	4,780,096
A42	4,814.81	43,040.81	2,133.20	4,780,096
A43	5,055.57	43,152.86	2,126.98	5,004,486
A44	5,055.57	43,152.86	2,126.98	5,044,486
A45	5,265.19	43,250.42	2,120.62	5,196,410
A46	5,265.19	43,250.42	2,120.62	5,196,410
A47	5,474.81	43,327.98	2,144.76	5,388,366
A48	5,474.81	43,347.98	2,144.76	5,388,366
A49	5,735.57	43,469.33	2,105.76	5,620,968
A50	5,735.57	43,469.33	2,105.76	5,620,968
A51	5,945.19	43,566.89	2,099.97	5,810,386
A52	5,945.19	43,566.89	2,099.97	5,810,386
A53	6,151.81	43,663.05	2,091.82	5,988,985
A54	6,151.81	43,663.05	2,091.82	5,988,985
A55	6,395.57	43,776.50	2,083.24	6,200,764
A56	6,396.57	43,776.50	2,083.24	6,200,764
A57	6,605.19	43,874.06	2,075.74	6,380,949
A58	6,605.19	43,874.06	2,075.74	6,380,949
A59	6,814.81	43,971.61	2,068.23	6,559,619
A60	6,814.81	43,971.61	2,068.23	6,559,619
A61	7,055.57	44,083.66	2,057.51	6,756,163
A62	7,055.57	44,083.66	2,057.51	6,756,163
A63	7,265.19	44,182.22	2,048.94	6,927,917
A64	7,265.19	44,182.22	2,048.94	6,927,917
A65	7,474.81	44,278.78	2,039.93	7,096,468

Table 4.6-3 Photovoltaic SPS Power Sector Summary (Cont'd)

POWER SECTOR	DISTANCE TO ROTARY JOINT ~ M.	MAIN BUS VOLTAGE ~ VDC	SECTOR CURRENT = AMPS	MAIN BUSS I <sup>2</sup> R LOSS - WATTS
B1	7,474.81	42,178.78	2,144.80	7,461,287
B2	7,715.57	42,290.83	2,139.22	7,681,575
B3	7,715.57	42,290.83	2,139.22	7,681,575
B4	7,925.19	42,388.38	2,134.29	7,872,073
B5	7,925.19	42,388.38	2,134.29	7,872,073
B6	8,134.81	42,485.94	2,130.65	8,066,513
B7	8,134.81	42,485.94	2,130.65	8,066,513
B8	8,395.57	42,607.30	2,124.64	8,301,606
B9	8,395.57	42,607.30	2,124.64	8,301,606
B10	8,605.19	42,704.86	2,120.14	8,490,864
B11	8,605.19	42,704.86	2,120.14	8,490,864
B12	8,814.81	42,802.41	2,115.42	8,678,320
B13	8,814.81	42,802.41	2,115.42	8,678,320
B14	9,055.57	42,914.46	2,110.28	8,893,691
B15	9,055.57	42,914.46	2,110.28	8,893,691
B16	9,265.19	43,012.02	2,104.70	9,075,509
B17	9,265.19	43,012.02	2,104.70	9,075,509
B18	9,474.81	43,109.58	2,099.34	9,257,208
B19	9,474.81	43,109.58	2,099.34	9,257,208
B20	9,715.57	43,221.63	2,091.84	9,458,527
B21	9,715.57	43,221.63	2,091.84	9,458,527
B22	9,925.19	43,319.18	2,086.05	9,635,840
B23	9,925.19	43,319.18	2,086.05	9,635,840
B24	10,134.81	43,416.74	2,078.54	9,803,933
B25	10,134.81	43,416.74	2,078.54	9,803,933
B26	10,375.57	43,528.79	2,072.11	10,005,784
B27	10,375.57	43,528.79	2,072.11	10,005,784
B28	10,585.19	43,626.35	2,063.96	10,167,789
B29	10,585.19	43,626.35	2,063.96	10,167,789
B30	10,794.81	43,723.90	2,057.10	10,334,665
B31	10,794.81	43,723.90	2,057.10	10,334,665

 $\Sigma 5.282937 \times 10^8$  $\Sigma M = 933,210 \text{ kg}$

D180-22x76-3

Table 4.6-4. Photovoltaic SPS Power Sector Summary

	MASS Kg	$I^2R$ LOSS MEGAWATTS
MAIN POWER BUSES	1,866,420	1,056.6
ACQUISITION BUSES	36,838	10.0
SWITCHGEAR	78,000	NFG.
DISCONNECTS	78,000	NEG.
CELL STRING FEEDERS	38,800	INCL. IN ARRAY
ENERGY STORAGE	20,000	-
TOTALS	2,118,058	1,066.6
% LOSS		6.10

Table 4.6-5 Photovoltaic SPS Power Sector Summary

POWER SECTOR	DISTANCE TO ROTARY JOINT ~ M.	MAIN BUS VOLTAGE ~ VDC	SECTOR CURRENT = AMPS	MAIN BUSS $I^2R$ LOSS - WATTS
A1	11,902	44,066.4	24,601.6/2	34,157,122
A2	9,168	43,269.9	25,020.4	61,797,886
A3	6,434	42,533.3	25,441.8	44,098,272
A4	3,700	41,796.8	14,034.0	13,989,091
A5	6,434	42,533.3	25,441.8	44,098,272
A6	9,168	43,269.9	25,020.4	61,797,886
A7	11,902	44,006.4	24,601.6/2	34,157,122
B1	10,300.46	41,474.9	26,103.4/2	28,607,563
B2	7,566.46	40,738.4	26,575.2	54,170,888
B3	10,300.46	41,474.9	26,103.4/2	28,607,563
B4	3,700	39,696.8	12,521.4	12,481,332

$$\Sigma I^2R = 4.179.63 \times 10^8$$

$$\Sigma M = 2.147 \times 10^5$$

ORIGINAL PAGE IS  
OF POOR QUALITY



**D180-22876-3**

**Table 4.6-6. Thermal Engine Satellite Power Distribution Summary**

	MASS Kg	I <sup>2</sup> R LOSSES MEGAWATTS
MAIN POWER BUSES	4,295,232	835.9
ACQUISITION BUSES	42,950	6.0
SWITCHGEAR	230,400	NEG.
DISCONNECTS	230,400	NEG.
ENERGY STORAGE	<u>198,896</u>	<u>-</u>
TOTALS	4,997,878	841.9
% LOSS		4.87%

**Table 4.6-7. Satellite Power Distribution System Comparisons**

	THERMAL ENGINE SPS	PHOTOVOLTAIC SPS
NUMBER OF MAIN BUSES	3	3
CONDUCTOR I <sup>2</sup> R LOSSES (MEGAWATTS)	841.9	1,066.6
CONDUCTOR MASS (METRIC TONS)	4,338	1,942
SWITCHGEAR QUANTITY	582	198
ENERGY STORAGE (WATT HOURS)	8,000,000	800,000
CONDUCTOR OPERATING TEMP (°C)	50	100

### D180-22876-3

The selected design for the electrical rotary joint is shown in Figure 4.6-9. The following paragraphs discuss the rationale used in accomplishing the slip-ring design:

**Brush-Slip Ring**—Candidate brush and slip-ring materials were reviewed for applicability to the SPS. Based on the results of the review, coin silver (90% silver and 10% copper) was selected for the slip-ring material and a silver-molybdenum disulfide brush with 3% graphite was selected. The characteristics of this combination are shown in Figure 4.6-10. The use of these two materials for the rotary joint is extremely attractive. With a design using a brush current density of 10 amps/cm<sup>2</sup> only about 40 kW of power is dissipated in the rotary joint. Included in the review were materials shown in Table 4.6-8 which were acceptable for extended testing in tests performed by COMSAT on candidate brush/slip-ring materials for application on communications satellites.

Early designs we made for the electrical slip-ring/brush assembly had a diameter of 350 meters. Subsequent review of materials availability showed that for the large slip-ring over 5% of the world's total silver reserve (known and projected) would be required. This material constraint caused a redesign effort for either a smaller slip-ring or the use of coin silver plating over another conductor material for the slip-ring. The large slip-ring will require assembly in space. A smaller design which could be assembled on earth and checked out and launched as an assembly is an attractive option. The selected design shown in Figure 4.6-9 satisfies this set of requirements.

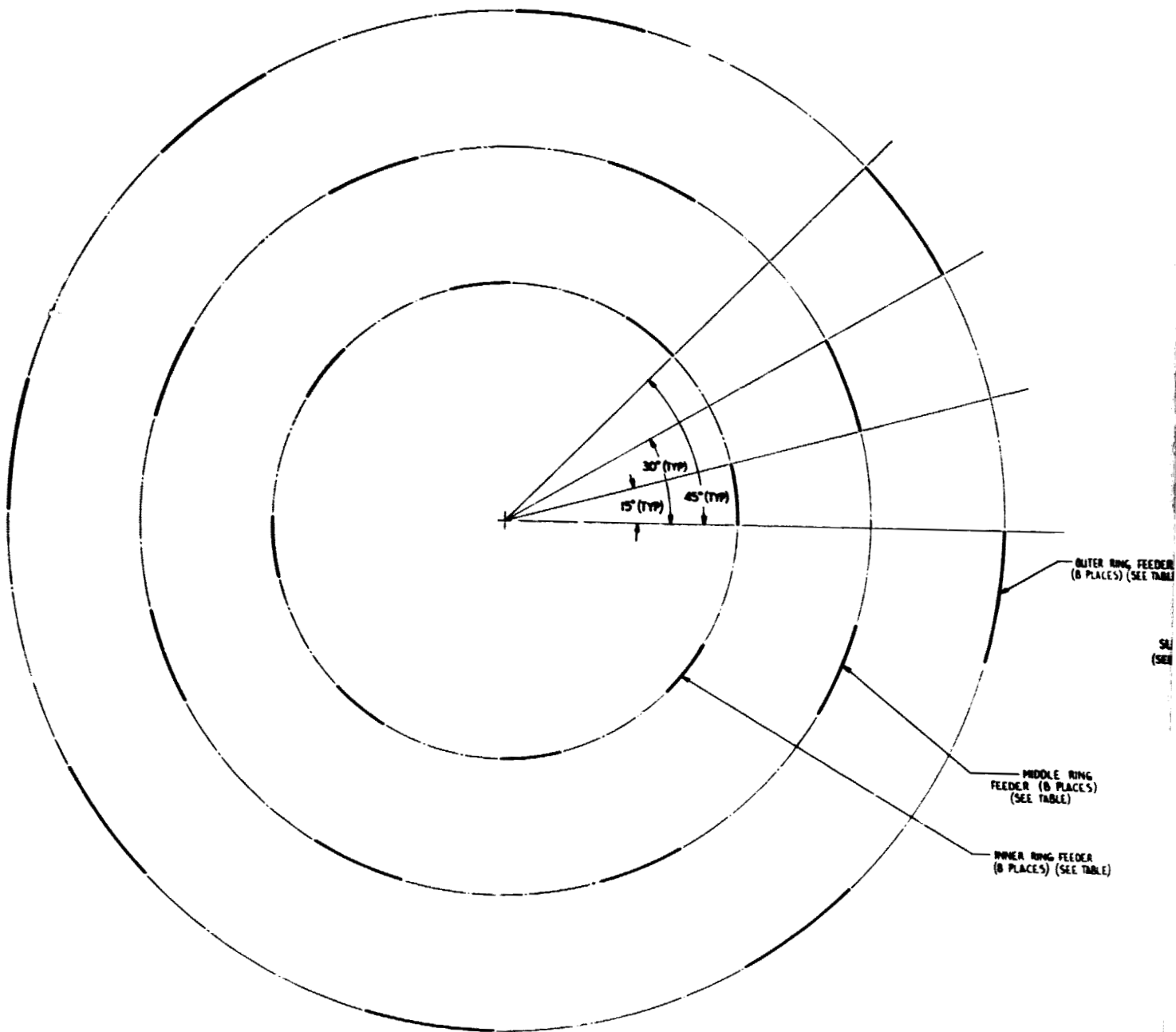
The selected materials combination performs exceedingly well in vacuum. Care must be taken in earth-based testing, however. Operation in the earth's atmosphere results in high wear rates.

The installation of a single brush assembly on a circular slip-ring causes unwanted deflections due to asymmetrical loading. For this reason, the slip-ring/brush assembly was designed for symmetrical loading as shown in Figure 4.6-9. Brush drag (with a coefficient of friction of 0.14) at a brush pressure of 4PSI (25.6KPa) was computed to be 307N, 387N and 463N (69 pounds, 87 pounds, and 104 pounds force) for each inner, middle and outer slip-ring brush assembly.

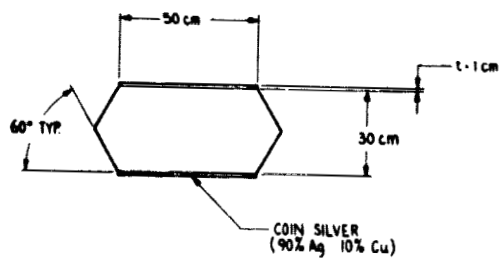
The coin-silver slip-ring is a bright surface and, hence, rejects heat very poorly. Coin silver is a very good conductor. However, the combinations of the two result in fairly high slip-ring temperatures as is shown in Figure 4.6-11. For this calculation, it was assumed that no heat is rejected through the slip-ring feeders. Actual operating temperatures will thus be somewhat lower than shown since the feeders are designed to operate at a much lower temperature and will help in removing slip-ring waste heat.

**Ring Feeders**—Feeders from the main power distribution buses to the slip-ring are designed to operate at a current density of only 100 amps/cm<sup>2</sup>. Feeders are spaced 45 degrees apart (centerline to centerline) and are spaced at 15 degree intervals as shown in Figure 4.6-9. The temperature of the feeders are shown in Figure 4.6-12 and reflect the advantage of the feeder placement shown in Figures 4.6-9 and 4.6-13.

# WELDOUT FRAME



VIEW C-C  
SCALE 1:25  
(FEEDER GEOMETRY)



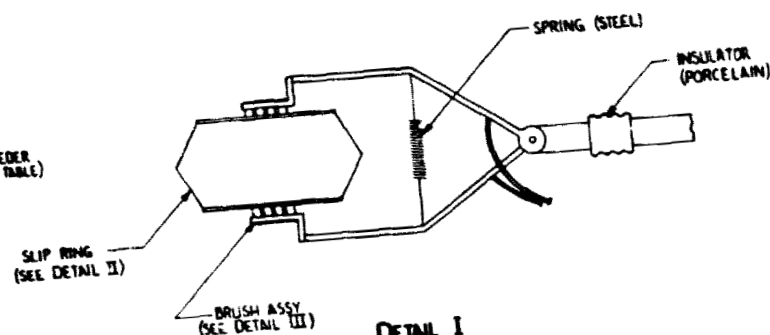
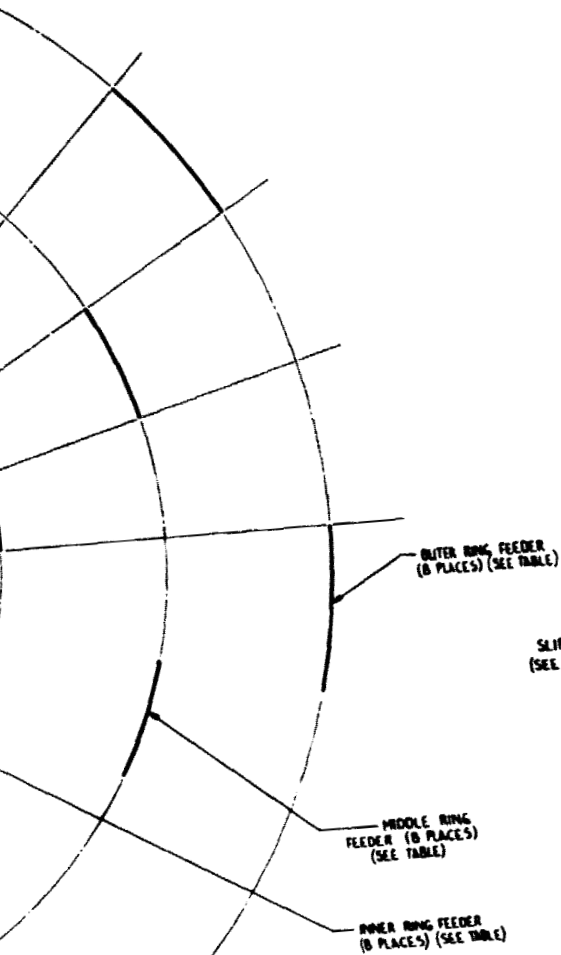
DETAIL II  
SCALE 1:1.5

ORIGINAL PAGE IS  
POOR QUALITY

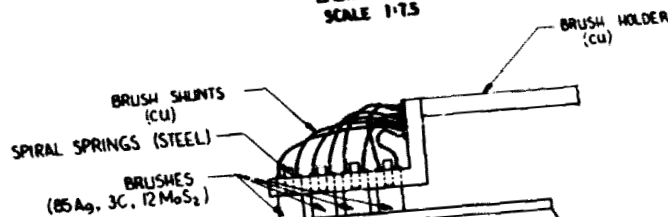
BRUSH  
AT SLI

FOLDOUT FRAME ✓

FEATURE	RING		
	INNER	MIDDLE	OUTER
<b>CURRENT</b>			
Amps	59,800	139,560	199,360
<b>BRUSHES</b>			
N° of BRUSHES	128	320	384
N° of BRUSH ASSYS	8	16	16
BRUSH ASSY SPACING (DEGREES)	45°	22.5°	22.5°
BRUSH CONFIGURATION (ROWS x COLUMNS)	4 x 2	5 x 2	4 x 3
BRUSH CURRENT DENSITY	9.34 A/Cm <sup>2</sup>	8.72 A/Cm <sup>2</sup>	10.38 A/Cm <sup>2</sup>
<b>SLIP RINGS</b>			
Ø DIAMETER (METERS)	7	11	15
<b>FEEDERS</b>			
N° of FEEDERS	8	8	8
FEEDER WIDTH (CM)	91.63	143.99	196.35
FEEDER THICKNESS (CM) (400 A/Cm <sup>2</sup> )	.20	.30	.32
FEEDER LENGTH (METERS)	11	8	5
FEEDER SPACING (METERS, EDGE-TO-EDGE)	1.83	2.88	3.93
FEEDER SPACING (DEGREES, CENTER-TO-CENTER)	45°	45°	45°

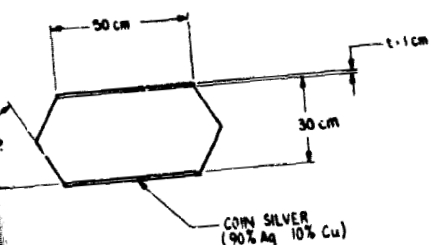


DETAIL I  
SCALE 1:7.5



BRUSH ASSY LOCATIONS  
STAGGERED  
AT SLIP-RING INTERFACE

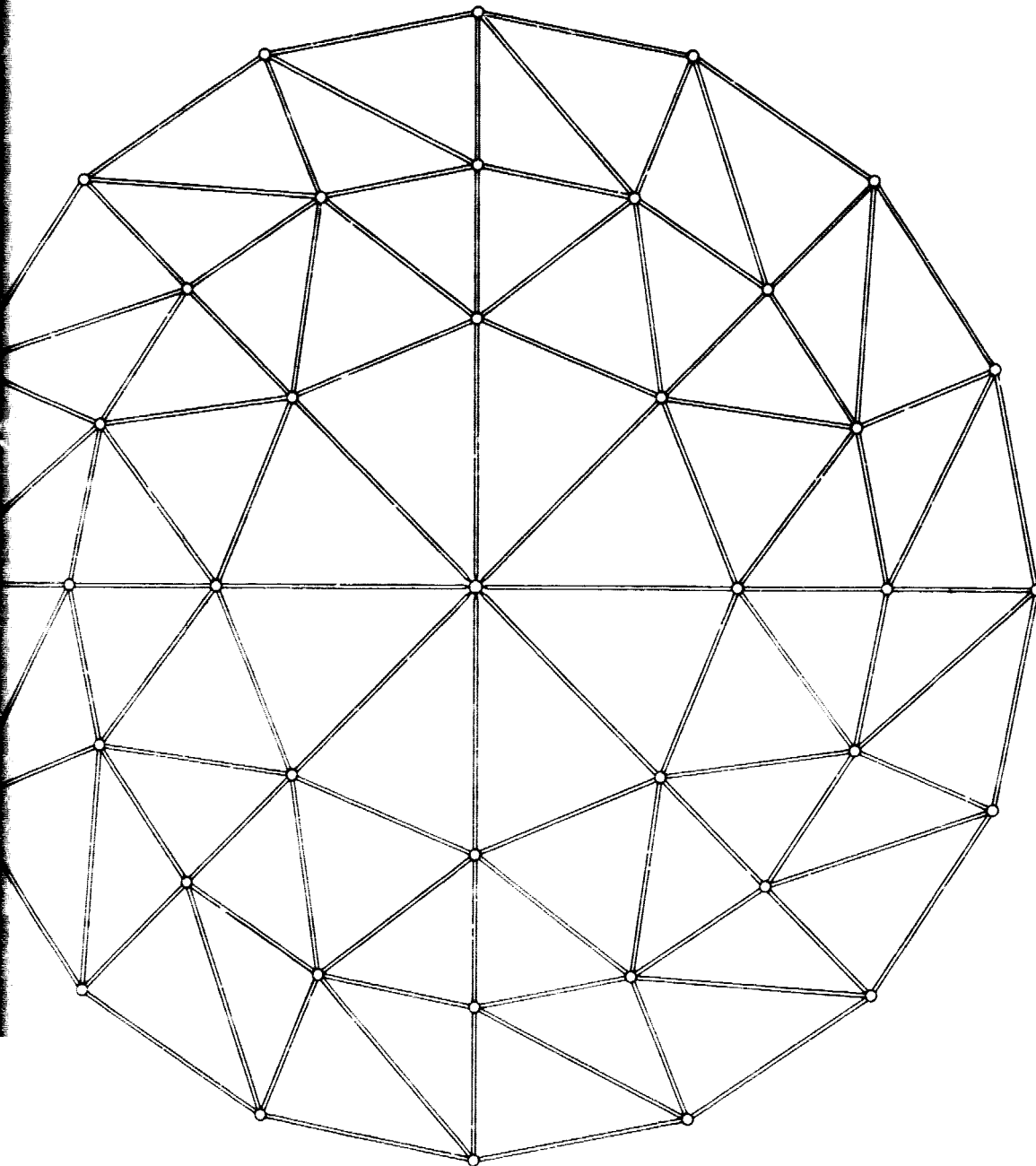
DETAIL III  
SCALE 1:2.5



DETAIL II  
SCALE 1:7.5

ORIGINAL PAGE IS  
OF POOR QUALITY

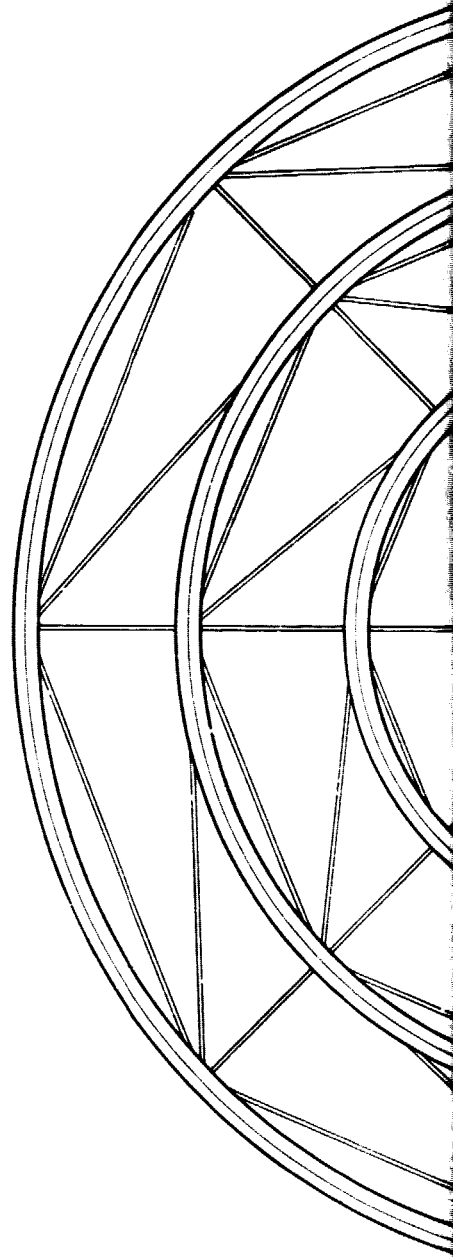
FOLDOUT FRAME 3



VIEW B-B

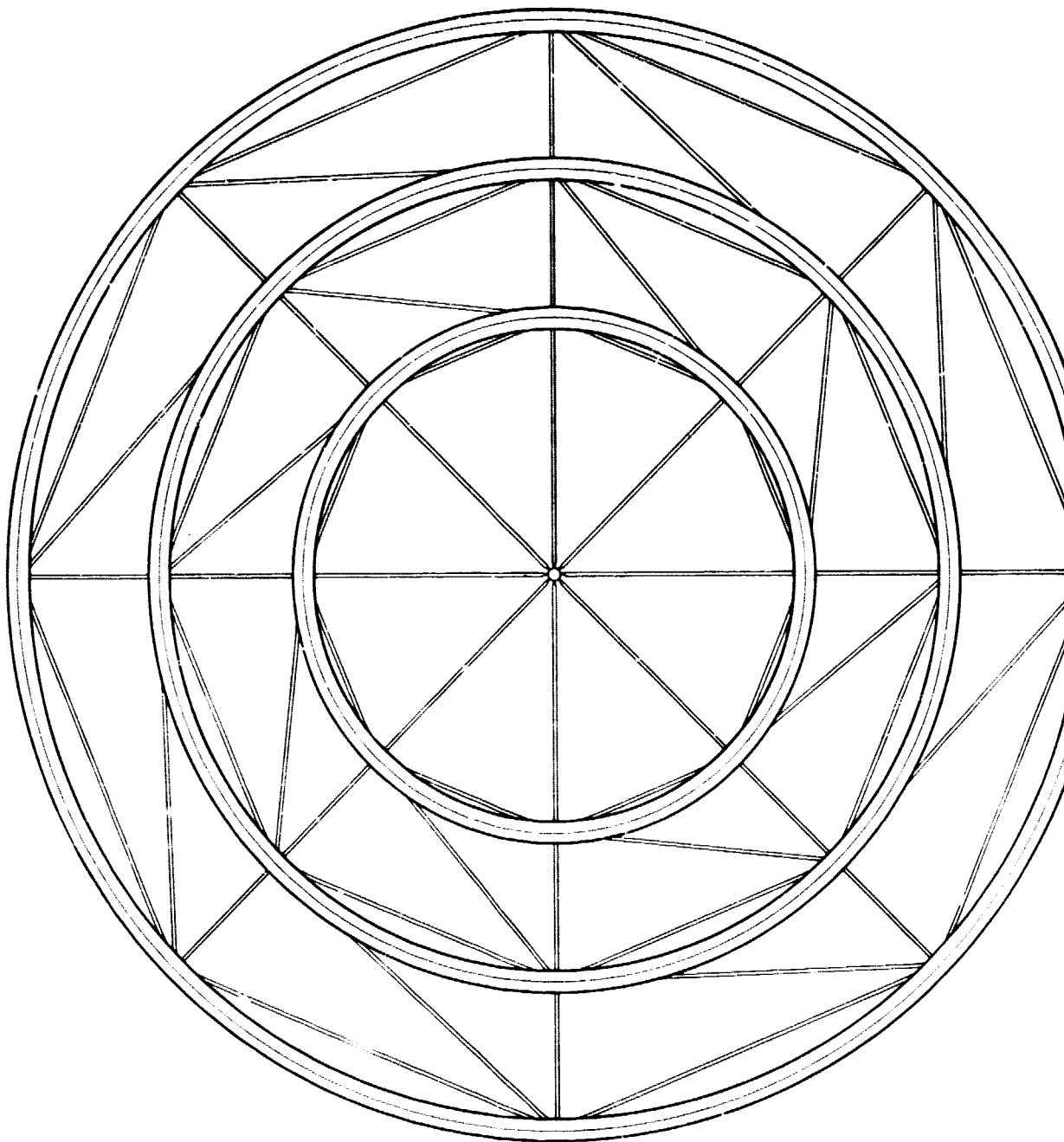
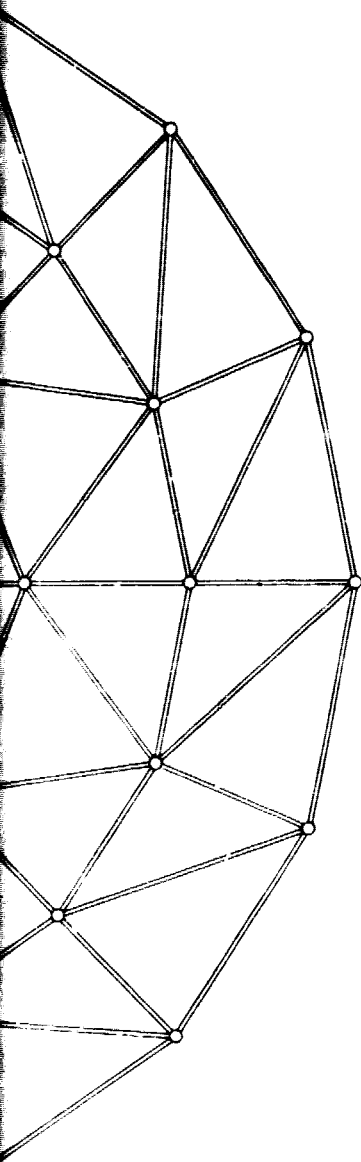
SCALE 1:25

(BRUSH ASSY SUPPORT STRUCTURE GEOMETRY)



3

FOLDOUT FRAME 4



VIEW A-A  
SCALE 1:25  
(RING SUPPORT STRUCTURE GEOMETRY)

FOLDOUT FRAME 4

FOLDOUT FRAME 5

D180-22876-3

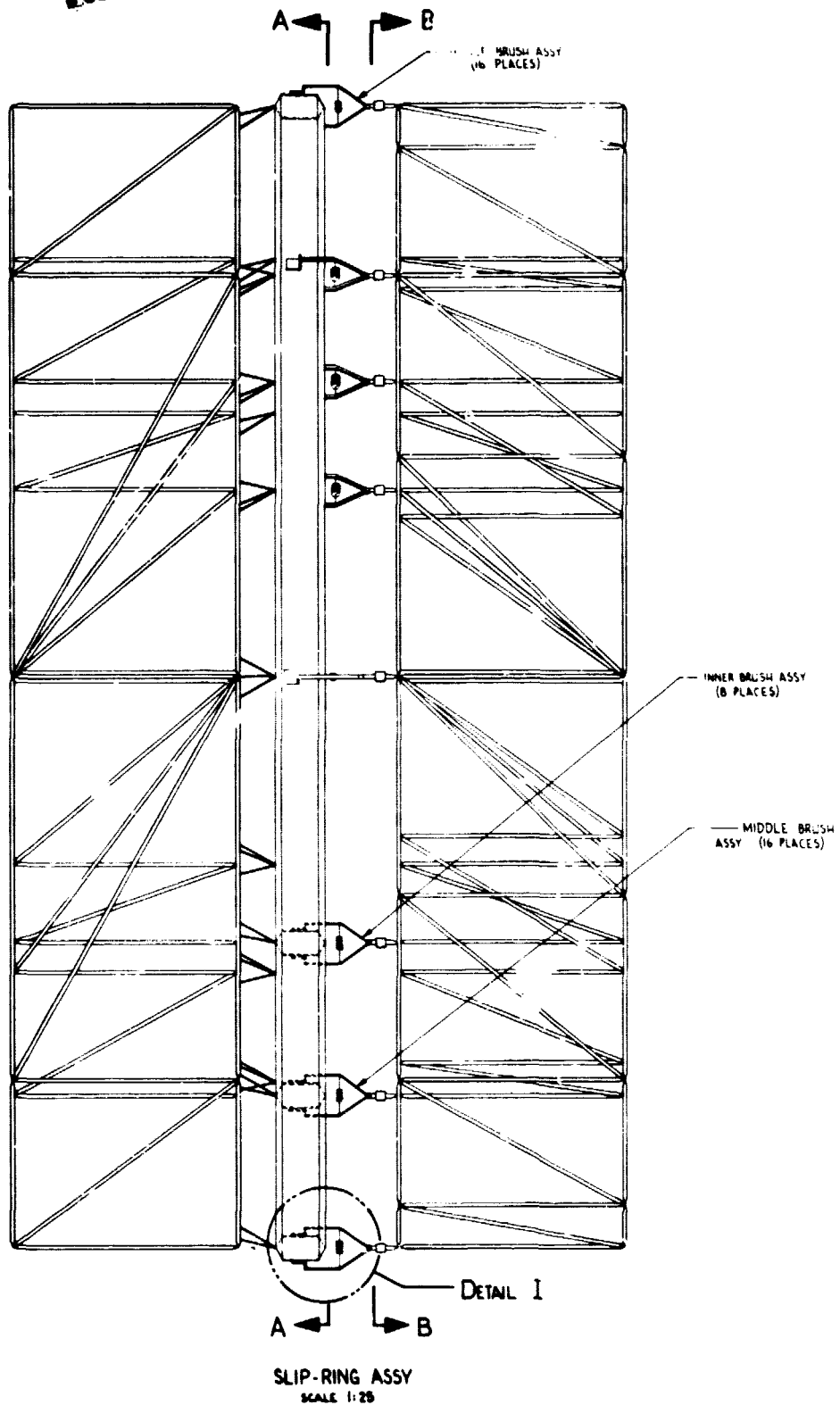
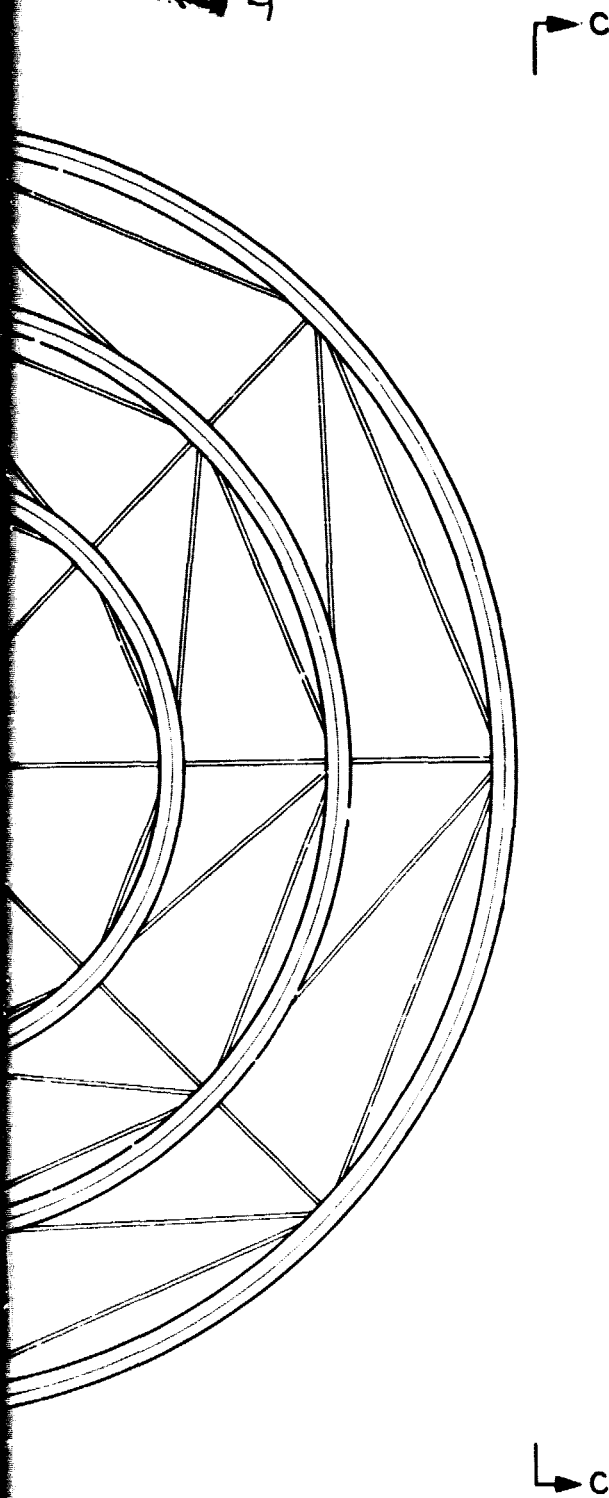


Figure 4.6-9 Electrical "Slip-Ring" Assembly

D180-22876-3

SPS-4377

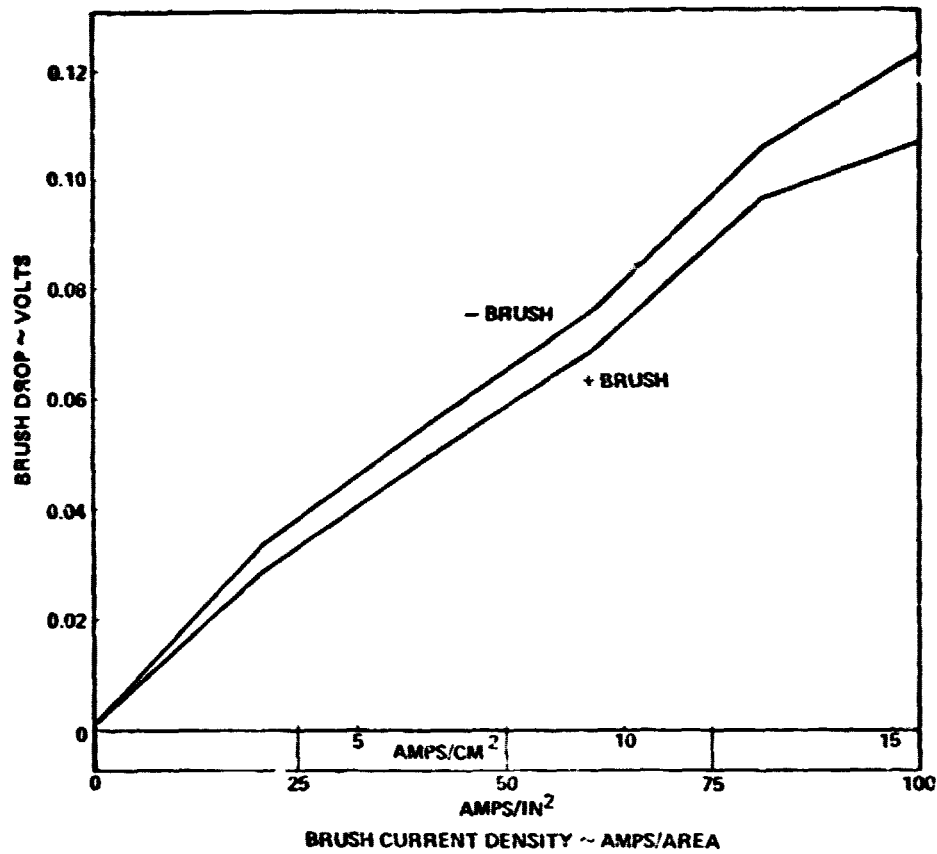


Figure 4.6-10. Silver Slip Ring Grade 26 Brush 85 Ag 3 Gr 12 Mo S<sub>2</sub>

Table 4.6-8 COMSAT Selected Brush/Slip Ring Materials for Space Applications

BRUSH MATERIAL	SLIPRING MATERIAL
COMPACT 046-45	HARD GOLD PLATE Au-1Ni ON NICKEL PLATE
Ag-12 Nb Se <sub>2</sub>	COIN SILVER Ag-12Cu
Ag-12MoS <sub>2</sub> -3C	COIN SILVER Ag-12Cu $\delta = 10.3 \text{ gm/cm}^3$ $P = 3 \times 10^{-6} \Omega \text{ cm}$



D180-22876-3

SPS-1376

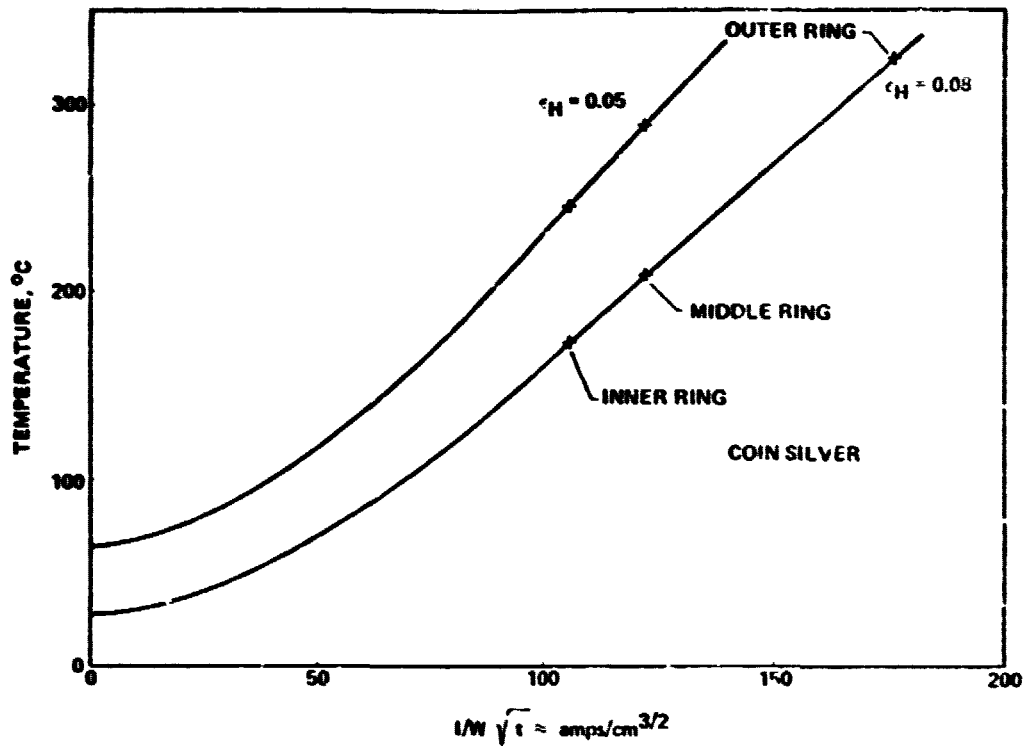


Figure 4.6-11. Slip Ring Temperatures

SPS-1376

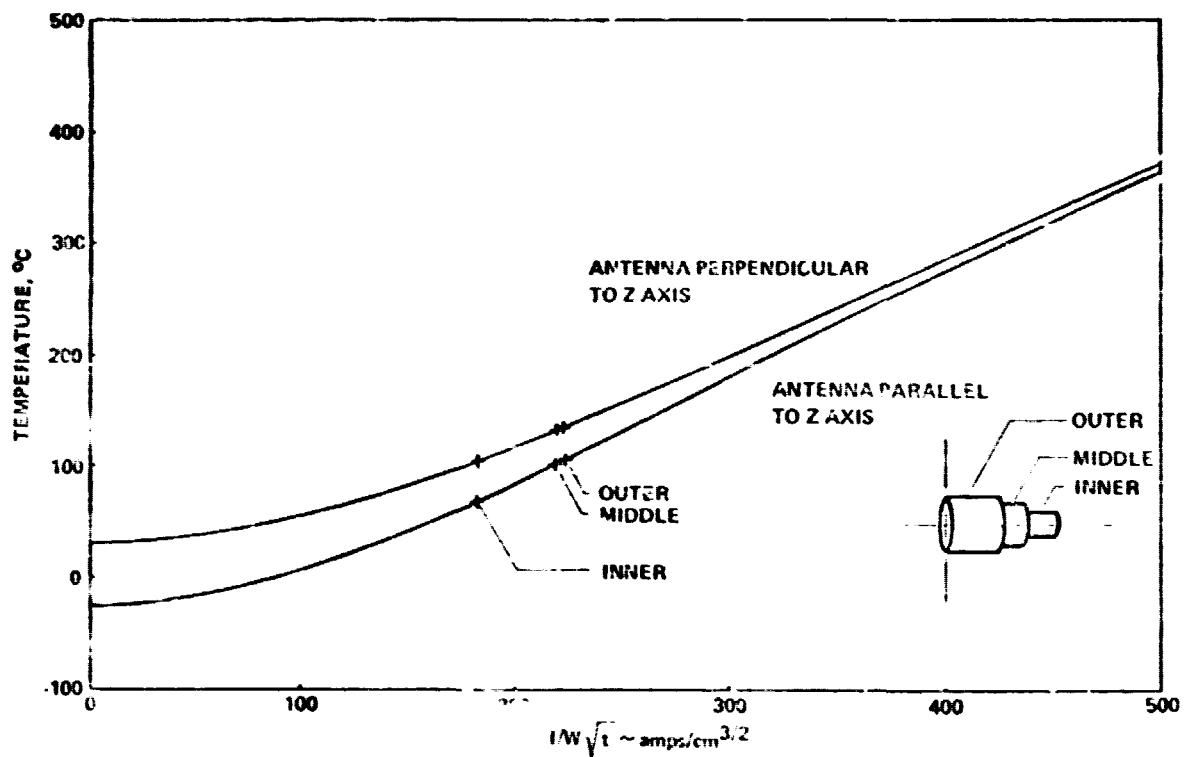


Figure 4.6-12. Gimbal Assembly Feeder Conductor Temperatures

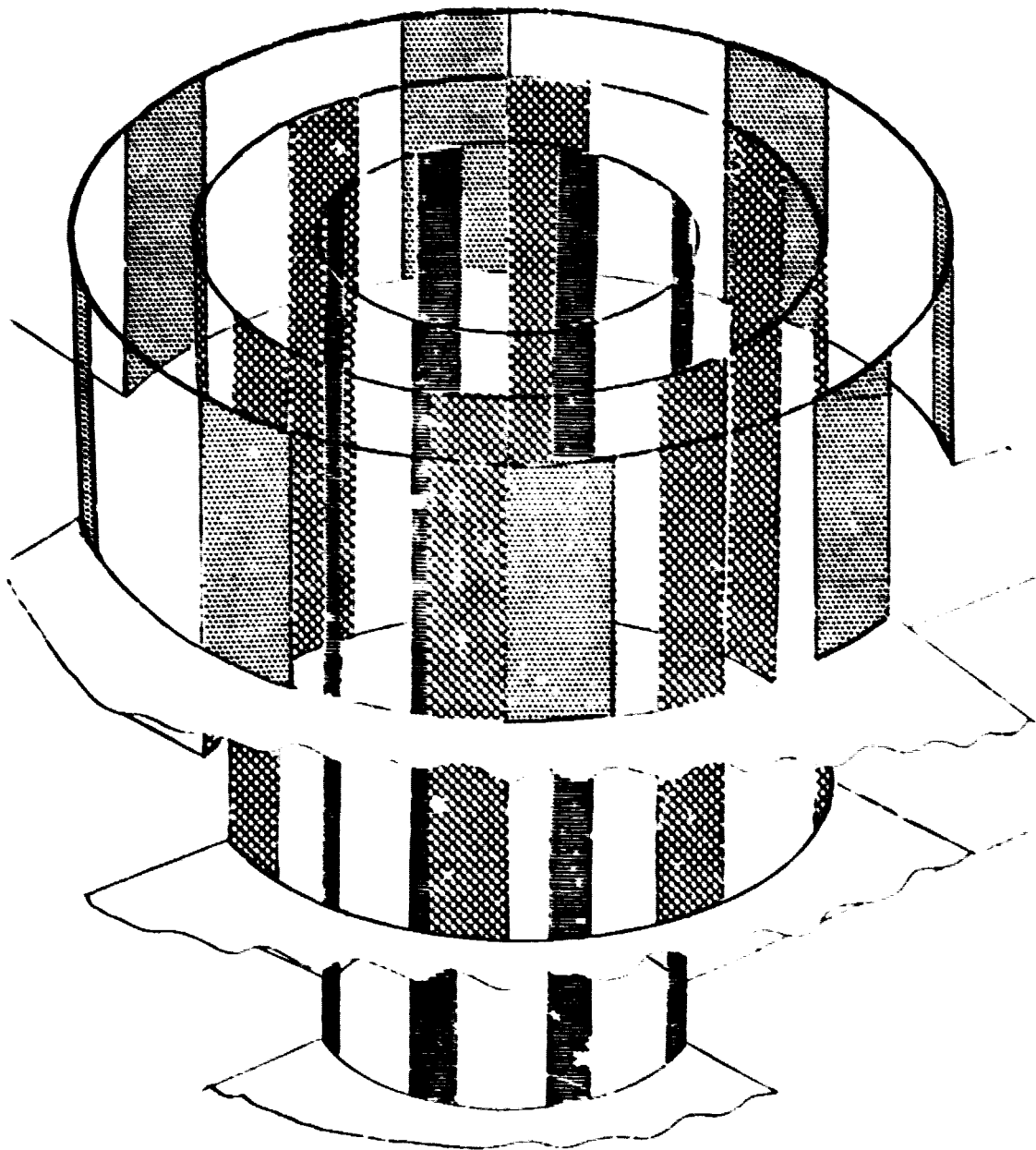


Figure 4.6-13. Slip Ring Feeders

### **D180-22876-3**

A similar thermal analysis of the NASA/JSC ball joint design was performed. The results are shown in Figures 4.6-14 and 4.6-15. The feeder temperatures are approximately the same although the effective conductor area of the feeders for the ball joint is approximately twenty times greater than the feeders for the concentric ring design. The primary reason is that the inner of the coaxial feeder conductors must radiate to the outer conductor which then must reject the heat of both conductors.

The current induced forces of the concentric ring feeders were determined. The resultant radial and tangential components of these forces are shown in Figure 4.6-16. The resultant forces are small.

General Electric provided rotary joint design concepts and analysis. Their analysis is shown in Appendix A and includes an analysis of brush/slip-ring wear. The projected wear is very small. (.0289 to .0617 CM<sup>3</sup>/year)

## **4.7 PHOTOVOLTAIC REFERENCE ATTITUDE CONTROL**

The reference photovoltaic SPS was sized to be oriented perpendicular to the orbital plane (POP) to minimize required attitude control thrust. This orientation results in the lowest mass and least complex system to meet attitude control requirements.

The POP orientation imposes a 23.5 degree cosine loss on the photovoltaic SPS at each solstice. This loss is partially compensated for by increased solar cell efficiency resulting from lower temperature operation during these periods.

An attitude control system mass summary (Table 4.7-1) was completed for the reference configuration. This system provides for a twenty percent control authority margin with the listed assumptions. A comparable system for an orientation perpendicular to the ecliptic plane (PEP) would have 5.6 times the hardware mass and 3.5 times the propellant consumption as for the POP orientation.

Since the PEP orientation does not impose the cosine losses of POP, it is about a break-even trade from the mass and efficiency standpoint. Due to the added system complexity associated with a PEP orientation, it should only be adopted if it provides a significant enough design advantage (as it does for the thermal engine SPS).

## **4.8 INTERFACE TO TRANSPORTATION SYSTEM**

### **4.8.1 Photovoltaic SPS**

A brief summary of the packaging analysis is represented in this section for major components only, with a more detailed analysis provided in Space Operations, Volume V.

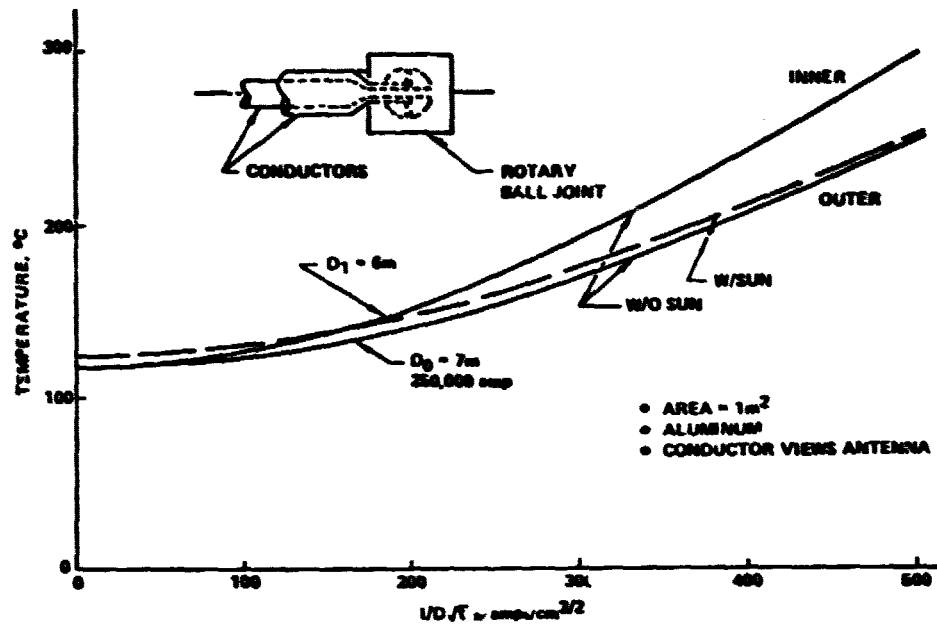


Figure 4.6-14. Conductor Temperatures

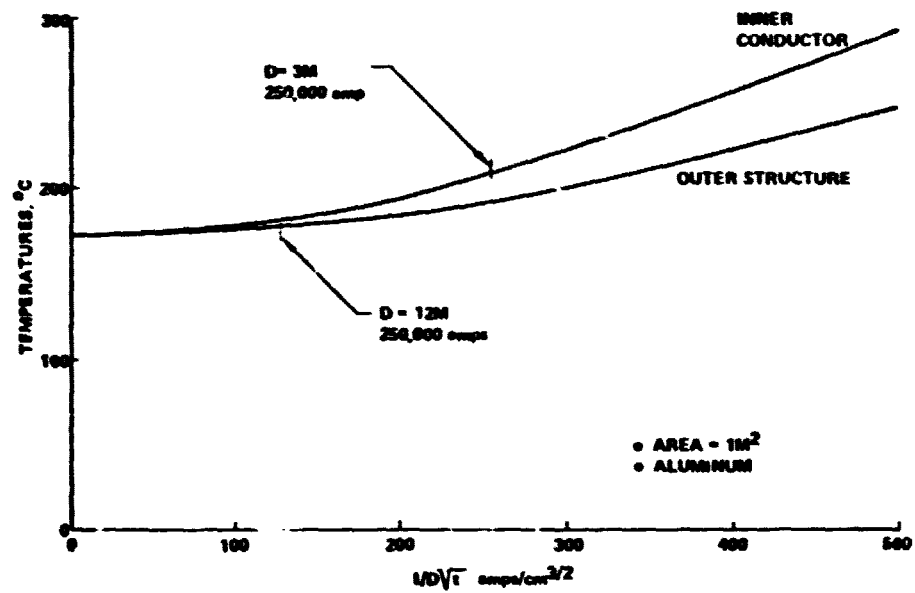


Figure 4.6-15. Rotary Ball Joint Temperatures

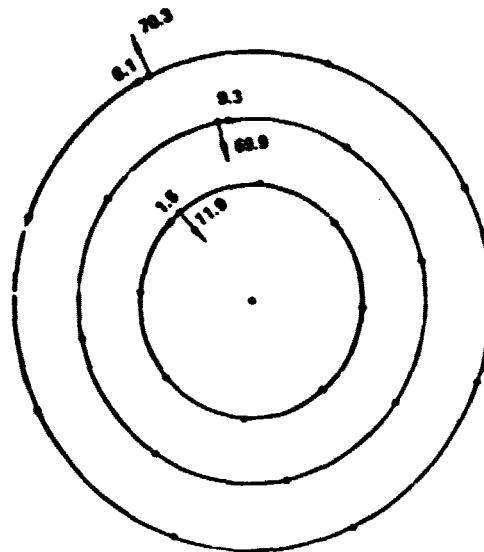


Figure 4.6-16. Ring Feeder Induced Forces in Newtons/Meter of Depth. (Current Induced Forces)

SPS-1023

Table 4.7-1. Photovoltaic Reference Attitude Control Summary

• ELECTRIC ION PROPULSION

THRUST PRODUCTION EQUIPMENT	23.3 MT
POWER PROCESSORS	90.0 MT
INSTALLATION HARDWARE	16.8 MT
NON REOCCURING TOTAL	130.1 MT
ANNUAL PROPELLANT (ARGON)	48.0 MT/YEAR
1-YEAR TOTAL	178.1 MT

ASSUMPTIONS:

OPTIMIZED  $I_{sp} \sim 20,000$  SEC

SINUSOIDAL DUTY CYCLE (30 MW PEAK, 32 MW AVG)

PERFECT CONTROL LAWS (NO WASTED PROPELLANT)

CHEMICAL PROPULSION FOR CONTROL IN EQUINOCTAL OCCULTATIONS  
( $I_{sp} \sim 400$  SEC REQUIRES 1.0 TO 1.5 MT/YEAR PROPELLANT)

▶ ALL CHEM. PROPELLANT REQ'T WOULD BE 2100 MT/YEAR.

The component packaging characteristics (Figure 4.8-1) for major photovoltaic system components is very favorable. A first estimate for the mixing of various system components for delivery to LEO is illustrated in Figure 4.8-2. The number of flights indicated is that associated with the mix of components and is not meant to be indicative of the actual launch sequence. As indicated, the dominating component was the antenna subarrays included in 246 out of 247 total flights (of identifiable hardware).

In the Part I analysis 25 to 30% of the payload shroud was used to transport the undefined antenna system. A more complete understanding of the antenna, along with the desire to deliver the subarrays fully assembled, has led to the use of the full length of the payload shroud in order to achieve mass limited launch conditions. Fortunately, the high density solar arrays can be used to offset the low density antenna subarrays during most of the launches.

#### **4.9 ANNEALING**

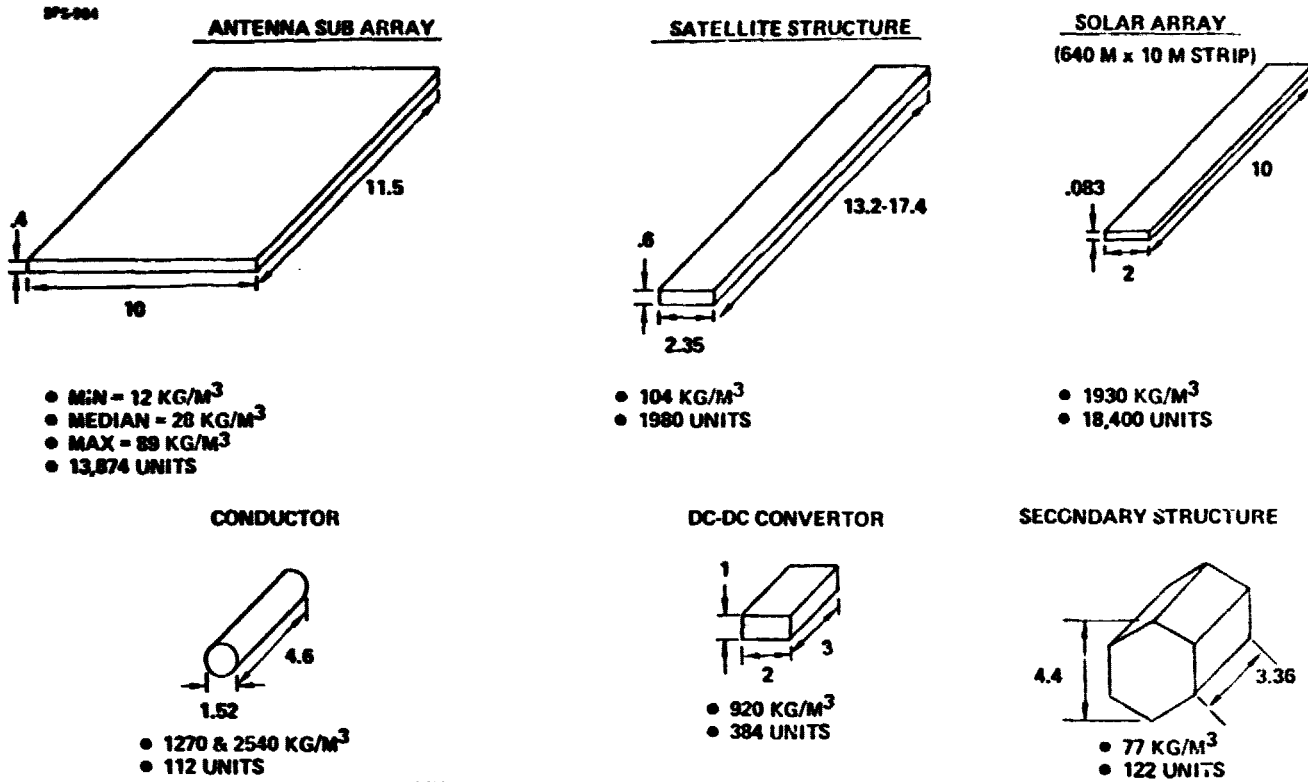
Analysis and tests of silicon solar cell annealing were conducted by Simulation Physics, Incorporated, and were presented in Part I, Volume II, Section 3.2.5.3.

Three methods of solar cell annealing were considered: thermal bulk annealing, electron beam annealing and laser beam annealing. Thermal bulk annealing uses a heat source to achieve and hold the entire solar cell at the annealing temperature for the desired length of time. To do this, the heat source must be relatively close to the solar cell and be designed to not exceed the thermal limitations of the solar array components. The required annealing time at temperature and the imposed thermal limitations result in this being the most time consuming method of annealing. This method has the largest data base.

Recent annealing developments employ directed energy. An electron beam can be used to deposit energy in the damaged region of the solar cell. This method localizes the thermal environment in the solar cell and makes it possible to achieve very high temperatures in the silicon without exceeding the thermal limitations of other blanket materials. The main potential advantage is significantly shorter anneal times. Some solar cell manufacturers use this method to anneal out ion implantation damage. The electron beam method requires the beam to be generated relatively close to the solar cell.

Laser beam annealing has many of the advantages of the electron beam device and the added potential of annealing a large area from one location. At present it is not known whether an electron beam can be used to anneal through a cover glass, but preliminary tests indicate that the laser method can be so used. Laser annealing is receiving an increasing amount of attention which will lead to the development of a much better data base.

D180-22876-3



NOTE: PACKAGING WITHIN PAYLOAD  
SHROUD TFNDS TO REDUCE COMPONENT DENSITY

Figure 4.8-1. Component Packaging Characteristics

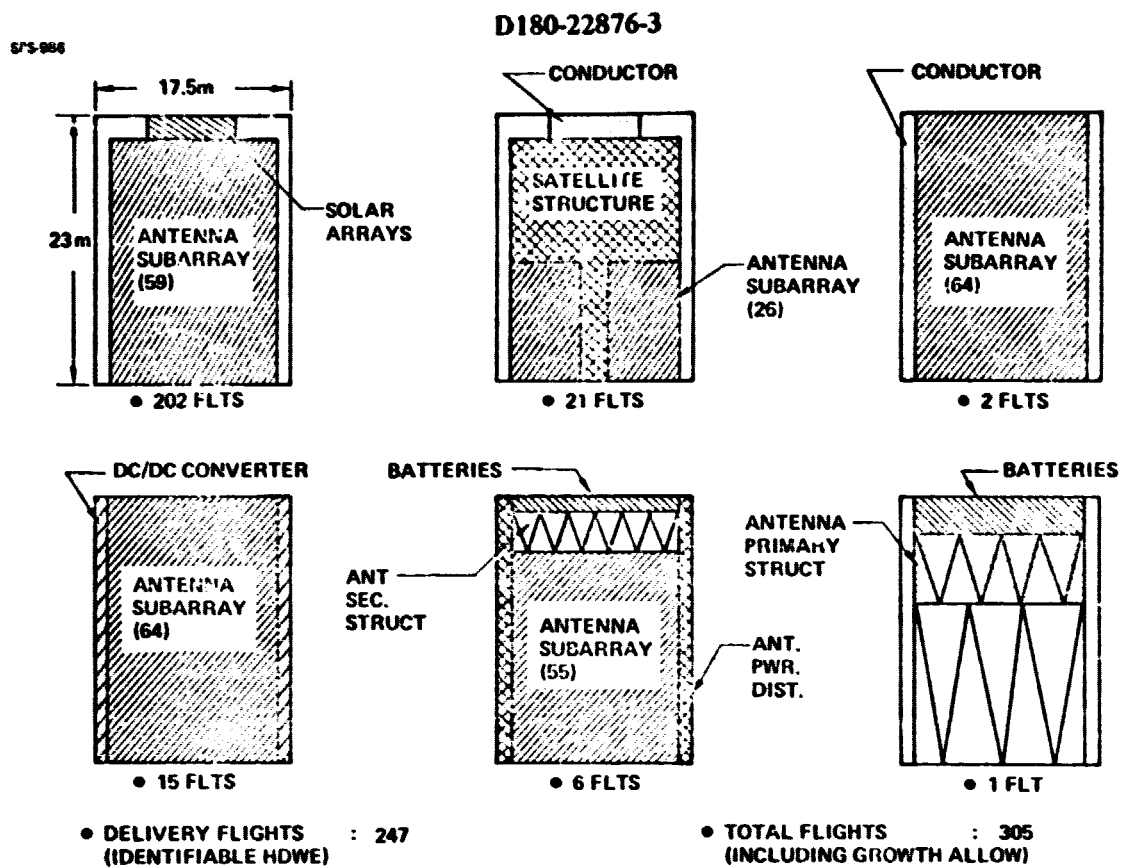


**Figure 4.8-2. Component Mix Per Delivery Flight**



### **D180-22876-3**

**Future annealing issues that need to be resolved are temperature versus time requirements, repeatability of the annealing process, degree of recovery, and the development of a better data base.**

**Since most of the previous work in annealing was done for the recovery of damage sustained in ion-implementation and not from the proton fluence received by cells in geosynchronous orbit, these issues are primarily important for SPS applications.**

**Simulation Physics, Incorporated, again under subcontract, will be annealing proton damage from solar cells using both laser and electron beam methods. Laser annealing will be conducted on conventional solar cells that are electrostatically bonded to 7070 glass covers and irradiated with a proton fluence by Boeing. The subcontractor will also design and manufacture ion-implanted cells with deep junctions under the contacts, to attain greater annealability, and use laser annealing to recover proton radiation damage. Solar cells with 75  $\mu\text{m}$  covers will also be irradiated with a proton fluence and an electron beam will be used to anneal the damage.**

**These tasks should demonstrate the feasibility of a solar cell blanket in which performance degradation caused by solar flare protons is periodically removed by an annealing process.**

## 5.0 CONFIGURATION SELECTION

### 5.1 CONFIGURATION SELECTION TRADES

#### 5.1.1 Silicon Photovoltaic

Part I of the study contract was devoted primarily to the selection of a configuration that could be taken to an additional level of depth for the reduction of uncertainties in Part II. This section will summarize the results and recommendations of Part I, update the information presented in Part I and conclude with the final configuration used in the Part II analysis.

##### 5.1.1.1 Part I Conclusions

A summary of the major parts of Part I are that:

- Silicon Costs Not "Too High"
- Silicon System Not Sensitive to Cell Performance
- CR-1 Preferable to CR-2
- Annealing Critical to Silicon System
- LEO Assy. & Self Power Show to Advantage with Annealing
- Gallium Supply & \$\$ in Question
- GaAs Thin Film Critical Technology
- If Gallium Supply & Thin Film Okay –GaAs Attractive and not as sensitive to annealing or LEO/GEO trade
- Other thin films look competitive but poor data base

With respect to the cost of silicon solar cells, we found that the large number ( $\approx 2 \times 10^{10}$ ) of 5 by 10 cm cells required for each solar power satellite could be manufactured in automated factories which would be entirely different from today's solar cell production facilities, and that the cell cost would be as proportionately low as today's high-volume semiconductor-products. The "mature industry" approach to pricing indicated that the cost of the satellite would indeed be reasonable. The weight and cost of the satellite was not too sensitive to solar cell performance. Practical satellites could be designed around solar cells having efficiencies even as low as 15.0 percent: this is achievable today.

In concentration ratio trades, the non-concentrating array always came out best from cost and weight standpoints. The key factor was the radiation degradation in reflectance of aluminized Kapton films. Project Able tests indicated that the 85 percent reflectance of the aluminized Kapton films would degrade to 63 percent, with most of the degradation occurring within the first few years of the 30-year projected satellite life.

### **D180-22876-3**

Work done by Simulation Physics, Inc., showed that in solar cells the radiation damage caused by solar-flare protons can be annealed out, avoiding the loss of significant power sales revenue. Laser light, electron beams and infrared radiation are possible heating methods. Thermal annealing is worth developing.

Low-earth-orbit turned out to be the most practical place to assemble the solar power satellites, provided electric thrusters could be used to transfer the completed satellite modules to geosynchronous orbit. Geosynchronous-orbit assembly required shipping huge quantities of propellants to low-earth orbit. Essential to the low-earth-orbit assembly approach is the thermal annealing of radiation damage occurring during transit through the Van Allen radiation belts.

Gallium arsenide solar cells were found to be advantageous because of their probable 21 percent conversion efficiency and their moderate loss in performance as they became warmer (as with solar concentration). However, gallium availability turned out to be questionable. Gallium was not concentrated sufficiently in seawater to be worth recovering. Gallium is at present a by-product of aluminum and zinc refining, with coal fly-ash being a potential source. The projected United States coal consumption and aluminum production will not be great enough to support the construction of several solar power satellites per year unless the gallium arsenide layer in the solar cells is made thin, say under 10  $\mu\text{m}$ . The U.S. Department of Energy (DOE) has funded Batelle Northwest to carefully investigate gallium availability.

Some work has suggested that radiation damage in thin layers of gallium arsenide can be annealed out at fairly low temperatures—perhaps at only 398K (256°F). Also, gallium arsenide cells are more resistant than silicon solar cells to radiation damage, making them more applicable to powering the transfer of a completed solar power satellite from low-earth orbit to geosynchronous orbit.

Thin film solar cells, many types of which are being developed by DOE, are characterized by great but unproven potential. Their low weights and thin cross-sections make possible ideal satellite design. Some offer the potential of good efficiency, for example 15 percent in single-crystal indium-phosphide/cadmium sulfide. However, the generation of sizeable crystals on thin films has not yet been realized. The best achieved efficiency in other than single-crystal cells has been around 8 percent—for cadmium sulfide, which has not yet been proven to be stable in performance.

Using a comparison matrix to illustrate the good or poor points of the various types of systems (Table 5.1-1) also leads to the conclusion that a single crystal silicon, CR-I system is the best choice for Part II emphasis. The choice of best alternatives for an advanced technology system appears to be thin film or thin cell GaAs.

D180-22876-3

Table 5.1-1. Photovoltaic Energy Conversion Comparisons

SPS-1527

	PERFORMANCE	RADIATION DEGRADATION	THERMAL DEGRADATION	SYSTEM SIZE	SYSTEM MASS	SYSTEM COMPLEXITY	SYSTEM MAINTAINABILITY	MATERIAL AVAILABILITY	TECHNOLOGY ADVANCEMENT REQUIREMENTS
<b>SINGLE CRYSTAL CELLS</b>									
SILICON CR-1	MED	FAIR	FAIR	FAIR	MED	GOOD	GOOD	GOOD	LOW
SILICON CR-2	MED	FAIR	FAIR	FAIR	MED	FAIR	MED	GOOD	LOW
GaAs CR-1	HIGH	FAIR	GOOD	GOOD	LOW	GOOD	GOOD	POOR	LOW
GaAs CR-2	HIGH	FAIR	GOOD	GOOD	LOW	FAIR	MED	POOR	LOW
GaAs CR>2	V. HIGH	FAIR	GOOD	GOOD	LOW	POOR	POOR	MARGINAL	LOW
<b>ADVANCED THIN FILMS</b>									
SILICON CR-1	LOW	GOOD	FAIR	FAIR	MED	GOOD	GOOD	GOOD	V. HIGH
SILICON CR-2	LOW	GOOD	FAIR	FAIR	MED	FAIR	MED	GOOD	V. HIGH
GaAs CR-1	HIGH	EXCELLENT	GOOD	GOOD	LOW	GOOD	GOOD	FAIR	HIGH
GaAs CR-2	HIGH	EXCELLENT	GOOD	GOOD	LOW	FAIR	MED	FAIR	HIGH
GaAs CR>2	HIGH	EXCELLENT	GOOD	GOOD	LOW	POOR	POOR	FAIR TO GOOD	HIGH
CADMIUM SULFIDE	LOW	EXCELLENT	GOOD	POOR	LOW	GOOD	GOOD	GOOD	V. HIGH
COPPER INDIUM SELENIDE	LOW	EXCELLENT	GOOD	POOR	LOW	GOOD	GOOD	POOR	V. HIGH

ORIGINAL PAGE 1  
OF POOR QUALITY

These items led to the recommendation of a silicon, concentration ratio of one (CR1) and annealable reference photovoltaic system. The major reasons for this recommendation were that it provided the best data base with the least amount of extrapolation, lowest system complexity and therefore was the best candidate for reduction of uncertainties.

A CR-2 silicon system had an end-of-life effective concentration ratio of 1.31 which provided about a break-even situation with at including increased system complexity and uneven illumination problems associated with CR-2. A nominal mass summary for the Part I recommended configuration is shown as Table 5.1-2.

Other recommendations at the end of Part I were to carry gallium arsenide photovoltaics as an advanced technology system until more is known about the gallium availability and thin cell technology questions. Also recommended was to discontinue thin film photovoltaics until a better data base was available.

#### 5.1.1.2 Part II Objectives

The objective of Part II was to establish a system that was designed to a depth which would allow a reduction in the uncertainties by a factor of two. To do this it was necessary to:

Improve reference satellite definition

- Pursue those areas already defined to an additional level of depth:
  - Solar array
  - Primary structures
  - Power distribution
- Define those significant areas previously accepted from JSC green book
  - MPTS
  - Attitude control
  - Secondary structure
  - Rotary joint
- Pursue key issues
  - Silicon annealing
  - Cost data base

#### 5.1.1.3 Outline of Part II Effort

To generate baseline designs, we adopted a cell size and type, a cover and substrate material, and an interconnecting technique. An important consideration was appropriateness to automated manufacture. With the blanket designed we could then proceed with preliminary designs of primary structure, end buses and control for carrying the power from the solar array to the rotary joint. Minimum manhours in orbital assembly was an important requirement of the structure.

D180-22876-3

ORIGINAL PAGE IS  
OF POOR QUALITY

Table S.1-2. Part I Nominal Mass Summary Weight in Metric Tons

SPS-1000

COMPONENT	ORIENTATION	CR-2		CR-1		
		MIDTERM	PART I FINAL	PART I FINAL	PART II MIDTERM	PART II FINAL
<b>1.0 SOLAR ENERGY COLLECTION SYSTEM</b>	<b>(36,616)</b>	<b>(59,313)</b>	<b>(49,512)</b>	<b>(56,367)</b>		
1.1 PRIMARY STRUCTURE	2,483	14,970	8,000	2,334		
1.2 SECONDARY STRUCTURE	100	200	200	200		
1.3 MECHANICAL SYSTEMS	40	40	40	40		
1.4 MAINTENANCE STATION	85	—	—	—		
1.5 CONTROL	340	340	340	340		
1.6 INSTRUMENTATION/ COMMUNICATIONS	4	4	4	4		
1.7 SOLAR-CELL BLANKETS	25,746	37,582	34,111	51,887		
1.8 SOLAR CONCENTRATORS	5,149	2,978	3,276	—		
1.9 POWER DISTRIBUTION	2,570	3,180	3,532	1,589		
<b>2.0 MPTS</b>	<b>15,371</b>	<b>15,371</b>	<b>15,371</b>	<b>15,371</b>		
SUBTOTAL	51,987	51,987	64,883	71,728		
GROWTH	25,994	25,994	32,442	35,864		
TOTAL	77,981	112,026	97,325	107,592		

### **D180-22876-3**

Other areas requiring definition include the microwave power transmission system, attitude control, secondary structure and rotary joint.

We were to also investigate gallium arsenide solar cells further, particularly with respect to their use in concentrated sunlight, considering the reflectors, supporting structure and performance during anticipated mis-orientations.

An important key issue in the use of silicon solar cells is annealability. Many years ago the U.S. Naval Research Laboratory demonstrated that radiation damage can be annealed out of silicon solar cells. However, no one has annealed cells repeatedly, so we do not know what is the unannealable fraction of radiation damage. More work in this field is recommended.

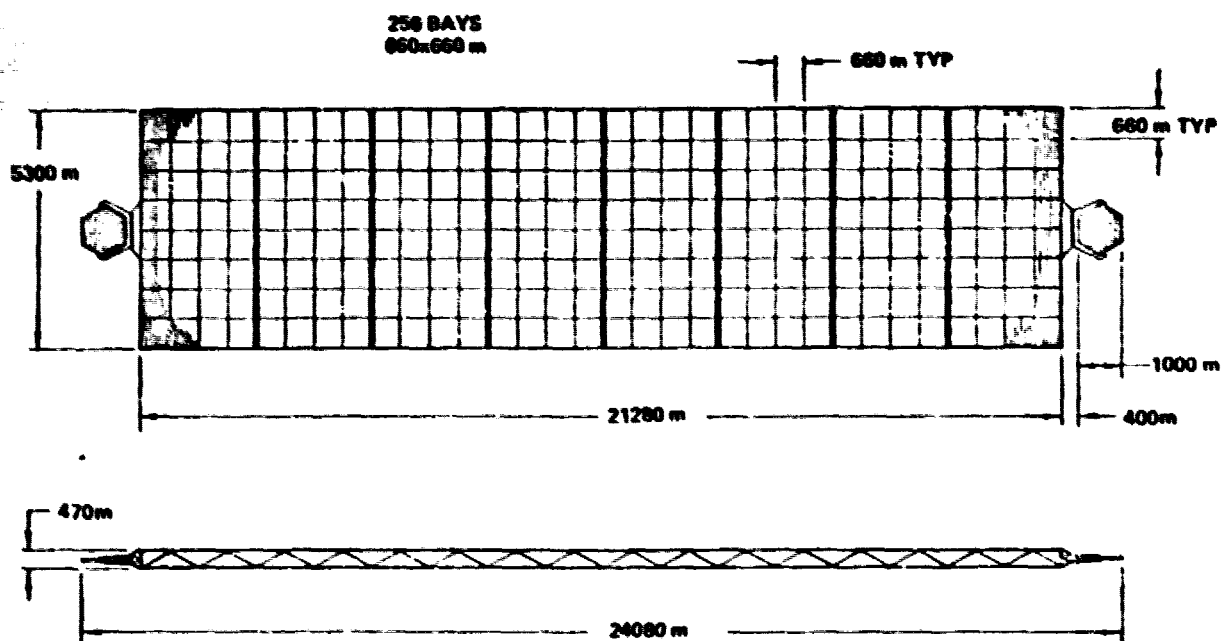
A full preliminary design of the solar power satellite was not possible with the available funding. However, the available resources did permit in-depth explorations of those portions of the design that significantly contribute to the uncertainties of mass and cost.

As an example, previous work was hampered by lack of a data base for thin-film solar cells. Additional investigation revealed that at this time an adequate data base on thin-film cells is not available because the necessary inventions and processes have not been developed. However, in other development work, the single-crystal silicon solar-cell technology had advanced to the point where 12.5 percent efficiencies are being obtained with 50  $\mu\text{m}$  thick cells, and the COMSAT-invented technique of texturing solar cell surfaces turned out to improve hardness to radiation. As a result we were able to develop, with reasonable extrapolations of thin single-crystal silicon cell technology, a blanket design that is probably very close in performance to that which will be provided by thin-film cells when they become available.

Other sources of uncertainty, which resulted from design complexity and analytical difficulty, were likewise resolved. The resulting array concept was one which is achievable with reasonable extrapolation of the present state-of-the-art, rather than requiring new invention. The corresponding interim configuration is shown in Figure 5.1-1; a mass summary is given in Table 5.1-3.

#### **5.1.1.4 Incorporation of Technology Advances**

There were advances in solar cell technology which occurred during Part II that may affect the future selection for a photovoltaic SPS. These advances are discussed in more detail in the section on solar cells (Section 4.4). Briefly, there has been large grain growth (25  $\mu\text{m}$ ) on thin (2  $\mu\text{m}$ ) polycrystalline GaAs using laser recrystallization. There also has been 20.5 percent efficient homojunction GaAs cells demonstrated in AM-1 sunlight. With a better data base on gallium availability another investigation of a GaAs photovoltaic system may be appropriate in the near future.



TOTAL SOLAR CELL AREA: 97.34 Km<sup>2</sup>  
 TOTAL ARRAY AREA: 102.51 Km<sup>2</sup>  
 TOTAL SATELLITE AREA: 112.78 Km<sup>2</sup>  
 OUTPUT: 16.43 GW MINIMUM 10 SLIPRINGS

Figure 5.1-1. Part II Midterm Photovoltaic Reference Configuration

Table 5.1-3. Part II Midterm Nominal Mass Summary Weight in Metric Tons

SPS-1020

CR = 2 (10 GW B.O.L.)

CR = 1 (10 GW MINIMUM 30 YRS)

COMPONENT	ORIENTATION	MIDTERM	CR = 2 (10 GW B.O.L.)				CR = 1 (10 GW MINIMUM 30 YRS)			
			PART I FINAL	PART I FINAL	PART II MIDTERM	PART II FINAL	PART I FINAL	PART I FINAL	PART II MIDTERM	PART II FINAL
1.0 SOLAR ENERGY COLLECTION SYSTEM	(36,616)	(59,313)	(19,512)	(56,357)	(56,164)					
1.1 PRIMARY STRUCTURE	2,493	14,970	8,000	2,334	6193					
1.2 SECONDARY STRUCTURE	189	209	209	209	—					
1.3 MECHANICAL SYSTEMS	40	40	40	40	67					
1.4 MAINTENANCE STATION	85	—	—	—	—					
1.5 CONTROL	340	340	340	340	150					
1.6 INSTRUMENTATION/ COMMUNICATIONS	4	4	4	4	4					
1.7 SOLAR CELL BLANKETS	25,746	37,592	34,111	51,897	47,319					
1.8 SOLAR CONCENTRATORS	5,149	2,978	3,276	—	—					
1.9 POWER DISTRIBUTION	2,570	3,180	3,532	1,589	2451					
2.0 MPTS	15,371	15,371	15,371	15,371	(24,384)					
SUBTOTAL	51,987	74,684	64,683	71,728	80,568					
GROWTH	25,994	37,342	32,442	35,864	20,142					
TOTAL	77,981	112,026	97,325	107,592	100,710					



### **D180-22876-3**

Another significant advance relates to the radiation degradation characteristics of 50  $\mu\text{m}$  (2 mil) silicon solar cells. Plotting data on irradiated solar cells, from JPL's "Solar Array Design Handbook," revealed that there was a significant advantage with thinner cells (Fig. 5.1-2). This was further substantiated by a degradation vs fluence chart (Fig. 5.1-3) for 2 mil silicon cells published by Solerex. With a 30 year fluence of equivalent 1-Mev electrons the 2 mil cell has only degraded to approximately 90 percent of its initial power. This lower degradation suggests that annealing is not as critical an issue as was previously anticipated.

In part I the CR1 vs CR2 trade assumed that the aluminized Kapton reflectors degraded 28 percent in 30 years due to the radiation environment. This assumption was based on Project Able data (Fig. 5.1-4) which has since been updated. It is now accepted that in thin aluminized Kapton the reflectivity does not effectively degrade with a 30 year fluence of the geosynchronous radiation environment.<sup>(3)</sup>

Using new reflector degradation data from Wm. Carroll of JPL, another analysis was made to determine the effect on the CR1 vs CR2 trade. The effective concentration ratio ( $\text{CReff}$ ) of a geometric CR2 system was 1.31 using the Project Able degradation. With no reflector degradation  $\text{CReff} = 1.36$ . The small change is due to the fact that the major portion of the power degradation in a CR2 system is from increased solar cell operating temperature.

The slight increase in  $\text{CReff}$  alone does not make a CR"2" system more advantageous. Other problems associated with the CR"2" system are uneven illumination and the effects of shadowing on solar cell string output (Fig. 5.1-5). These facts plus increased system complexity with CR"2" still shows the CR1 system to be the best choice for a reference.

#### **5.1.1.5 Structural Design Options**

A comparison of continuous and non-continuous chord structural approaches is given in Appendix B, along with a discussion of the associated ramifications.

#### **5.1.1.6 Final Configuration Selection**

The solar cell selection (Table 5.1-4) was based on known or anticipated, 1985, performance characteristics. A solar cell efficiency of 15.75 percent is somewhat lower than previously shown and is more conservative since an 18 percent 50  $\mu\text{m}$  solar cell is still possible by 1985. The "V-Groove" cover adds about 10 percent to the solar cell efficiency which results in an effective efficiency of 17.3 percent. The major reason for using a lower cell efficiency was to reduce the effect of solar cell efficiency on system uncertainties.

The configuration for the reference system is based on a CR1, silicon photovoltaic, annealable system with an aspect ratio of approximately four. The structure will be composed of tapered tube members forming 20 meter beams (Fig. 5.1-6).

D180-22876-3

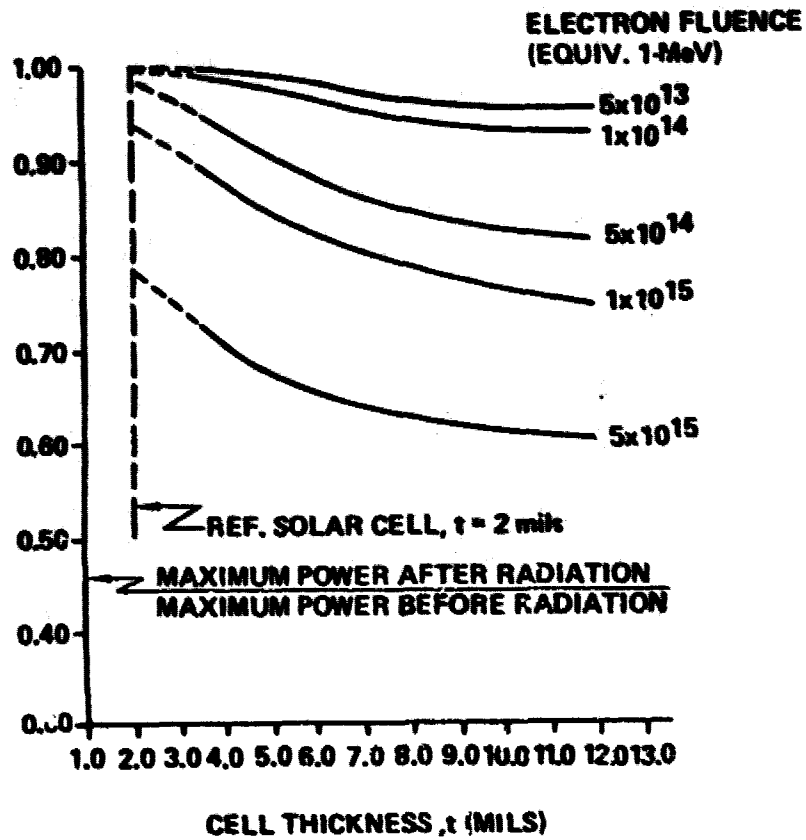


Figure 5.1-2. Thin Cells Exhibit Lower Radiation Degradation

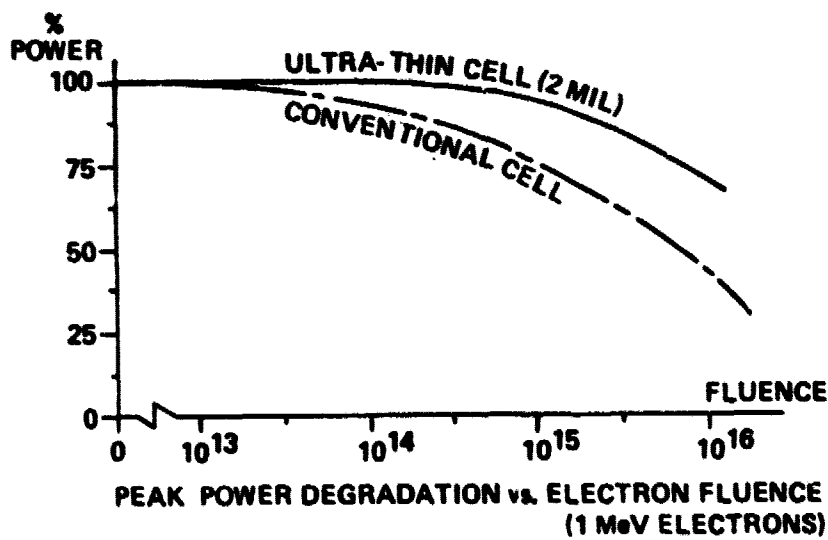


Figure 5.1-3 Thin Cells Exhibit Lower Degradation

D180-22876-3

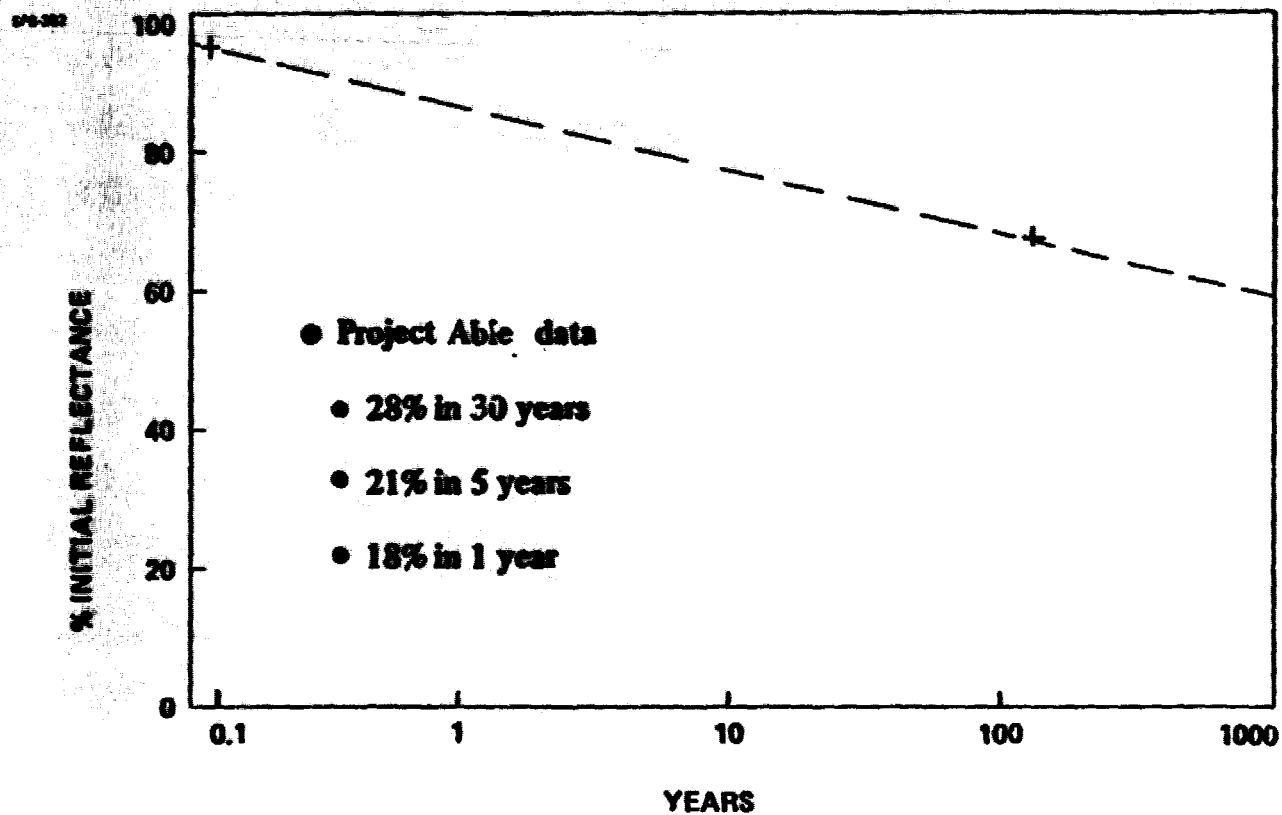


Figure 5.1-4. Reflector Radiation Degradation

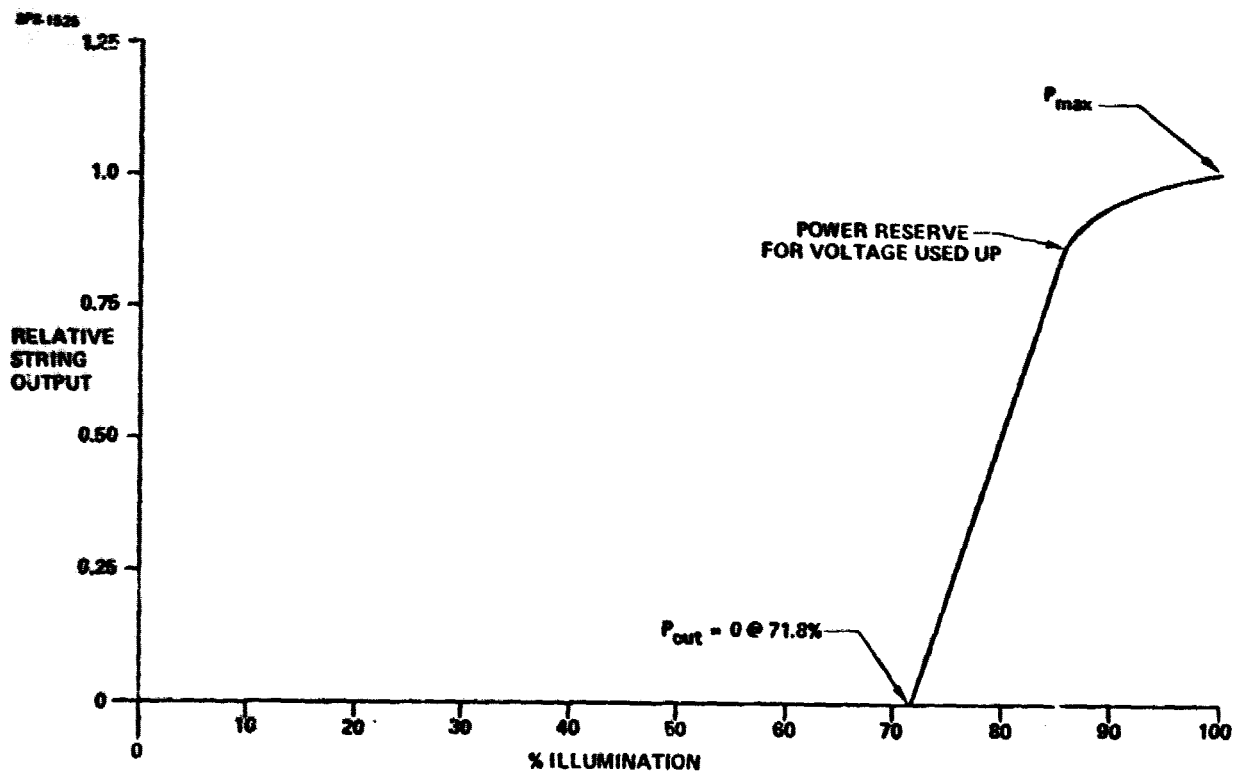


Figure 5.1-5. Shadowing Affects String Output

Table 5.1-4 Solar Cell Selection

FEATURE	SELECTION	RATIONALE
Type	Silicon	Designated as baseline
	N-on-P	More radiation-resistant than P-on-N
Resistivity	2 ohm-cm	Boeing tests have shown that 2 ohm-cm violet cells had the highest output after irradiation with $7 \times 10^{10}$ 1-MEV protons
Cell size	Approx. 50 cm <sup>2</sup>	Adjust length and width to optimize lost area factors on solar array
Connections	On back of cell	Compatible with automated assembly of array blanket
Thickness	50 $\mu$ m	Lower blanket mass and much lower radiation degradation
Efficiency	15.75% (AM=O @ 25°C)	Appears achievable for 50 $\mu$ m production cells by 1985
Cover	3-mil borosilicate microsheet with V-grooves over grid lines	The cover should provide a 10 percent increase in cell efficiency and good radiation protection. Electrostatic bonding to cell is still applicable.
Substrate	2-mil microsheet	Radiation protection with electrostatic bonding and annealing compatibility

SPS-1010

D180-22876-3

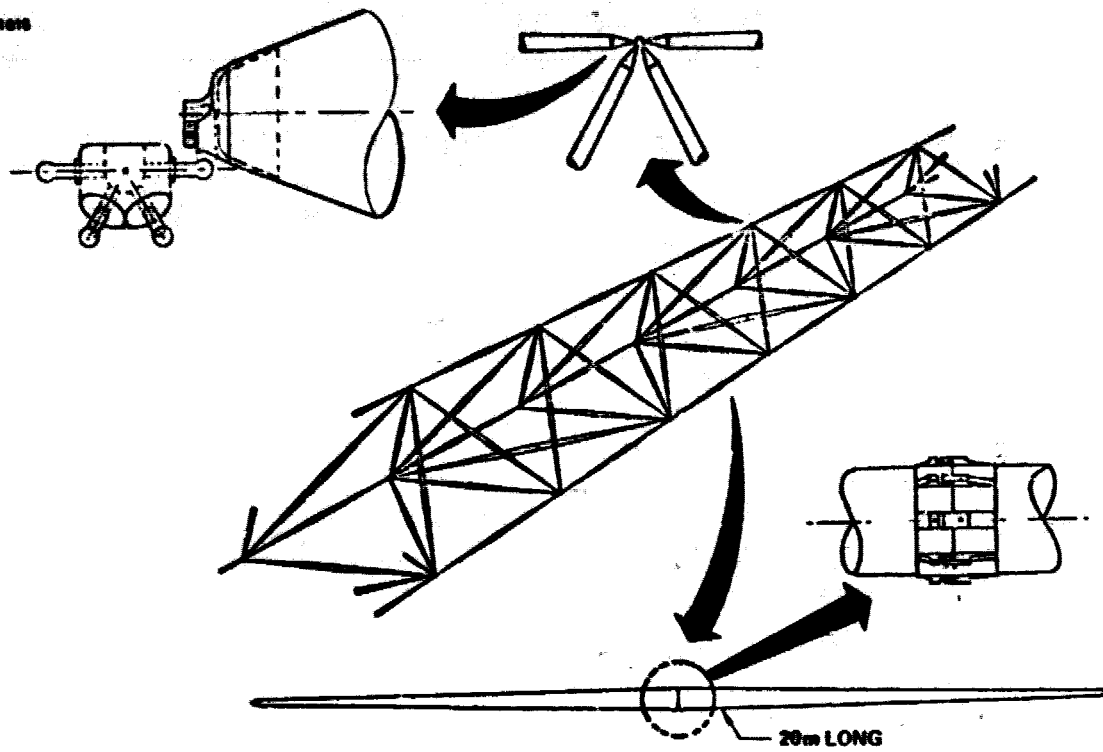


Figure 5.1-6. Photovoltaic Reference 20 Meter Beam Structure

This configuration provided a design point that could be taken to an additional level of detail for the reduction of uncertainties in Part II. The section on configuration definition (Sec. 6.1.1) will show greater detail of the system and subsystem components along with the mass and uncertainties that evolved in this part of the study.

### 5.1.2 Rankine Thermal Engine

In this section will be described the design trades leading to a final configuration definition. The most important "trade" is the selection of the cycle temperature ratio, since it has a large impact on system mass.

#### 5.1.2.1 Cycle Temperature Ratio Selection—First Principles

The following is a description of a parametric analysis of the effect on thermal engine SPS power generation mass of a range of cycle temperature ratio. Study resources did not permit numerous "point designs"; however, the parametrics are "anchored" by a few mass estimates, including turbine mass estimates by General Electric.

As explained in Section 4.5.5, the heat rejection required is:

$$P_{rej} = P_{out} \left( \frac{1}{\eta} - 1 \right),$$

where  $P_{out}$  is the useful, shaft, power and  $\eta$  is the cycle efficiency.

$$\eta = \frac{P_{out}}{P_{in}}$$

The cycle efficiency parametric used was

$$\eta = 0.8 \frac{T_{in} - T_{out}}{T_{in}},$$

where  $T_{in}$  is the turbine inlet temperature and  $T_{out}$  is the radiator surface temperature. The turbine inlet temperature is, of course, the boiler outlet temperature, and the radiator surface temperature is assumed equal to the turbine outlet temperature. The cycle temperature ratio is defined as the ratio of  $T_{out}$  to  $T_{in}$ .

The vapor pressure of the potassium working fluid is a function of temperature, as shown in Figure 5.1-7.

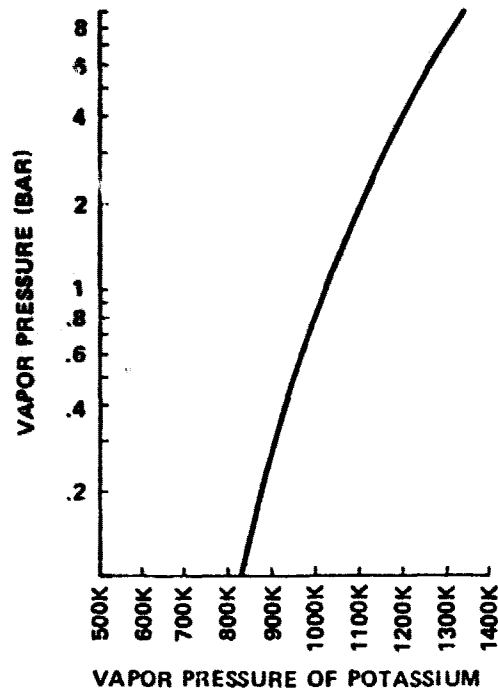


**Figure 5.1-7. Potassium Vapor Pressure Vs. Temperature**

One advantage of the use of alkali metals, such as potassium, rather than water is immediately apparent. The vapor pressure at high temperatures is much lower, which allows lighter ducting. High temperature is, of course, necessary for the combination of good efficiency and lightweight radiators.

The cycle temperatures thus influence the turbine inlet and outlet pressures. Section 4.1.3 explained how columbium was selected for the turbine housing. The turbine inlet temperature should be about

1242K (1776°F). At this temperature the vapor pressure is approximately 531 kPa (77 psi). In the temperature selection trade,  $T_{in}$  was kept constant at 1242 K. Low turbine outlet temperatures mean low outlet vapor pressures and a consequent high pressure ratio:

$$\frac{P_{in}}{P_{out}} = \frac{\text{Pressure in (at turbine inlet)}}{\text{Pressure out (at turbine outlet)}}$$

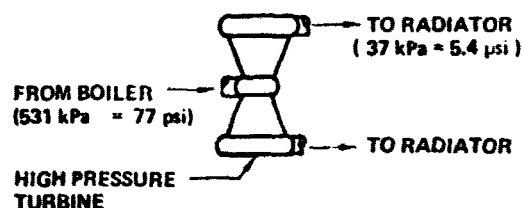
High pressure ratios mean a large number of turbine stages and large housings. The last turbine stages ("back end") become very large due to the low pressure. General Electric has concluded that the maximum number of stages (rotor/stator sets) should be five in a given housing. Beyond five, two separate turbine assemblies should be provided, a "high pressure turbine" and a "low pressure turbine." These have separate shafts and are interconnected by ducting as shown in Figure 5.1-8.

SPS 1148

**SYSTEM (B)**

$$\frac{\text{TURBINE OUTLET TEMPERATURE}}{\text{TURBINE INLET TEMPERATURE}} = 0.75$$

$$\text{TURBINE EFFICIENCY} = 18.82\%$$

**SYSTEM (D)**

$$\frac{\text{TURBINE OUTLET TEMPERATURE}}{\text{TURBINE INLET TEMPERATURE}} = 0.65$$

$$\text{TURBINE EFFICIENCY} = 26.33\%$$

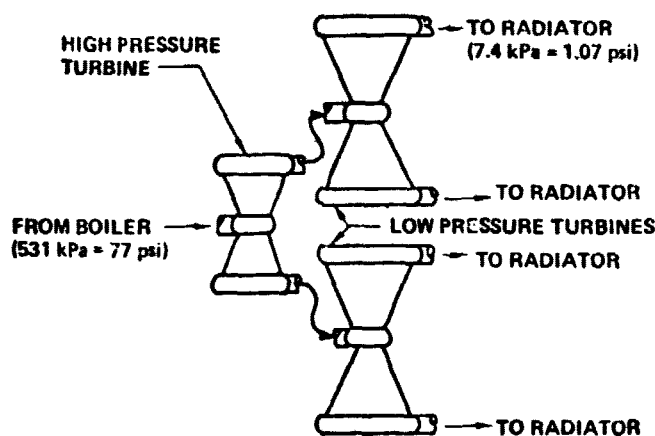


Figure 5.1-8. High and Low Pressure Turbines

### 5.1.2.2 Cycle Temperature Ratio Selection—Turbine Mass

A method was required for determining the weight of potassium vapor turbines for different thermal cycles. Normally this would require a preliminary turbine design, the preparation of drawings and a weight analysis of components. Time and scope did not permit this.

Turbine designs and weight analysis were available from a previous study of potassium vapor turbines as topping devices for steam power plants (ECAS). Weights were available for turbines with 2.03M (80 inch) disc diameters in a 1422K/1061K (2100°F/1450°F) high pressure turbine (HPT) and a similar sized 1061K/867K (1450°F/1100°F) low pressure turbine (LPT). As indicated in the



### D180-22876-3

plot of enthalpy vs vapor specific volume for potassium (Fig. 5.1-9), the area under the curve within cycle temperature limits is representative of turbine size (and weight). Area vs weight comparisons for both the HPT and LPT ECAS turbines indicated relatively good agreement. Note that relatively small areas under the curve are associated with enthalpy (temperature) increments at high temperatures whereas very large areas (and large turbine weights) are associated with enthalpy (temperature) increments at lower temperatures. Limiting the range of cycle temperatures reduces cycle efficiency and, of course, requires the addition of more compensating turbine weight. Increasing heat rejection temperatures eliminates much of the large "back end" portion of the turbines and favors reduction in radiator weight, while reduction of a portion of the high temperature part of the cycle also reduces efficiency but optimizes the use of more plentiful materials in a more reliable temperature range.

Cycle A and Cycle B turbine weights were extrapolated from weight vs area comparisons with the ECAS turbines at a given power level and correcting that weight for the relative efficiencies of the two cycles.

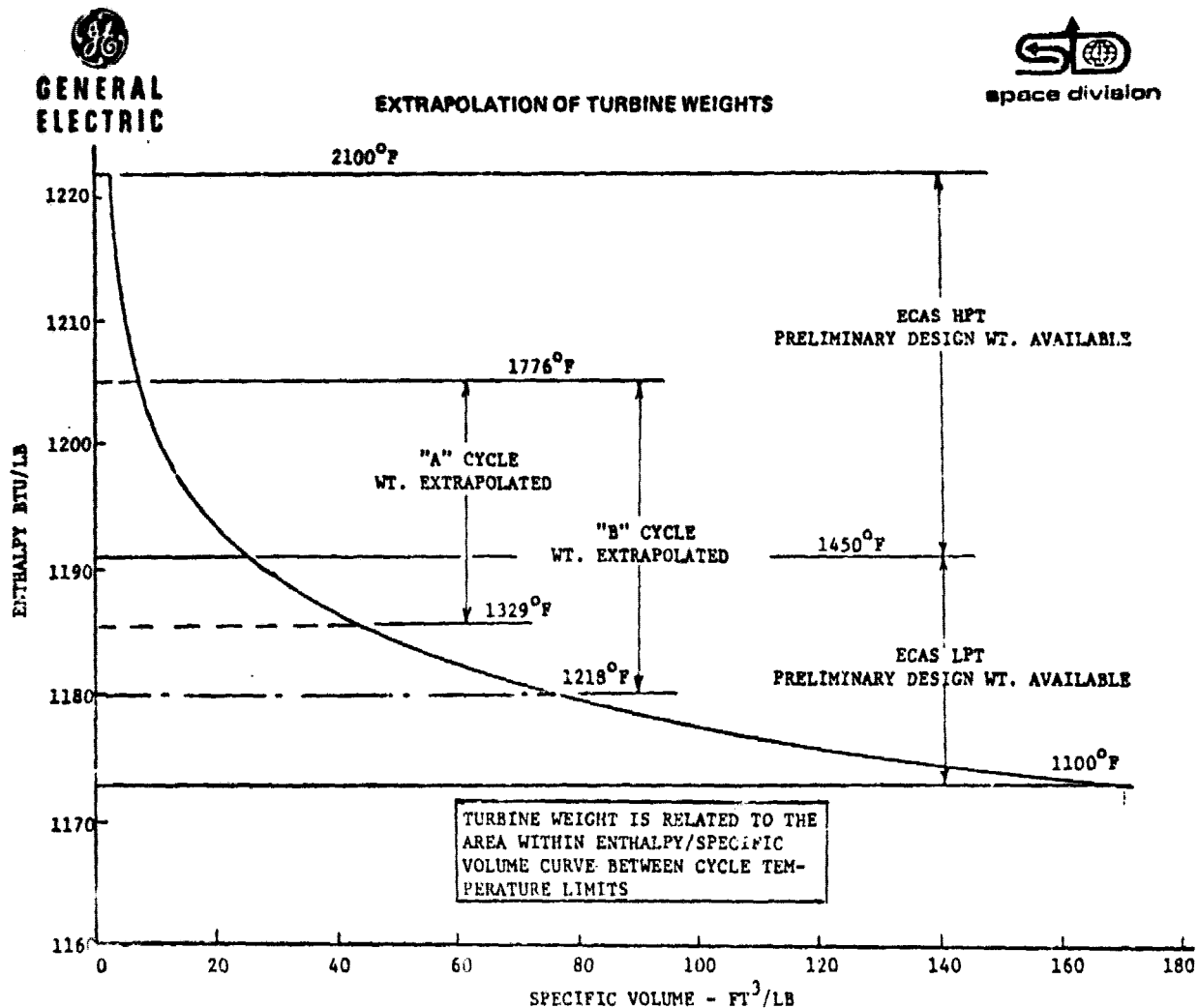


Figure 5.1-9. Extrapolation of Turbine Weights

### D180-22876-3

The graphical method was used to estimate turbine weights for new cycle temperatures from weights calculated from preliminary turbine designs of a prior thermal cycle. The specific turbine weights were then determined for the new cycle at the prior cycle turbine size. Then the specific weights, individual turbine weights and turbine weights per cavity heat source were calculated by considering that specific weight varies with diameter (weight varies with  $D^3$  and power varies with  $D^2$ ).

SYSTEM DEFINITION	CYCLE EFFICIENCY	4800 MWe - 80" DISC. TURBINE SYSTEM		1078 MWe - 40" DISC. - 34 TURBINE SYSTEM		
		TOTAL WT.	SPECIFIC WT.	SPECIFIC WT. <sup>A</sup>	TURBINE WT.	TOTAL WT.
ECAS CYCLE 2100°F/1100°F	0.278	18.572 x 10 <sup>6</sup> LB	3.87 LB/KW	-	-	-
"A" CYCLE 1776°F/1329°F	0.1522	7.826 x 10 <sup>6</sup> LB	1.63 LB/KW	-	-	-
"B" CYCLE 1776°F/1218°F	0.1882	11.941 x 10 <sup>6</sup> LB	2.49 LB/KW	1.66 LB/KW	52.6 x 10 <sup>3</sup> LB	1.79 x 10 <sup>6</sup> LB

<sup>A</sup>SPECIFIC WT. SCALED FROM 80" DISC. SIZE TO 40" DISC SIZE BASED ON VARIATION OF THE SPECIFIC WEIGHT DIRECTLY WITH THE DIAMETER.

BECAUSE OF THE UNCERTAINTIES IN MAKING EXTRAPOLATED WEIGHT ESTIMATES, IT IS ANTICIPATED THAT LATER TURBINE DESIGN AND WEIGHT ANALYSIS COULD RESULT IN ACTUAL TURBINE WEIGHTS AS MUCH AS 20% HIGHER OR AS MUCH AS 35% LOWER THAN THOSE SHOWN WITH 80% PROBABILITY.

#### 5.1.2.3 Cycle Temperature Ratio Selection—Radiators

The parametric used was a mass of 5.0 kilograms per square meter (1.02 lbm/ft<sup>2</sup>) of radiating area. The radiating area is twice the projected area. This mass allowance includes manifolding and closely approximates the specific mass of the final design. Radiating area was found by:

$$A_{\text{rad}} = \frac{P_{\text{rej}}}{\sigma (T_{\text{out}})^4 (0.1)}$$

where  $\sigma$  is the Stephan-Boltzman constant.

#### 5.1.2.4 Cycle Temperature Ratio Selection--Concentrators and Remaining Elements

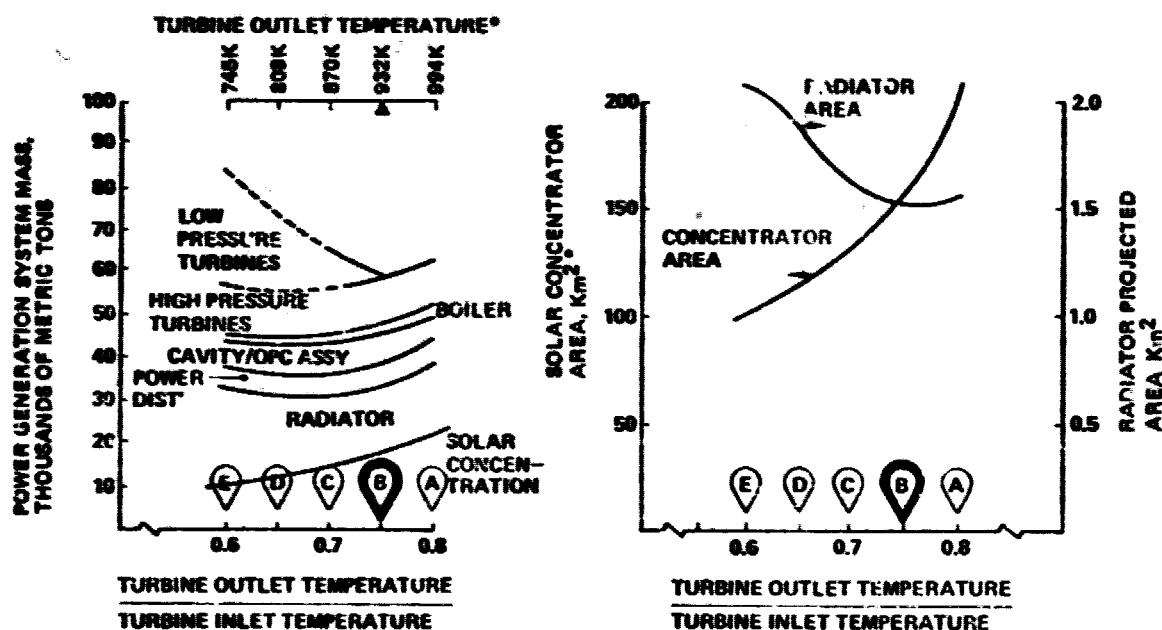
The concentrator mass was taken as 0.1 kg/M<sup>2</sup> (0.02 lbm/ft<sup>2</sup>). This includes the reflector facets, support structure for the facets and the cavity support arms.

### 5.1.2.5 Cycle Temperature Ratio Selection—Areas and Masses

Figure 5.1-10 shows concentrator and radiator areas versus cycle temperature ratio. It also shows the mass trends. Fortunately, minimum mass is obtained without the complication of a low pressure turbine. From a material cost standpoint this is good, because some of the highest price raw materials are used in the turbine.

The cycle temperature ratio is therefore set at 0.75. Thus the turbine outlet temperature is 932K (1218°F). The turbine outlet vapor pressure is 37.9 kPa (5.5 psi). Since at least 10 kPa (1.5 psi) is required at the electromagnetic pump inlet to prevent cavitation, the pressure drop around the radiator must be relatively small. Very high cycle pressure ratios tend to be impractical for this reason.

SPS-1100



\*TURBINE INLET TEMPERATURE = 1242K = 1776°F

\*\*INCLUDES OVERSIZE FOR METEOROLIDS (2.25%) AND RADIATION DEGRADATION (30%)

Figure 5.1-10. Cycle Temperature Ratio Selection

Note the points "A" through "E" in Figure 5.1-10. These correspond to specific design points. In Figure 5.1-10 can be seen the physical significance of cycle pressure ratio for two examples, "B" and "D".

### 5.1.2.6 Radiator Design Selection—Heat Pipe Spacing

As explained in Section 4.5.5.2, heat pipes have been selected as the radiating element. Figure 5.1-11 shows candidate heat pipe working fluids. For the radiator temperature of 932K (1218°F), sodium is appropriate. The freezing point of sodium is 371K (208°F). The freezing point of potassium is lower; 336K (145°F). This insures that the heat pipes will "shut off" while the potassium is still liquid.

Optimum heat pipe spacing is influenced by these factors:

- (1) Closely spaced pipes have a poor view factor to space, reducing the effective emissivity of their surface, so that more surface, and consequently mass, is required.
- (2) Increasing pipe spacing improves emittance and reduces heat pipe mass; however, this increases the length of the "throughpipes" which mount the heat pipes. The length of the inlet and outlet manifolds also tends to increase.

The view factor of one heat pipe to another is

$$F_{1-2} = \frac{2}{\pi} \left[ 2 \left[ \left( \frac{a}{3600} \right) \pi + \frac{1}{2D} \cos a \right] - \frac{P}{D} \right]$$

where  $a = \sin^{-1} \frac{D}{P}$ ,

D is the heat pipe diameter,

and P is the pitch (center to center spacing).

The "net emissivity" is  $\epsilon (1 - 2F_{1-2} \epsilon)$ .

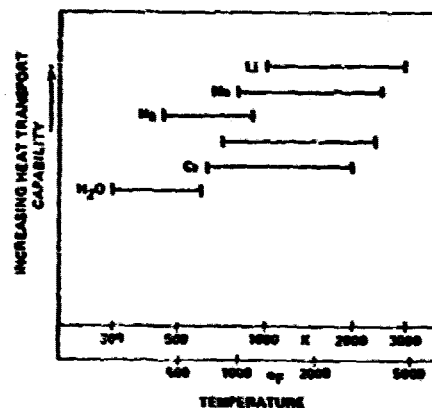


Figure 5.1-11 Candidate Heat Pipe Working Fluids

Figure 5.1-12 shows the effect of spacing (P/D) on the view factor and net emissivity.

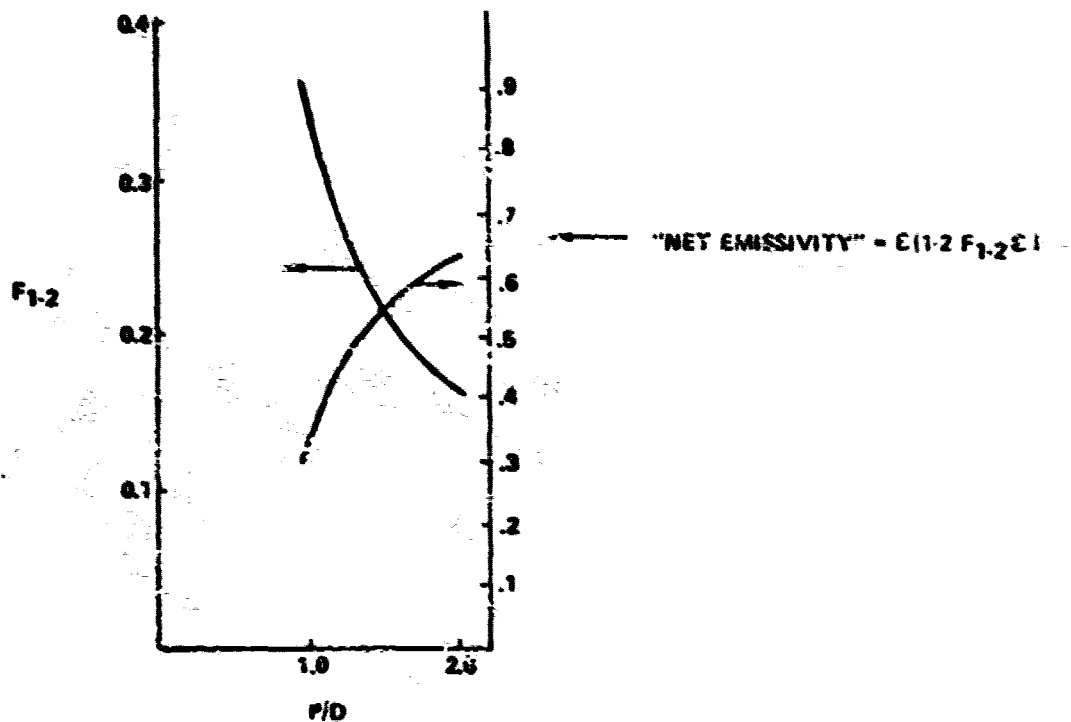


Figure 5.1-12. Influence of Heat Pipe Spacing on Emissivity

For the selected spacing ( $P/D = 1.6$ ) the net emissivity is 0.57 (the basic surface emissivity for a view factor of 1.0 is taken as 0.90). For a radiator surface temperature of 928K (1210°F), the heat pipes will radiate 24.0 kW/m<sup>2</sup>.

The ratio of actual area of a heat pipe to its projected area is  $\pi$ .

#### 5.1.2.7 Radiator Design Selection—Meteoroid Protection

As explained in Section 4.5.5, it is advantageous to fly the radiators "edge on" the apparent meteoroid flux. When this is done, the effect of the flux is reduced approximately 60%. The next consideration is what penetration rate should be allowed. The penetration problem can be broken down into two parts: the heat pipes and the manifolds. Due to the inherent nature of these elements, the following approaches were baselined:

- (1) Heat pipes: An excess shall be provided such that, after the penetrations resulting from 30 years of operation, the remaining pipes can dissipate the waste heat associated with full SPS power output. Thus there will be an initial excess capability (extra heat pipes). No maintenance is required.

- (2) **Manifolds:** Meteoroid bumpers are provided such that the penetrations resulting from 30 years of operation shall result in approximately a 10% loss of the total potassium inventory. Isolation valves at both ends of the throughpipes provide redundant isolation of the large liquid mass in the return manifold from the large surface area of the vapor manifold. A penetration of a liquid manifold therefore results in the loss of the majority of the potassium inventory for that engine/radiator (reduction of the local pressure near a hole allows vaporization; eventually all of the liquid will boil-off). When a penetration occurs, the associated engine is shut down. After repair of the penetration, probably during annual maintenance, the potassium is topped off and the engine restarted. The selection of a 10% inventory loss in 30 years is arbitrary, since no comparison of operation and maintenance (O&M) costs with initial launch costs has been made. Heavy meteoroid bumpers increase initial launch costs but reduce penetrations and therefore O&M costs.

Radiator mass was estimated for allowances of 30%, 10% and 5% heat pipe penetrations: the total mass was least with 10%. The use of relatively small heat pipes was critical, since this breaks up the radiating area into a large number of individual elements. A heat pipe diameter of 0.6 cm (0.24") and condensor section length of 0.5M (19.7") gives a projected area of  $3 \times 10^{-3} \text{ M}^2$  (4.64 square inches). The radiating area required for the SPS is  $3.21 \times 10^6 \text{ M}^2$  ( $3.45 \times 10^7 \text{ ft}^2$ ) to dissipate 77 GW. The corresponding projected area is:

$$\frac{3.21 \times 10^6 \text{ M}^2}{\pi} = 1.02 \times 10^6 \text{ M}^2 = 1.1 \times 10^7 \text{ ft}^2$$

Thus the total number of heat pipes, with 10% allowance for heat pipe damage and 3% for through-pipe penetration is:

$$\frac{1.1 \times 1.02 \times 10^6 \text{ M}^2}{3 \times 10^{-3} \text{ M}^2/\text{pipe}}$$

(The total area is  $1.15 \times 10^6 \text{ M}^2 = 1.24 \times 10^7 \text{ ft}^2$ ).

Thirty years is  $9.5 \times 10^8$  seconds. The meteoroid penetration rate, for the heat pipes, is thus:

$$\frac{(0.1) \times 3.83 \times 10^8 \times 0.399}{1.15 \times 10^6 \text{ M}^2 \times 9.5 \times 10^8 \text{ seconds}} = 1.4 \times 10^{-8} \text{ "hits" M}^{-2} \text{ sec}^{-1}$$

The factor 0.399 is the allowance for "edge-on" radiator penetration.

Per Figure 3-1, the largest particle corresponding to this flux rate is about  $2.6 \times 10^{-7} \text{ gm}$ . The diameter, for a specific gravity of 0.05, is  $9.98 \times 10^{-5} \text{ M}$  (0.004"). For steel, the "vulnerability thickness" is approximately 1.97 times the particle diameter. Thus the heat pipe shell thickness should be at least  $1.97 \times 10^{-4} \text{ M}$  (0.008") to insure 90% of the pipes survive the requisite 30 years.

### **D180-22876-3**

Meteoroid protection for the manifolds was based on design principles given in Boeing Document D2-24056 "Meteoroid Protection For Spacecraft Structures" (NAS3-2570).

The lightest protection system described therein employs triple bumpers, i.e., three layers of protective material are spaced outside of the item to be defended. Meteoroids are broken up by the first sheet; the other two layers stop the resultant debris.

#### **5.1.2.8 Attitude Control: P.O.P Versus P.E.P**

The SPS will require station keeping by thrusters in order to overcome forces which tend to displace it from the desired location in geosynchronous orbit (GSO). This is true for any type of SPS. The satellite must also be stabilized in attitude. Two primary orientations are possible:

##### **P.O.P.: Perpendicular-to-Orbit-Plane**

In this orientation the north-south axis of the satellite (which is parallel to the solar concentrator) is flown perpendicular to the orbit plane and hence perpendicular to the equatorial plane.

##### **P.E.P.: Perpendicular-to-Ecliptic Plane**

In this orientation the north-south axis of the satellite is flown perpendicular to the ecliptic plane and hence perpendicular to the solar rays.

The primary differences between these two orientations are: (1) that when flying P.O.P. torques on the satellite from gravity gradients are much less than when flying P.E.P. and (2) when flying P.O.P. the sun moves through an apparent arc of approximately 47 degrees. When flying P.E.P., the solar rays are always perpendicular to the solar concentrator.

In Part I of this study the P.O.P. orientation was baselined. The solar concentrator employed steerable solar facets (heliostats) to maintain focus at the cavity absorber despite the apparent annual solar motion ( $47^\circ$ ). The heliostats had individual power supplies, sensors for the sun and cavity, pointing logic and servomechanisms. Over 100,000 of these units were required per SPS. The facets incorporated a central post mounting (with a pivot system) and radial members, per Figure 5.1-13.

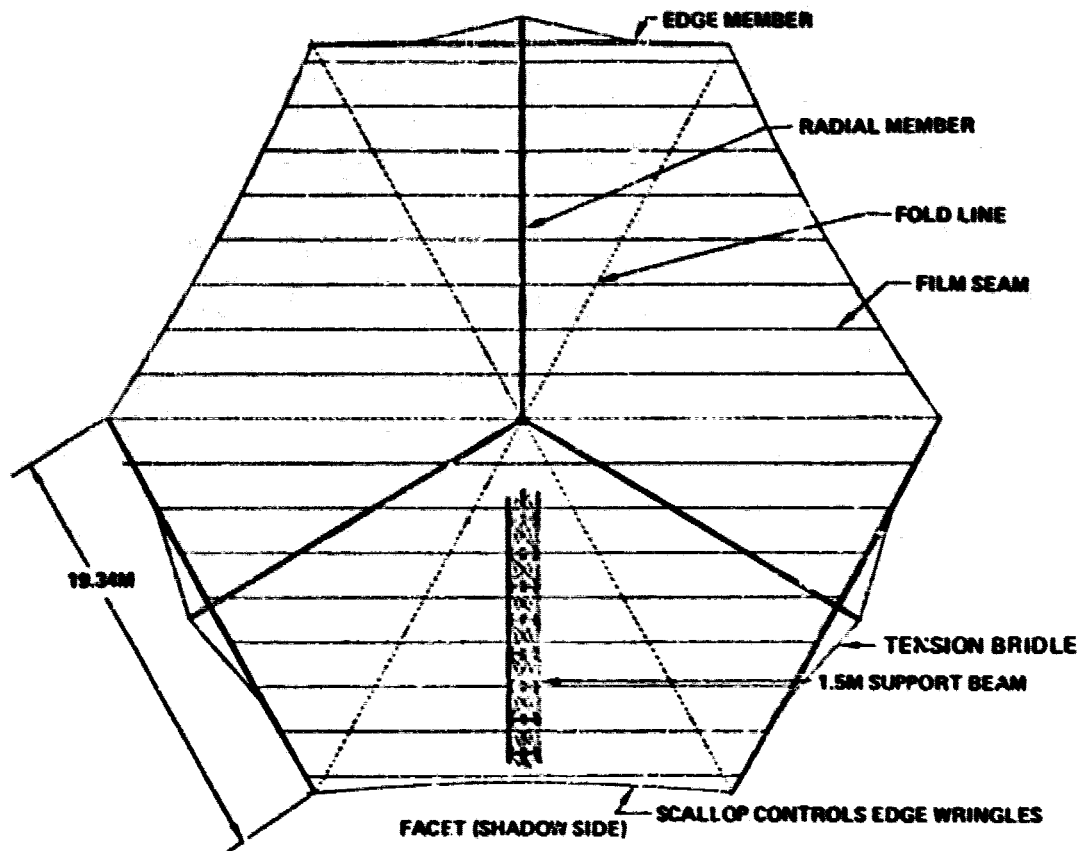
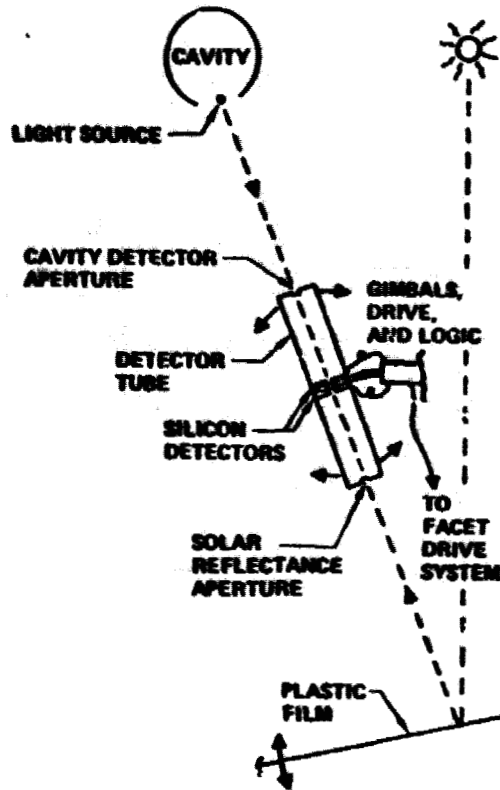


Figure 5.1-13. Steerable Facet (Heliostat)

Figure 5.1-14 shows a potential sensing system for such facets and Figure 5.1-15 shows how these systems would be incorporated in the facet hub.





**Alignment sequence:**

1. Without cavity light source, facet drive is commanded to end of travel (no power to cavity).
2. When modulation of light source is as required, detector tube aligns with light source.
3. Facet drive system positions facet such that reflected rays from facet are aligned with detector tube axis and hence are aimed at cavity.
4. If modulation is removed, logic causes facet drive to gimbal stop.

**Figure 5 1-14. Pointing the Facets**

D180-22876-3

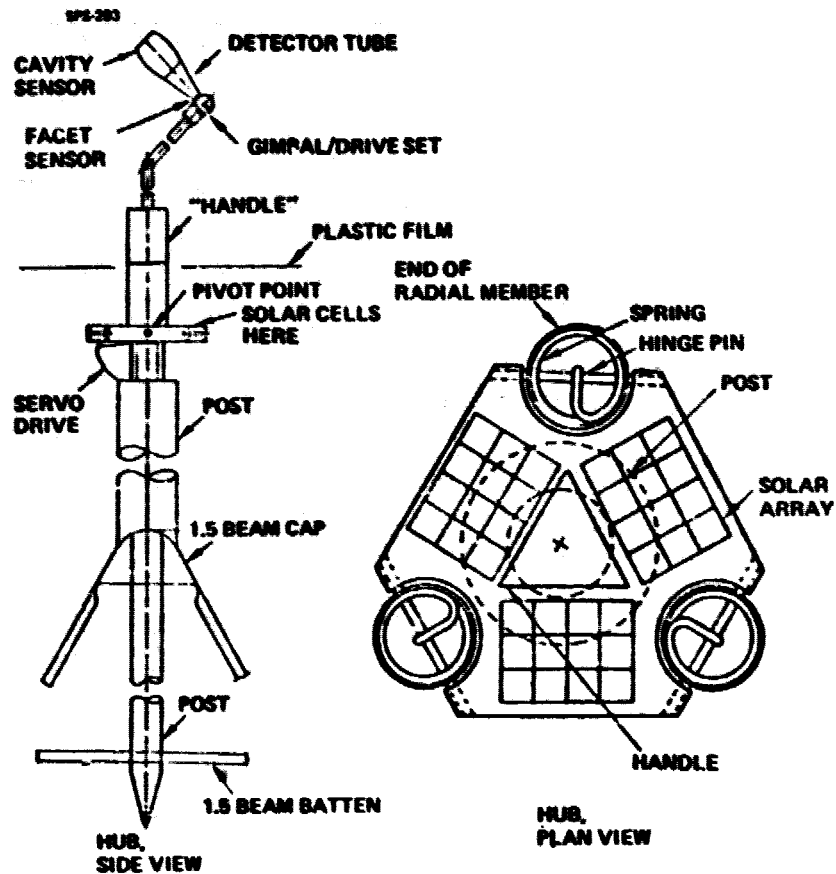


Figure 5.1-15. Facet Hub

With a P.E.P. orientation the sun stays "fixed." Hence a properly shaped concentrator can provide the necessary focusing without movable facets. The facets do not require a hub mechanism or radial members and are considerably simpler in design.

Attitude control requirements are at GEO dominated by gravity gradient effects. Orbit trim requirements are dominated by solar pressure. A good flight control strategy will combine the corrections, using unbalanced couples to provide translation corrections for solar pressure while applying torque to counter gravity gradients. Solar pressure for an absorptive surface is readily calculated as:

$$F = \frac{P}{C} = \frac{1353 \text{ watts/m}^2}{3 \times 10^8 \text{ m/sec}} = 4.51 \times 10^{-6} \text{ n/m}^2$$

### D180-22876-3

The reference photovoltaic system has a projected area of  $119 \text{ km}^2$ ; the solar pressure is  $4.51 \times 10^{-6} \times 119 \times 10^6 = 537 \text{ N}$ .

Gravity gradient torques around the 3 SPS axes are given by:

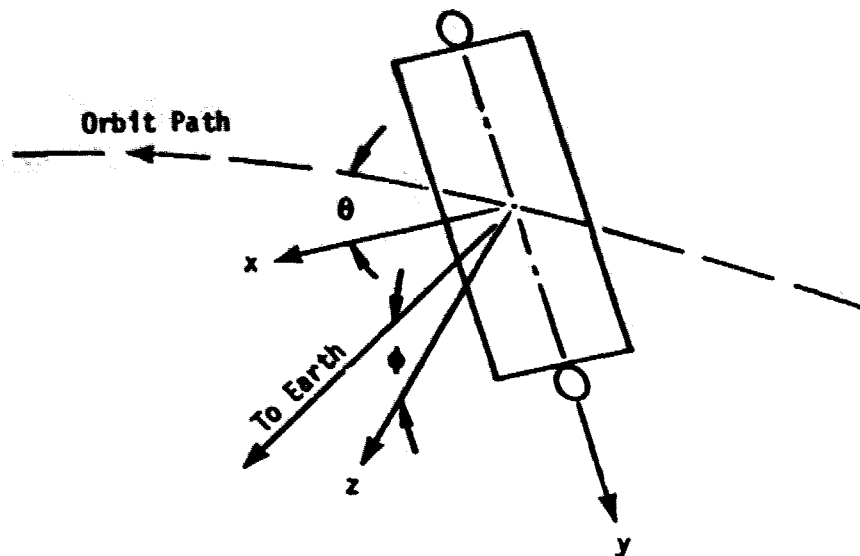
$$T_x = 3/2p^3 (I_z - I_y) \cos^2 \theta \sin 2\phi$$

$$T_y = 3/2p^3 (I_z - I_x) \sin 2\theta \cos \phi$$

$$T_z = 3/2p^3 (I_x - I_y) \sin 2\theta \sin \phi$$

Axes and angles are defined in Figure 5.1-16 is gravitational potential and  $p$  is orbit radius.

$$\mathbf{T} = 3/p^3 \mathbf{U} \times [\mathbf{I}] [\mathbf{U}]$$



$\theta$  is around  $y$  axis

$\phi$  is around  $x$  axis

Euler angles for 3, 2, 1 sequence

Figure 5.1-16. Definition of Angles & Axes

where bold-face symbols are vectors,  $\mathbf{U}$  is a unit vector directed radially outward from the Earth's center through the spacecraft mass center, and  $\mathbf{I}$  is the inertia tensor. Square brackets signify matrix multiplication.

### D180-22876-3

For the reference photovoltaic SPS with the JSC "green book" antenna masses, the inertia differences are:

$$I_z - I_y = 3.9137 \times 10^{15} \text{ kg-M}^2$$

$$I_z - I_x = 1.258 \times 10^{14} \text{ kg-M}^2$$

$$I_x - I_y = 3.7879 \times 10^{15} \text{ kg-M}^2$$

The current antenna mass estimate will increase the  $I_z - I_y$  and  $I_x - I_y$  values about 30%.

The force components required to control the gravity gradient torques are  $T_i/S_i$  where  $S_i$  are the moment arms.

#### Flying POP

In this case,  $\phi = 0$  by definition and only the  $F_y$  term is operative. The peak thrust required is 390n. (100n. each 4 places). The duty cycle is that for a sinusoid, 0.64.

The mass penalty for gravity gradient control includes: 1) thrust production hardware: thrusters plus power processing; 2) generating capacity required to power the thrusters; 3) propellant required. The correct propellant quantity penalty reflects the time value of the cost of propellant resupply; the penalty should be the *net present value* (in economic terms) of the lifetime propellant requirement. The value ranges from 10 years' annual supply (10% discount for 30 years) to 14 years' annual supply (7½% discount, infinite life).

Propulsion system  $I_{sp}$  is a variable, assuming electric electric propulsion. As  $I_{sp}$  is increased, propellant mass penalty decreases but hardware penalty increases. Accordingly, an optimum occurs (Fig. 5.1-17). 20,000 seconds  $I_{sp}$  is selected as a representative value. For POP operation, assuming perfect control laws (no control authority margin, no wasted propellant) about 250 tons of hardware (including generating capacity) and 41 tons/year argon propellant are required. (Electric propulsion characteristics were taken from Part I technical report Vol. 5.) About 50 megawatts peak, 32 megawatts average, power is required to drive the thruster system. Chemical propulsion will be needed to provide control during equinoctial occultations. Despite the low  $I_{sp}$  (400 sec), only 1 to 1½ tons of propellant is needed annually due to the small duty cycle.

#### Flying PEP

All 3 terms are operative.  $\phi$  varies from 0 to  $23\frac{1}{2}^\circ$  by  $\sin \phi = \sin i \sin \theta$  where  $i = 23.5^\circ$ .  $\theta$  varies from 0 to  $360^\circ$ . An approximate numerical integration gives peak thrust (total 4 corners) as 2230 newtons with an average duty cycle of 0.4. Therefore, the hardware penalty is 5.6 x that for flying POP (1390 tons) and the propellant penalty is 3.5 x that for flying POP (144 tons/yr). This is a 1.4% hardware mass penalty (for about 3% gain in output due to sun orientation) and a propellant

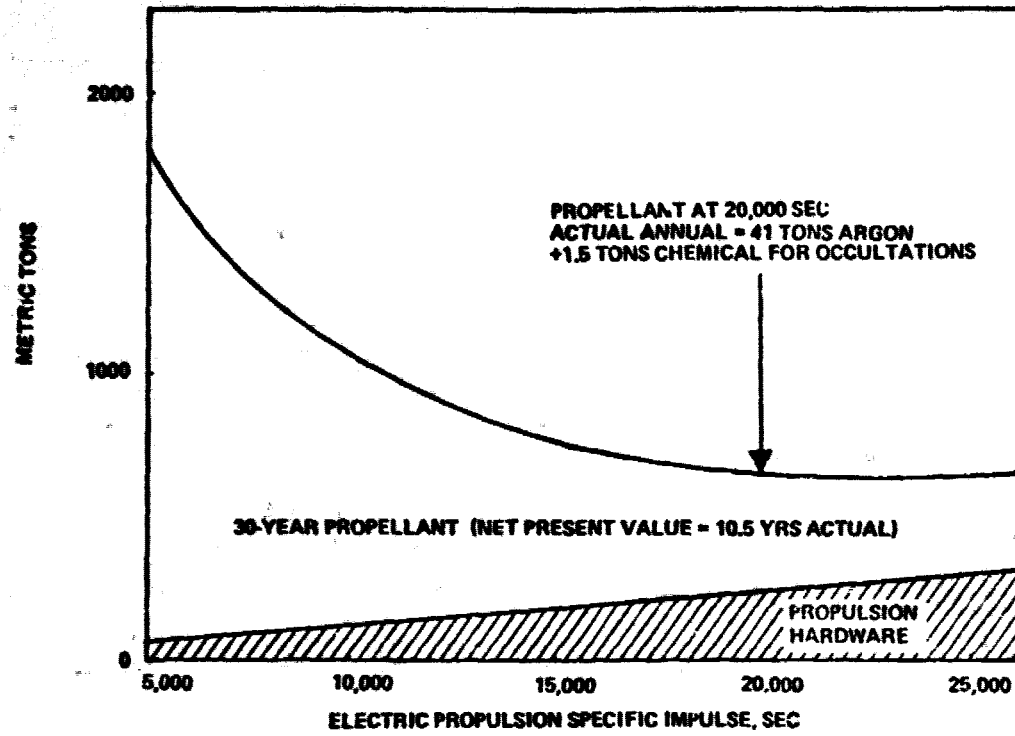


Figure 5.1-17. Attitude Control Propellant-Photovoltaic POP

### **D180-22876-3**

penalty roughly equivalent to one chemical OTV flight to GEO every 2.75 years. The hardware plus NPV propellant penalty is about 3% compared to output gain of also about 3%.

Thus flying PEP is about a break-even and should be adopted only if it provides design advantages (as it does for the thermal engine).

Additional aspects of the choice of a P.F.P. orientation for the thermal engine SPS are given in Figure 5.1-18.

DP-1212

#### **DISADVANTAGES**

- HIGHER PROPELLANT CONSUMPTION (UNLESS CONFIGURATION IS INERTIALLY SYMMETRIC, USES MAGNETIC TORQUEING OR SOLAR PRESSURE EFFECTS)
- BEST PERFORMANCE REQUIRES TIGHTER ATTITUDE CONTROL LIMITS (E.G.,  $0.1^\circ$ , NOT  $0.5^\circ$ )
- REQUIRES ADDITIONAL (SEASONAL) AXIS ON ANTENNA
- 300 MW PEAK POWER REQUIRED TO OPERATE THRUSTERS

#### **ADVANTAGES**

- FACETS NEED NOT FOLLOW SEASONAL SUN MOTION
- ELIMINATES COSINE EFFECT ON SIZING
- FACETS NEED NOT BE SPACED APART TO ALLOW MOTION
- LOWER METEOROID FLUX ON RADIATORS
- ADDITIONAL ANTENNA AXIS PERMITS TRANSMISSION TO VARIOUS RECTENNA LONGITUDES WITHOUT POLARIZATION LOSS (FROM GIVEN ORBIT LONGITUDE)
- ADDITIONAL ANTENNA AXIS PERMITS COMPENSATION FOR DIURNAL IONOSPHERIC FARADAY POLARIZATION ROTATION
- RADIATOR IS ALWAYS EDGE ON TO THE SUN
- CONSTANT THERMAL ENVIRONMENT FROM FIXED SOLAR ORIENTATION

**Figure 5.1-18. Perpendicular-to-Ecliptic Plane Orientation**

## **5.2 OTHER SPS OPTIONS**

This section describes alternate SPS configurations and systems that appear promising but have a need for either a better data base or a technological breakthrough. The best choice for the photovoltaic alternate was a Gallium Arsenide system with a Brayton cycle as the best alternate for the thermal engine system.

## 5.2.1 Gallium Arsenide Photovoltaic Alternate

### 5.2.1.1 Status at the End of Part I

A thin cell gallium arsenide SPS was selected as the best alternate (Sec. 5.1.1.1, Table 5.1-1). Even though the GaAs system was significantly less massive than the silicon system, there was a lack of data base with respect to gallium availability and cost.

Some of the results of the Part I analysis were CR1 vs CR2 (Fig. 5.2-1) system sensitivity to solar cell efficiency (Fig. 5.2-2) and system sensitivity to solar cell thickness (Fig. 5.2-3). It is apparent that gallium availability, cost and cell thickness are the major drivers in the use of GaAs for a successful SPS system. New breakthroughs in the areas of thin cell production, efficiencies and a better data base on gallium availability could make a GaAs SPS most attractive.

### 5.2.1.2 Part II Objectives

With respect to gallium arsenide, the main objectives of Part II were to investigate the areas of higher concentration ratios and gallium availability. To accomplish these tasks several systems with geometric concentration ratios of six were analyzed using thinner GaAs solar cells.

### 5.2.1.3 Part II Conclusions

The investigation of higher concentration ratios leads to the use of reflectors that are non-planar (Sec. 4.2). Compound parabolic concentrators were used at a geometric concentration ratio of six.

To investigate the reflector characteristics and to determine the orbital orientation, computer analysis was accomplished on CPC's with various acceptance half-angles. The results are shown in Table 5.2-1.

$\theta_c$	--	acceptance half-angle
$\theta_o$	--	angle of offset of the incoming light rays to the axis of the CPC
Ir/lo	--	fraction of beam incident on the receiver to that which enters the CPC
$\langle n \rangle$	--	the average number of reflections
$\theta_{ir}$	--	average angle of incidence of reflected light rays on the reflector surface

It is noted that as  $\theta_o$  approaches  $\theta_c$  the value of Ir/lo decreases rapidly. Therefore, if large values of  $\theta_o$  must be realized,  $\pm 23.5$  degrees for POP orientation,  $\theta_c$  must also be very large. With three-dimensional CPC's,  $CR_g = 1/\sin^2\theta$  so 24 degrees is about the maximum  $\theta_c$  for  $CR_g = 6.0$ . With a  $\theta_c = 24$  degrees and a  $\theta_o = 23.0$  degrees Ir/lo = .6682 which is not acceptable.

As  $\theta_c$  is increased, to decrease the effect of  $\theta_o$  the  $CR_g$  also decreases (Fig. 5.2-4). This is also unacceptable if higher concentration ratios are needed.

# D180-22876-3

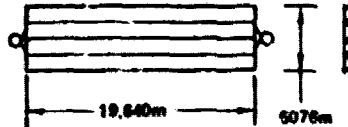
SPS 743

CR 1 and CR 2 are Very Close in GaAs, (1%) with the Higher Cost of the GaAs Array reducing the CR 1 Advantage Seen in Silicon

GaAs-10 GW MIN. FOR 30 YRS. VIA ARRAY ANNEALING-GEL ASSEMBLY

## CR-2

TOTAL AREA: 98.7 Km<sup>2</sup>  
ACTIVE ARRAY AREA: 46.6 Km<sup>2</sup>  
MASS: 42,736 MT  
PRODUCTION COST: \$ ~ 10<sup>6</sup> 4882.9  
TOTAL COST: \$ ~ 10<sup>6</sup> 8346.9



## CR-1

TOTAL AREA: 88.4 Km<sup>2</sup>  
ACTIVE ARRAY AREA: 66.4 Km<sup>2</sup>  
MASS: 42,150 MT  
PRODUCTION COST: \$ ~ 10<sup>6</sup> 5026.9  
TOTAL COST: \$ ~ 10<sup>6</sup> 8442.7

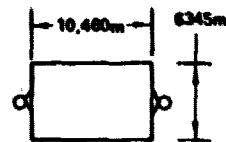


Figure 5.2-1. GaAs Satellite, CR 2 Vs CR 1

SPS 747

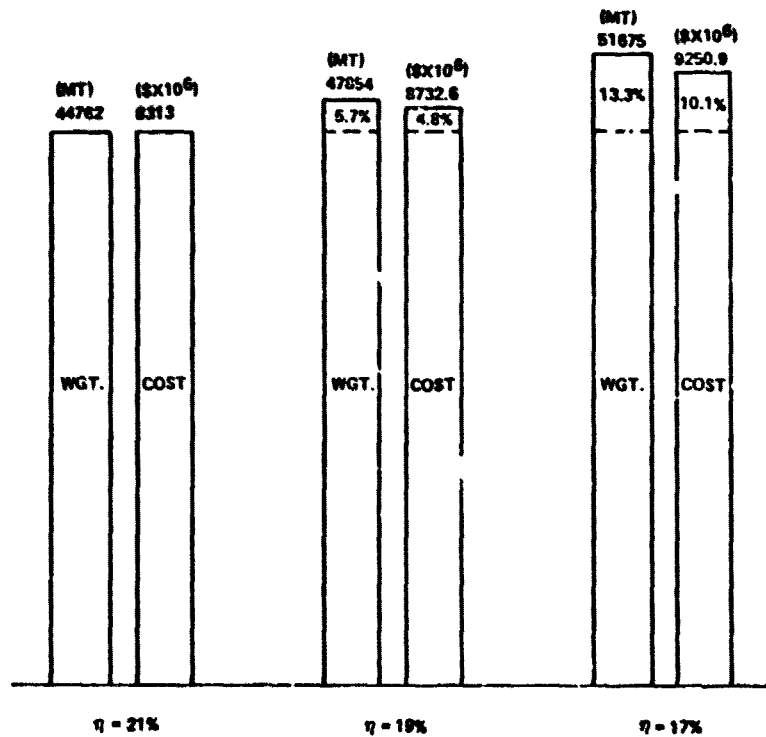


Figure 5.2-2. GaAs Satellite Sensitivity to Cell Performance



D180-22876-3

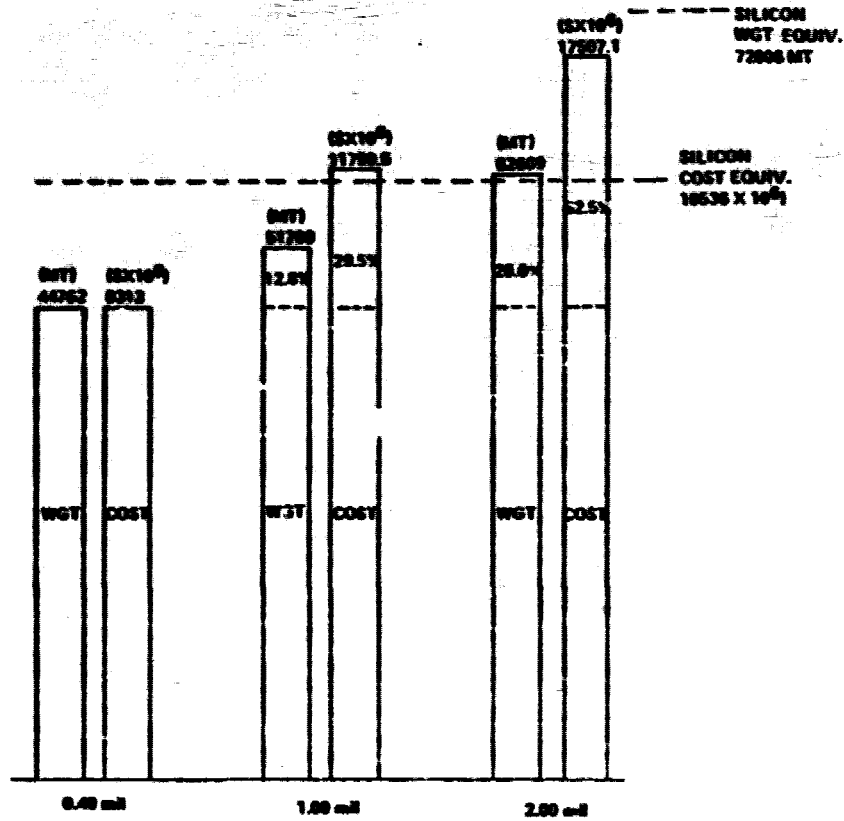


Figure 5.2-3. Sensitivity of Satellite Mass and Cost to GaAs Solar Cell Thickness

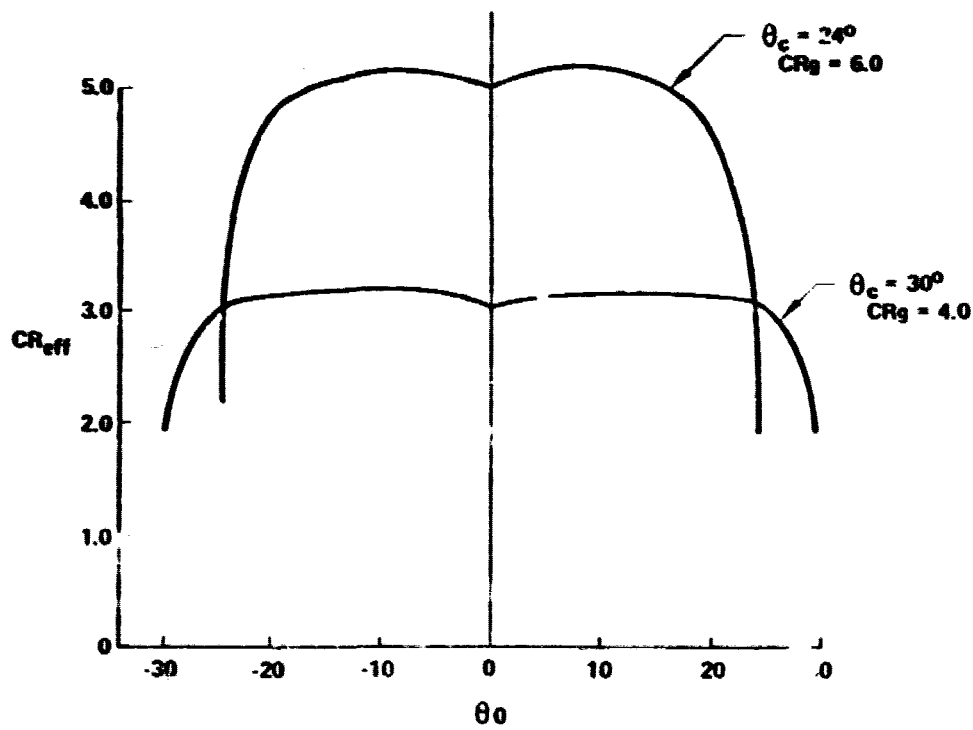


Figure 5.2-4. CPC Operation

D180-22876-3

Table S.2-1 CPC Characteristics

$\theta_c$	$\theta_a$	$I_r/I_0$	$\langle n \rangle$	$\theta_{ir}$
24	23	0.6682	1.354	60.0
	19	0.8220	1.171	64.3
	15	0.8456	1.008	67.5
	10	0.8488	0.941	70.7
	5	0.8392	0.991	74.0
	0	0.8354	1.047	75.5
22	19	0.8408	0.987	62.0
	15	0.8562	0.909	65.7
	10	0.8634	0.898	69.7
	5	0.8650	0.894	71.6
	0	0.8614	0.893	72.3
8	5	0.871	0.806	59.6
	4	0.869	0.808	59.5
	3	0.879	0.809	59.9
	2	0.876	0.816	59.9
	1	0.881	0.815	60.0
	0	0.875	0.808	60.1
5	5	0.835	0.797	59.6
	4	0.870	0.808	57.8
	3	0.880	0.806	57.7
	2	0.880	0.817	57.7
	1	0.880	0.816	57.8
	0	0.875	0.806	57.9
3	5	0.627	0.728	60.0
	4	0.688	0.752	57.6
	3	0.829	0.797	56.5
	2	0.880	0.817	56.3
	1	0.881	0.818	56.8
	0	0.876	0.806	56.5

### D180-22876-3

Another analysis was accomplished to determine the effect of flying PEP or modified POP. This causes an attitude control, equipment and propellant, penalty but is overshadowed by the advantage gained in effective concentration ratio.

Another method of reducing the effect of the  $\theta_0$  losses is to use a two-dimensional (cylindrical) CPC oriented such that the 23.5 degree tilt is accepted in the direction of the trough, perpendicular to the CPC axis.

Three final cases were investigated for  $CR_g = 6.0$ , GaAs systems (Fig. 5.2-5). All of the options shown use a geometric CR ( $CR_g$ ) of 5.0 and were obtained by truncation of Compound Parabolic Concentrators (CPC's). Option 1 uses a conic (3-dimensional) CPC with an acceptance half angle of  $24^\circ$  truncated slightly to achieve a  $CR_g = 6.0$  and oriented Perpendicular to the Orbital Plane (POP). Option 2 also uses a conic CPC but is oriented Perpendicular to the Elliptic Plane (PEP) and uses an acceptance half angle of  $5^\circ$  truncated to a  $CR_g = 6.0$ . Option 3 uses a cylindrical (2-dimensional) CPC oriented POP with an acceptance half angle of  $5^\circ$  truncated to a  $CR_g = 6.0$ .

With the higher concentration ratios another factor that must be considered is the effect of the increase in solar cell temperature. Even though GaAs cells have a lower coefficient of thermal degradation, the high temperatures involved reduce the operating efficiency significantly. Thermal analysis revealed that the nominal steady state operating temperature of the cells was approximately  $220^\circ\text{C}$ . This caused a reduction in cell operating efficiency to 14 percent, a significant decrease for a GaAs solar cell.

Addition of a thermal radiator (aluminum fin) will reduce the operating temperature (Fig. 5.2-6) but with a significant mass penalty for the system. The effect of the thermal radiator on solar cell efficiency, GaAs mass required and representative system mass for the three options are shown (Figs. 5.2-7 and 5.2-8). Mass assumptions are listed in Table 5.2-7.

It was evident that the addition of a thermal radiator to the solar cells caused a small gallium mass benefit but a large system mass penalty. It is suggested that if a thermal radiator is used it should be very thin and will not give a significant gain in system operating efficiency. From the system standpoint, the most favorable system appeared to be the cylindrical (two-dimensional) CPC configuration oriented POP.

The main advantage noted was the decrease in gallium mass required compared to a CR 2.0 system. The increase in system mass, compared to a CR 2.0 system, is caused by addition of reflectors, added support structure and, in some cases, thermal radiators.

The availability of gallium is still in question as the first report from Battelle Northwest Laboratories to DOE has not yet been made available. When it is made available, it should include a comprehensive picture of gallium availability. Using a projection on possible annual U.S. gallium

D180-22876-3

1. CONICAL CPC,  $\theta_c = 34^\circ$ ,  $CR_0 = 6.0$

$R_r = 5.0\text{cm}$

$R_b = 12.3\text{cm}$

$H = 44.3\text{cm}$

$\theta^0 > 3^\circ$

$\theta^0 < 0, < 18^\circ \rightarrow 4.85 < C_{\text{REFF}} < 5.14$

MOD. POP ORIENTATION

2. CONICAL CPC,  $\theta_c = 5^\circ$ ,  $CR_0 = 6.0$

$R_r = 5.0\text{cm}$

$R_b = 12.3\text{cm}$

$H = 10.3\text{cm}$

$\theta^0 < 0, < 3^\circ$

$\rightarrow 5.20 < C_{\text{REFF}} < 5.28$

3. CYLINDRICAL CPC,  $\theta_c = 5^\circ$ ,  $CR_0 = 6.0$

$W_r = 5.0\text{cm}$

$W_b = 39.0\text{cm}$

$H = 39.0\text{cm}$

$\theta^0 < 0, < 3^\circ$

$\rightarrow 4.85 < C_{\text{REFF}} < 5.10$

POP ORIENTATION

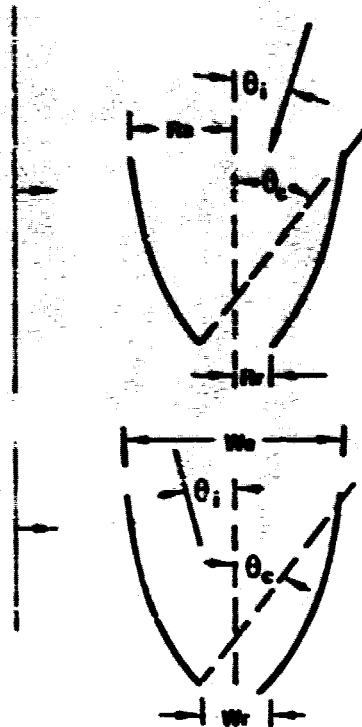


Figure 5.2-5. GaAs,  $CR > 2$ , Options

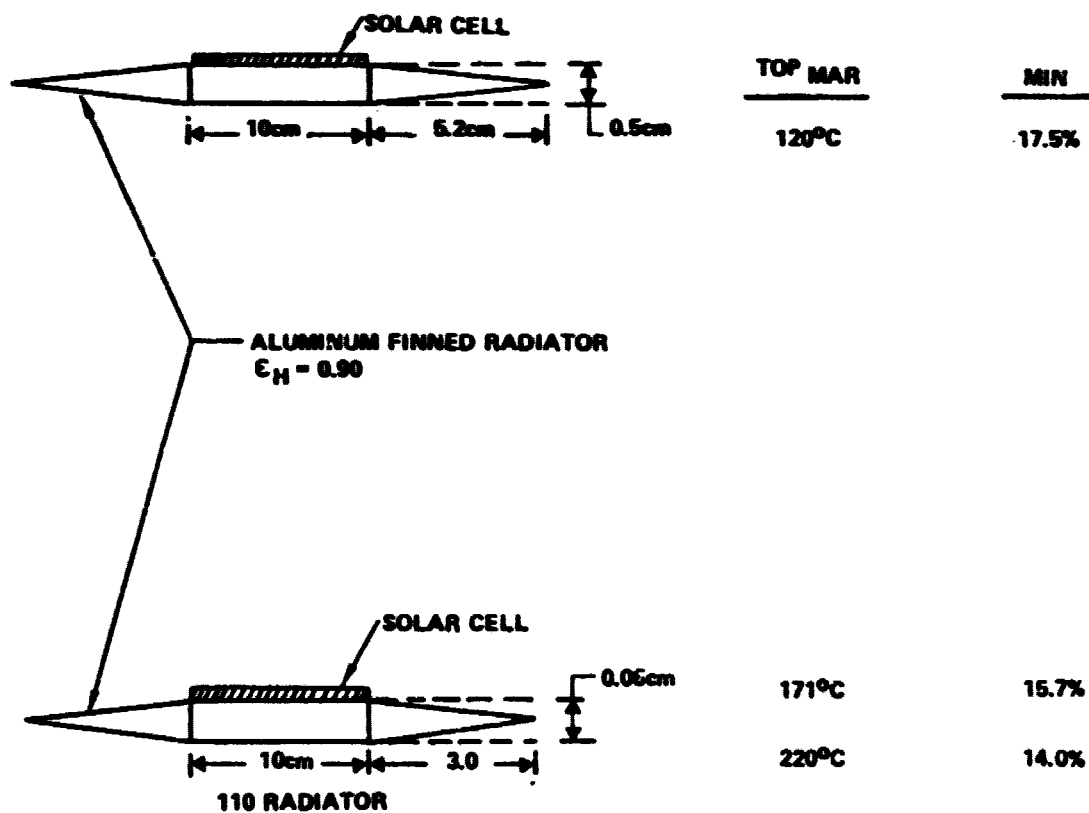
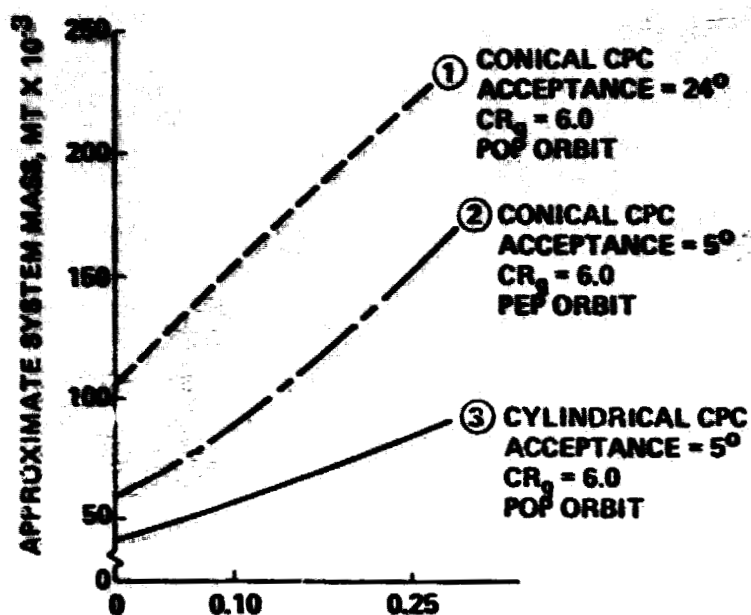


Figure 5.2-6. Passive Thermal Control for GaAs Options

D180-22876-3

SP-1028

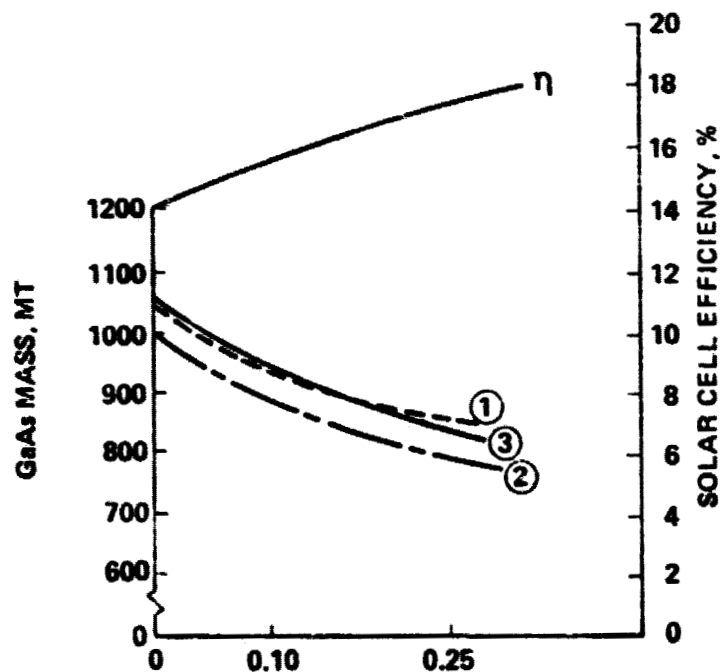
● CR=1, SYSTEM MASS ≈ 45,100 MT



THERMAL RADIATOR THICKNESS, CM

Figure 5.2-7. System Mass Characteristics for CR>2 Options

● CR=1, GaAs MASS ≈ 3340 MT



THERMAL RADIATOR THICKNESS, CM

Figure 5.2-8. GaAs Requirements for CR>2 Options

**D180-22876-3**

**Table 5.2-2 Mass Assumptions for CR >2 Options**

	<b>S.G.</b>	<b>Thickness (mils)</b>
<b>Covers - Borosilicate Microsheet</b>	<b>2.20</b>	<b>2.0</b>
<b>Cells - GaAs</b>	<b>5.32</b>	<b>0.40</b>
<b>Substrate - Titanium</b>	<b>4.50</b>	<b>0.50</b>
<b>Interconnects - Copper</b>	<b>8.94</b>	<b>0.50</b>
<b>Reflector - 1 Kapton</b>	<b>1.42</b>	<b>3.0</b>
<b>                  2 Aluminum</b>	<b>2.70</b>	<b>1.6</b>
<b>Radiator - Aluminum</b>	<b>2.70</b>	<b>Variable</b>

### D180-22876-3

production quantities, from "Availability of Gallium and Arsenic" by Dr. R. N. Anderson (Fig. 5.2-9), the  $CR_g = 6.0$  system and a Part I,  $CR = 1.0$ , GaAs system were plotted to compare the effect of CR on gallium usage. The  $CR_g = 6.0$  gallium requirement was that for the highest gallium usage of the three systems shown previously, cylindrical CPC with no thermal radiator. For this case, approximately 450 MT per satellite of gallium is required and for a production of four satellites per year, 1800 MT per year of gallium would be used. Using a recovery of 30 percent of the gallium available from bauxite and coal fly-ash would supply the necessary amount of gallium for four satellites per year.

#### 5.2.2 Brayton Thermal Engine

Closed cycle helium Brayton energy conversion for SPS was investigated under NASA MSFC contract NAS8-31628 ("Systems Definition, Space Based Power Conversion Systems") and in part one of this study. A simplified schematic of the Brayton system is given in Figure 5.2-10.

The solar concentrator reflects and focuses intense solar energy into the cavity absorber aperture. The cavity absorber is an insulated shell lined with heat exchanger tubing. Helium gas flowing through this tubing becomes heated (simultaneously preventing cavity overheating).

Hot helium expands through the turbine, doing the work of turning the compressor and the generator. The compressor forces the helium flow around the cycle loop. Minimum gas temperature occurs at the exit of the cooler, which is a gas-to-liquid heat exchanger interfacing the helium loop to the radiator system. The recuperator is a gas-to-gas heat exchanger which increases the system efficiency by exchanging energy between the "hot" and "cold" sides of the cycle. The recuperator causes the average turbine temperature to be higher and the average compressor temperature lower for given maximum and minimum cycle temperatures.

Waste heat is rejected by a liquid metal radiator system. The working fluid is a sodium-potassium eutectic (NaK). NaK pumping is by a motor/pump system drawing power from the generator.

To achieve relatively low system mass a high turbine inlet temperature was baselined: 1610K (2438°F). This was only obtainable by the use of ceramic (silicon carbide) turbine components and insulated helium ducts. Optimization studies of the helium loop using machine processing of parametric models indicated that minimum system mass would be obtained with compressor outlet pressure of approximately 4140 kPa (600 psi). Columbium was selected for the primary heat absorber, which is exposed to this pressure and, at the outlet, the full turbine inlet temperature.

Figure 5.2-11 shows how insulation allowed use of a cool (and thereby stronger) outer shell.

D180-22876-3

SPS-1028

ANNUALLY AVAILABLE  
GALLIUM FROM U.S. PRODUCTION  
OF ALUMINUM AND COAL  
FLY-ASH

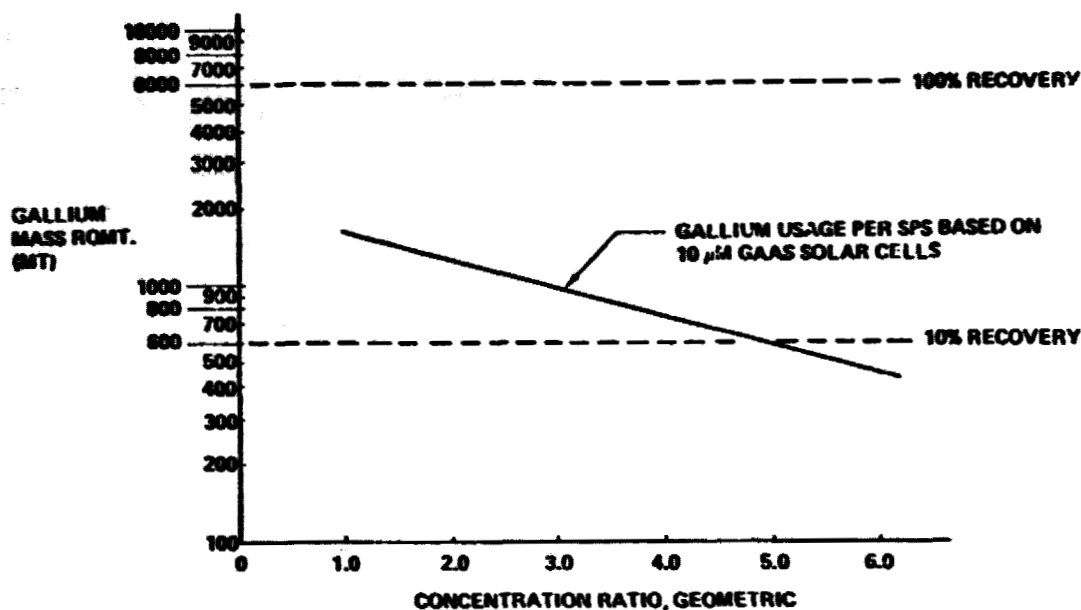


Figure 5.2-9. Reduction in Gallium Required for CR>2 System

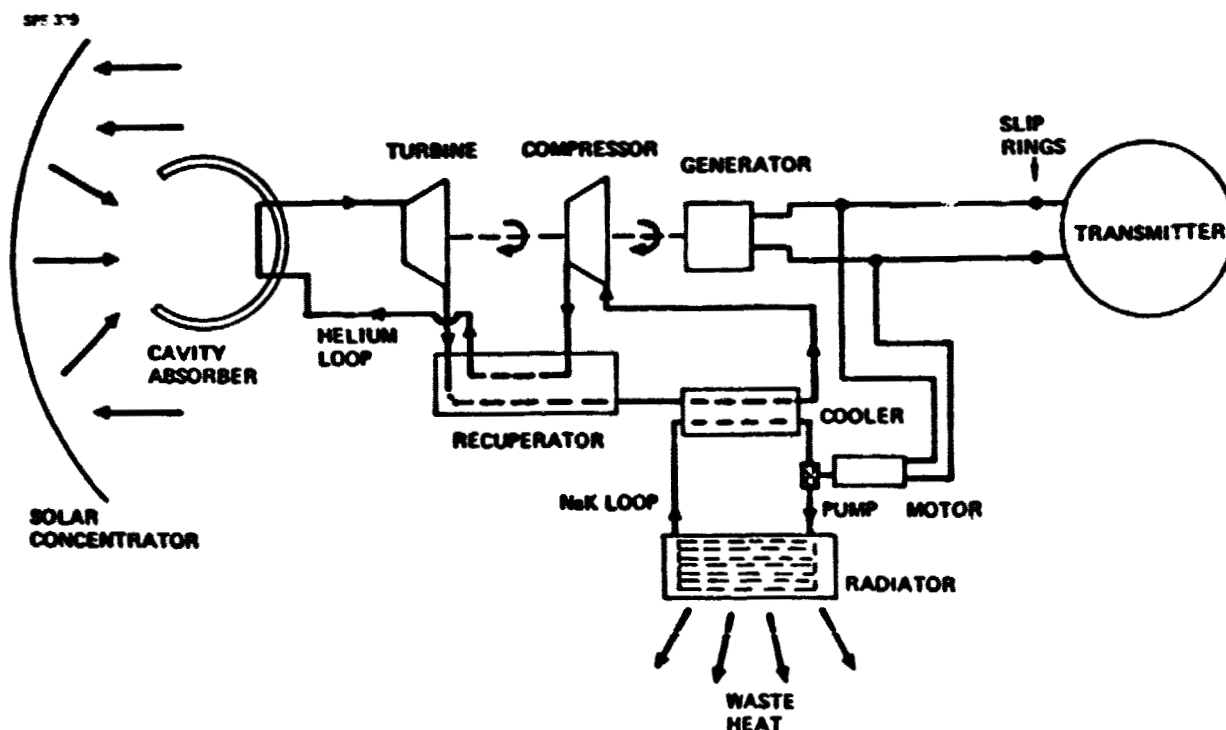


Figure 5.2-10. Solar Brayton Cycle



D180-22876-3

SPS 021

●  $M_0$  - 10 W - 2.5Z, 30 YEAR CREEP RUPTURE

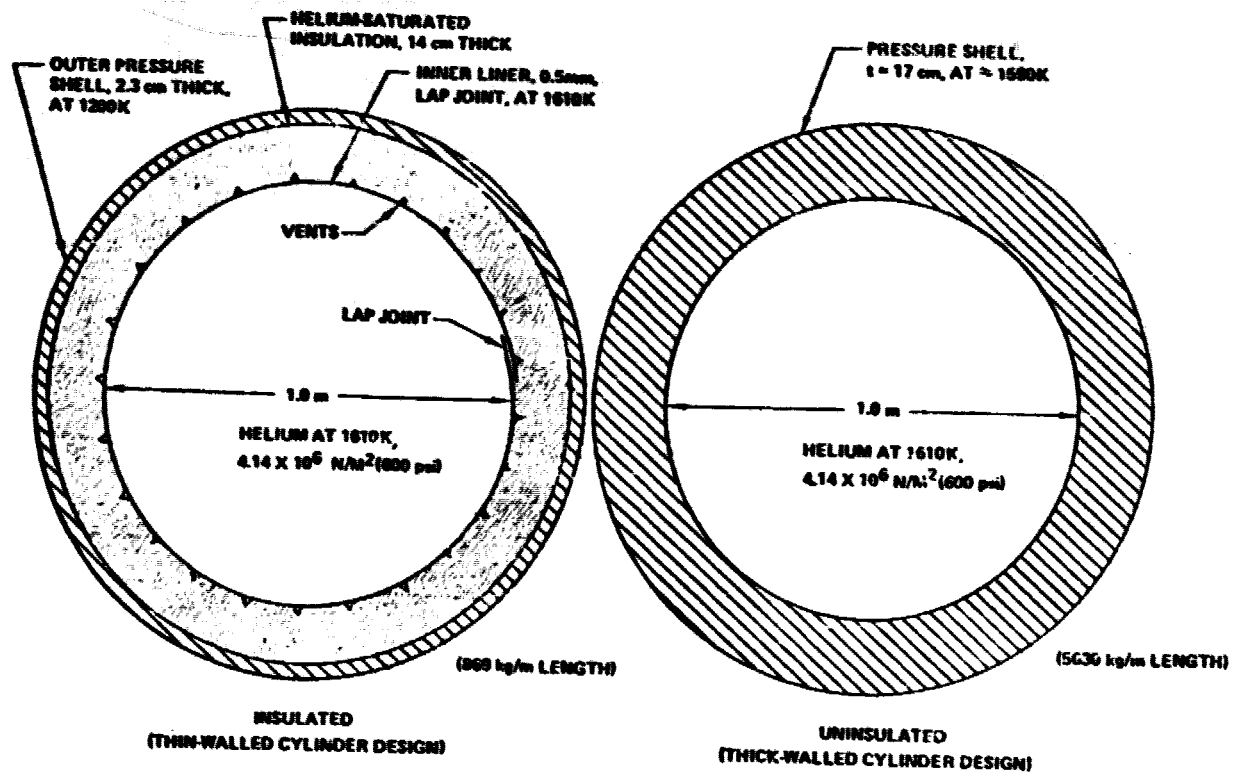


Figure 5.2-11 Insulated Helium Ducts Reduce Mass

As explained in Section 4, Brayton radiators tend to be relatively large. With a cycle temperature ratio of 0.25 (determined as optimum), the projected area of the radiator was approximately  $4.5 \times 10^6 \text{ M}^2$  ( $4.8 \times 10^7 \text{ ft}^2$ ). A sixteen module Brayton SPS was configured. One module of this satellite is shown in Figure 5.2-12.

The overall configuration is shown in Figure 5.2-13.

This configuration employed a 47% oversize of the solar concentrator, since at that time this was considered necessary to offset the radiation-induced degradation. A mass statement for this configuration is given in Figure 5.2-14.

Now at the end of Part 2 of this study, two microwave transmitters are expected to have a mass 24,384 metric tons, rather than the 15,370 shown. This change would bring the total mass to 88,615 metric tons. After adjusting this total for the current concept of no concentrator radiation damage, the total mass becomes approximately 85,000 metric tons. This is about six percent more than the potassium Rankine SPS (with its lower turbine inlet temperature).

However, the Brayton system is capable of further mass reductions through advanced technology. For example, ceramic heat exchangers could possibly save several thousand metric tons. The Brayton system inherently avoids the potential erosion problems of the potassium Rankine system. It is therefore appropriate to consider it as a promising alternative to the potassium Rankine SPS.

SPS-618.

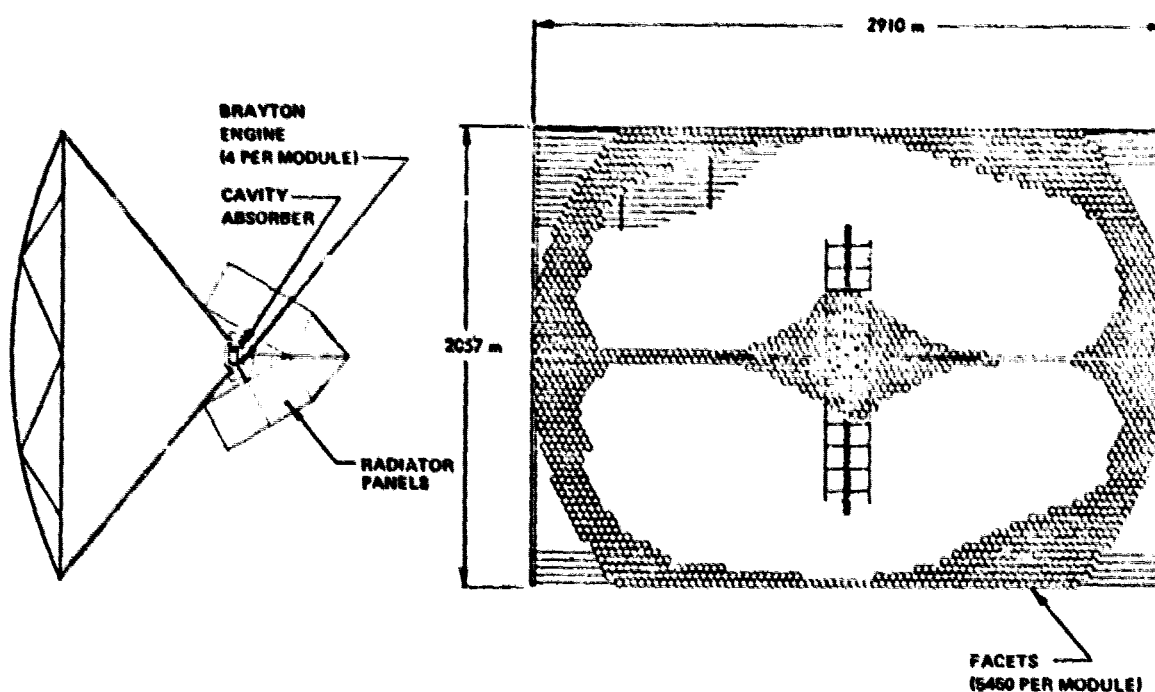
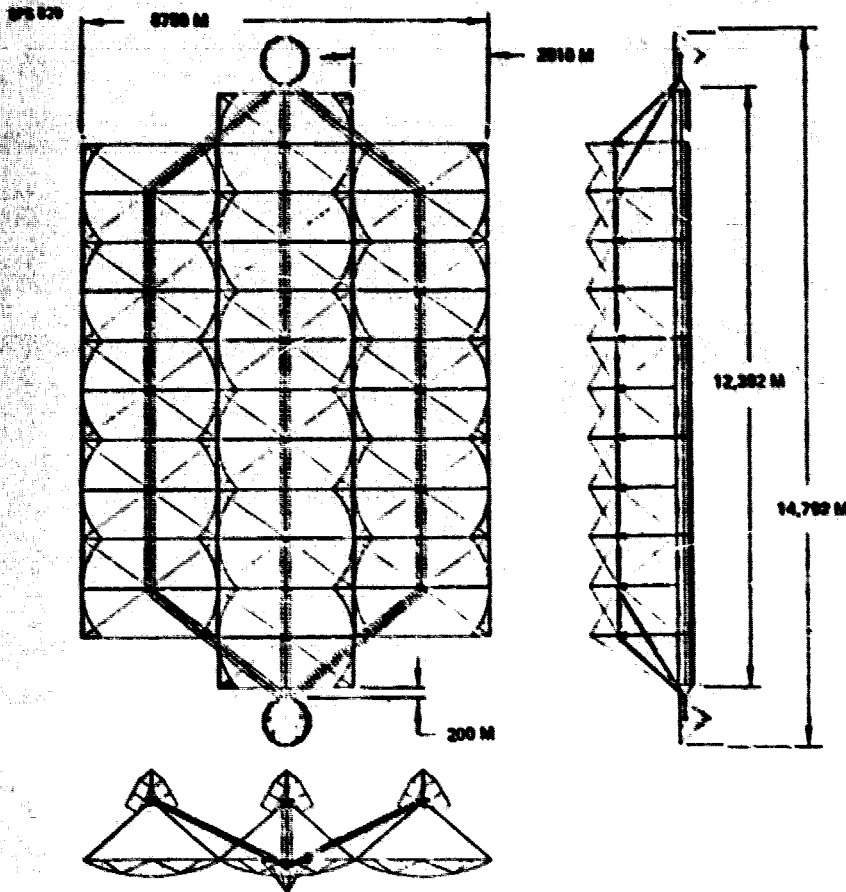


Figure 5.2-12. One Module, Brayton SPS

D180-22876-3



- 10 GW, AT 30 YEARS
- 79,810 METRIC TONS
- 80.88 Km<sup>2</sup> PROJECTED REFLECTOR AREA
- 96.77 Km<sup>2</sup> PROJECTED STRUCTURE AREA
- 16 MODULES, 4 ENGINES EACH
- P.O.P. ATTITUDE
- 1610K TURBINE INLET TEMP.

Figure 5.2-13. Brayton SPS Configuration

SPS-628

ITEM	10 <sup>6</sup> Kg
RADIATOR SYSTEM	30.951
TRANSMITTERS & SLIP RINGS	15.370
PRIMARY HEAT ABSORBER	9.070
RECUPERATOR/COOLERS	4.860
GENERATORS	4.320
FACETS, INCLUDING STRUCTURE*	4.200
POWER DISTRIBUTION	3.370
STRUCTURE	2.730
TURBOMACHINES	1.950
CAVITY ASSEMBLIES	1.420
GENERATOR COOLING	0.620
SWITCH GEAR	0.400
ATTITUDE CONTROL/STATION KEEPING	0.340
LIGHT SHIELD ASSEMBLIES	0.200
ONE YEAR'S CONSUMABLES	0.200
<b>BRAYTON SPS</b>	<b>79.801</b>

\*STRUCTURE SYSTEM ASSOCIATED WITH PLASTIC FILM TENSIONING

Figure 5.2-14. Brayton SPS Mass Statement

## 6.0 SATELLITE CONFIGURATION DEFINITION

### 6.1 CONFIGURATION

#### 6.1.1 Silicon Photovoltaic

##### 6.1.1.1 Reference Design

This section is devoted to the definition of the photovoltaic reference configuration as selected in Section 5.1.1. The reference design is discussed from the major base assumptions, system component definition, structure and subsystems definition, and system characteristics. Mass and cost summaries are covered in Sections 6.2.1 and 6.3.1, respectively.

**6.1.1.1.1 Baseline Data**—The reference configuration selected in Section 5.1.1 is a silicon, concentration ratio one, annealable photovoltaic system. The solar array uses 50  $\mu\text{m}$  (2 mil) silicon solar cells electrostatically bonded to borosilicate microsheet glass, to provide an annealable blanket configuration. A more complete definition is provided in the next section.

A listing of the reference efficiency and energy conversion chain, along with initial sizing requirements, is provided in Table 6.1-1. The major changes from earlier results are solar cell initial efficiency, blanket factors and 30 year non-annealable radiation degradation.

The initial solar cell efficiency is 15.75 percent instead of the 18.0 percent assumed at the end of Part I. At the Part II midterm briefing the initial cell efficiency was 16.5 percent but increased to 18 percent with the addition of a V-groove cover. Since a thinner solar cell is being used now, and to reduce the uncertainties, the lower efficiency was adopted.

The blanket factor appears somewhat larger than in Part I, 0.9453 vs. 0.9081, but actually has not changed. The lost area factor was removed from the blanket factor so there would be no degradation of "lost area". The lost area factor was included in the sizing analysis. The other items included in the blanket factor were updated. An analysis of the blanket  $I^2R$  loss revealed that it was significantly less than previously estimated. The cell mismatch used previously was re-evaluated but not changed. To be somewhat more conservative on the expected UV degradation, the decrease in  $I^2R$  loss was compensated for by an increase in the UV degradation which kept the blanket factor constant.

The other major change in the conversion efficiency was in the 30 year non-annealable radiation degradation factor. Recent results for 50  $\mu\text{m}$  silicon solar cell radiation degradation, discussed in Sections 4.4 and 5.1.1, revealed a significantly lower degradation than previously anticipated. Using the annealing scheme seemed to warrant a decrease in the non-annealable radiation degradation. The change was not that significant, 0.97 vs. 0.95, but due to the lower degradation actually received in a 30 year period, it suggests that annealing only has to be 70 percent effective.

**D180-22876-3**

**Table 6.1-1. Part II Reference System Energy Conversion/Sizing**

SPS-1530

	OUTPUT - W/M <sup>2</sup>
● BASIC CELL PERFORMANCE @ AMO-25°C (.1575)	213.1
● 10% IMPROVED PERFORMANCE DUE TO TEXTURED COVERS (.1733)	234.4
● BLANKET FACTORS (.9453) (STRING I <sup>2</sup> R, UV LOSSES, & MISMATCH)	221.8
● SUMMER SOLSTICE COSINE LOSS (.9190)	203.8
● APHELION INTENSITY FACTOR (.9675)	197.0
● TEMPERATURE LOSSES (36.5°C @ SUMMER SOLSTICE = 0.9540)	198.0
● 30 YEAR NON-REPAIRABLE RADIATION DEGRADATION (0.970)	182.3
● POWER REQUIRED TO BUS (INCLUDES I <sup>2</sup> R LOSS)	17.55 (10) <sup>9</sup> WATTS
● SOLAR CELL AREA (1% OVERSIZE FOR ENERGY STORAGE, ATTITUDE CONTROL REGULATION, AUX. PWR & ANNEALING CAPABILITY)	97.3 km <sup>2</sup>
● ARRAY AREA (CELL, PANEL, STRING AND SEGMENT LOST AREAS)	102.5 km <sup>2</sup>
● SATELLITE AREA (BEAM, CATENARY & ATTACHMENT LOST AREA FACTOR)	112.8 km <sup>2</sup>

The sizing criteria include a one-percent oversize to provide power regulation during the summer solstice and also provide auxiliary power including attitude control, energy storage and annealing capabilities.

#### 6.1.1.1.2 Reference Configuration

**6.1.1.1.2.1 Array Dimensions**—The final reference configuration for the photovoltaic SPS is illustrated in Figure 6.1-1. This configuration evolved from the integration of system, subsystem, component and operational requirements.

An illustration of the solar cell blanket is provided in Figure 6.1-2. A silicon solar cell must be provided with a cover to increase front-surface emittance from around 0.25 to around 0.85, and to protect the cell from low-energy proton irradiation. Cerium-doped borosilicate glass is a good cover material because it costs only a fraction of the best alternate, 7940 fused silica, matches the coefficient of thermal expansion of silicon, and yet resists darkening by ultraviolet light. Borosilicate glass can be electrostatically bonded to silicon to form a strong and permanent adhesiveless joint. In ATS-6 flight tests the cells having integral 7070 borosilicate glass covers lost only  $0.8 \pm 1.1$  percent of their output because of ultraviolet degradation. These cells had no cover adhesive. Other cells having cell-to-cover adhesives degraded twice as much. Jena Glaswerk Schott & Gen., Inc., in West Germany, expects to be able to manufacture 75  $\mu\text{m}$  borosilicate glass sheets one meter wide by several meters long.

The cell cover is embossed during bonding with grooves which refract sunlight away from the grid lines and buses on the cell surface. COMSAT Labs expects an 8 to 12 percent increase in cell output from this feature in cell covers.

Solar cells only 50  $\mu\text{m}$  thick recently made by Solarex had an air-mass-zero efficiency of 12.5 percent without a back-surface field or anti-reflection treatment. Texturing the sun-facing surface makes the incoming light arrive at the back surface of the cell at an angle of over  $31^\circ$ , so the light rays that have not been absorbed are reflected off the back surface with virtually no loss, the critical angle in a silicon-air junction being 15.3 degrees. This feature not only improves photon collection efficiency, when compared with thicker cells, by lengthening the light path in silicon for infrared photons, but also improves radiation resistance. Since all charge carriers are generated within 50  $\mu\text{m}$  of the P-N junction which is 0.2  $\mu\text{m}$  under the sun-facing surface, the cell can absorb radiation damage until the diffusion length in the bulk silicon is reduced to 50  $\mu\text{m}$  by radiation-generated recombination centers.

The cells are designed with both P and N terminals brought to the backs of the cells. This feature makes it possible to use simple 50  $\mu\text{m}$  silver-plated copper interconnections which are formed on the substrate glass. Complete panels are assembled electrically by welding together the module-to-module interconnections.

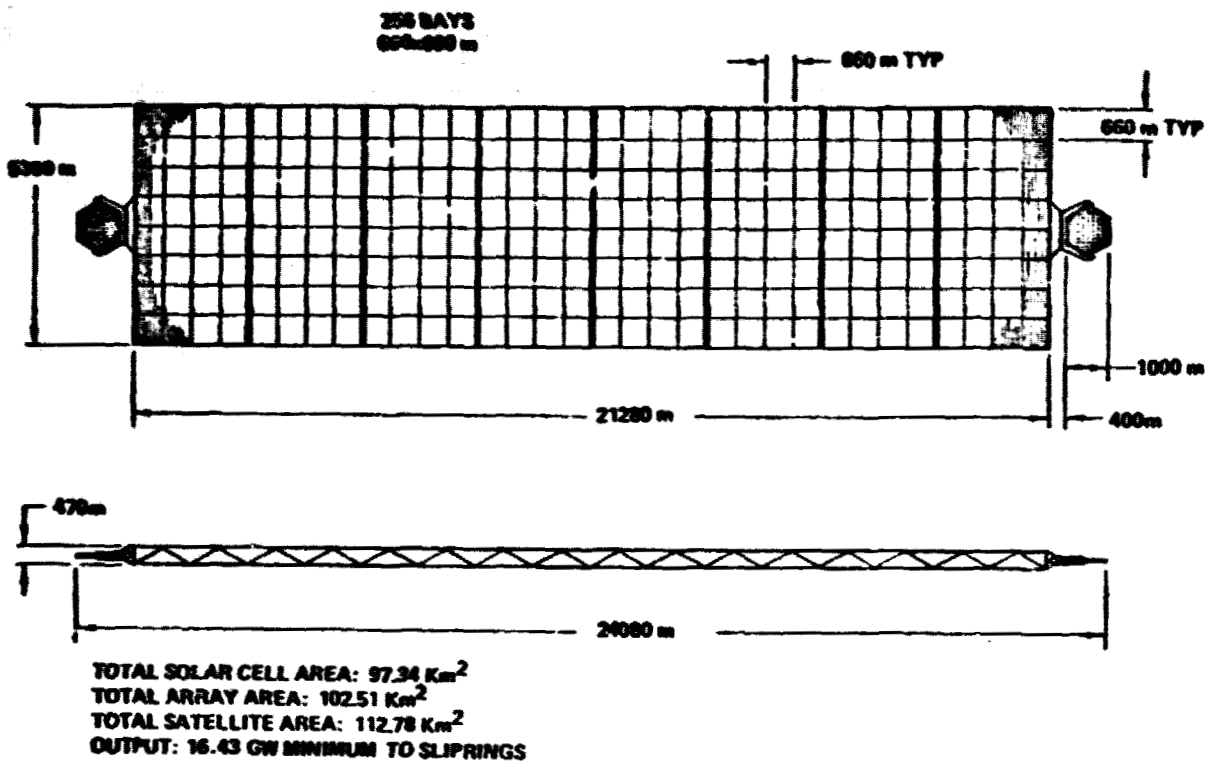


Figure 6.1-1. Photovoltaic Reference Configuration

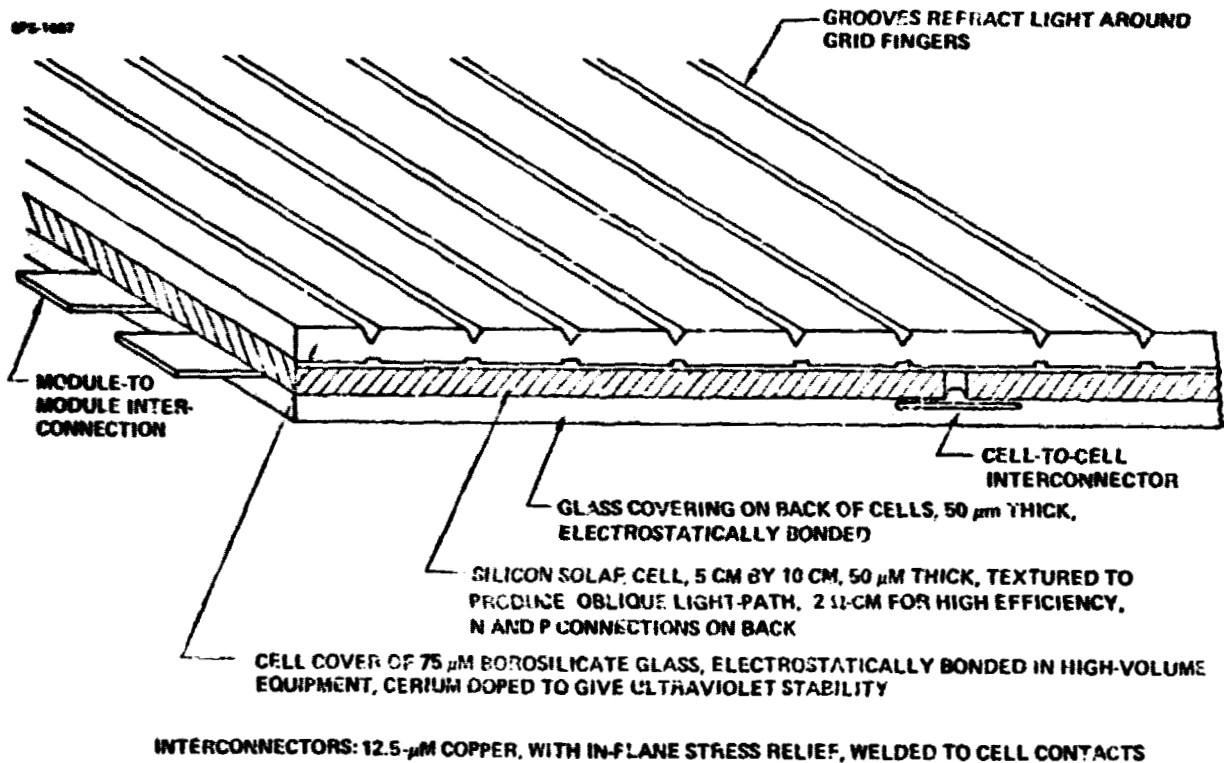


Figure 6.1-2. Low Cost Annealable Blanket Structure

Glass was chosen for the substrate to enable annealing of radiation damage by heating. With all glass-to-silicon bonds made by the electro-static process there are no elements in the blanket which cannot withstand the 773K (931°F) annealing temperature which at present seems to be required. One researcher suggests that 773K (931°F) may not be needed for annealing out the radiation damage from solar-flare protons. However, his theory has not yet been confirmed by experiment.

The solar array fundamental element is the blanket panel (Fig. 6.1-3) which was adopted for design studies. It has a matrix of 252 solar cells, each 6.4 by 7.7 cm in size, connected in groups of 14 cells in parallel by 18 cells in series. The cells are electrostatically bonded between two sheets of borosilicate glass. Spacings between cells and edge spacings are as shown. Tabs are brought out at two edges of the panel for electrically connecting panels in series. Cells within the panel are interconnected by conducting elements printed on the glass substrate.

Important panel requirements were these:

- The panel components and processes should be compatible with thermal annealing at 773 (931°F)
- Presence of charge-exchange plasma during ion-engine operation may necessitate insulating the electrical conductors on the panel.
- The panel design should be appropriate for the high-speed automatic assembly required for making the some 78 million panels required for each satellite.
- Low weight and low cost are important.

The glass-encapsulation technology, while not in use today, seems to be achievable by 1985. Simulation Physics has made excellent electrostatic bonds of covers to cells. Schott in West Germany is making thin microscope slides from borosilicate glass. The alternate panel design, using adhesives for bonding cells, covers, and substrate, may also be feasible by 1985.

The panel-to-panel assembly (Fig. 6.1-4) is accomplished to provide the larger elements required for the solar array. The interconnecting tabs of one panel are welded to the tabs of the next panel in the string, and then the interconnections are covered with a tape that also carries structural tension between panels. After joining, the panels are accordion-folded into a compact package for transport to the low-Earth-orbit assembly station.

The 0.5 cm spacing between panels provides room for welding electrodes, and also permits reasonable tolerances in the large sheet of 75  $\mu$ m glass that covers the cells and the 50  $\mu$ m sheets of substrate glass.



**NO SCALE**

**Figure 6.1-3. Photovoltaic Reference Configuration Solar Array Fundamental Element "Blanket Panel"**

**SECT A-A**

**Figure 6.1-4. Photovoltaic Panel to Array Assembly**

The method of joining the panels to both other panels and to support is illustrated in Figure 6.1-5. The tapes provide biaxial support requirements for the array blanket and to the satellite bay structure (Fig. 6.1-6).

Primary support of the array is accomplished by the use of a spring loaded piston cylinder at the 20 meter support points. This provides a constant force to the array support catenaries. It also provides for a movement of up to 2 meters, in both X and Y directions, which may occur due to a LEO-GEO transfer acceleration of  $10^{-4} g$ .

A mass summary for the array blanket is shown in Table 6.1-2. A comparison is provided for the blanket make-up at the end of Part I. Even though significant changes have occurred to the blanket, only a small variation in the unit mass has resulted.

#### 6.1.1.2.2 Structural Analysis

The structure for the reference photovoltaic SPS had design constraints that were used in the development of the final configuration. It was attractive to use a modular structural concept for construction in LEO with transfer to and final assembly at GEO.

The modular concept includes eight modules of equal size and is composed of square grid sections that would form a system with an aspect ratio of four on final assembly. The satellite is comprised of 256 bays, each 660 meters square. They are arranged eight wide by thirty-two long to provide the aspect ratio of four as was shown in Figure 6.1-1. Each module is 8 bays by 4 bays; the modules are joined together along the 8-bay edges.

A loads analysis was conducted on the satellite structure to identify the critical beams. The module configuration used is shown (Fig. 6.1-7) for the case of LEO-GEO transfer with an antenna payload. The critical beams are noted and were used to size the structural members.

A section view of a truss-end (Fig. 6.1-8) reflects the geometry of the basic structure used. This arrangement provides squared ends which provide docking points on the top and bottom of the satellite modules. The dimensions shown are those used in the reference configuration. Details of the method of joining the beam sections are shown in Figure 6.1-9. Construction considerations are addressed in Volume 5, Section 3.2.1.1.4.1.

The structural beam sections were optimized for cost and mass as illustrated in Figure 6.1-10. A 20-meter beam was chosen because it was both structurally compatible and near the cost/mass optimization point.

An edge loading analysis was accomplished on the array to establish structural load criteria (Fig. 6.1-11). This established strut design end-loads and sizing criteria (Table 6.1-3 and Fig. 6.1-12) for the graphite epoxy tapered tube beam members. Results were used to establish a mass summary for a 20 meter beam section (Table 6.1-4). It was noted that since the critical beams were in the upper

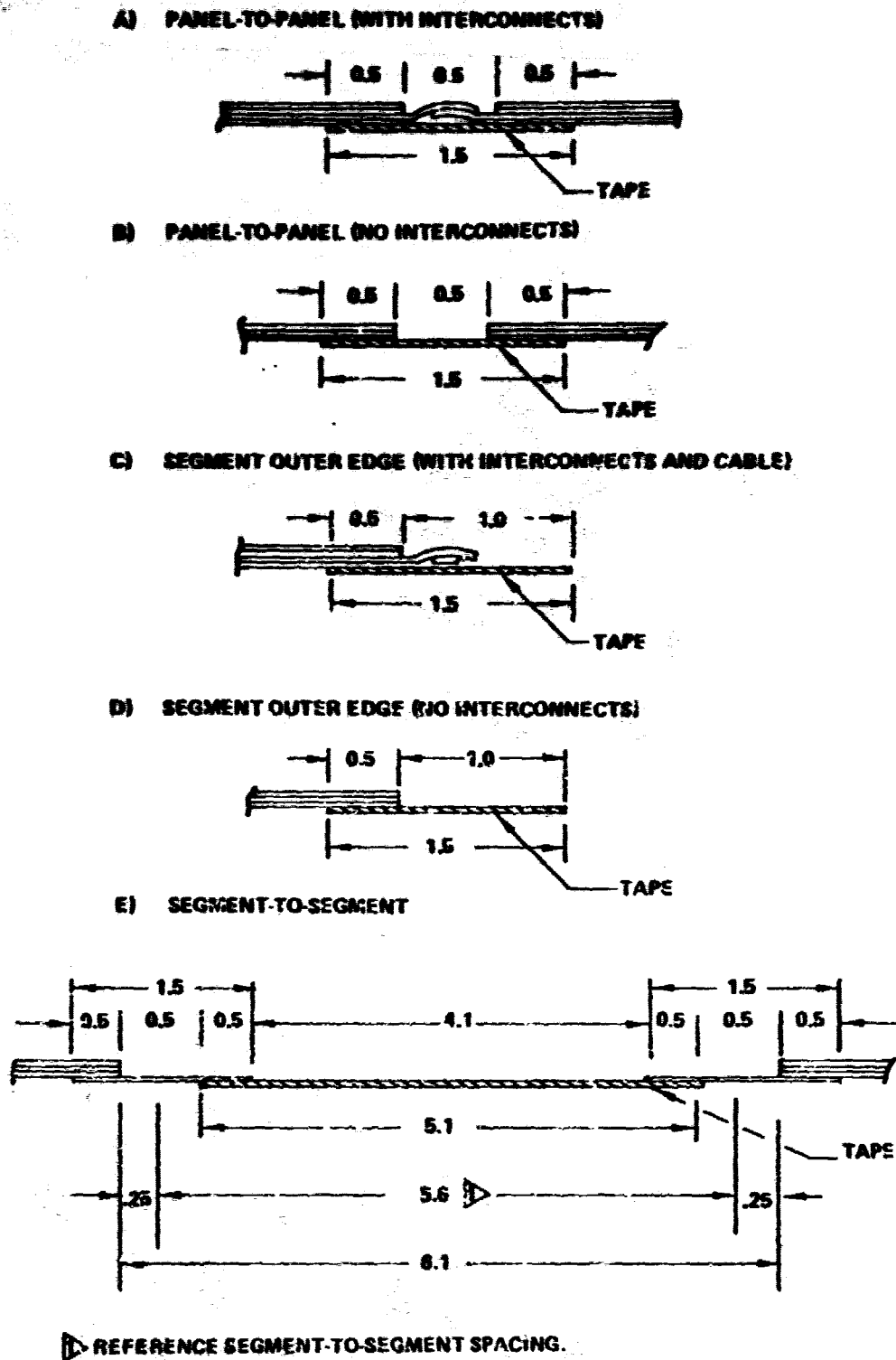


Figure 4.1-5 Joint Tape Configuration (All Dimensions in Centimeters)

D180-22876-3

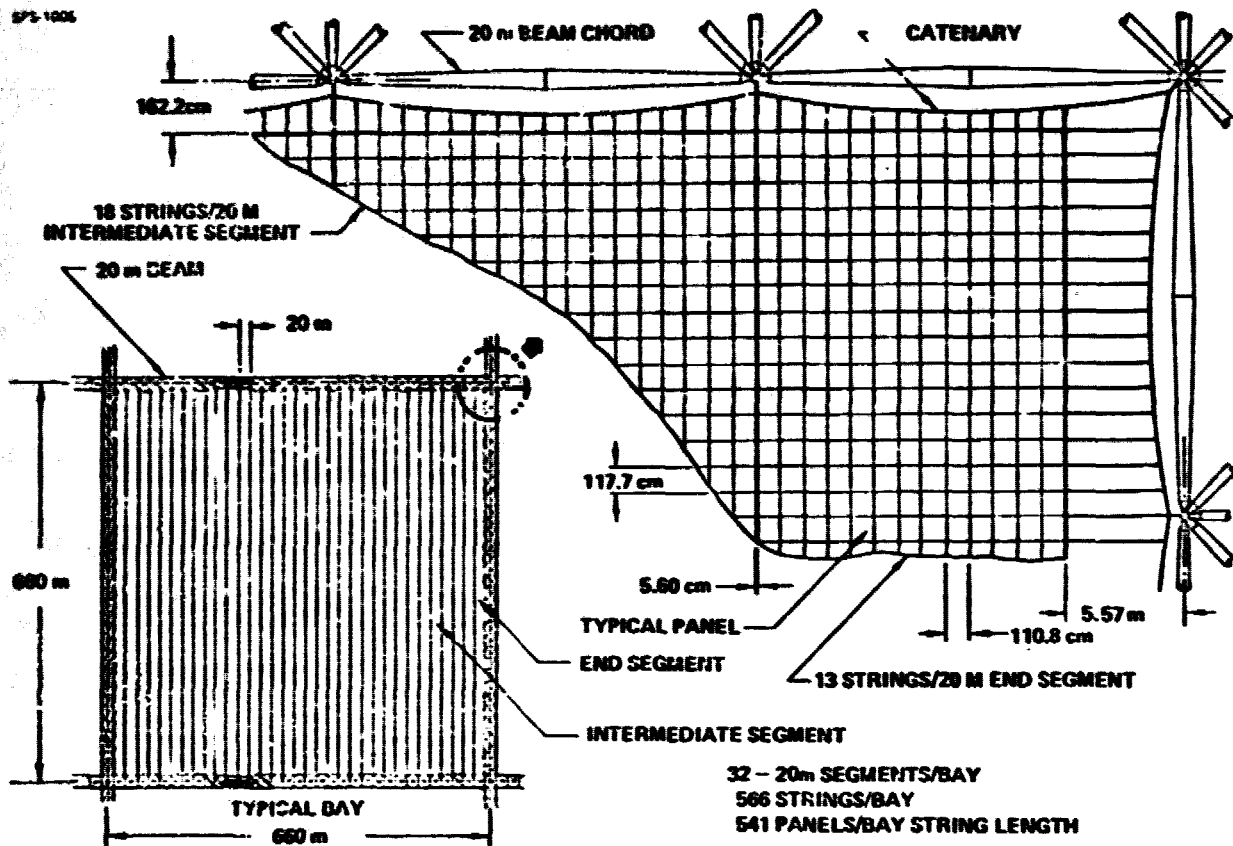


Figure 6.1-6. Photovoltaic Reference Solar Array Arrangement and Attachment

ORIGINAL PAGE IS  
OF POOR QUALITY

D180-22876-3

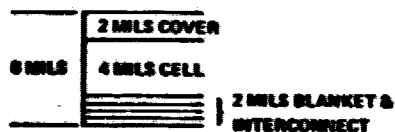
Table 6.1-2. Photovoltaic Blanket Weight Buildups

SPS-1002

**SILICON SOLAR CELL BLANKET WEIGHT @ PART I FINAL**

ITEM	DENSITY (G./CM <sup>3</sup> ) (g./m <sup>2</sup> /MIL)		THICKNESS (MILS)	AREA FACTOR	WEIGHT (g/m <sup>2</sup> )
COVERS—FUSED SILICA	2.20	98.00	2.00/3.00	0.900	107.90/161.94
CELLS—SILICON	2.30	98.94	4.00	0.960	231.61
INTERCONNECTS—COPPER	8.94	227.00	0.50	0.300	22.71
SUPPORTING FILM—KAPTON*	1.42	35.07	2.00	0.900	32.46
ADHESIVE, CELLS TO FILM	1.40	35.95	0.50	0.900	16.60
ADHESIVE, KAPTON TO KAPTON	1.40	35.95	0.50	0.000	14.22

62.68



THEORETICAL WEIGHT	424.96/478.94
TOLERANCES & INSTALLATION (15 %)	63.74 / 71.86
ESTIMATED ACTUAL WEIGHT	488.7/550.8

**AVAILABLE BLANKET @ PART II INTERIM**

COVERS—FUSED SILICA	2.20	98.00	3.0	1.0	107.94
CELLS—SILICON	2.30	98.94	2.0	0.9007	195.17
INTERCONNECTS—COPPER	8.94	227.00	.5	0.100	11.35
SUBSTRATE—FUSED SILICA	2.20	98.00	2.0	1.0	111.76



THEORETICAL PANEL WEIGHT	405.92
TOLERANCES ALLOWANCE (5%)	20.30
ESTIMATED PANEL WEIGHT	426.22
PANEL AREA FACTOR (.9913)	422.51
SEGMENTS AREA FACTOR (.9972)	421.34
JOINT/SUPPORT TAPPS	2.93
CATENARY SYSTEM	2.52

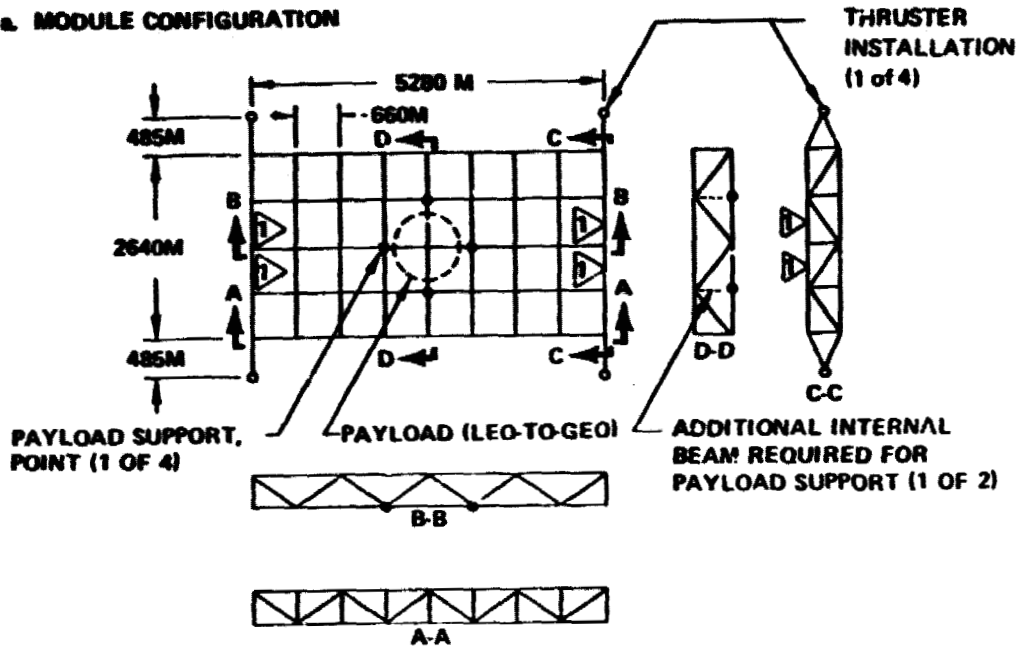
CELL AREA = 380,264 m<sup>2</sup>/BAY  
 PANEL AREA = 385,643 m<sup>2</sup>/BAY  
 ARRAY AREA = 400,434 m<sup>2</sup>/BAY  
 NO. OF BAYS = 256

ESTIMATED ARRAY WEIGHT 426.78

ORIGINAL PAGE IS  
OF POOR QUALITY

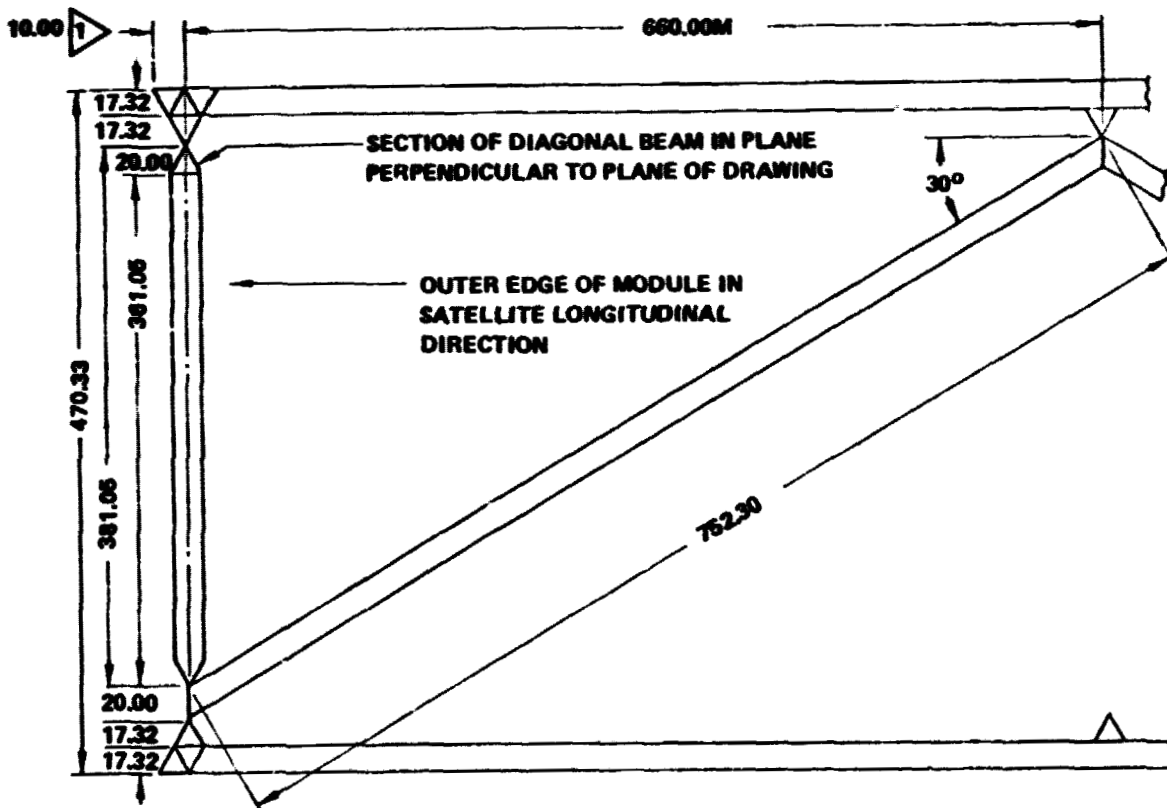
D180-22876-3

a. MODULE CONFIGURATION



1 CRITICAL BEAM (FOR CASE OF UPPER SURFACE IN COMPRESSION)

Figure 6.1-7 Loads Analysis and Loads/Sizing Summary for Critical Beam in Upper Surface



1 DELTA LENGTH AT EDGE. (28 PLACES/SURFACE/MODULE, INCLUDING 2 PLACES/CORNER/SURFACE.)

Figure 6.1-8. Reference Length of 20M Beams

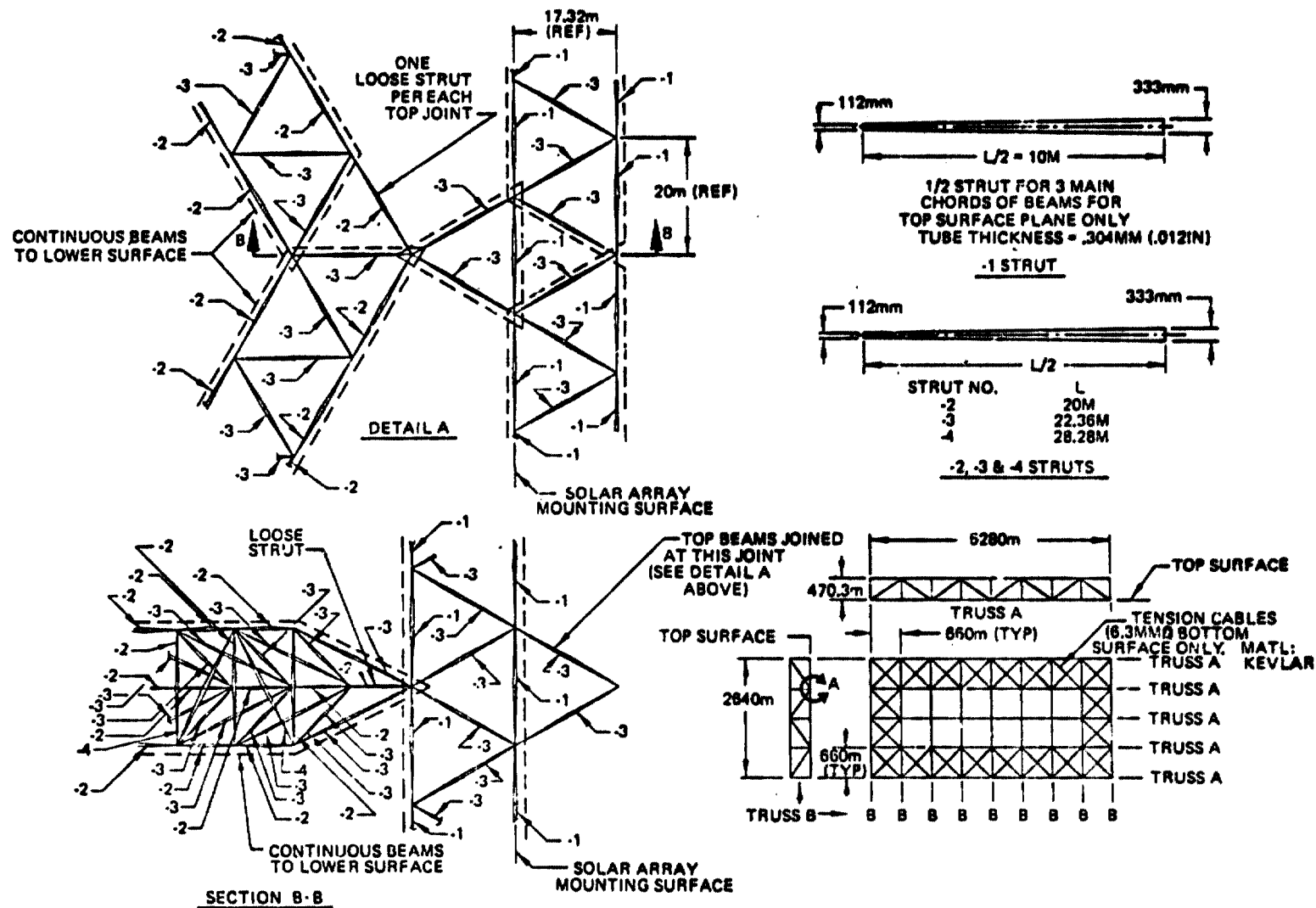


Figure 6.1-9 Photovoltaic Satellite Structural Details

D180-22876-3

ORIGINAL PAGE IS  
OF POOR QUALITY

SPS-1350

MANUFACTURING COST ONLY  
(EARTH FABRICATION & LEO ASSEMBLY)

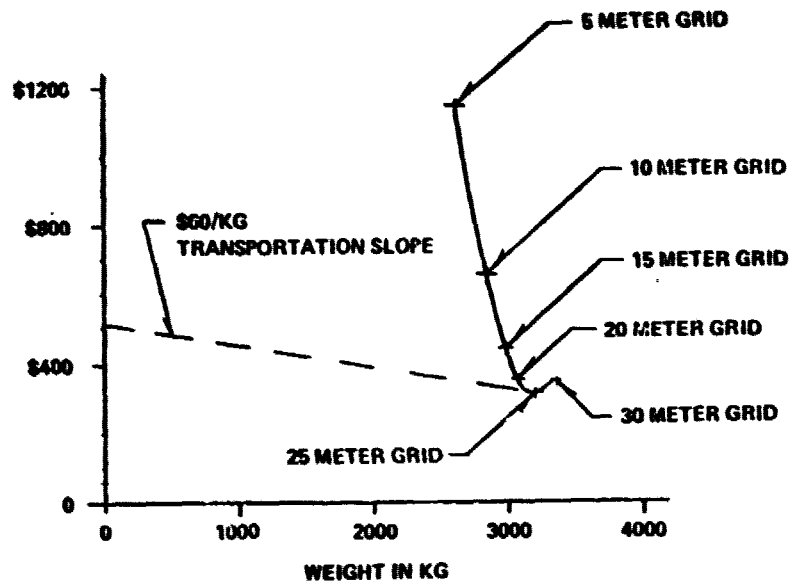


Figure 6.1-10. 680 Meter Beam Cost &amp; Weight Size Selection

- ARRAY FIRST MODE FREQUENCY = 12 CYCLES/HOUR
- ARRAY CONSIDERED AS A SQUARE MEMBRANE UNDER UNIFORM BIAXIAL LOADING

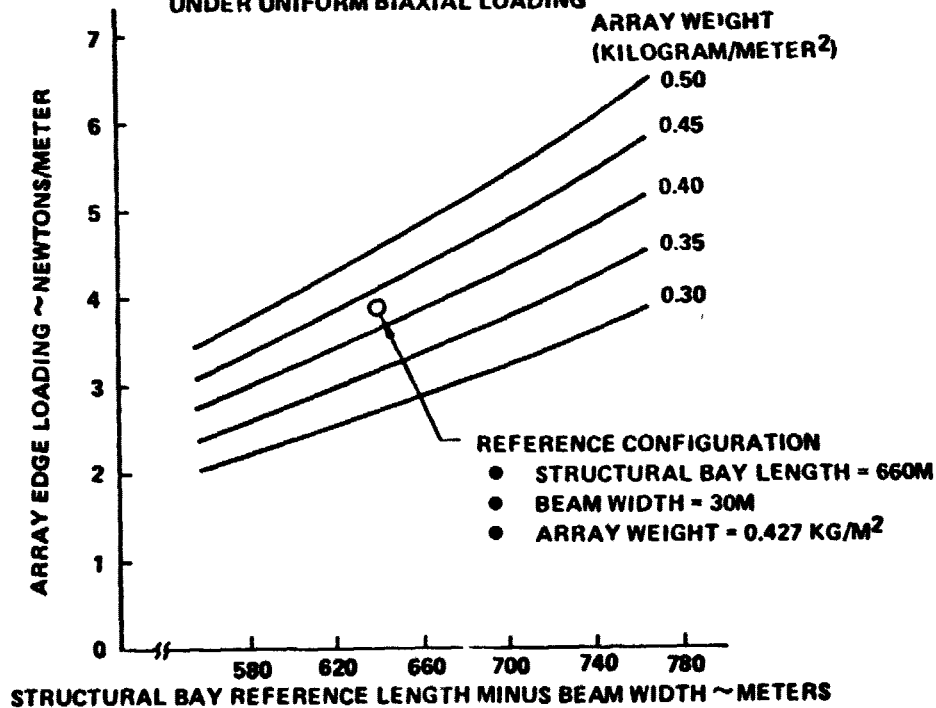




Figure 6.1-11 Array Edge Loading



Table 6.1-3. Loads/Sizing Summary for Critical Beam in Upper Surface

DESIGN CONDITION	APPLIED (LIMIT) LOADS ON CRITICAL BEAM			DESIGN (ULTIMATE) COLUMN LOAD ON CRITICAL STRUT P (LB) 	SIZE DATA FOR 20 METER LONG TAPERED TUBE 		
	UNIFORM LOADING ALONG BEAM		COLUMN LOAD ON BEAM P (LB)		D <sub>MAX</sub> (IN)	t (IN)	A <sub>AVE.</sub> (IN <sup>2</sup> )
	W <sub>1</sub> (LB/IN)	W <sub>2</sub> (LB/IN)					
• ARRAY PRETENSION	.0223	—	289	2536	12.96	.0181	.518
• ARRAY PRETENSION, MODULE SELF TRANSPORT, NO PAYLOAD	.0223	.0004	478	2655	13.07	.0195	.534
• ARRAY PRETENSION, MODULE SELF TRANSPORT, P/L = X ANTENNA	.0223	.0004	582	2712	13.12	.0197	.541
• ARRAY PRETENSION, MODULE SELF TRANSPORT, P/L = ANTENNA	.0223	.0004	834	2883	13.27	.0202	.561

ARRAY PRETENSION = 3.9 NEWTONS/METER  
 MAX T/W CAPABILITY DURING SELF TRANSPORT = 0.0001  
 MODULE WEIGHT = 6,500,000 kg  
 ANTENNA WEIGHT = 12,200,000 kg

— — — INDICATES BASELINE DESIGN CONDITION

$$P = \left[ \frac{W_u L^2}{12H} + \frac{X}{3} \left( \frac{W_s L^2}{12H} + P \right) \right] \times \text{U.F.S.}$$

where

L = 67.0M = 26,984 IN.

W = 20M = 787 IN.

H = 17.3M = 682 IN.

U.F.S. = 1.5

$$\text{triangle 2} \quad D_{MIN}/D_{MAX} = 1/3$$

Table 6.1-4. Mass Definition for 20M Beam Section (Upper Surface Beams)

ITEM	MATERIAL	PRINCIPAL DIMENSIONS (IN.)	WT/ITEM (LB)	NO. OF ITEMS	TOTAL WT (LB)
<b>TAPERED TUBES</b>					
CHORD HALF SECTION	G/E	D = 13.3, d = 4.4, L = 386.9, t = .020	13.12	6	(169.20)
SIDE DIAGONAL HALF SECTION	"	" " " " 433.4, t = .010	7.34	8	78.72
BASE DIAGONAL HALF SECTION	"	" " " " 549.9 "	8.32	2	58.72
BASE BATTEN HALF SECTION	"	" " " " 386.9 "	6.56	2	18.64
					13.12
<b>TUBE CENTER JOINTS</b>					
CHORD CTR. JOINT HALF SECTION	ALUM	FITS TUBE END WITH D = 13.3	0.81	6	( 10.98)
DIAG./BATTEN CTR. JT. HALF SECTION	"	" " " " " "	"	12	3.68
					7.32
<b>TUBE END FITTINGS</b>					
CHORD END FITTING	ALUM	FITS TUBE END WITH d = 4.4	0.28	6	( 5.18)
DIAG./BATTEN END FITTING	"	" " " " " "	"	12	1.68
STUD RETENTION SPRING	INCONEL	" " " " " "	0.0002	36	3.36
SPRING INSTALLATION BOLT	STEEL	" " " " " "	0.0009	72	0.07
SPRING INSTALLATION NUT	"	" " " " " "	0.0003	36	0.06
					0.01
<b>STRUT INTERCONNECT FITTINGS</b>					
APEX FITTING	ALUM	L = 2.25, W = 2.25, H = 1.65	0.35	1	( 1.40)
BASE FITTING	"	" " W = 1.65, "	0.30	2	0.36
BALL-END STUD	STEEL	D <sub>BALL</sub> = 0.375, L = 1.35	0.025	18	0.60
					0.45
				219	186.76 LB

NOTE: FOR LOWER SURFACE BEAMS AND INTRA SURFACE BEAMS, USE 147.40 LB  
 (3.34 kg/M) BASED ON CHORD THICKNESS = 0.010 IN.

(4.24 kg/M)

D180-22876-3

ORIGINAL PAGE IS  
OF POOR QUALITY

- OUTER LAYER IS GY-70/904 @ 90° (20% OF TOTAL THICKNESS)
- CENTER LAYER IS GY-70/904 @ 0° (60% OF TOTAL THICKNESS)
- INNER LAYER IS GY-70/904 @ 90° (20% OF TOTAL THICKNESS)
- $E_x = 25.8 \times 10^6$  PSI
- $C = 0.8/(R/Z)^{0.50}$
- PINNED ENDS
- TUBE OPTIMIZED FOR LONG COLUMN BUCKLING
- AND LOCAL CRIPPLING AT MIDSPAN

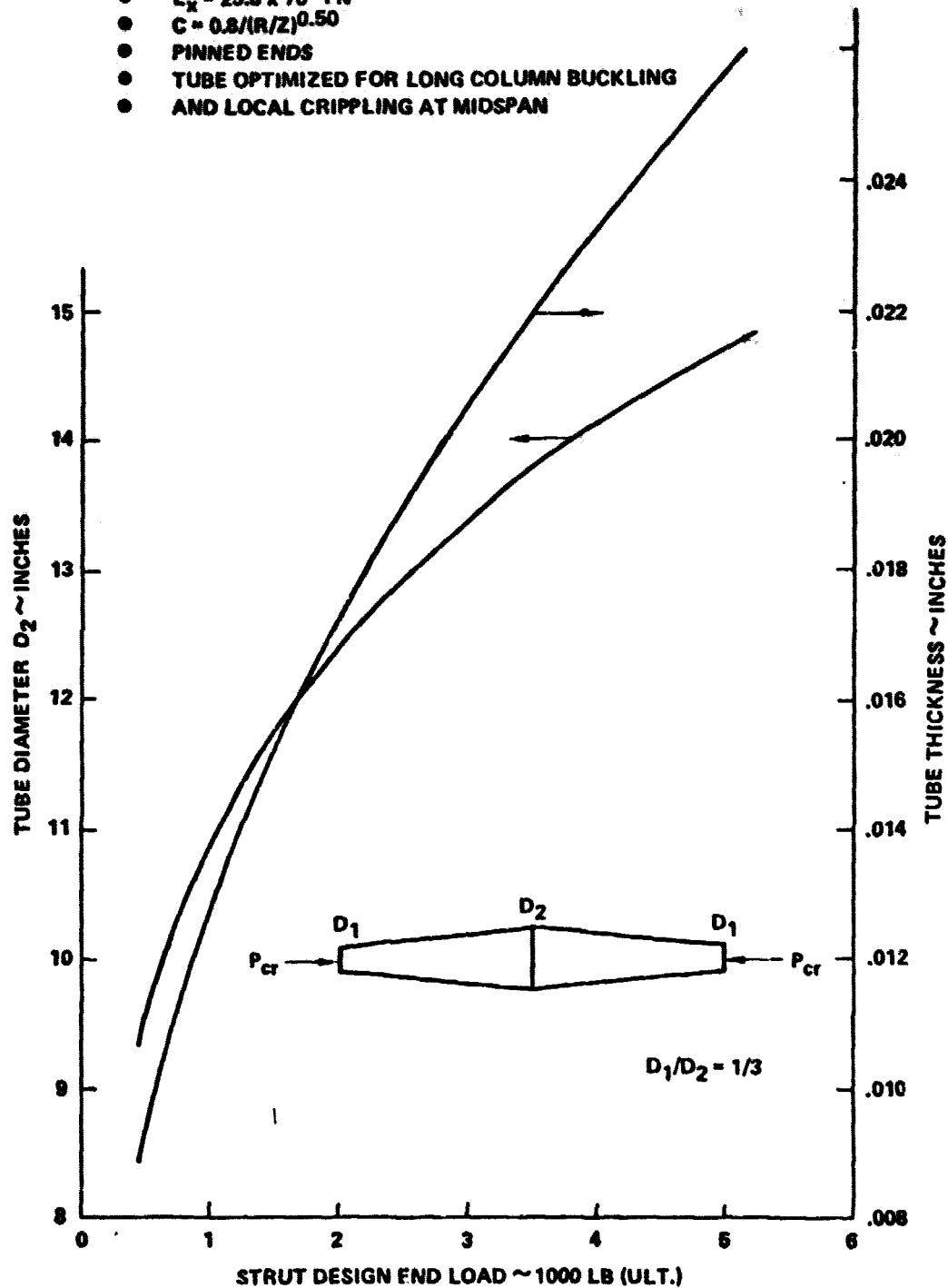


Figure 6.1-12 Sizing Data for a 20 Meter Long Tapered Tube of Graphite Epoxy

surface, the lower surface beams could be fabricated from minimum gauge thicknesses at a significant mass benefit.

#### **6.1.1.1.2.3 Subsystems**

The major subsystems are power distribution, electrical rotary joint, mechanical rotary joint, antenna support structure, attitude control, and instrumentation and controls.

The reference power distribution system is a no-lateral-bus-bar configuration. The main busing is run longitudinally along the centerline of satellite. The solar array strings are run laterally starting at the satellite centerline with a connection to the main bus, running to the edge of the satellite, then returning to the centerline and connecting to the main bus through a set of switchgear. Aluminum sheet conductors are used for both main busing and string jumpers at the edge of the satellite. The main busing is terminated at the electrical rotary joint which provides energy transfer capabilities across the mechanical joint with the antenna. A complete description of the power distribution system including switchgear and the electrical rotary joint is covered in Sections 4.6.1 and 4.6.2.

To provide a means of pointing the antenna toward the earth while the energy conversion system is continually oriented toward the sun, it was necessary to design an interface between the energy collection and transmission sections of the satellite. The method chosen was to provide a support structure on the satellite and a yoke structure, to support the antenna, joined by a mechanical and electrical rotary joint (Fig. 6.1-13).

The antenna support structure provides the interface between the main satellite structure and the mechanical rotary joint. It is composed of the 20 meter tapered tube beams discussed in the structural definition section. The antenna support structure also provides a base on which the mechanical rotary joint is attached.

The mechanical rotary joint provides the interface between the antenna support structure and the antenna yoke structure and also provides the drive mechanism to rotate the antenna with respect to the main section of the satellite. The mechanical rotary joint is composed of two circular-geometry, 20 meter beams (Fig. 6.1-14), one on the antenna support structure and one on the antenna yoke structure. The circular beams are arranged concentrically with the adjacent members 73.2 cm apart with a drive and roller assembly between them (Fig. 6.1-15).

The antenna yoke structure is the interface between the mechanical rotary joint and the antenna. This structure is composed of five meter beams of the same geometry as the twenty meter beams described previously. The antenna yoke structure also provides a flexible coupling at the yoke/antenna joint to allow tilt control of the antenna for alternate receiver locations. This coupling allows for an antenna tilt of up to eight degrees with respect to the yoke and does not require an electrical rotary joint.

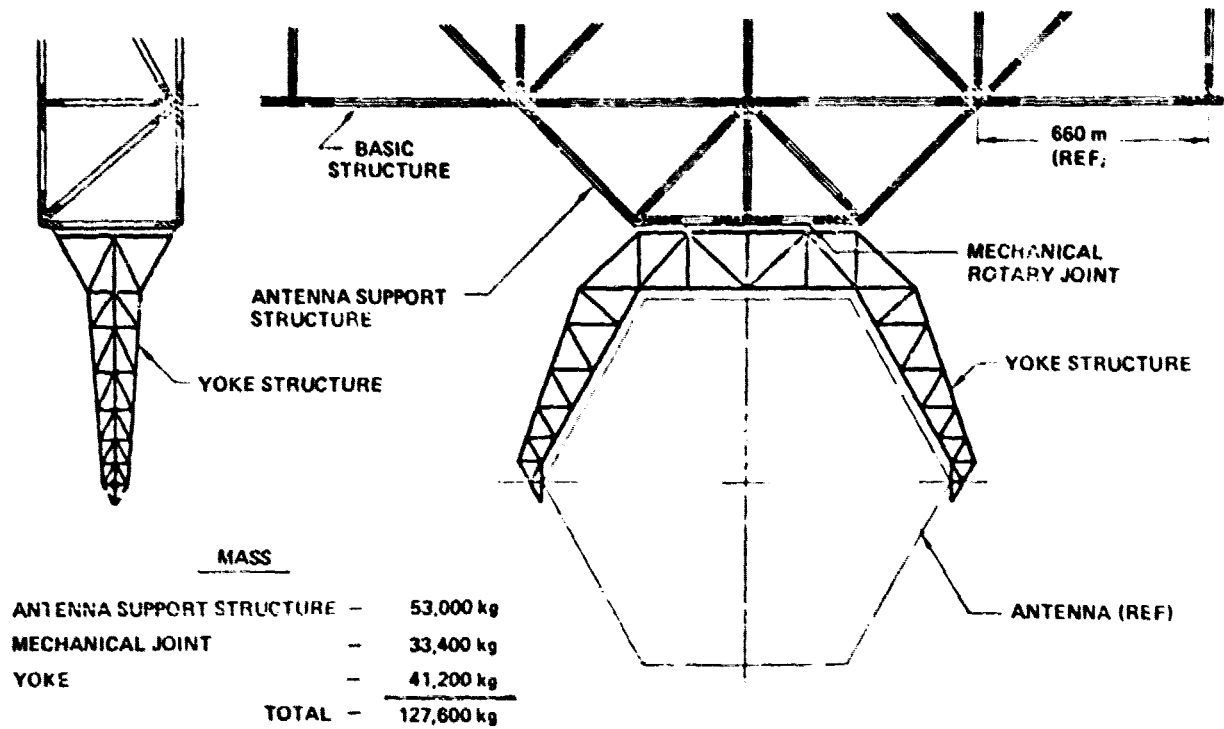


Figure 6.1-13. Antenna Support and Mechanical Joint Weights

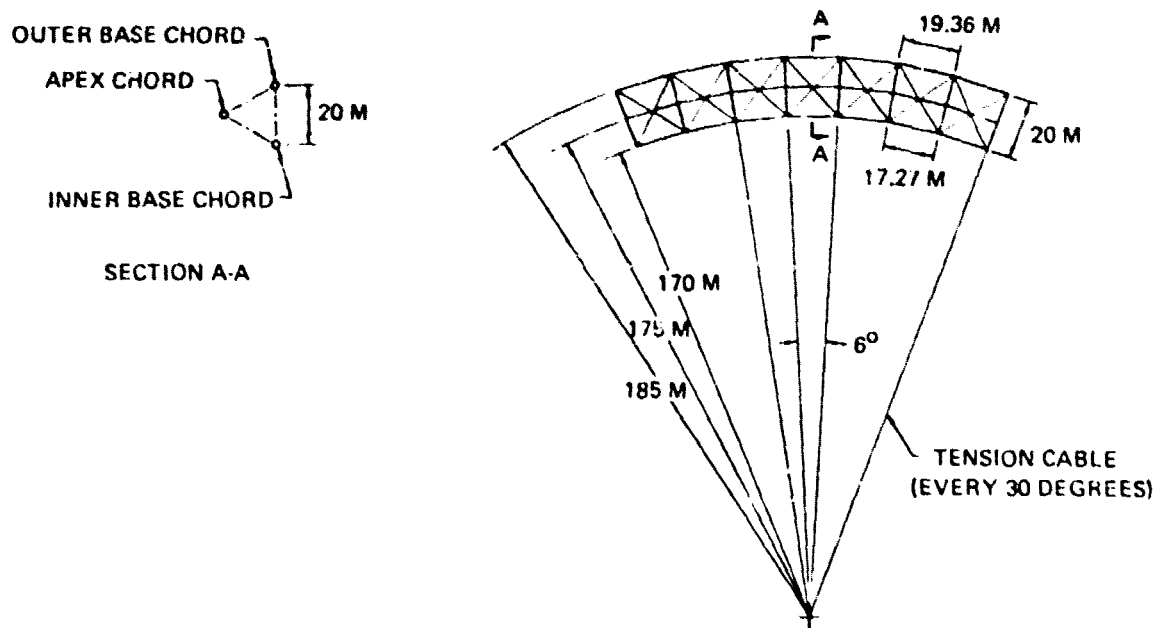
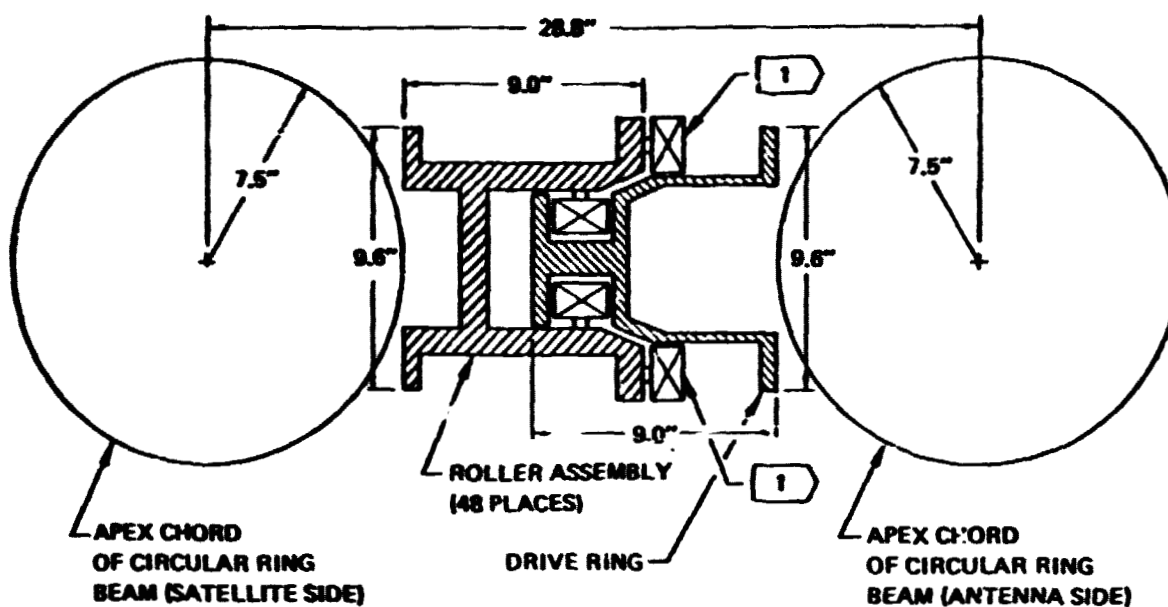


Figure 6.1-14. Circular Ring Beam Geometry



- 1 A ROLLER/DRIVE ASSEMBLY IS LOCATED AT 12 PLACES (EVERY TENSION CABLE) AROUND THE PERIPHERY OF THE CIRCULAR BEAM (SATELLITE SIDE). THIS ASSEMBLY IS SIMILAR TO THAT SHOWN EXCEPT THAT THE WHEELS INDICATED BY FLAG 1 ARE MOTOR DRIVEN FRICTION WHEELS WHICH ARE SPRING LOADED ACROSS THE ASSEMBLY.

Figure 6.1-15. Drive Ring and Roller Assembly Location Relative to Outer Base Chords of Circular Ring Beams

ORIGINAL PAGE 13  
OF POOR QUALITY

Attitude control requirements were investigated in Part II. Table 6.1-5 lists the assumptions and mass summary for the attitude control system that was used for the reference photovoltaic SPS oriented perpendicular to the orbital plane. Electric propulsion thrusters were used wherever possible but some added chemical propulsion equipment was necessary to provide attitude control during occultations.

Another task that was accomplished in Part II was the compilation of an instrumentation and control list. Table 6.1-6 provides a listing of instrumentation and control components along with their function and the number of units required.

#### **6.1.1.2 Reference Configuration Characteristics**

Most of the major system characteristics have been discussed either in Section 5.1.1 or 6.1.1.1. One of the interesting characteristics that has not been discussed is the actual operating point of the solar cells at different locations on the array.

All of the solar cell strings have the same number of solar cells in the same configuration. To compensate for power bus voltage drops, the strings and thus the solar cells must operate at different voltages dependent on their location with respect to the load. An illustration of the operating point for an average solar cell at various locations is shown as Figures 6.1-16 through 6.1-19. Another point that can be noted from these figures is that the solar cells operate near the maximum power points during different times of the year and at different locations within the system.

The available power of the reference photovoltaic SPS varies throughout the year. This is a result of the variation in solar flux seen by the energy conversion system and the resulting effect on solar cell operation.

The power output of a solar array depends on the intensity of illumination at the cells and the temperature of the cells. The maximum-power points of the cells diminish as the cells become hotter. In geosynchronous orbit the temperature of the solar cell is related to the intensity of sunlight for any given panel configuration.

Sunlight is most intense at SFS perihelion, which occurs around winter solstice when the orientation of the array is such that the sun's rays arrive at 23.5 degrees off of normal incidence. The worst-case illumination is at summer solstice where the 23.5-degree misorientation is accompanied by aphelion where the intensity of sunlight is 0.9675 of average. However, the solar array temperature is also down, being 36.6°C rather than 46.5°C as at the spring and autumn equinoxes.

A plot of the yearly power availability variation is shown in Figure 6.1-20. Not included in this plot is the effect of occultations. No power is available when the system is occulted.

Table 6.1-5. Photovoltaic Reference Attitude Control

SP-1023

## ● ELECTRIC ION PROPULSION

THRUST PRODUCTION EQUIPMENT	23.3 MT	
POWER PROCESSORS	90.0 MT	
INSTALLATION HARDWARE	16.8 MT	
NON REOCCURRING TOTAL	130.1 MT	
ANNUAL PROPELLANT (ARGON)	48.0 MT/YEAR	▷
1-YEAR TOTAL	178.1 MT	

## ASSUMPTIONS:

OPTIMIZED  $I_{sp} \sim 20,000$  SEC

SINUSOIDAL DUTY CYCLE (50 MW PEAK, 32 MW AVG)

PERFECT CONTROL LAWS [20% CONTROL MARGIN]  
[NO WASTED PROPELLANT]CHEMICAL PROPULSION FOR CONTROL IN EQUINOCTAL OCCULTATIONS  
( $I_{sp} \sim 400$  SEC REQUIRES 1.0 TO 1.5 MT/YEAR PROPELLANT)

▷ ALL CHEM. PROPELLANT REQ'T WOULD BE 2100 MT/YEAR.

D180-22876-3

Table 6.1-6. Photovoltaic Satellite Instrumentation and Control

<u>Switchgear</u>		<u>Measure</u>	<u>Number of Components</u>
<u>Circuit Breakers</u>	(210)		<u>1,680</u>
Status		Open-Closed	
Current		Amps.	
Voltage		Volts	
Temperature		°C	
Overcurrent		On - Off	
Under voltage		On - Off	
Reverse Current		On - Off	
<u>Disconnects</u>	(210)		
Status		Open-Closed	
<u>Main Bus</u>			<u>4</u>
Current "A"		Amps	
Voltage "A"		Volts	
Current "B"		Amps	
Voltage "B"		Volts	
<u>DC-DC Converters</u>	( 14)		<u>70</u>
Voltage	(2)	Volts	
Current	(2)	Amps	
Temperature		°C	
<u>Rotary Joint</u>			<u>149</u>
Voltage Drop	(40)	Volts	
Current	(40)	Amps	
Position	(2)		
Drive Motor Current	(12)	Amps	
Drive Motor Voltage	(12)	Volts	
Brush Holder Position	(40)		
Temperature	(3)	°C	



Table 6.1-6. (Continued)

Power Sectors1152

Voltage	(192)	Volts	
Current	(192)	Amps	
Temperature	(768)	°C	1 Temp/Bay/Pwr. Sect.

Solar Cell StringsMay not  
be needed

Voltage	(18,112)	Volts
Current	(18,112)	Current

---



---

Total Sensors = 39,279

---



---

CONTROLS

<u>Circuit Breakers</u>	(210)	Open/Closed
-------------------------	-------	-------------

<u>Disconnects</u>	(210)	Open/Closed
--------------------	-------	-------------

Rotary Joint

Drive Motor Command	(12)	Command
Drive Motors	12	On/Off

Brush Holders

Command	(40)	Command
Operators	(40)	Open/Closed

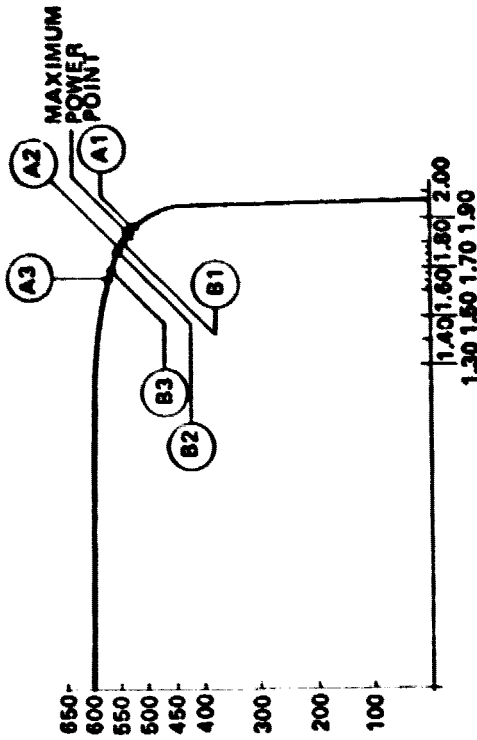


Figure 6.1-17 Autumnal Equinox

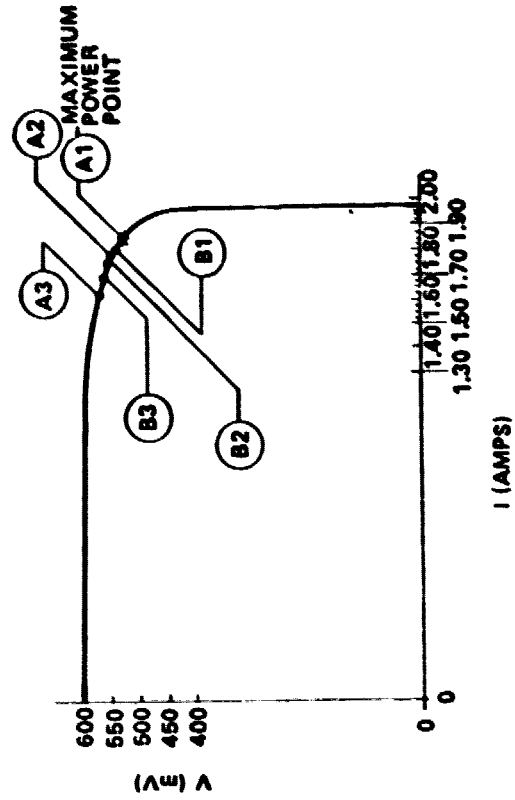


Figure 6.1-19 Spring Equinox

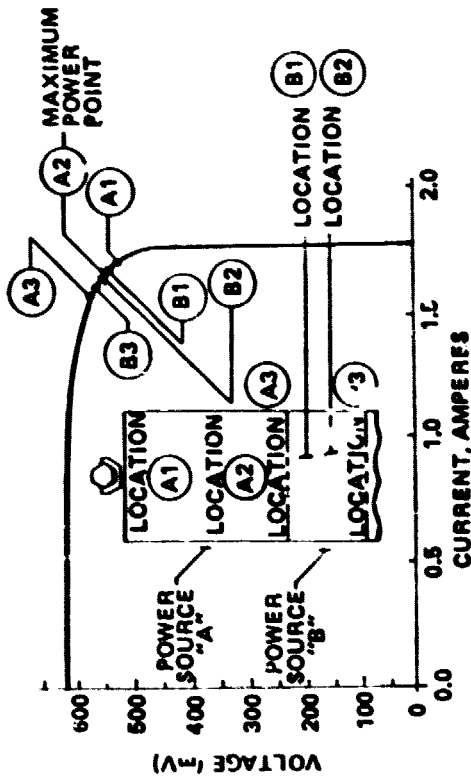


Figure 6.1-16 Summer Solstice

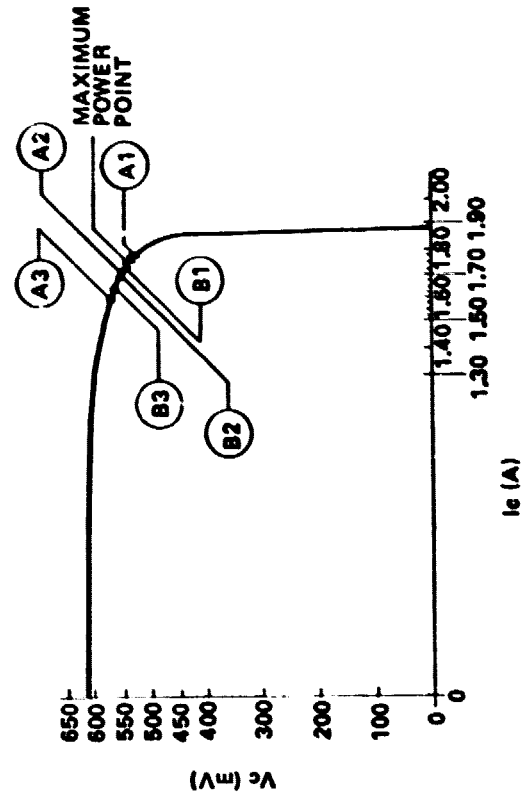


Figure 6.1-18 Winter Solstice

D180-22876-3

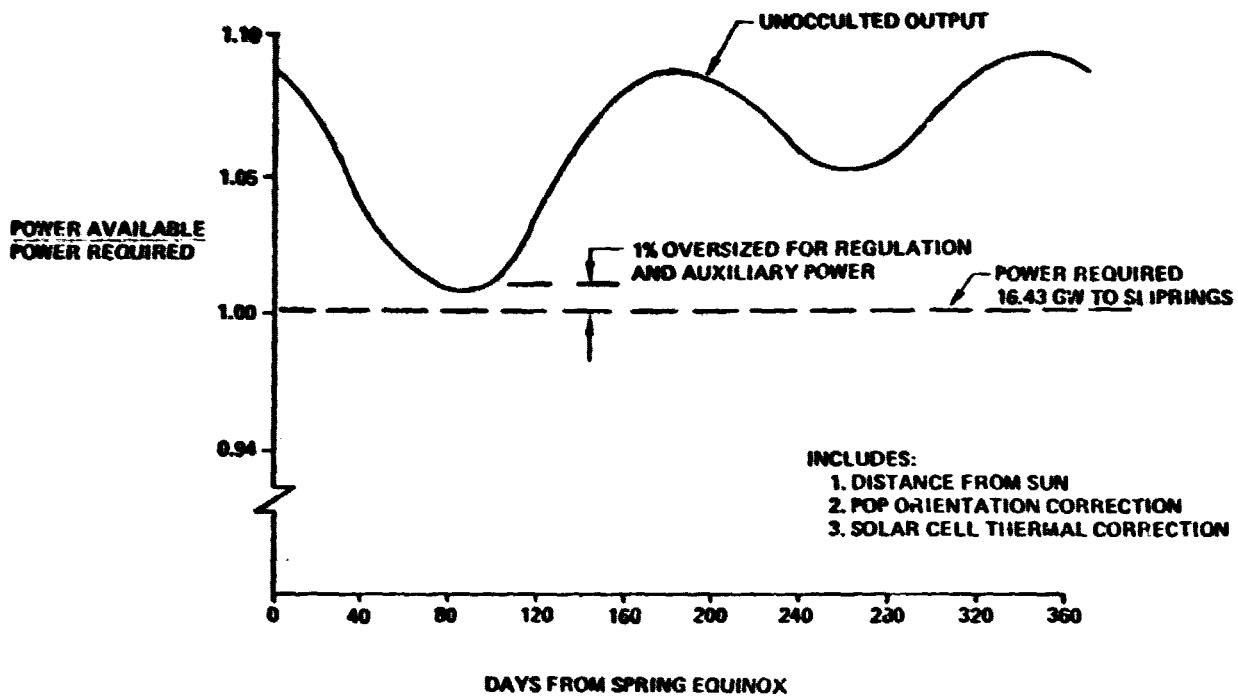


Figure 6.1-20. Annual Power Variation

## 6.1.2 Rankine Thermal Engine

### 6.1.2.1 Sizing

Sizing of an SPS must proceed iteratively; for example, the satellite must be sized to produce not only the transmitter power input but also parasitic loads such as power distribution losses. But power distribution losses are a function of the distribution path length which is a function of system size. Several iterations were involved in producing the power budget and physical size data which follows.

Per requirement 2 (see Section 2.0) the satellite power generation system must produce full power under "worst" conditions, corresponding to maximum parasitic power consumption at aphelion. The consequent power budget is as follows:

Element	Power, GW	
Transmitters	16.430	
Power Distribution Losses	0.898	
Potassium Pumping	0.282	
Attitude & Station Control	0.300	(Max)
<u>Miscellaneous</u>	<u>0.003</u>	
Bus Bar	17.913	

Since this power is to be produced by 570 (of the 576) generators, each generator must be capable of 31.426 MW output.

With a generator efficiency of 0.984, each turbine must have a shaft output of 31.937 MW (a total of 18.204 GW). The cycle efficiency is 0.189, hence the boilers must add

$$\frac{18.204 \text{ GW}}{0.189} = 96.317 \text{ GW}$$

of thermal power.

Several loss mechanisms are associated with the cavity absorber. One of these is reradiation from the boiler tubes and hot cavity interior walls. A "worst case" calculation of these losses is performed as follows: The cavity aperture is assumed to have an unobstructed view of space and black body characteristics, i.e., an emissivity of unity. The total aperture area is 59,828 M<sup>2</sup> (643,755 ft<sup>2</sup>). The *average* cavity internal temperature is estimated at 1260K (1808°F). Consequently, each square meter of aperture can radiate a maximum of 143 kW. The maximum total aperture reradiation is consequently 8.836 GW thermal. Note that this is 9.2% of the useful power to be added in the boilers.

Reflection losses from the cavity walls must also be considered; i.e., energy which enters the cavity and is reflected out again, after one or more passes, without being absorbed. Tests currently being conducted on subscale ("bench model") cavity absorbers for ground solar thermal engine systems (Power Tower) indicate reflection losses can be held to approximately 5%.

The insulation of the cavity walls limits heat transfer. A low emissivity external coating should also be used; approximately 0.04 should be easily obtained. Using characteristics for molybdenum Multifoil (a product of the Thermo Electron Corporation, Waltham, Mass.) a total wall loss of 500 MW was estimated. The exterior wall temperature will be about 905K (1169°F). A lower wall temperature could be produced by the use of more insulation. The resultant mass increase would not offset the solar concentrator mass reduction (less solar concentrator is required when cavity losses reduce).

A one percent allowance is made for additional losses (such as from the walls of the manifolds which connect the boilers to the turbines). A summary of the cavity thermal energy balance is as follows:

Element	Power, GW
Useful Power to Turbines	96.317
Reradiation	8.836
Reflection (5%)	5.620
Wall Losses	0.500
<u>Miscellaneous</u>	<u>1.124</u>
Total	112.397

The "cavity efficiency" can be considered to be:

$$\frac{96.317 \text{ GW}}{112.397 \text{ GW}} = 85.7\%$$

The compound parabolic concentrator (CPC) at the cavity aperture acts a "light channel" to increase the effective aperture opening. Figure 6.1-21 gives the general configuration.

Since the geometric concentration ratio is low:

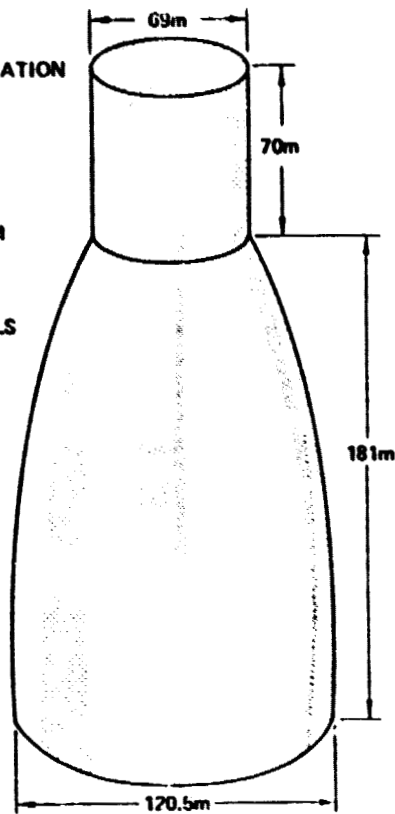
$$\frac{\text{CPC Entrance Area}}{\text{Cavity Absorber Area}} = 3.05.$$

many of the rays from the concentrator are not reflected by the CPC, they directly enter the cavity absorber. A ray trace program, developed under IR&D, indicates that 66% of the rays will have an average of one reflection, 34% directly enter the aperture. A plating of rhenium on the molybdenum foil walls is expected to yield a reflectivity of 0.8. The net CPC reflectivity should be approximately 0.865. Per Section 4.2, the facet end-of-life reflectivity is baselined at 0.878. An additional allowance of 5 percent is made for facet scallops, spacing, wrinkling, etc. For an aphelion solar flux of 1.309 kW/M<sup>2</sup>, the required reflector projected area is 119.06 km<sup>2</sup>. After allowance for shadowing by the cavity absorbers, etc., a total projected area of 119.56 km<sup>2</sup> is selected for the reference design. This is 7.473 km<sup>2</sup> for each of the 16 modules.

D180-22876-3

SPS-1610

- CPC GEOMETRIC CONCENTRATION RATIO IS 3.05
- CPC LIGHT ACCEPTANCE ANGLE =  $30^\circ$ .
- CAVITY WALLS ARE 5 LAYERS OF MOLYBDENUM MULTIFOIL.
- ALL BOILER TUBES MOUNT ON CAVITY INTERIOR WALLS
- CPC WALLS ARE MOLYBDENUM FOIL WITH RHENIUM INTERIOR COATING.



- CPC ACCEPTS : LARGER IMAGE FROM FACETS:
  - ALLOWS FEWER, LARGER FACETS
  - ACCEPTS POINTING ERRORS & DISTORTIONS.

Figure 6.1-21. Cavity Absorber and Compound Parabolic Concentrator

### 6.1.2.2 Overall Configuration

Figure 6.1-22 gives plan and side views of the Rankine SPS. It will be noted that the two transmitters are mounted a considerable distance from the "corner" power modules. This is to allow an unobstructed field of view from the transmitters to the ground receivers. The "southern" antenna requires the greatest clearance ( $31^{\circ}$ ) if it is to "see" a rectenna at  $50^{\circ}$  North latitude. This clearance angle is, of course, due to the perpendicular-to-ecliptic plane (PEP) orientation. The photovoltaic SPS, flying perpendicular-to-orbit plane (POP) does not require as much angular clearance.

The sixteen modules are arranged in a "4 X 4" pattern. They are connected at their corners and, at the cavity absorber level, by "20 meter" beams. These beams provide, in addition to structural integrity, supports for the aluminum bus bars of the power distribution system. Note that the radiators of the modules are arranged such that they are "edge-on" to the apparent meteoroid stream resulting from the orbital motion of the Earth. Consequently, the radiators are parallel.

In the side view, it will be evident that the transmitters are located at an elevation intermediate to those of the solar concentrator and the cavity absorber. The position shown corresponds to the level of the overall center of gravity. This was done to minimize the effects of the once-a-day transmitter rotation on the attitude control system.

The P.E.P. orientation requires that each antenna mount have two rotational axes, diurnal and seasonal. The diurnal axes are kept parallel to the rotational axis of the Earth by rotation of the "dogleg" structure about the seasonal axes.

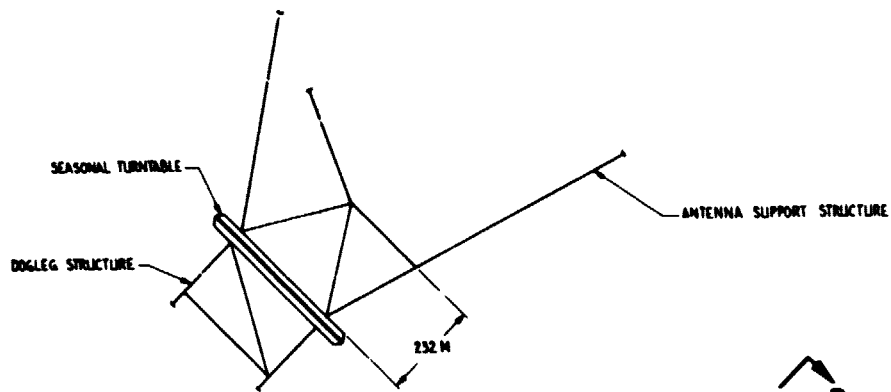
### 6.1.2.3 Power Generator Module

Figure 6.1-23 gives details of one of the power generation modules. The basic form of the solar concentrator dish is an element of a sphere of radius 6740 m (22,100 ft). The concentrator frame supports the facets, which are adjusted at installation to produce a common focal point at the entrance to the compound parabolic concentrator (CPC).

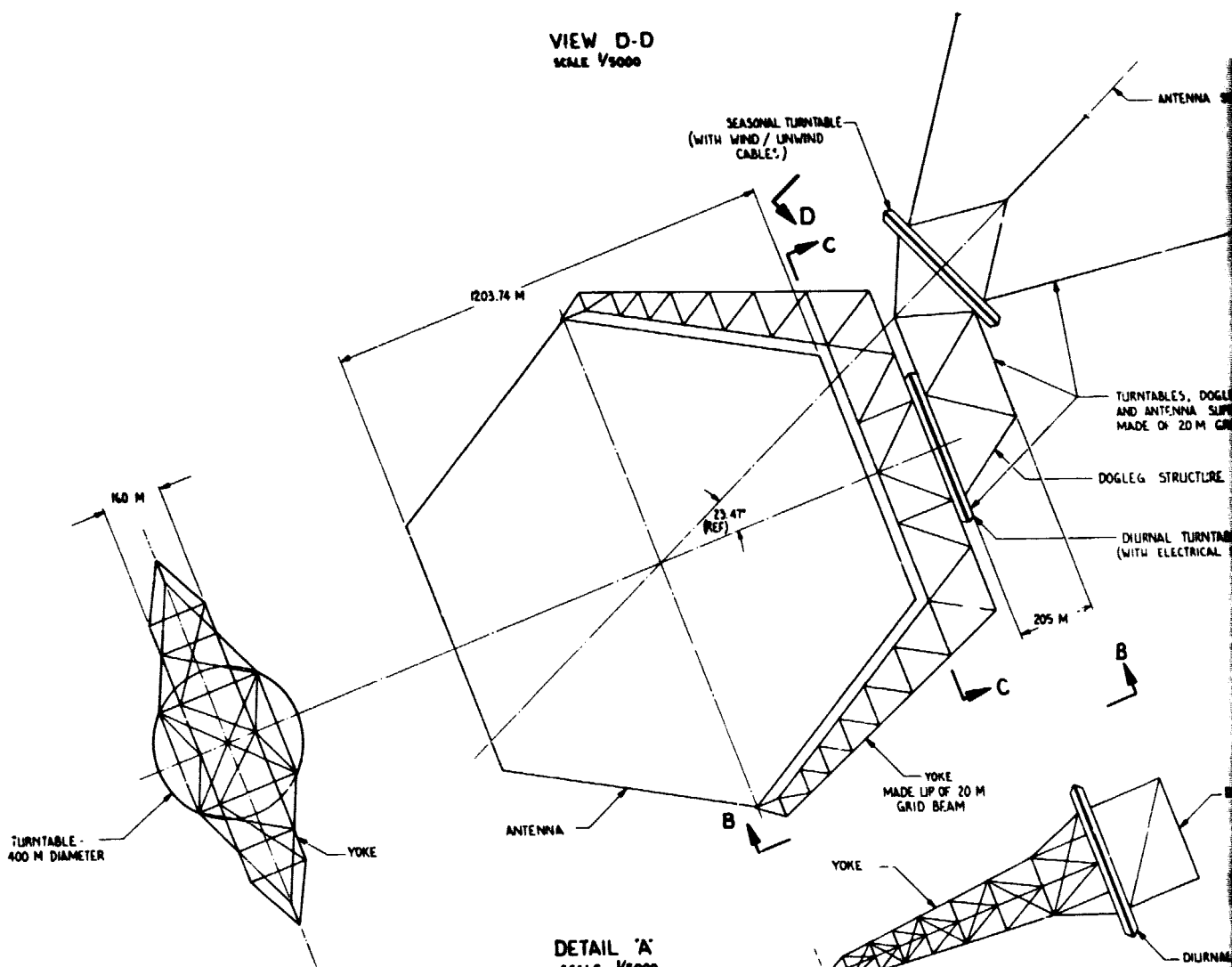
The focal point assembly is held in proper position by four "cavity support arms" (20M beams). The focal point assembly consists of the cavity absorber, CPC turbogenerators, radiators, and a steel tube support frame.

The "small" radiator system for the generators is located above the cavity absorber and between the two uprights which mount the turbogenerator pallets. See Figure 6.1-24. A power generation module as shown here is the basic "self-power transport" element for the low Earth orbit (LEO) assembly option. Figure 6.1-24 shows the locations for attachment of the three electric propulsion systems.

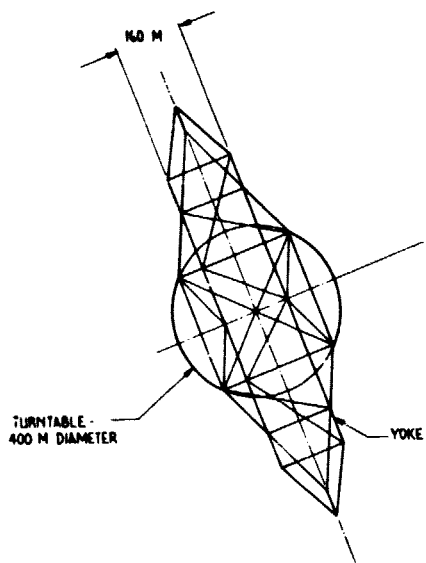
# BOLDOVE FRAME



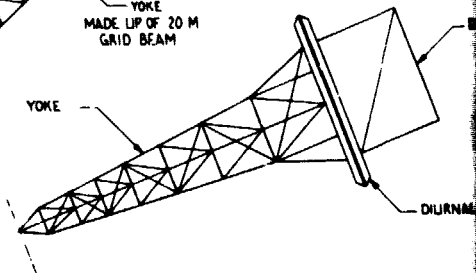
VIEW D-D  
SCALE 1/5000



DETAIL 'A'  
SCALE 1/5000



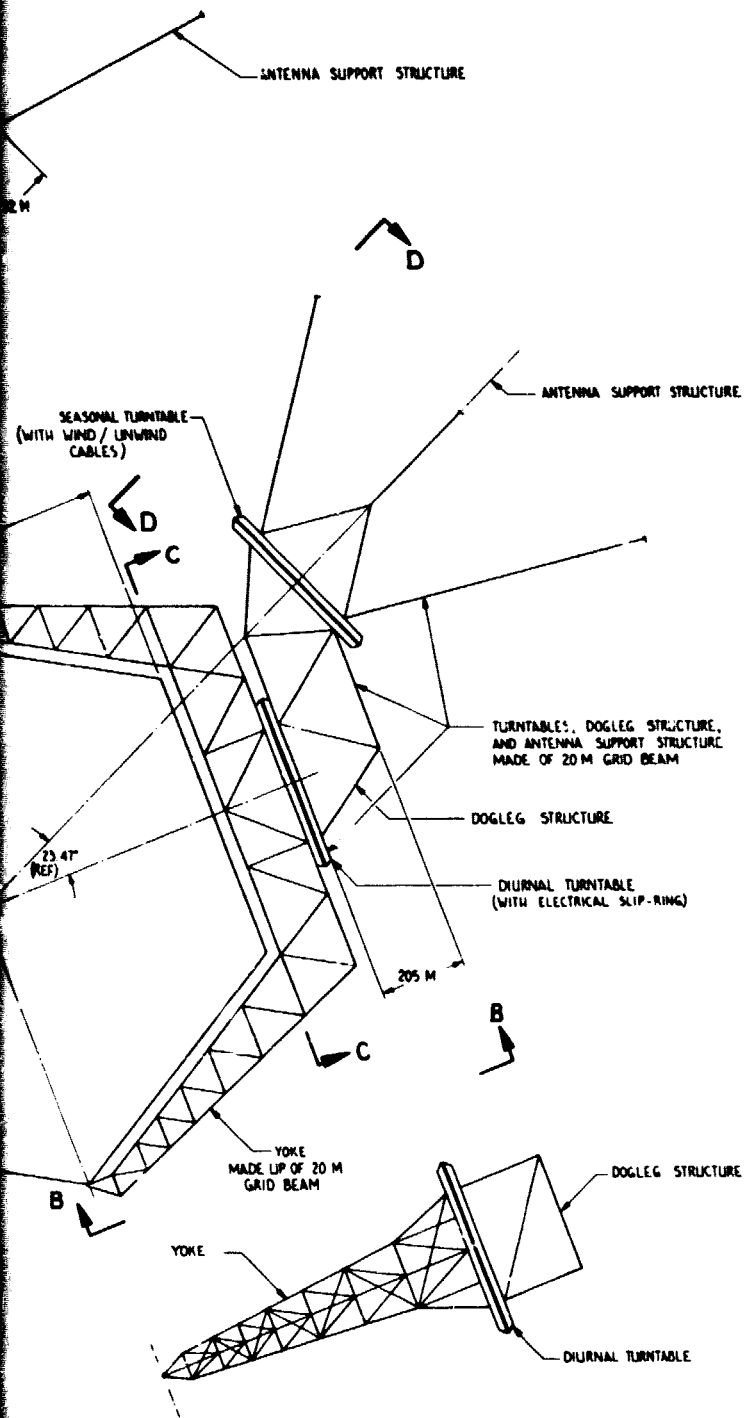
SECT C-C  
SCALE 1/5000



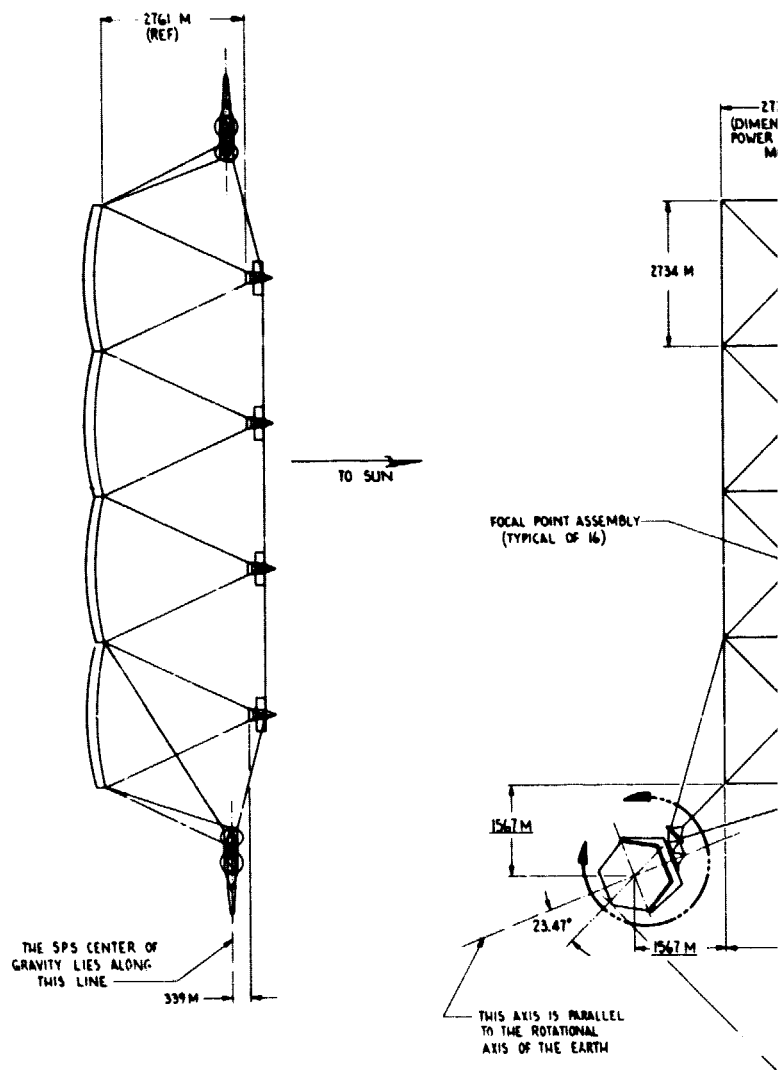
VIEW B-B  
SCALE 1/5000



# FOLDOUT FRAME



VIEW B-B  
SCALE 1/5000



OUT FRAME

FOLDOUT FRAME 3

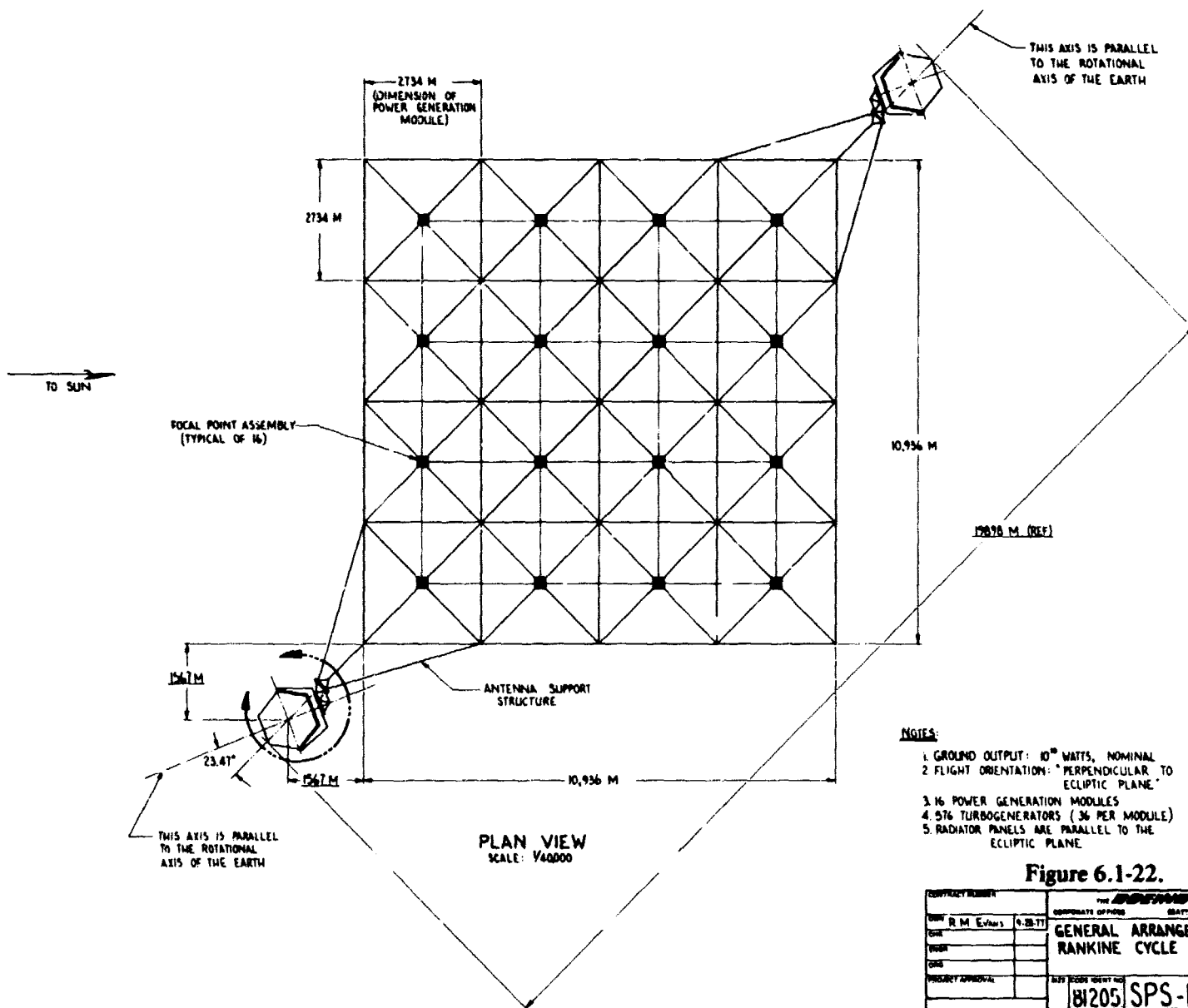


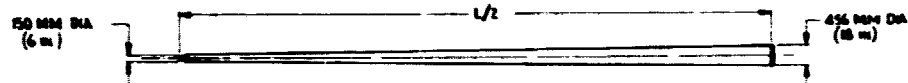
Figure 6.1-22.

CONTRACT NUMBER		THE <b>BOEING</b> COMPANY SEATTLE, WASHINGTON 98108	
DATE	R. M. Evans	9-28-77	
TO	GENERAL ARRANGEMENT - RANKINE CYCLE SPS		
FROM			
ORG			
PROJECT APPROVAL	SPS-LO-57	181205	
SCALE	1/40000	BY	OF

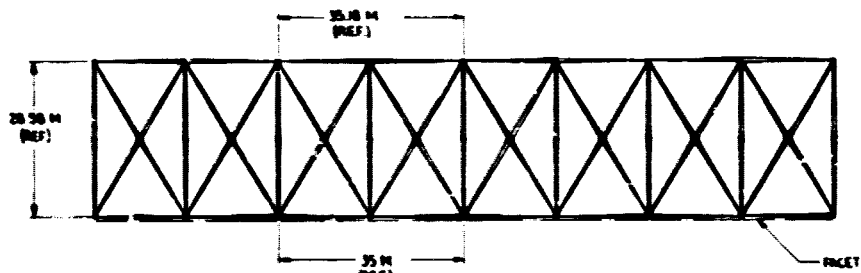
# FOLDOUT FRAME /



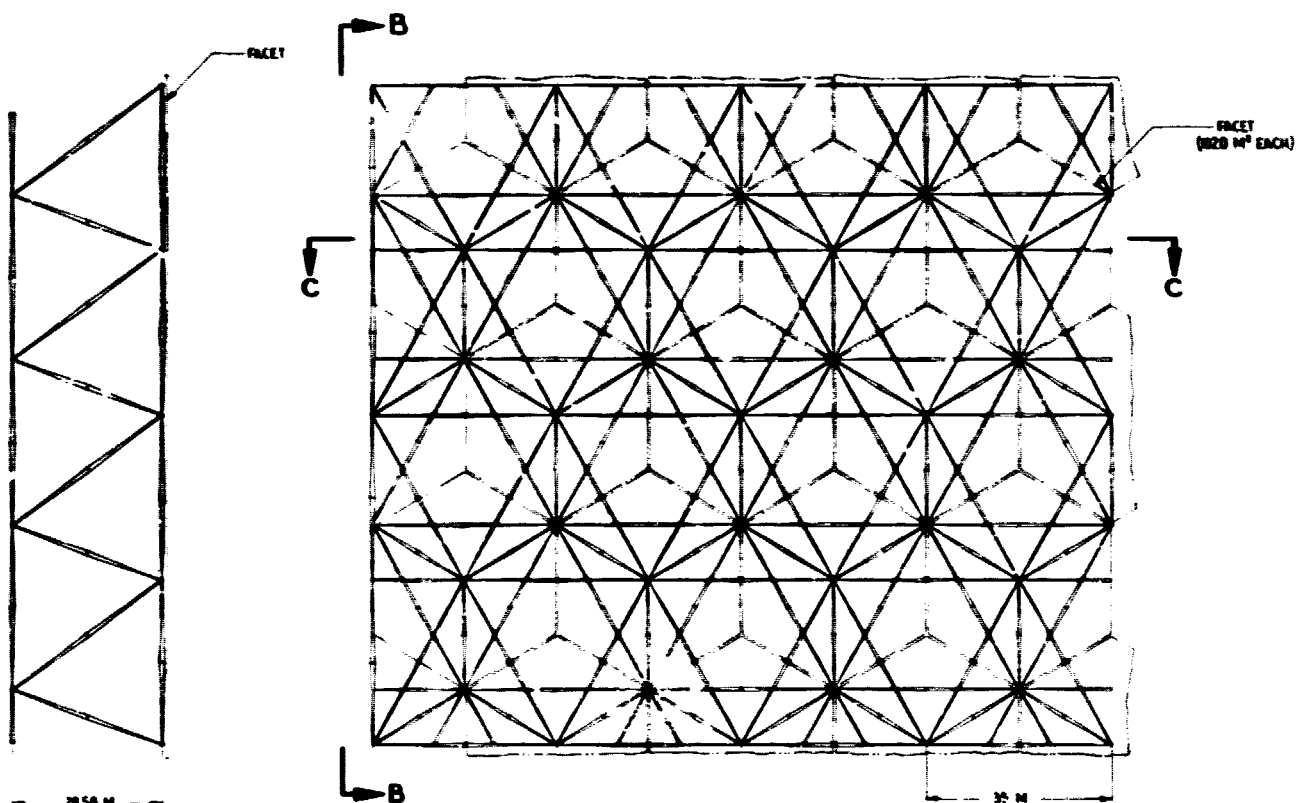
**GRID STRUT**  
20 mm (.008 in) WALL THICKNESS  
SCALE: 1/50



**END BEAM STRUT**  
25 mm (.010 in) WALL THICKNESS  
SCALE: 1/50

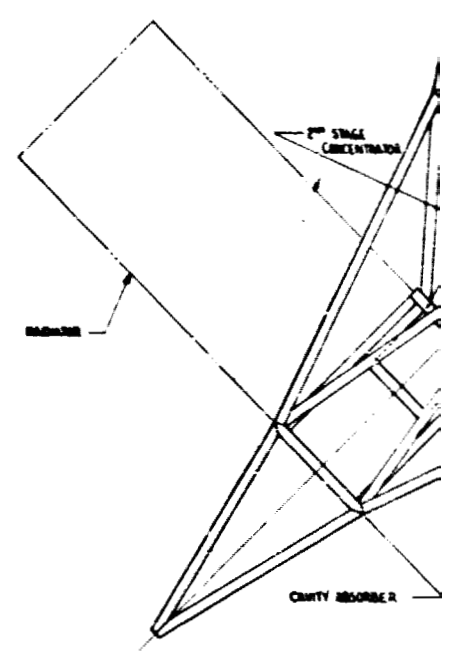
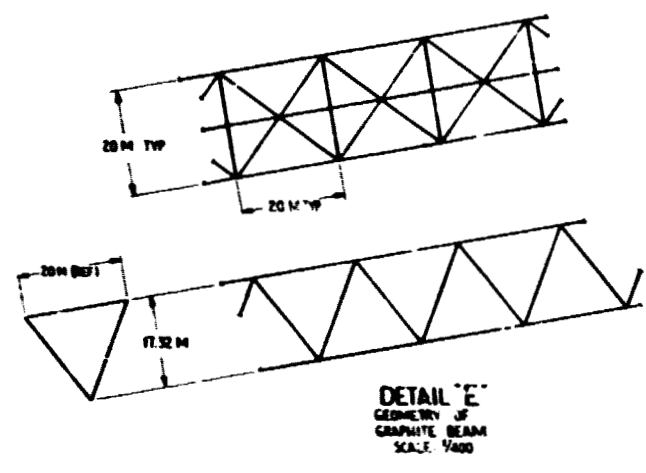
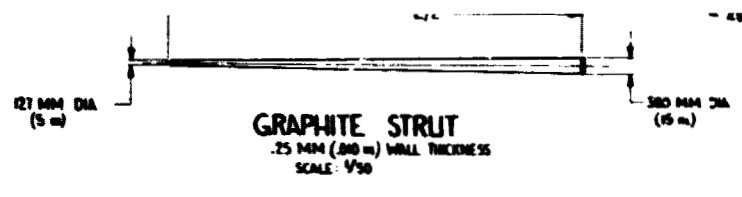
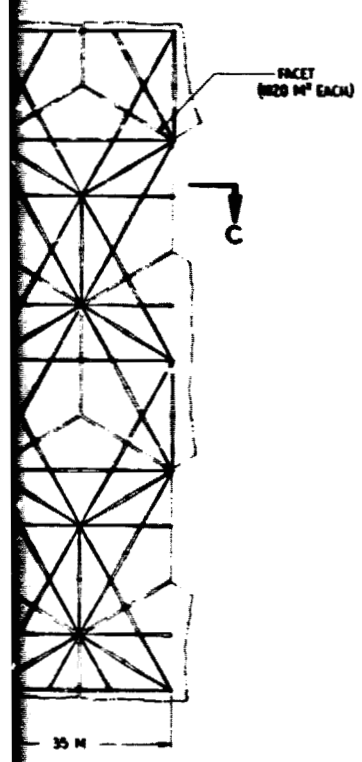
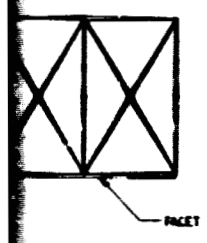
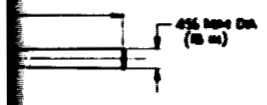


**SECTION C-C**  
SCALE: 1/400

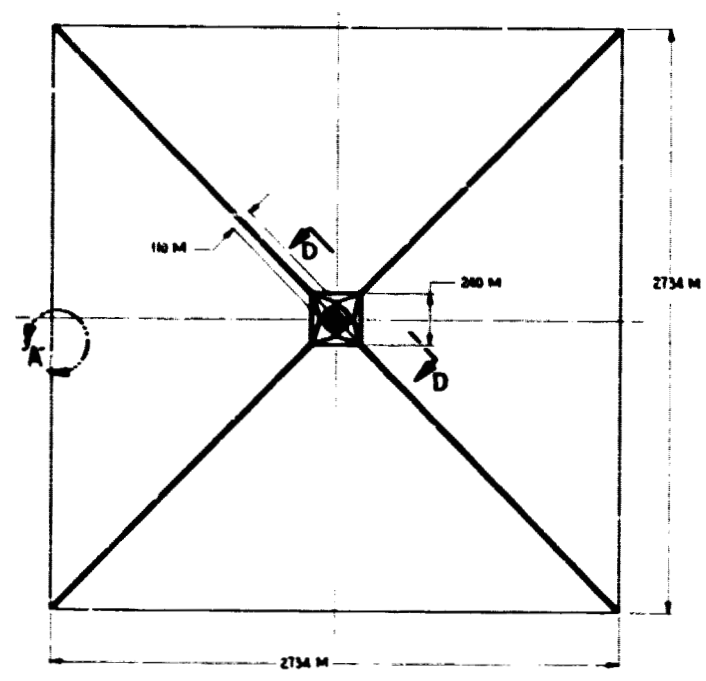


**VIEW B-B**  
END BEAM  
SCALE: 1/400

**DETAIL 'A'**  
FLAT DEVELOPMENT  
SCALE: 1/400



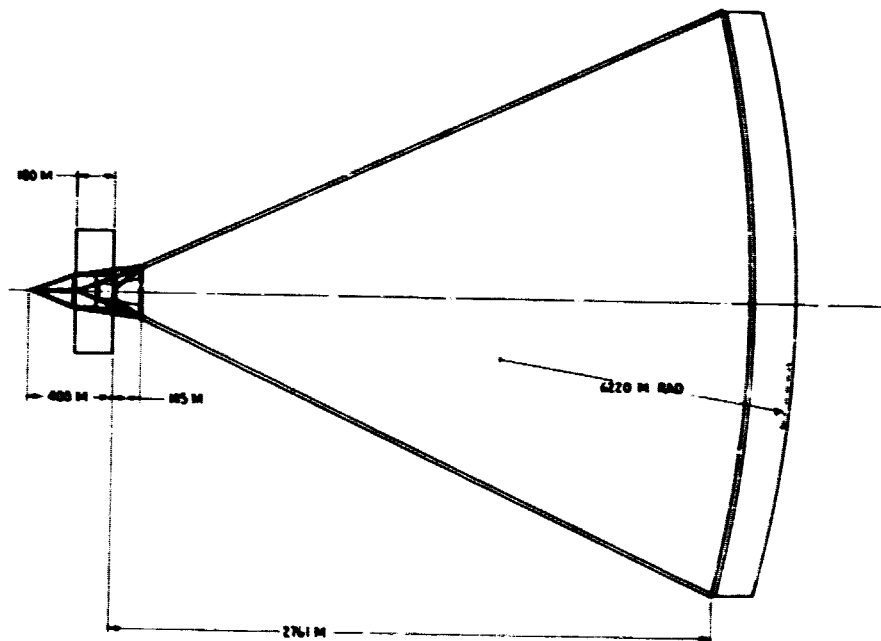
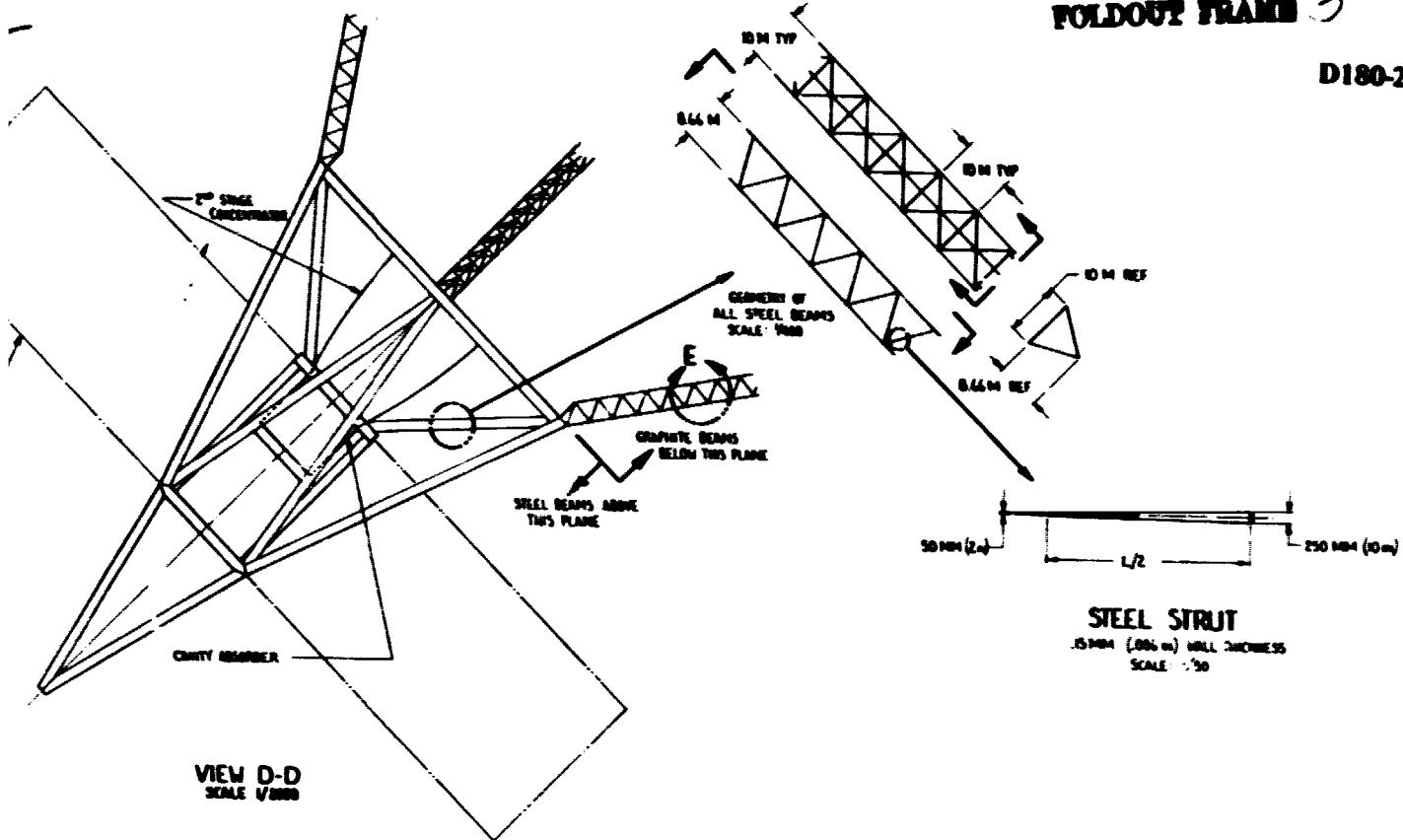
VIEW D-D  
SCALE: 1/2000



PLAN VIEW  
SCALE: 1/10000

# FOLDOUT FRAME

D180-22876-3



PROFILE  
SCALE: 1/1000

Figure 6.1-23.

DESIGNATION		REVISION	
DATE	BY	DATE	BY
10/10/77	R. M. E. (see 10.5.11)		
GENERAL ARRANGEMENT - RANKINE MODULE, SOLAR POWER SATELLITE			
PROJECT NUMBER		81205/SPS-L0-58	
SCALE		1/1000	

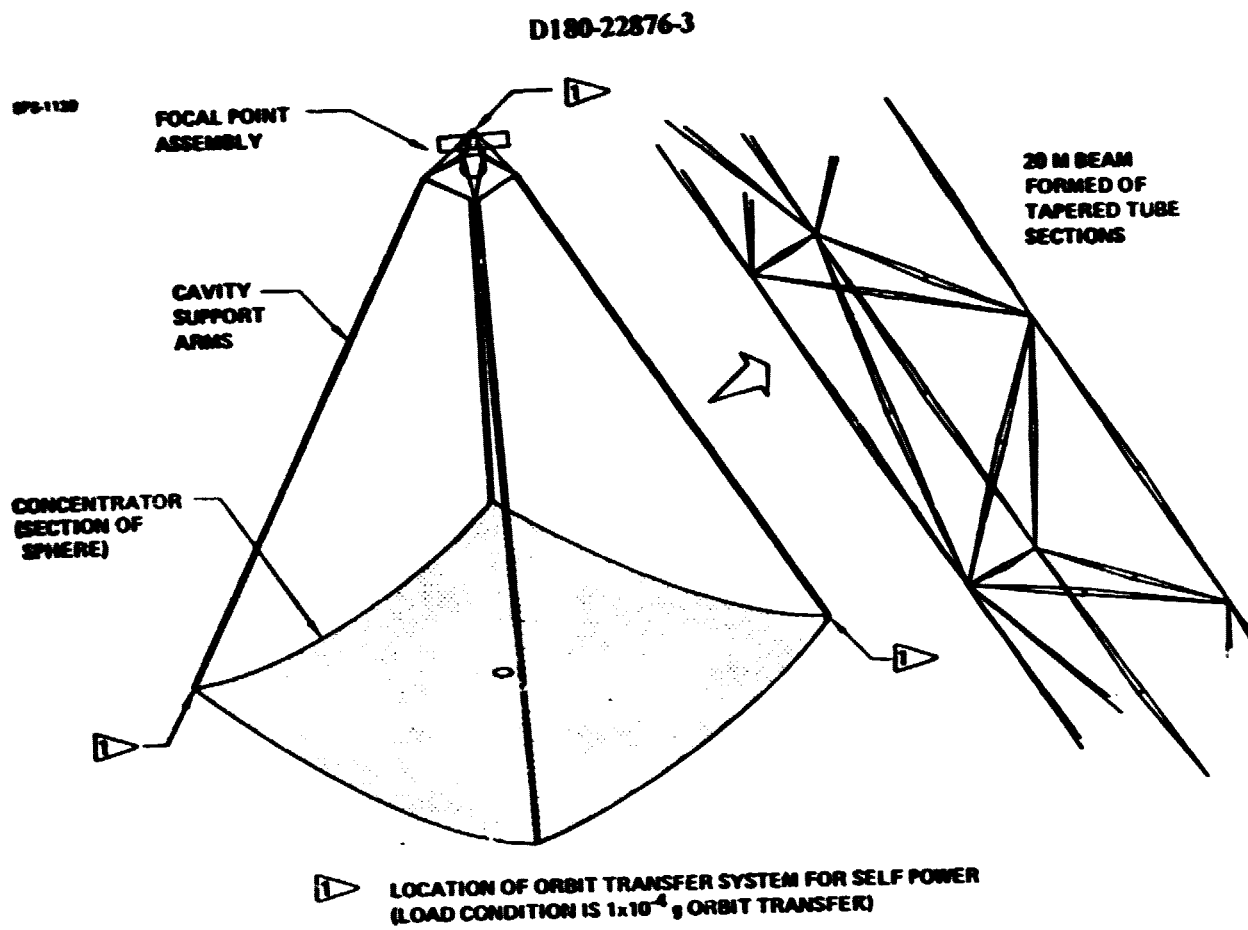


**Figure 6.1-24. Modules Consist of Concentrator & Focal Point Assemblies**

The curved concentrator surface which supports the reflector facets is formed of tapered graphite epoxy tubes which are joined by "sockets." The "lower" members of this structure are longer than the corresponding members in the "upper" (facet side) surface; this produces the required curve.

Figure 6.1-25 is a photograph of a toothpick model of a portion of the facet support structure. This facet support structure forms the concentrator assembly and is covered by reflector facets. The support structure is made up of tapered graphite epoxy tubes joined at socket assemblies. The reflector facets are mounted on the upper level of the support structure. This structure, while extremely rigid, is also relatively heavy. The total mass of concentrator support structures for the thermal engine SPS is approximately 6,000 metric tons. Considerable assembly effort is also required in low orbit. A structure of lower mass and with a lower assembly time would be desirable.

An alternative configuration for facet support might consist of one, or 1.5, meter beams assembled by beam machines and arrayed across a framework of larger members such as twenty meter beams. The mass of this system would be approximately the same, however, construction time might be reduced. In Figure 6.1-26 is shown how a main frame formed of 20 meter beams would be used to support a grid of 1.0 to 1.5 meter beams formed by automatic "beam machines." The reflector facet mounts would be located on these smaller beams. This approach would require a lower investment in assembly machines than the approach shown on the previous chart; a mass comparison has not been made.

Tapered tubes are also used to form the structure of the focal point assembly. However, due to the temperature environment (the radiators run at 928K = 1210°F), type 316 steel is baselined rather than the graphite-epoxy used elsewhere.

#### 6.1.2.4 Reflector Facets

Figure 6.1-27 shows a reflector facet. The reflector facets are hexagons of thin aluminized Kapton. The Kapton is 3 micrometers thick (0.00012"). It is tensioned by 3 rigid end members, pulled outward, by bridles. This tensioning system causes the three edge members to be coplanar, so that a flat reflector is produced. The rocker arm and spring canister systems which pull outward on the bridle are mounted to the concentrator frame. A "scallop" at the three free edges of the facet controls wrinkling at the facet edges.

The three bridles of the reflector facet are attached to the rocker arms, which mount to the mid-point of the concentrator tube structural elements. The springs, contained in canisters, provide the pull that causes the rocker arms to tension the plastic film. Note then that the facet is mounted directly to the concentrator support structure and does not include radial arms and a hub system as shown in Part I of this study.

D180-22876-3

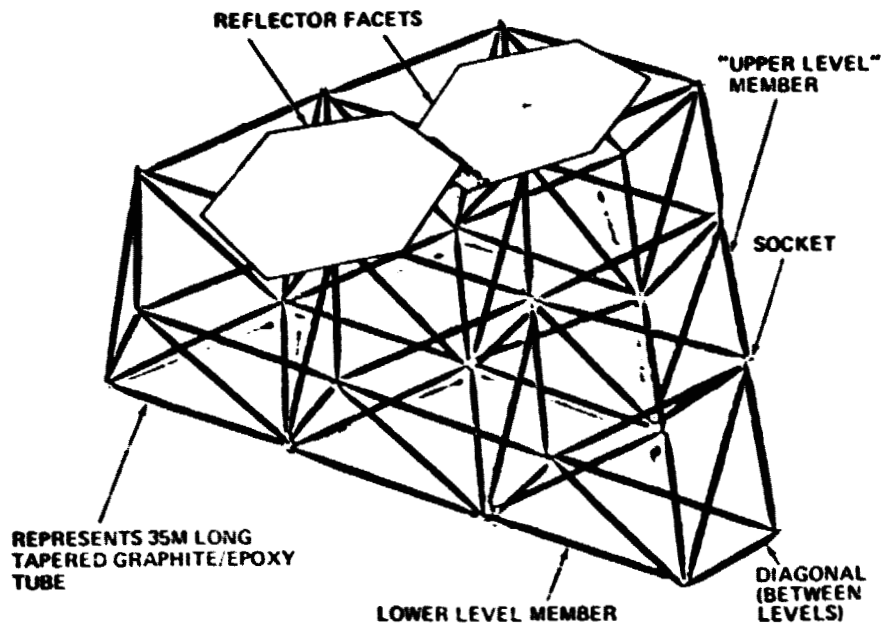


Figure 6.1-25. Facet Support Structure

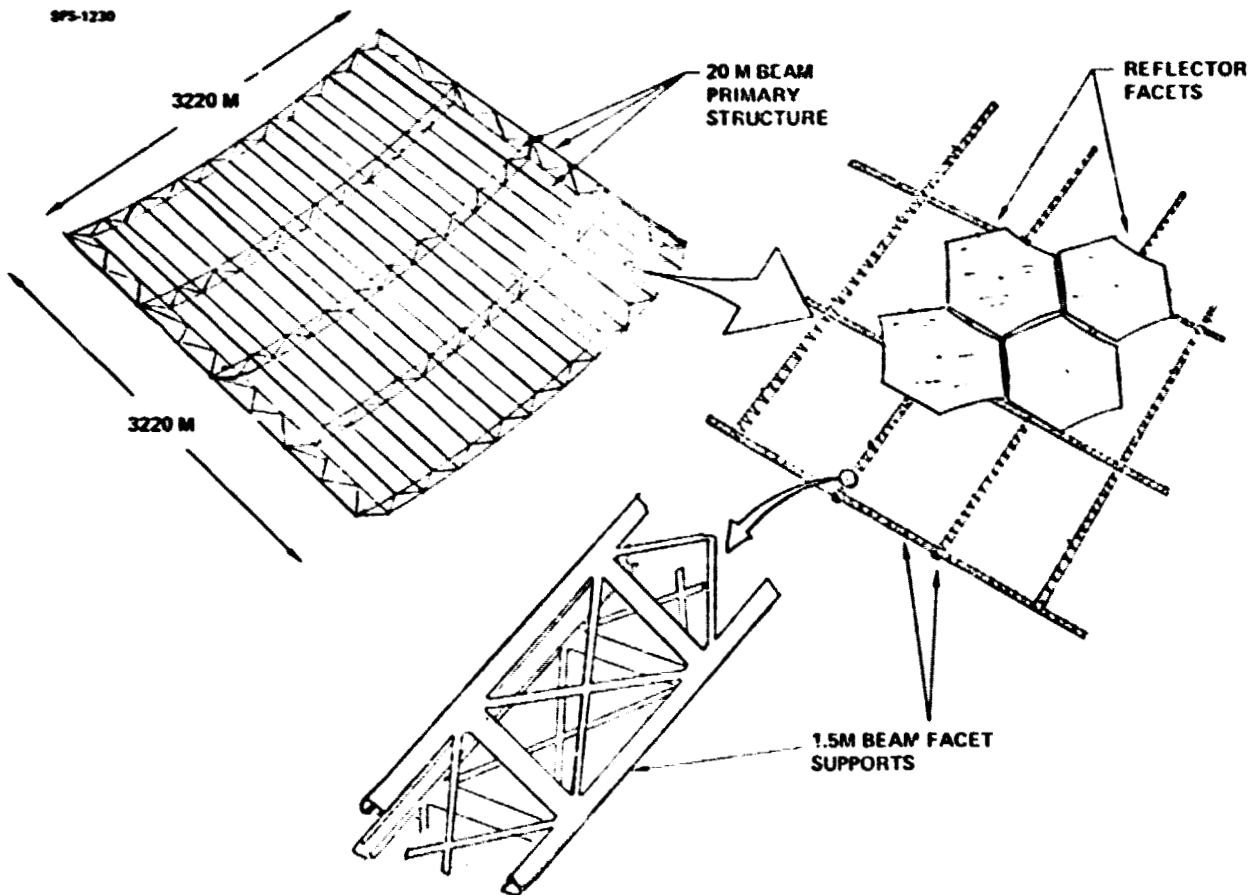


Figure 6.1-26. Alternate Structure Approach



Di80-22876-3

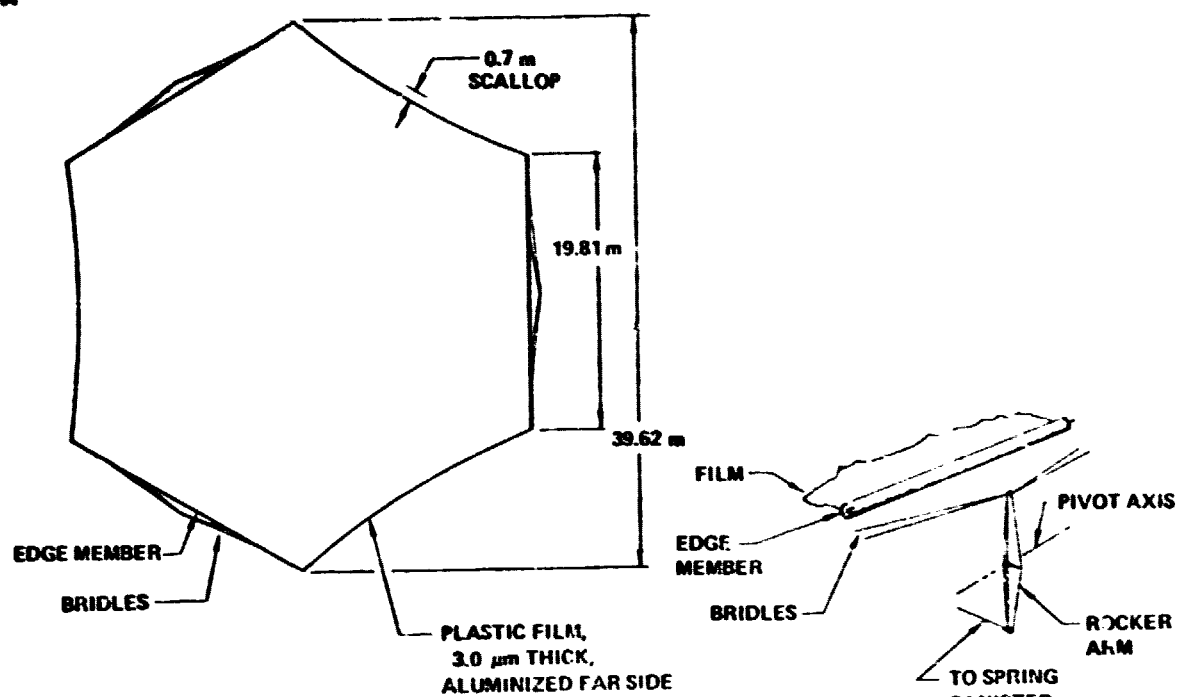


Figure 6.1-27. Reflector Facet

#### 6.1.2.5 Thermal Energy Control

Figure 6.1-28 shows the CPC aperture door assembly. This door assembly is composed of molybdenum foil panels mounted on cables driven by pulley assemblies attached to the cavity support arm frame. The doors are shown in the open position. The rhenium reflective coating on the doors is used to maintain a low temperature for the door panels when they are fully closed and exposed to the full output of the solar concentrator assembly.

#### 6.1.2.6 Turbogenerator Pallets

Figure 6.1-29 shows a turbogenerator "pallet." These pallets are launched preassembled and are consequently stressed for high ( $\approx 5g$ ) acceleration. The generator is directly driven by the double ended turbine; the steel tube framework maintains alignment between these elements. The electromagnetic pumps and their associated heat pipe radiator are also mounted on the pallet.

The intent is that these pallets be as self-contained as possible. However, five major duct attachments are required. The two outlet connections to the radiator are 1.6M (5.25 ft) in diameter; the other three ducts are: turbine inlet, 0.55M (1.80 ft); boiler inlet, 0.145M (0.48 ft); and pump inlet 0.55M (1.80 ft). There will be several electrical control systems which must be connected at the time of pallet installation.

#### 6.1.2.7 Turbines

Figure 6.1-30 is a section through the turbine reference design, as produced by General Electric. Potassium vapor from the boiler at 1242K (1776°F) is admitted at the center and flows outward through the two five stage turbine assemblies. The expanded, and consequently cooler (932K = 1218°F), vapor from the last turbine stages is collected in output plena at the two extremes of the assembly. Although multiple inlets and double outlets are shown, it would probably be best to go to a single inlet and a single outlet at each end. To feed the multiple inlets shown could require a toroidal distribution manifold which fits around the center of the turbine. This manifold would accept the boiler flow and distribute to the multiple inlets shown. A lighter solution would probably be to merely enlarge the current inlet system and provide a single inlet.

Bearings support the turbine shafts at each end. One end is the drive output to the generator; the other end is closed. In the alkali metal space power testing of the 1960's, hydrodynamically lubricated pivot pad bearings were developed and tested under load at temperatures in the 700-811K (800-1000°F) range in liquid potassium for hundreds of hours. The stability of hydrodynamic bearings and shaft assemblies were also evaluated in "easy" fluids as a means of developing bearing stability prediction criteria. The technology of alkali metal bearings also included extensive work on the characterization of potential alkali metal bearing materials such as refractory alloys and metal-bonded carbides, particularly in friction and wear characteristics under vacuum and liquid potassium.

D180-22876-3

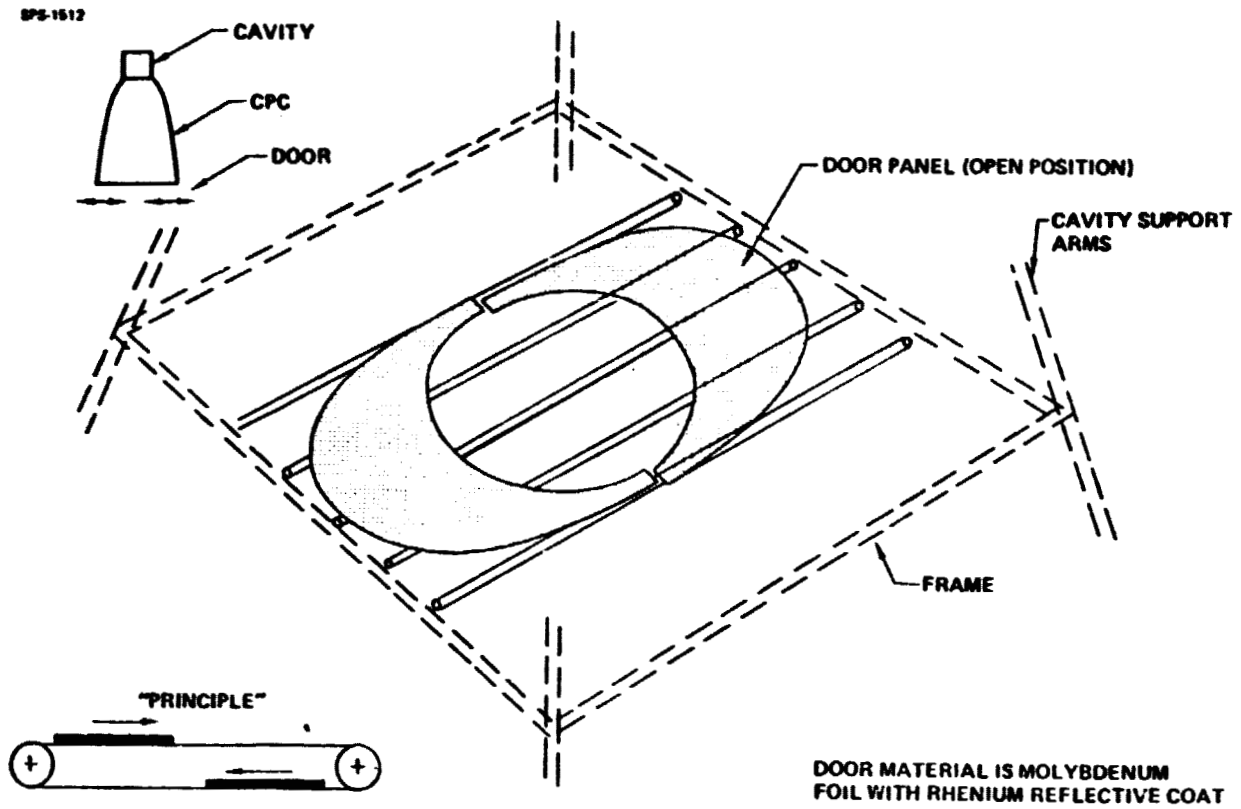


Figure 6.1-28. CPC Aperture Door Assembly

SPS-1636

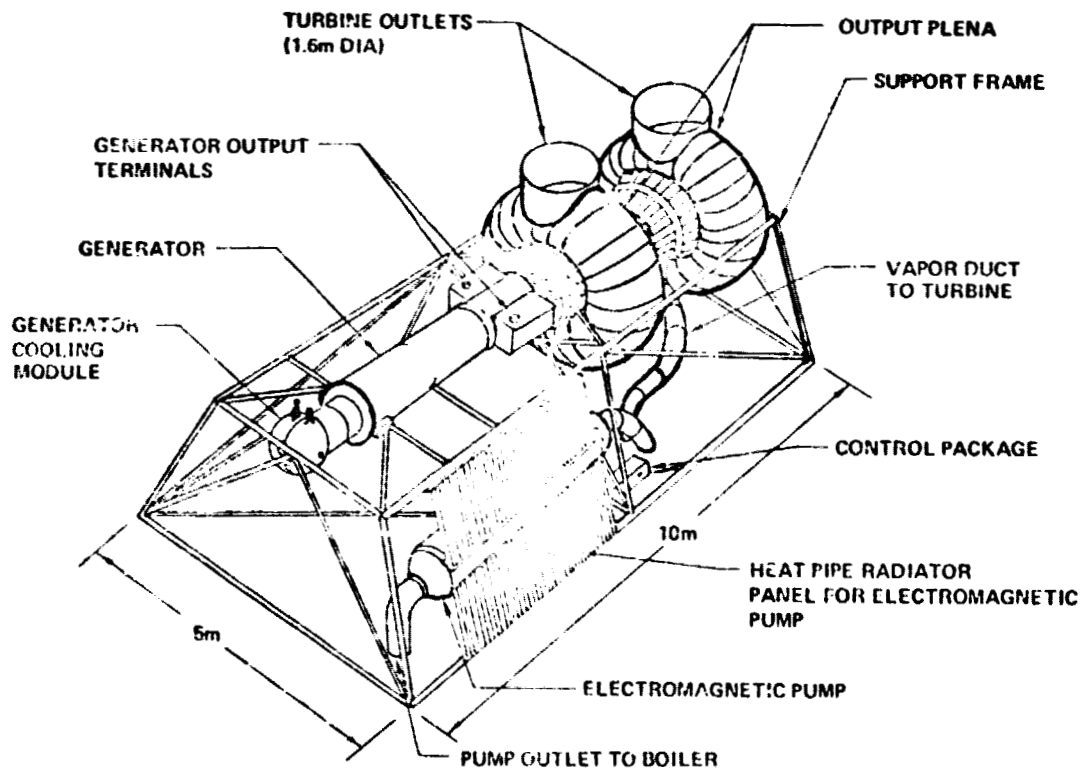
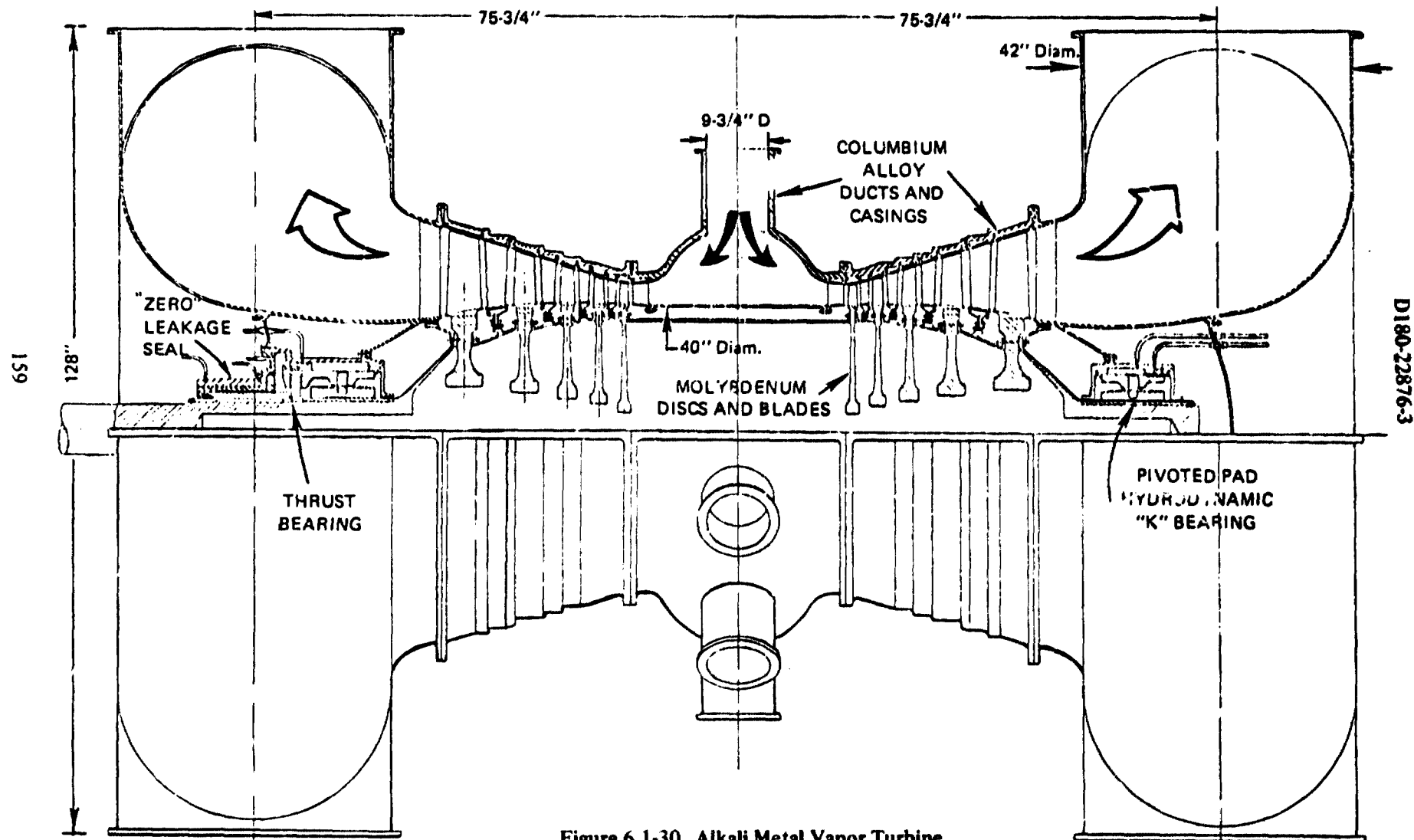


Figure 6.1-29. Turbogenerator Pallet



D180-22876-3

Figure 6.1-30. Alkali Metal Vapor Turbine

### **D180-22876-3**

Testing of alkali metal rotating seals was also undertaken in the test facility.

The pressure feed lines for the potassium bearings are shown at each end of the assembly.

Not shown is any moisture extraction system. Droplets forming in the third stage region are a potential source of erosion damage to the last two stages.

No droplet impact erosion was observed on molybdenum alloy or on nickel base superalloy blades in 5000 hours operation of a two stage turbine at a temperature of 1240°F and a moisture content at the turbine exit of 8%.

Very negligible impact erosion was observed on molybdenum alloy blades in the last stage of a three stage turbine tested for 5000 hours at about 1200°F and 7-9% moisture content. From these tests it was estimated that turbine blades would perform satisfactorily for at least 50,000 hours.

Erosion tests under more severe wetness conditions were performed in the 5000 hour three stage potassium turbine test. TZM molybdenum alloy inserts were located in a position behind the third stage turbine blade tips where moisture content in the vapor stream was about 13% and a high concentration of droplets was shed from the blade tips. Highly localized droplet impact damage pointed to the advantage of using trailing edge turbine blade moisture extraction methods to remove liquid which would otherwise collect at the outer diameter flow surfaces.

Figure 6.1-31 shows impact damage examples.

Following 10,000 hours of endurance testing in the two stage and three stage potassium turbines, the three-stage turbine and the turbine facility were modified to incorporate moisture extraction devices for brief performance tests. These devices included (1) extraction of liquid condensate (and some vapor) from the trailing edges of stator vanes, (2) centrifugal extraction of liquid from the trailing edges of turbine blade tip shrouds and (3) vortex separation of liquid from the vapor downstream of the third turbine stage. The latter liquid separation device was planned to be used as an interstage moisture extraction device located external to the potassium turbine in a 450 KW<sub>e</sub> potassium turboalternator which received extensive preliminary design effort for space power applications.

Figure 4.5-4 showed the three extraction approaches.

The rotor extraction device generally exceeded 30% effectiveness and the vortex separator achieved 80% effectiveness.

The demonstration of these extraction techniques indicates the availability of methods for removing damaging quantities of liquid from potassium vapor turbines and aiding in the minimization of droplet impact damage and liquid washing corrosion effects.



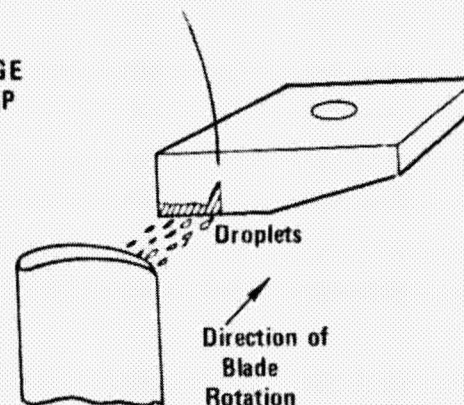
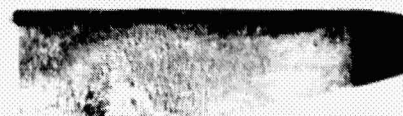
IMPACT  
EROSION  
EVIDENCE  
REQUIRES  
BINOCULAR  
INSPECTION



TEST CONDITIONS:  
5000 HOURS  
~1200°F  
838 fps TIPSPEED  
7-9% MOISTURE

TZM THIRD STAGE  
POTASSIUM TURBINE BLADE

WORM HOLING  
IMPACT DAMAGE  
0.015 INCH DEEP



STAGE 3 ROTOR BLADE

TEST CONDITIONS:  
5000 HOURS  
~1140°F  
838 fps TIPSPEED  
~13% MOISTURE

TZM EROSION INSERT  
BEHIND THIRD STAGE BLADE

D180-22876-3

Figure 6.1-31. Droplet Impact Damage

### **D180-22876-3**

Calculations were initially made for the "A" 1242K/994K (1776/1329°F) and "C" 1242K/870K (1776/1106°F) cycles and for their turbine weights. Costs were estimated from previous turbine designs which had 1.52M (60") discs for the HP turbine and 2.03M (80") discs for the LP rotor. The "A" cycle was selected because the weights and costs were much lower and because the LP turbine was eliminated. However, it was decided to size these turbines for 40" discs in order to retain a practical size for molybdenum disc production. A preliminary potassium flow estimate of 202 lb/sec was estimated for one double flow turbine with these 40" discs.

Before the turbine design calculations and flow areas were completed, it was determined that to use the "B" cycle 1242K/932K (1776/1218°F) was more optimum for the entire power system. A cycle calculation gave the flow required for the 1166 MWe "B" cycle. That cycle required 34 turbines at a flow rate of 91.63 kg/sec (202 lb/sec) each.

Reduction of the power requirement per solar heat source from the 1166 MWe system to the 1078 MWe interim system would logically reduce the number of turbines to 32 if the flow per turbine was unchanged. However, the turbine design calculations indicate that the last stage will limit the flow rate due to a large annulus area requirement. It was decided that 34 turbines at reduced flow per turbine were required for the 1078 MWe system. Later in this study it was determined to maintain the 10 gigawatt power level requirement as a minimum rather than as an average and to include additional power necessary to meet on-board peak power requirements related to satellite position and attitude control needs. The 34 turbine, 1078 MWe system for each cavity heat source was increased to a 36 turbine, 1136 MWe system. This revised system had a 1% power margin over the power required even under peak power requirements and peak power transmitter capability. This reserve increased when attitude control power was reduced and as the power transmission capability decreased through the year.

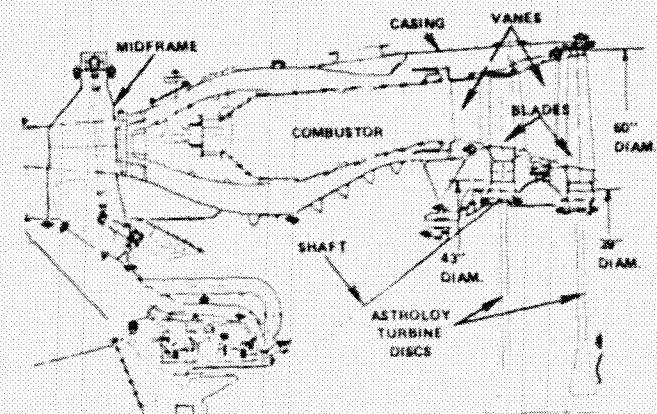
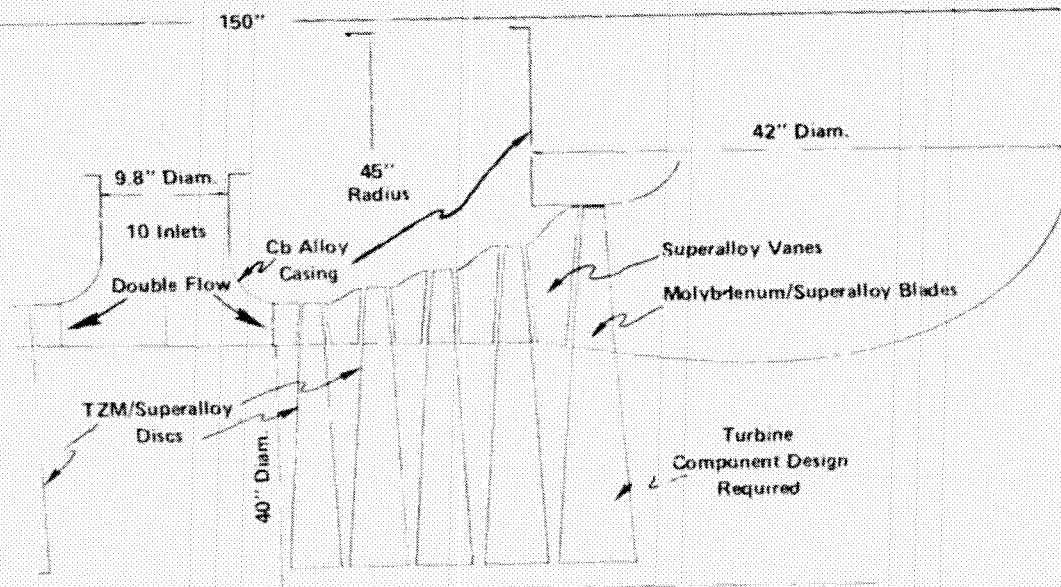
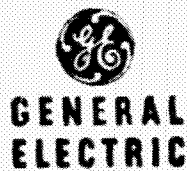
Using a specific turbine weight of 0.75 kg/kw (1.66 lb/kw), the total weight for the 1136 MWe system was  $8.48 \times 10^5$  kg ( $1.87 \times 10^6$  lb).

The percent effectiveness was based upon the total moisture in the vapor stream irrespective of such factors as droplet size or whether or not droplets were collected either on the turbine blade or on the inside wall of the swirl device.

Figure 6.1-32 relates the size of the rotating components of the SPS turbine to the turbine developed by GE for America's SST program.

The aircraft and land gas turbine industries in the USA have advanced the design, materials, processing and manufacturing technologies of superalloy turbine systems to a highly refined state. The development and manufacture of the potassium vapor turbine can use these existing technologies with a high degree of assurance. While specific preliminary design effort and later detailed component design work will be required to more exactly define potassium turbine hardware at the power

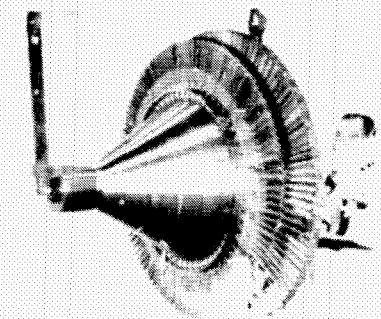




**TURBINE SECTION  
GE 4 BLOCK II ENGINE  
FOR THE SUPERSONIC TRANSPORT (SST)**

**FLOW PATH CONFIGURATION FOR  
31.7 MW<sub>e</sub> DOUBLE FLOW POTASSIUM VAPOR TURBINE**

- K TURBINE COMPARABLE IN SIZE TO GE 4 ENGINE
- SUPERALLOY DISCS 43 INCH DIAM. (1.1 DEMONSTRATED)
- TZM MOLYBDENUM DISCS BY POWDER MET OR STACKED PANCAKE FORGING PROCESSES
- USA HIGH TEMPERATURE LARGE TURBINE CAPACITY ABOUT 300-450 UNITS PER YEAR AT PRESENT
- HIGH TEMPERATURE MATERIALS TECHNOLOGY WELL DEVELOPED



**GE 4 TURBINE ROTOR ASSEMBLY**

**Figure 6.1-32. Turbine Size Is Within National Capability**

D180-22876-3



### **D180-22876-3**

levels required for solar power satellites, no major engineering breakthroughs are required nor do other serious technology barriers exist. Superalloy gas turbines of the size of the proposed potassium vapor turbine have been built. Large astroloy forgings of the size required by the potassium turbine have been made for the GE-4 engine for the supersonic transport. A production base of significant size exists in the USA for the manufacture of large high temperature turbines.

Newly developed powder metallurgy processing capabilities including large hot isostatic powder compaction presses provide the basis for preparing forgeable billets of molybdenum alloy, TZM, for the fabrication of turbine discs of the required size. Alternatively, conventionally arc-cast and extruded billets of this alloy could be forged and hot isostatically pressed in stacks to form forging billets of the required size for forging in existing facilities within the USA.

#### **6.1.2.8 Generators**

Each potassium Rankine turbine turns a generator as shown in Figure 6.1-33. These generators produce either 41,000 or 39,000 volts direct current as required by the microwave transmitters. The generators are oil cooled using coolant passages through both the rotor and stator. Although they are quite efficient the generators must dissipate waste heat at such a rate that their own surface area is not sufficient for this dissipation therefore external radiators are used. A high copper temperature is advantageous to reduce the area and mass of these radiators.

#### **6.1.2.9 Primary Radiator System**

Sections 5.1.2.3 through 5.1.2.6 explain the derivation and selection of the most important radiator parameters. This section describes the resultant radiator design, details of which are shown in Figure 6.1-34.

Shown here is a segment of the radiator for one turbogenerator. A vapor duct is at the top and the liquid return duct is at the bottom. The heat pipe panels with their throughpipes pass between the ducts. Also shown are the triple layers of meteoroid bumper installed on the ducting. At the lower left is a detail of the throughpipes and the wraparound sodium heat pipes. The sodium heat pipes are spaced apart such that their centerlines are 1.6 diameters from each other. This spacing is an optimum compromise between greater spacing, which would improve heat radiation, and reduced spacing which would reduce manifold mass by requiring fewer throughpipes. On the right is a cross section through two adjacent radiator systems showing how the vapor ducts share common meteoroid protection systems for a reduction in bumper mass.

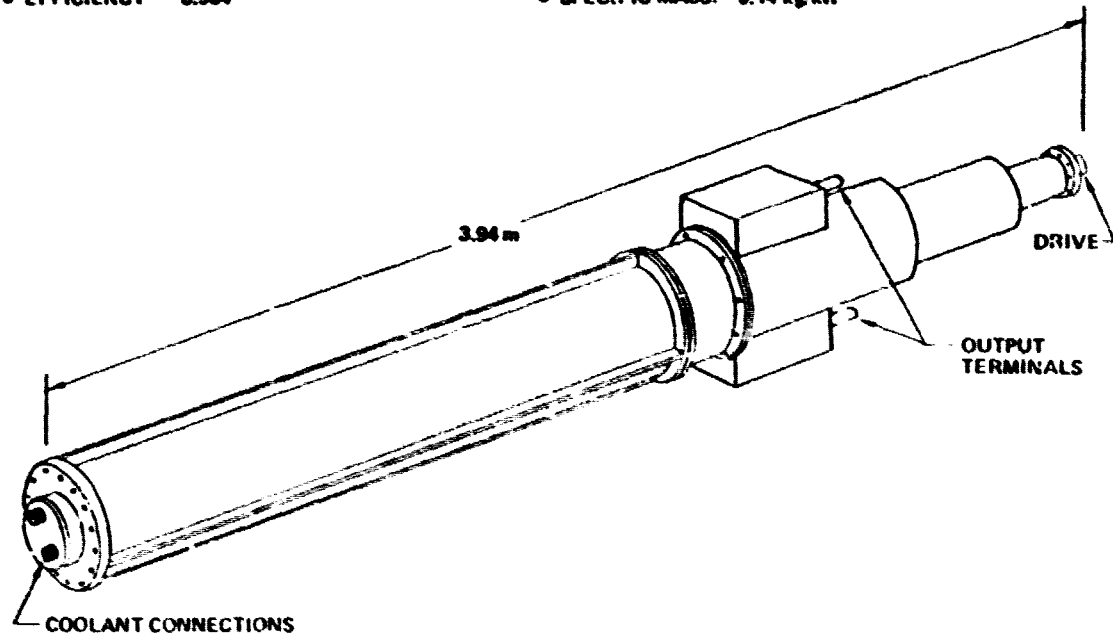
Each radiator extends 355M (1165 ft) from its turbogenerator, so that the liquid and vapor ducts each have that length. The vapor duct is tapered: at the turbine the diameter is 1.6M (5.25 ft). The liquid duct has a diameter (maximum) of 0.278M (0.91 ft). The throughpipes are 8 cm (3.15

# D180-22876-3

SPS-1513

- OUTPUT 31.43 MW
- ROTOR SPEED 7500 RPM
- COOLANT OIL (DC-203)
- EFFICIENCY 0.984

- VOLTAGES: EITHER 41000 OR 39000 VDC, NOMINAL
- COPPER TEMP: 478K (400°F)
- DUTY CYCLE: CONTINUOUS
- SPECIFIC MASS: 0.14 kg/kW



PRIMARY DATA BASE: AIRESEARCH MFG. CO. OF CA. STUDY FOR AIR FORCE, CONTRACT F33615-75 C 2071

Figure 6.1-33. Generator

SPS-1514

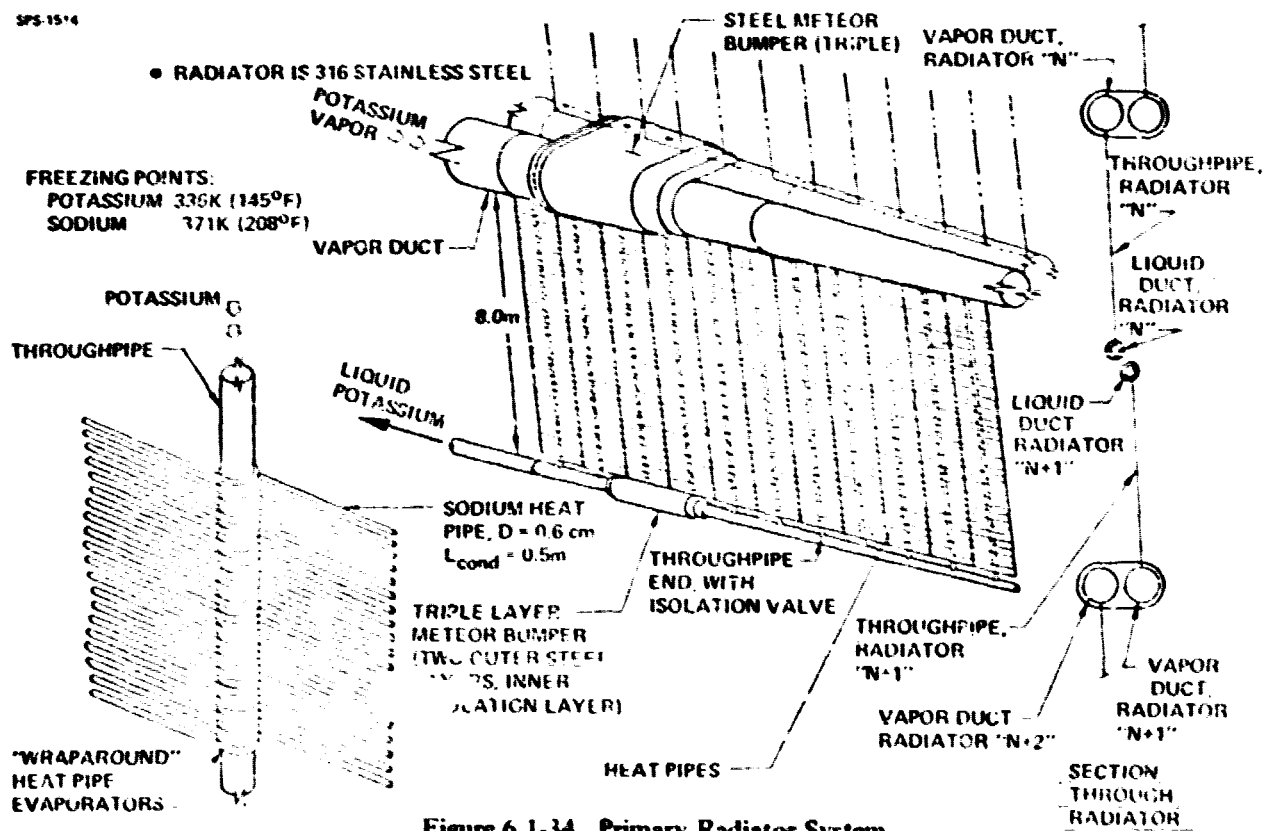


Figure 6.1-34 Primary Radiator System

inches) in diameter. Assuming that one half of the pressure recovery in condensation is usable, the total pressure drop in the radiator is 21.3 kPa (3.09 psia), making an NPSH of 16 kPa (2.31 psi) available to the pump.

The entire radiator system, including the heat pipe wicks, is type 316 stainless steel, which has excellent compatibility with both potassium and sodium.

Figure 6.1-35 gives a mass breakdown of the radiator system for one turbogenerator and for the entire SPS.

#### **6.1.2.10 Electromagnetic Pumps**

Electromagnetic (EM) pumps have been used extensively in the pumping of liquid metals. They have the advantages of absence of seals and bearings, operating reliability and reduced maintenance requirements.

For the Rankine cycle space power program, a lightweight 193 kg (425 lbs) electro-magnetic boiler feed pump, capable of operating at a liquid metal temperature up to 1033K (1400°F), was designed, built and tested for 10,000 hours. See Figure 4.5-4.

It pumped 811K (1000°F) potassium at flow rates up to 1.47 kg/sec (3.25 lbm/sec) at a developed head of 1648 kPa (240 psi), a NPSH of 7 psi and an efficiency of 16.5%. The pump features a T-111 alloy helical pump duct and a high temperature stator with a 811K (1000°F) maximum operating temperature; the stator materials consisted of Hipercro 27 magnetic laminations, 99% alumina slot insulators, type "S" glass tape interwinding insulation and nickel-clad silver conductors joined by brazing in the end turns. Pump windings were cooled by liquid NaK at 700-756K (800-900°F).

Large size annular linear EM pumps are under development for the Liquid Metal Fast Breeder Reactor. A 14,500 gpm (681 kg/sec) (1502 lb/sec) pump has been built and is awaiting test; pumps of larger sizes have been considered in the range of 30,000, 70,000, 80,000 and 130,000 gpm (1410, 3425, 3750 and 6110 kg/sec) (3108, 7573, 8280 and 13,470 lb/sec). Weight and cost estimates for commercial land based versions of these pumps have been initiated. While these pumps were designed for handling sodium at about 858°F, their development indicates pump scale-up experience well above that of the earlier higher temperature boiler feed pumps for Rankine space power systems.

Weight estimates for larger size pumps were prepared from present weights of the 14,500 GPM LMFBR EM pump. For space flight applications it was estimated that the liquid nitrogen cooled LMFBR pump, which weighed 31,752 kg (70,000 lbm), could be reduced by about 50% and then increased in weight by 20% to allow for added liquid metal cooling features. The flight weight

# D180-22876-3

SPS-1834

	PER ENGINE KG	PER SPS 10 <sup>3</sup> KG
<b>MANIFOLDS</b>	<b>3895</b>	<b>2.24</b>
<b>VAPOR DUCT</b>	<b>(1240)</b>	<b>(0.71)</b>
<b>LIQUID DUCT</b>	<b>(216)</b>	<b>(.12)</b>
<b>METEOROID PROTECTION</b>	<b>(2439)</b>	<b>(1.40)</b>
<b>THROUGHPIPIES</b>	<b>1500</b>	<b>0.86</b>
<b>THROUGHPIPIES (335/ENGINE)</b>	<b>(790)</b>	<b>(.46)</b>
<b>ISOLATION VALVES</b>	<b>(710)</b>	<b>(.41)</b>
<b>HEAT PIPES</b>	<b>13,299</b>	<b>7.66</b>
<b>SHELL</b>	<b>(10,838)</b>	<b>(6.24)</b>
<b>WICK</b>	<b>(1,29)</b>	<b>(0.99)</b>
<b>SODIUM</b>	<b>(732)</b>	<b>(0.43)</b>
<b>POTASSIUM</b>	<b>8046</b>	<b>4.63</b>
<b>TOTAL</b>	<b>26,740</b>	<b>15.39</b>

**Figure 6.1-35. Radiator Mass Summary**

pump was estimated to weigh 19,051 kg (42,000 lbm). For the larger proposed 70,000 GPM pump, the weight was derived from the above flight weight pump by scaling its weight upward from the 19,051 kg (42,000 lbm) pump in accordance with the increased flow capacity and then reducing weight by 30% for scaling efficiencies. Weights of other pumps for the "B" cycle at their prescribed flow rates, were then estimated from a weight vs. flow capacity curve derived from these flight weight pumps.

## 6.1.2.11 Boilers

The boiler tubes are located inside the cavity absorber where concentrated solar energy is available for the illumination. The boiler manifolds are located outside of the cavity absorber wall panels and are insulated with Multifoil (multiple layer refractory alloy insulation) to reduce energy waste. The manifolds and boiler tubes would be fabricated from niobium (columbium). The outlet manifold diameter is 0.55 m (1.80 ft); the inlet manifold diameter is 0.145 m (0.48 ft). The "working" region of the boiler tubes is 16M (33 ft) long. The boiler tubes are 1.52 cm (0.6 inch) diameter. The liquid potassium inlet temperature is 932K (1218°F); the potassium vapor outlet temperature is 1242K (1776°F). All design in this subsystem is for 30 year creep rupture capability, plus 50% for safety. If a boiler tube failure occurs inside the cavity, repair can be effected by isolating that boiler tube and welding off the resultant stubs outside of the cavity. Of course, this can only be done to approximately 5% of the tubes before a complete repair might be necessary.

### 6.1.2.12 Attitude Control

The attitude control and station keeping system consists of argon ion thrusters, chemical thrusters and the related auxiliary elements. The baselined specific impulse for the argon thrusters is 20,000 seconds (see Section 5.1.2.8). Characteristics of this system, including location, are given in Figure 6.1-36.

Maximum electric power is required when the system must produce maximum torque; the power level is approximately 300 MW. The SPS is sized to allow full transmitter output when the thrusters are drawing this power level. Average thruster power is about 120 MW.

The primary purposes of the chemical propulsion are attitude control when bus bar power is not available and recovery from a gravity gradient stable "upset" condition.

### 6.1.2.13 Future Development Requirements—A Preliminary Overview

The development of Rankine cycle power conversion systems can proceed on the basis of prior demonstration of the feasibility of a broad range of technology. However, considerable scale up in size and continued emphasis on improvement of component and system reliability will be required. A long term effort will be necessary to reinstate the alkali metal Rankine cycle test capability in

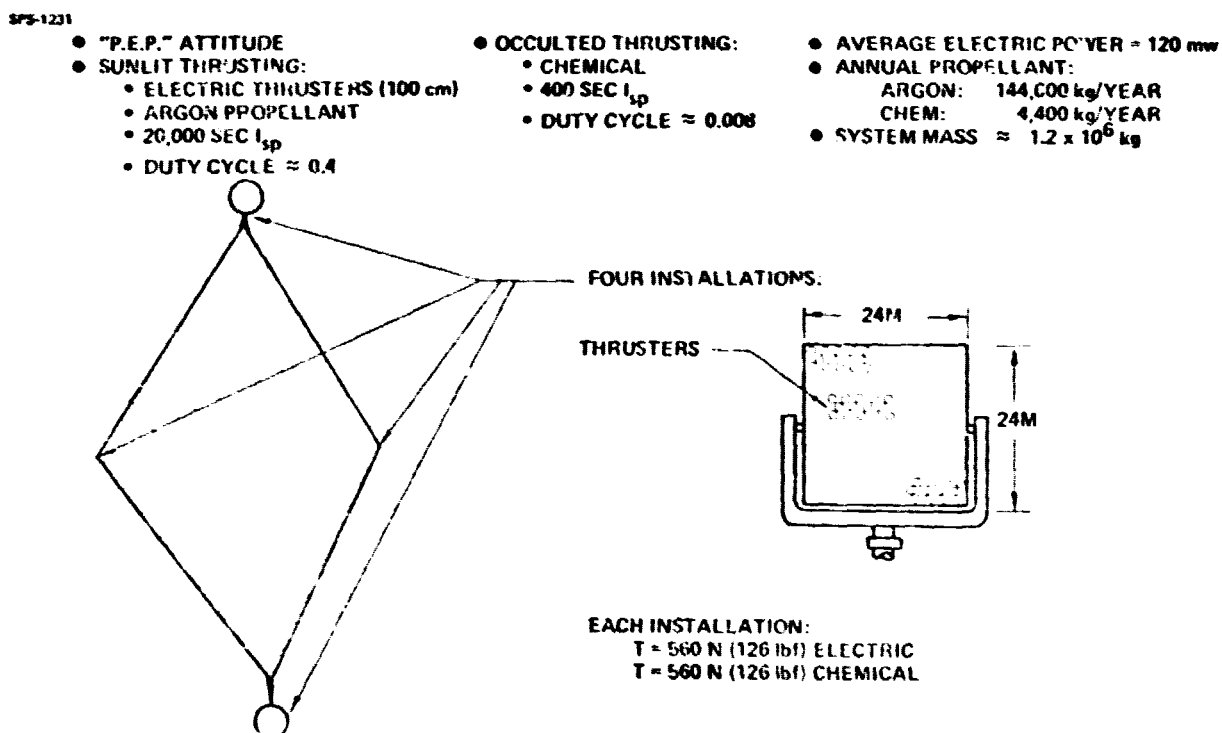


Figure 6.1-36 Attitude Control System

### **D180-22876-3**

facilities appropriate to SPS requirements. Nevertheless, there is a possible progressive approach which would permit considerable progress to be made on a cost effective basis.

In the near term, it is necessary to plan, cost estimate and schedule the broad outline of the programs required for the development of the power conversion system, to further optimize the system, to consider some of the anticipated operating, maintenance and power control situations and to initiate preliminary component design effort.

For the mid term, solid progress must be made in developing test facilities; in design, construction and test of components; and, in general, in developing a sound engineering basis for full size components. Initial component and facilities capabilities might be limited to the use of superalloys and air environment facilities for practical engineering achievement.

In the longer term, near "final" designs of refractory alloy components would be required, along with a capability of testing modular components in a space-like environment under IG conditions on Earth; during this period preparations could be planned for testing in space.

A program planned with definitive objectives and a logical progression of hardware development would provide a sound basis for consistent and economical progress toward the availability of reliable, cost competitive thermal power conversion systems for the solar power satellite.

## **6.2 MASS SUMMARY**

### **6.2.1 Silicon Photovoltaic Mass Summary**

A mass summary for the photovoltaic reference SPS listed by major WBS elements is given in Table 6.2-1. A more complete mass statement was provided in the definition sections for each of the WBS elements in this mass summary.

Table 6.2-2 provides a comparison of the mass summaries for the evolution of the final photovoltaic reference.

The growth for the final photovoltaic reference was determined from the system uncertainty analysis. Figure 6.2-1 provides the results of the size and mass uncertainty analysis. The complete uncertainty analysis is discussed in the Evaluation and Data Book (Volume 6).

### **6.2.2 Rankine Thermal Engine Mass Summary**

Figure 6.2-2 is a mass statement for the reference design (refer back to Figure 6.1-1 for the corresponding configuration). This mass statement does not include "growth." Volume 6 of this set contains a summary of a statistical analysis of potential size and mass growth. It gives a "most probable" Rankine thermal engine SPS mass of approximately 94,000 metric tons ( $2.076 \times 10^8$  lbm).

**D180-22876-3**

**Table 6.2-1. Reference Photovoltaic Final Mass Summary (Mass in Metric Tons)**

1.0	SOLAR ENERGY COLLECTION SYSTEM	51,782
1.1	PRIMARY STRUCTURE	5,385
1.2	SECONDARY STRUCTURE	1
1.3	MECHANICAL ROTARY JOINT	67
1.4	MAINTENANCE STATION	
1.5	CONTROL	178
1.6	INSTRUMENTATION/COMMUNICATIONS	4
1.7	SOLAR CELL BLANKETS	43,750
1.8	SOLAR CONCENTRATORS	
1.9	POWER DISTRIBUTION	2,398
2.0	MICROWAVE POWER TRANSMISSION SYSTEM(S)	25,212
3.0	SUBTOTAL (NO GROWTH)	76,994

1 DISTRIBUTED TO APPROPRIATE WBS ITEMS

D180-22876-3

ORIGINAL PAGE 15  
OF POOR QUALITY

Table 6.2-2. Photovoltaic Reference Configuration Nominal Mass Summary Weight in Metric Tons

SP5-1547

COMPONENT	ORIENTATION	CR = 2 (10 GW B.O.L.)		CR = 1 (10 GW MINIMUM/30 YRS)		
		MIDTERM	PART I FINAL	PART I FINAL	PART II MIDTERM	PART II FINAL
1.0 SOLAR ENERGY COLLECTION SYSTEM	(36,616)	(59,313)	(49,512)	(56,357)	(56,184)	51,782
1.1 PRIMARY STRUCTURE	2,483	14,970	8,000	2,334	6193	5385
1.2 SECONDARY STRUCTURE	189	209	209	209	—	—
1.3 MECHANICAL SYSTEMS	40	40	40	40	67	67
1.4 MAINTENANCE STATION	85	—	—	—	—	—
1.5 CONTROL	340	340	340	340	150	178
1.6 INSTRUMENTATION/ COMMUNICATIONS	4	4	4	4	4	4
1.7 SOLAR-CELL BLANKETS	25,746	37,592	34,111	51,897	47,319	43,750
1.8 SOLAR CONCENTRATORS	5,149	2,978	3,276	—	—	—
1.9 POWER DISTRIBUTION	2,570	3,180	3,532	1,589	2451	2398
2.0 MPTS	15,371	15,371	15,371	15,371	(24,384)	25,212
SUBTOTAL	51,967	74,684	64,883	71,728	80,568	76,994
GROWTH	25,994	37,342	32,442	35,864	20,142	20,480 <sup>1</sup>
TOTAL	77,961	112,026	97,325	107,592	100,710	97,474

<sup>1</sup> 26.6% GROWTH FROM UNCERTAINTY ANALYSIS



SPS-1679

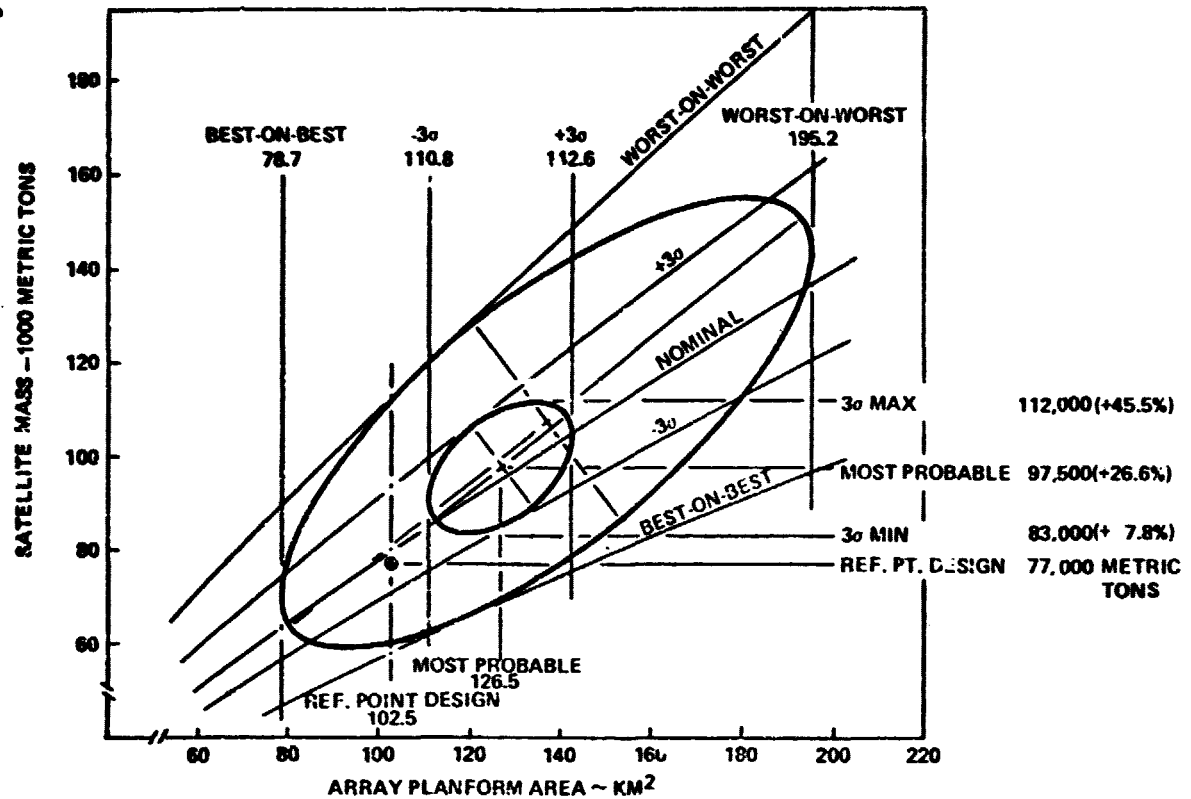


Figure 6.2-1. Mass/Size Uncertainty Analysis Results

ITEM	10 <sup>6</sup> kg
STRUCTURE	6.976
FACETS	1.837
RADIATOR (W/O POTASSIUM)	10.768
POV DIST	4.760
SW. GEAR	0.218
GENERATORS, ACCESSORY PACK	2.508
GENERATOR RADIATORS	1.140
TURBINES	13.755
PUMPS, PUMP RADIATORS	0.984
BOILERS & MANIFOLDS	3.296
CAVITY ASSYS	1.000
CPCS	0.299
LIGHT DOORS	0.025
MONITOR, COMMAND & CONTROL	0.160
ATTITUDE CONTROL	1.200
START LOCKS, CONTROLS	0.250
ANTENNA SUPPORT	0.286
MISC, INCLUDING STORAGE	0.200
POTASSIUM INVENTORY	6.058
POWER GENERATION	55.660
ANTENNAS	24.384
SPS	60.044

Figure 6.2-2. Potassium Rankine SPS Mass Statement

### 6.3 COST SUMMARIES

Note that the radiator mass does not include the potassium working fluids (which is given under "potassium inventory"). Thus the radiator mass does not correspond to that given in Section 6.1.2.9 since the potassium normally present in the radiation was included in that section's radiator mass summary.

#### 6.3.1 Silicon Photovoltaic Cost Summary

A cost analysis was accomplished on the reference photovoltaic SPS using a PCM to project the theoretical first unit (TFU) cost. A mature industry projection was then applied to the TFU along learning curves to estimate the system costs for various schemes.

Table 6.3-1 summarizes the cost of major WBS elements for the photovoltaic SPS. A comparison is provided for the LEO-GEO cost trade for one SPS per year and for the advanced production rate of four SPS's per year.

A detailed cost summary is provided in Evaluation and Data Book (Volume 6) and includes the installed system cost (\$/Kwe) and the energy cost to the customer (Mils/Kw-hr).

#### 6.3.2 Potassium Rankine Cost Summary

Table 6.3-2 summarizes capital cost elements for the thermal engine SPS system at two production rates.

D180-22876-3

Table 6.3-1. Reference Photovoltaic Final Cost Summary

SPS-1638

WBS	NAME	1 SPS PER YEAR		4 SPS's PER YEAR	
		LEO CONST.	GEO CONST.	LEO CONST.	GEO CONST.
A1.01.01.00	MULTIPLE/Common PROD. COST (\$ x 10 <sup>-6</sup> )	897	793	760	661
A1.01.01.01	ENERGY COLLECTION N/A	—	—	—	—
A1.01.01.02	ENERGY CONVERSION PROD. COST (\$ x 10 <sup>-6</sup> )	3731	3588	2793	2686
A1.01.01.03	POWER DISTRIBUTION PROD. COST (\$ x 10 <sup>-6</sup> )	138	133	82	79
A1.01.01.04	MPTS PROD. COST (\$ x 10 <sup>-6</sup> )	2676	2676	1952	1952
SUB TOTAL (\$ x 10 <sup>-6</sup> )		7442	7190	5587	5378
INSTALLATION COST (\$ x 10 <sup>-6</sup> )		7554	10906	5297	7648
TOTAL COST *(\$ x 10 <sup>-6</sup> )		14,996	18,096	10,884	13,026

\*INTEREST NOT INCLUDED

**Table 6.3-2. Capital Cost Summary—Thermal Engine SPS (Rankine) Dollars In Millions**

WBS NO.	ITEM	SOURCES & REFERENCES	1 SPS/YR		4 SPS/YR	
			LEO CONSTRUCTION	GEO CONSTRUCTION	LEO CONSTRUCTION	GEO CONSTRUCTION
1.01	Solar Power Satellite	o Mature Industry Estimate, Table 20	(7987)	(7987)	(5284)	(5284)
1.01.00	Multiple/Common & Pkg'g	o PCM Run, Table 21	1196	1196	846	846
	Energy Collection	o General Electric Turbine, Generator, & Pump Cost Estimates	374	374	374	374
	Energy Conversion	o Structural Mfr Estimate, 9th MPR	3365	3365	1890	1890
	Power Distribution	o Varian analysis of Klystron Productions	376	376	222	222
	Microwave Power Transmission	o MPTS Error Analysis	2676	2676	1952	1952
		o SPS Mass Estimate, Table 22				
1.02	Ground Receiving Station	(Same as Photovoltaic)	(4446)	(4446)	(4000)	(4000)
2.00	Construction & Space Support		(1716)	(1768)	(1716)	(1768)
2.01	Construction Base (Facility Write-down)	Writedown Summary, Table 23; Facility Mass & Cost Estimates, Tables 24 & 25	971	1010	971	1010
2.02	Space Support					
2.02.01	Staging Base	(Same as P/V)	N/A		N/A	
2.02.02	Crew Support	o Crew Support from Estimates, Table 12				
		o Crew Rqts from Construction Analyses (Part I Vol III & Part II Vol IV)	745	758	745	758
2.02.03	Other OPS Support		16		16	

175

D180-22876-3

ORIGINAL PAGE IS  
OF POOR QUALITY

**Table 6.3-2. (Continued)**

WBS NO.	ITEM	SOURCES & REFERENCES	1 SPS/YR		4 SPS/YR	
			LEO CONSTRUCTION	GEO CONSTRUCTION	LEO CONSTRUCTION	GEO CONSTRUCTION
3.00	Space Trans- portation	c Numbers of Flights & Costs Summary, Table 26	(7425)	(11182)	(4678)	(7275)
3.01	Earth-Leo					
3.01.01	Freight	c Other References Same as Photovoltaic	3900	3270	2527	2095
3.01.02	Crew		528	528	220	220
3.02	Leo-Geo		181	533	141	357
3.02.01	Freight		2816	6851	1790	4603
3.02.02	Crew					
	Interest during Construction		(700 days) (2068)	(450 days) (1563)	(566 days) (1215)	(366 days) (916)
	Growth	Table 27	(2946)	(3489)	(755)	(903)
			26588	28872	17648	20146

D180-22876-3

**D180-22876-3**

**APPENDIX A  
ROTARY JOINT ANALYSIS  
GENERAL ELECTRIC  
SPACE DIVISION**

D180-22876-3

### SPS SLIP RINGS

Two sizes of slip rings were evaluated, a single 350 meters diameter slip ring (2 per SPS) and three concentric 15 meters, 11 meters and 5 meters slip ring (2 sets per SPS). Also three materials were considered as likely candidates for the SPS slip rings. The coin silver (90% silver, 10% copper) is the least loss ( $I^2R$  losses) material and in conjunction with silver moly disulfides brushes provide the best performance.

Copper slip ring material cost is considerably less than coin silver with comparable weight and  $I^2R$  losses but vacuum operation experience is limited.

The disadvantage of aluminum slip rings are the high  $I^2R$  losses and very limited experience in vacuum operation. The additional problem with aluminum is that the surface oxide would have to be removed and protection provided in air by plating. Oxidation in space could also occur over long periods of time due to oxygen molecules.



#### SPS Slip Rings

	15, 11, 7m DIAMETER	350m DIAMETER
<b>COIN SILVER</b> - ADVANTAGES VACUUM OPERATION EXPERIENCE LOW WEAR LOW FRICTION LOW LOSSES ( $\rho = 1.59 \mu\Omega / \text{cm}^3$ ) LONG LIFE - DISADVANTAGES COST OF MATERIAL - (PER SPS) WEIGHT (PER SPS) AVAILABILITY OF SILVER	          \$1.7M 24,000 LBS	          \$8M 115,000 LBS
<b>COPPER</b> - ADVANTAGES COST OF MATERIAL - (PER SPS) WEIGHT (PER SPS) AVAILABILITY OF COPPER - DISADVANTAGES LIMITED LONG TERM EXPERIENCE IN VACUUM OPERATION	          \$30K 20,000 LBS	          \$175K 96,000 LBS
<b>ALUMINUM</b> - ADVANTAGES COST OF MATERIAL - (PER SPS) WEIGHT (PER SPS) AVAILABILITY OF ALUMINUM - DISADVANTAGES HIGH LOSSES ( $\rho = 2.79 \mu\Omega / \text{cm}^3$ ) SURFACE OXIDATION VERY LIMITED EXPERIENCE IN VACUUM OPERATION	          \$5K 6,500 LBS	          \$82K 30,000 LBS

0-3



D180-22876-3

SPS Brushes



- 85% Ag, 12% MoS<sub>2</sub>, 3% C

- ADVANTAGES

VACUUM OPERATION EXPERIENCE  
LOW WEAR  
LOW FRICTION  
LOW LOSSES  
LONG LIFE

- DISADVANTAGES

COST OF MATERIAL - \$250K PER SPS  
WEIGHT - 1,500 LBS PER SPS

- CARBON TYPE (MOLISULFIDE ADDITIVE)

- ADVANTAGES

<sup>K</sup>  
COST OF MATERIAL - \$10 PER SPS  
WEIGHT - 300 LBS PER SPS

- DISADVANTAGES

HIGHER LOSSES (TWICE THAT OF SILVER)  
HIGH FRICTION ( TWO TO FOUR TIMES THAT OF SILVER)



### **D180-44576-3**

An investigation was made to determine the magnitude of brush wear that could be experienced on the Solar Power Satellite (SPS).

The Solar Power Satellite has three different diameter slip rings with the following parameters:

Diameter (meters)	Current (amps)	Number of Brushes per ring
15	199,360	384
11	139,560	320
7	59,800	128
Brush Area		3 cm x 5 cm
Brush Pressure		4 psi
Rotational Speed		1 revolution per day
Brush Material		Ag MoS <sub>2</sub> C
Ring Material		Coin Silver

There is very little information concerning theoretical aspects of brush wear or actual brush wear occurring under vacuum operation.

Brush and slip ring wear is a complex phenomenon dependent upon many parameters such as the brush and slip ring material, mechanical pressure, sliding velocity, electrical current and the environmental conditions. Holm has expressed brush wear as

$$W = SP (W_0 + W_1 \sqrt{\frac{I}{10}}) \times 10^{-6}$$

Where:

$W$ = brush wear, cm <sup>3</sup>	$W_0$ = mechanical wear coefficient
$S$ = Sliding distance, Km	$W_1$ = electrical wear coefficient
$P$ = brush load, Kg	

Values of  $W_0$  between 0.6 and 20 have been given by Holm for brushes running on smooth copper rings. The lower value, 0.6, is for electrographite brushes and the higher value, 20, is for copper-graphite or bronze graphite. Value of  $W_1$  range from 0 to 20 depending upon the type of brush material as well as whether it is anodic or cathodic.

The brush wear was determined for SPS based on Holm for different types of brushes with the following results:

**D180-22876-3**

Material	Wear - $\text{cm}^3/\text{Km}/\text{brush}$	
	Without Current	With Current
Electrolytic graphite $W_o = .6$ $W_l = .6$	$.03 \times 10^{-4}$	$.2 \times 10^{-4}$
Natural graphite $W_o = 4$ $W_l = 4$	$.17 \times 10^{-4}$	$1.33 \times 10^{-4}$
Copper graphite $W_o = 20$ $W_l = 20$	$.85 \times 10^{-4}$	$6.7 \times 10^{-4}$

Lewis, et al., presents data for vacuum operation of Ag Mo S<sub>2</sub> C brushes and coin silver rings as follows:

Wear	$2.7 \times 10^{-9}$ in/in
Vacuum	$5 \times 10^{-8}$ torr
Brush pressure	170 grams
Brush current	8.33 amps
Current density	100 amps /in <sup>2</sup>

If this data is extrapolated for the SPS brush pressure and brush area, the wear will be  $36 \times 10^{-4}$   $\text{cm}^3/\text{Km}$  per brush. The wear for the brushes on the SPS rings will be:

Diameter Ring	Total Debris	Debris per Brush
15 m	23.7 $\text{cm}^3/\text{year}$	.0617 $\text{cm}^3/\text{year}$
11 m	14.5 $\text{cm}^3/\text{year}$	.0453 $\text{cm}^3/\text{year}$
7 m	3.7 $\text{cm}^3/\text{year}$	.0289 $\text{cm}^3/\text{year}$

The wear rate of  $36 \times 10^{-4}$   $\text{cm}^3/\text{Km}$  is considerably in excess of that calculated with Holm's equation and parameters. However, this represents wear in a vacuum with brush materials that Holm did not address.

It is not immediately apparent as to what occurs to this debris. Because of the low rotational speed as well as the vacuum and space environment, it is possible that the debris will remain in proximity to the brushes. It should be noted that the quantity of debris per brush per year is quite small between .0289  $\text{cm}^3/\text{year}$  and .0617  $\text{cm}^3/\text{year}$ . This debris is in the form of fine particles which could become charged and adhere to other surfaces.

The wear of aircraft brushes was determined based on data of the Carbon Products Department, General Electric Company. The brushes are graphite having molydisulfide cores and are used with

### D180-22876-3

both commutators and slip rings. The brushes used with slip rings have about 1.5 times the life as those used with commutators. The data provided was as follows:

Wear	.25"
Speed	4000 ft/min
Brush Pressure	4 psi
Brush Area	.5 in <sup>2</sup>
Commutator	

Wear	=	$.28 \times 10^{-4} \text{ cm}^3/\text{km/brush}$	Commutator
Wear	=	$.19 \times 10^{-4} \text{ cm}^3/\text{km/brush}$	Slip Ring

On aircraft applications, the wear of the slip ring and commutator is approximately the same as that of the brushes.

### References

Ragnar Holm, "Electric Contacts Handbook," Third Edition. Springer-Verlag, 1958.

Lewis, Cole, Glossbrenner and Vest, "Friction, Wear and Noise of Slip Ring and Brush Contacts for Synchronous Satellite Use," IEEE Transactions on Parts, Hybrids and Packaging, Vol. PHP-9, No. 1, March 1973.

**D180-22876-3**

**APPENDIX B  
ANALYSIS AND COMPARISON OF  
ALTERNATE STRUCTURAL APPROACHES**

### D180-22876-3

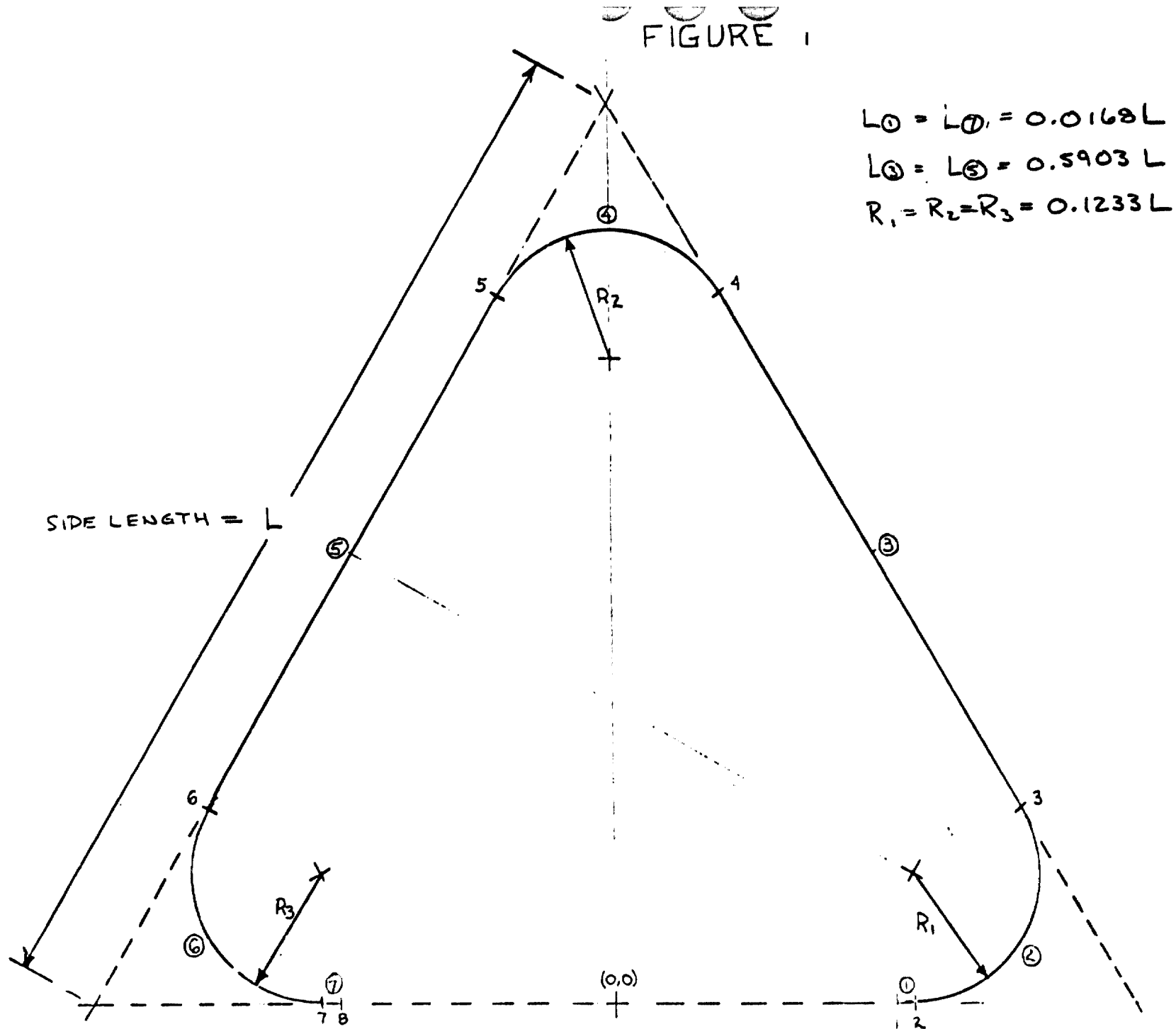
A comparison was made between continuous chord beams and the 20 meter tapered tube beam being used in our current reference satellite design. Solutions were found that met the load requirements of the tapered tube approach and resulted in relatively small mass increases.

The continuous chords investigated were of both open and closed section configurations. The open sections investigated were of the configuration shown in Figure 1. This is the basic configuration of the General Dynamics continuous chord approach (NAS9-15310) with the side length,  $L$ , varied from 3 inches to 15 inches. Figures 2 through 9 illustrate the relationship of critical load (in buckling) and load-to-mass ratio as a function of batten spacing and beam width. Solutions were sought that would give the optimum beam width and batten spacing with respect to load-to-mass ratio for each configuration.

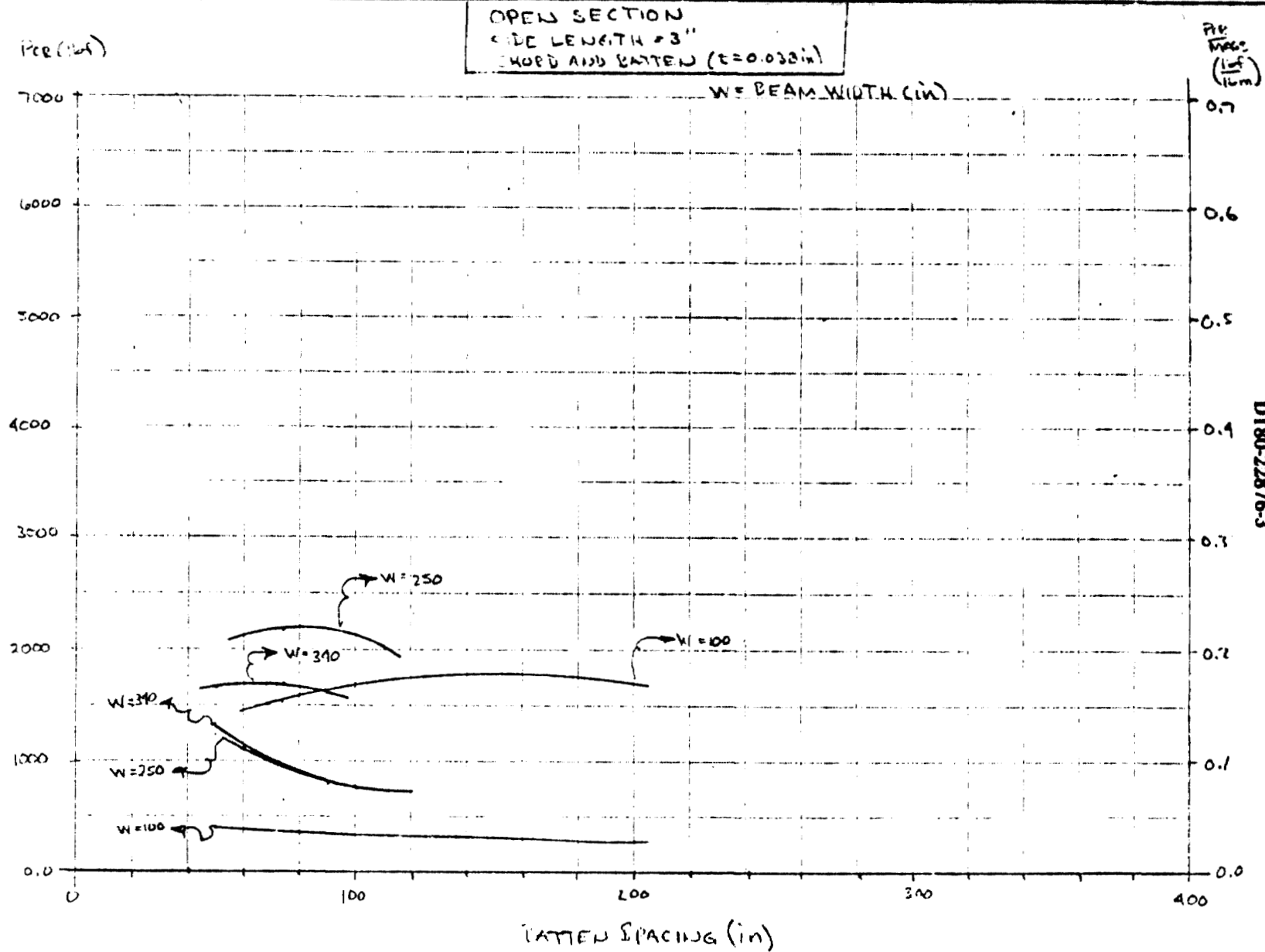
The closed section configurations that were used are shown in Figures 10 through 22 along with the optimization curves for each case investigated.

The conclusions from the investigation are:

1. The load carrying capability of the continuous chord beam is very sensitive to  $EI$  of both the chord and batten. This seems to suggest that the  $X_{chord}$  configuration should be used for the batten for the best performance.
2. For a given chord/batten configuration, solutions exist for chord width and batten spacing to give optimum load-to-mass ratios for that configuration. The trend is for wider beams to have smaller batten spacings for the optimum condition.
3. Closed section members have higher load-to-mass ratios for a given beam configuration.
4. Solutions exist for continuous chords that could replace the current tapered tube beams with a mass growth of approximately 20 percent for closed section members and 40 percent for open section members. Other solutions exist that may be closer to the tapered tube mass for the load requirements, but of the configurations investigated, Figures 23 through 26 illustrate the chosen solutions.



OPEN SECTION  
SIDE LENGTH = 3"  
CHORD AND BATTEN ( $t = 0.032$  in)



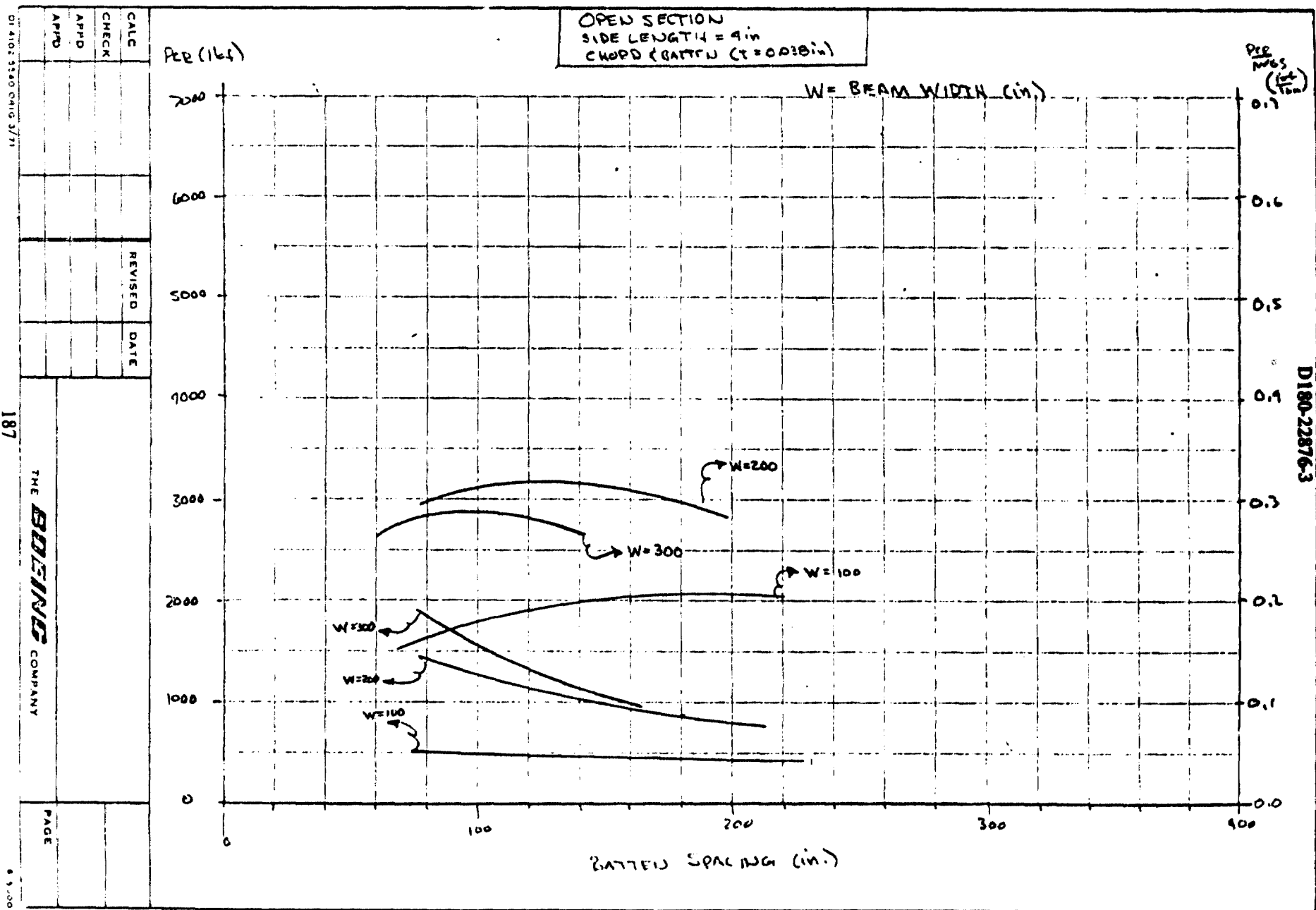
**ORIGINAL PAGE IS  
OF POOR QUALITY**

**D180-22876-3**

THE **GEORGE** COMPANY

PAGE

# FIGURE 3



DI 410-3560 (Rev. 3/71)



# FIGURE 4

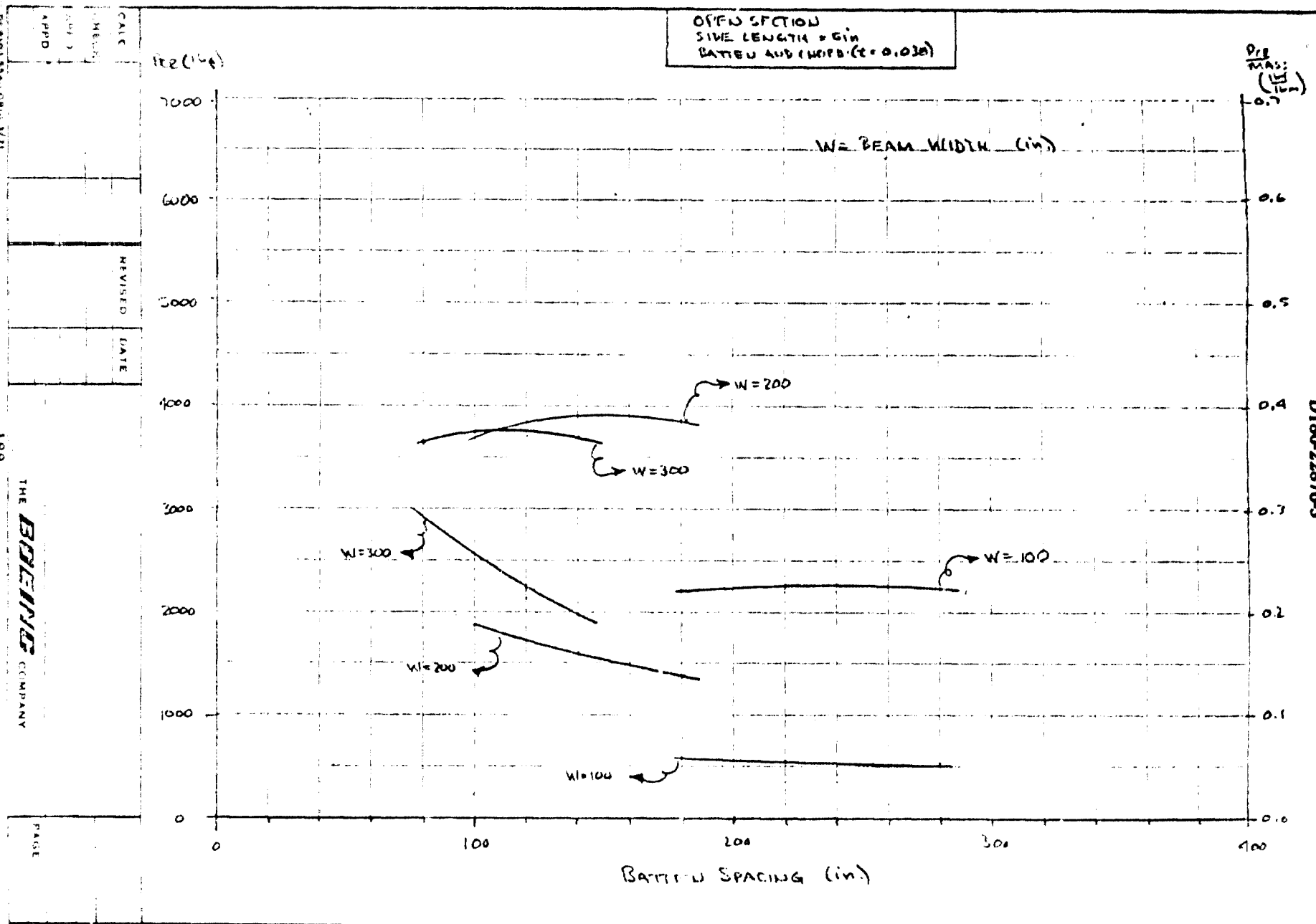


# FIGURE 5

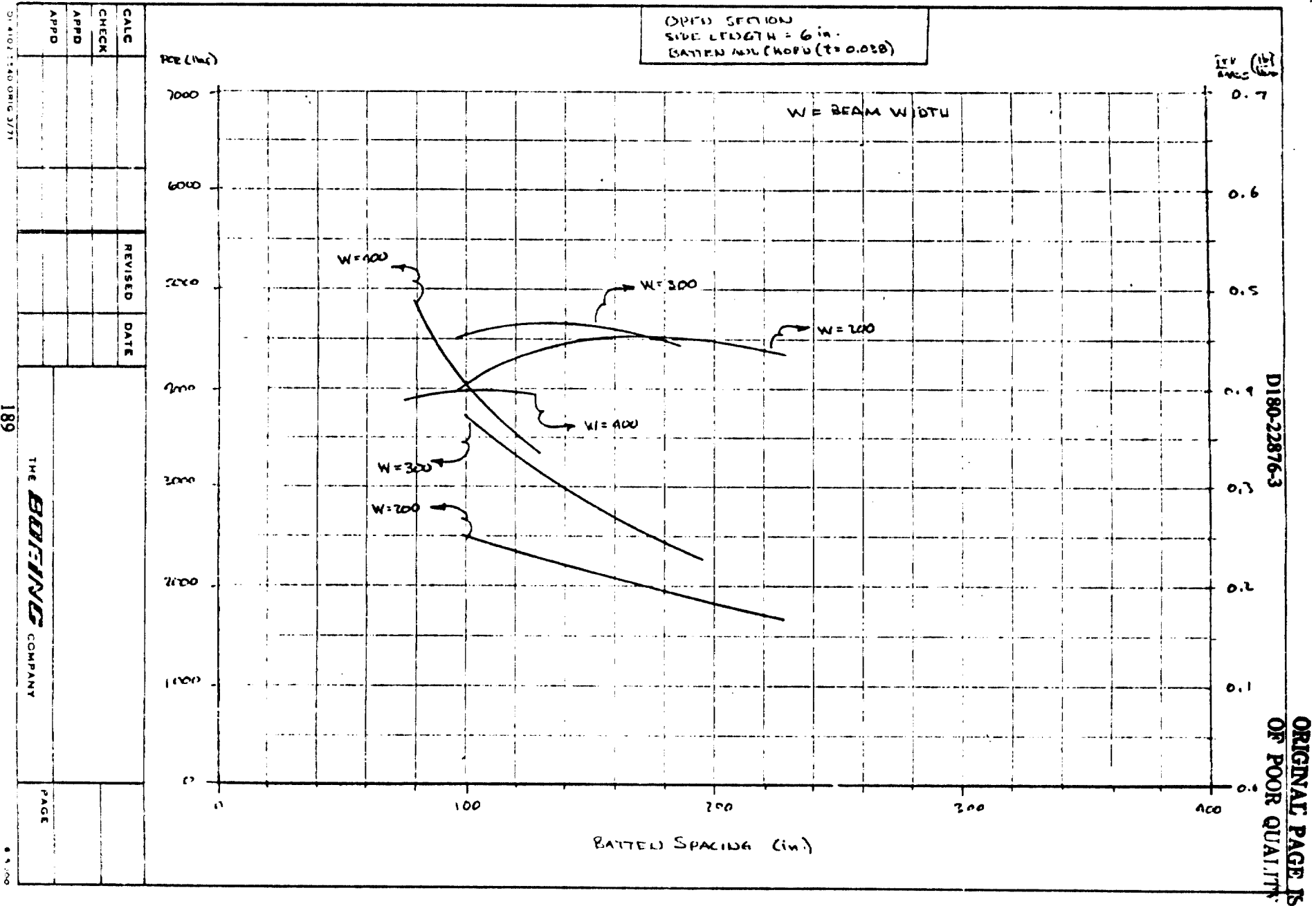


# FIGURE 6

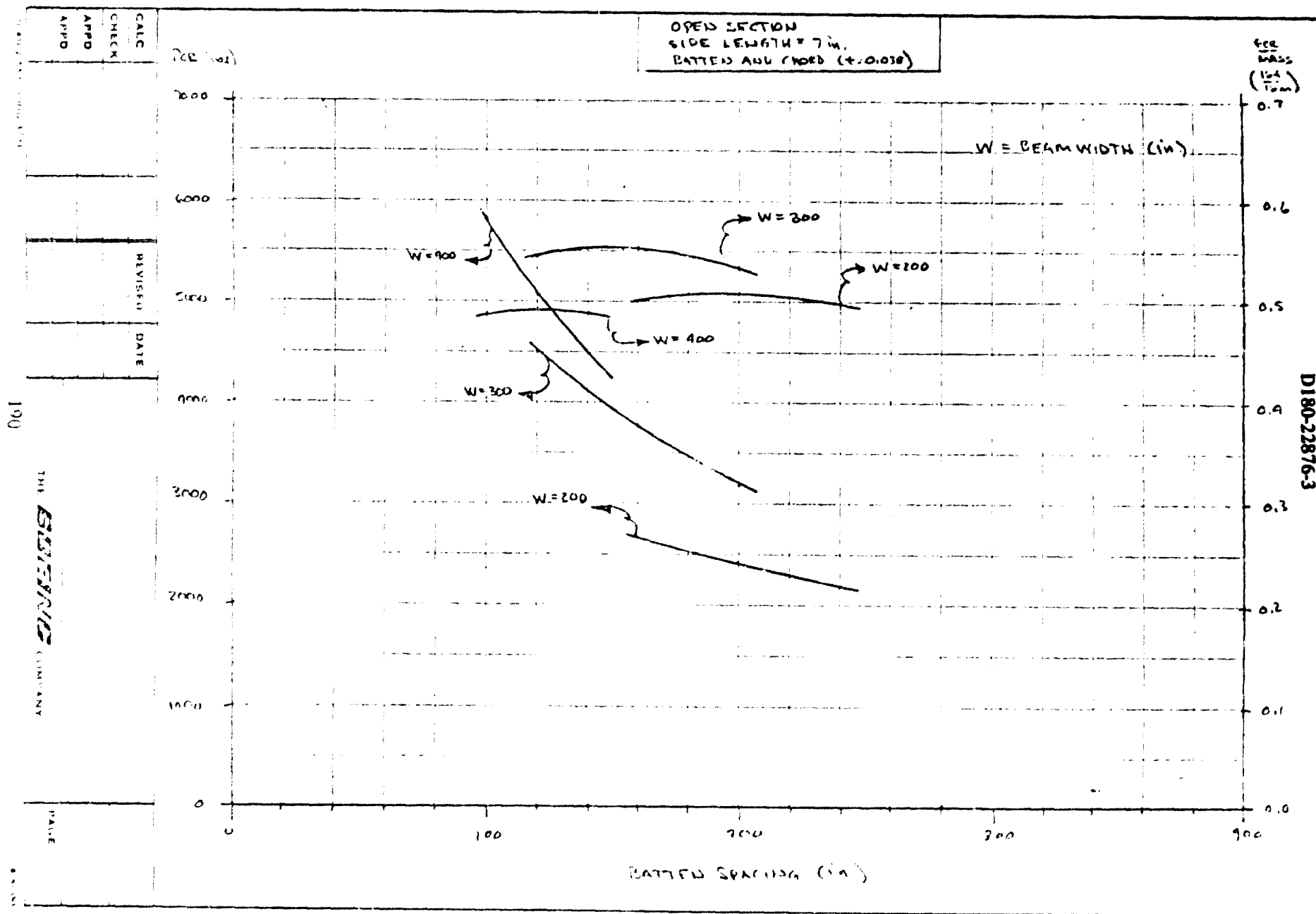




# FIGURE 8

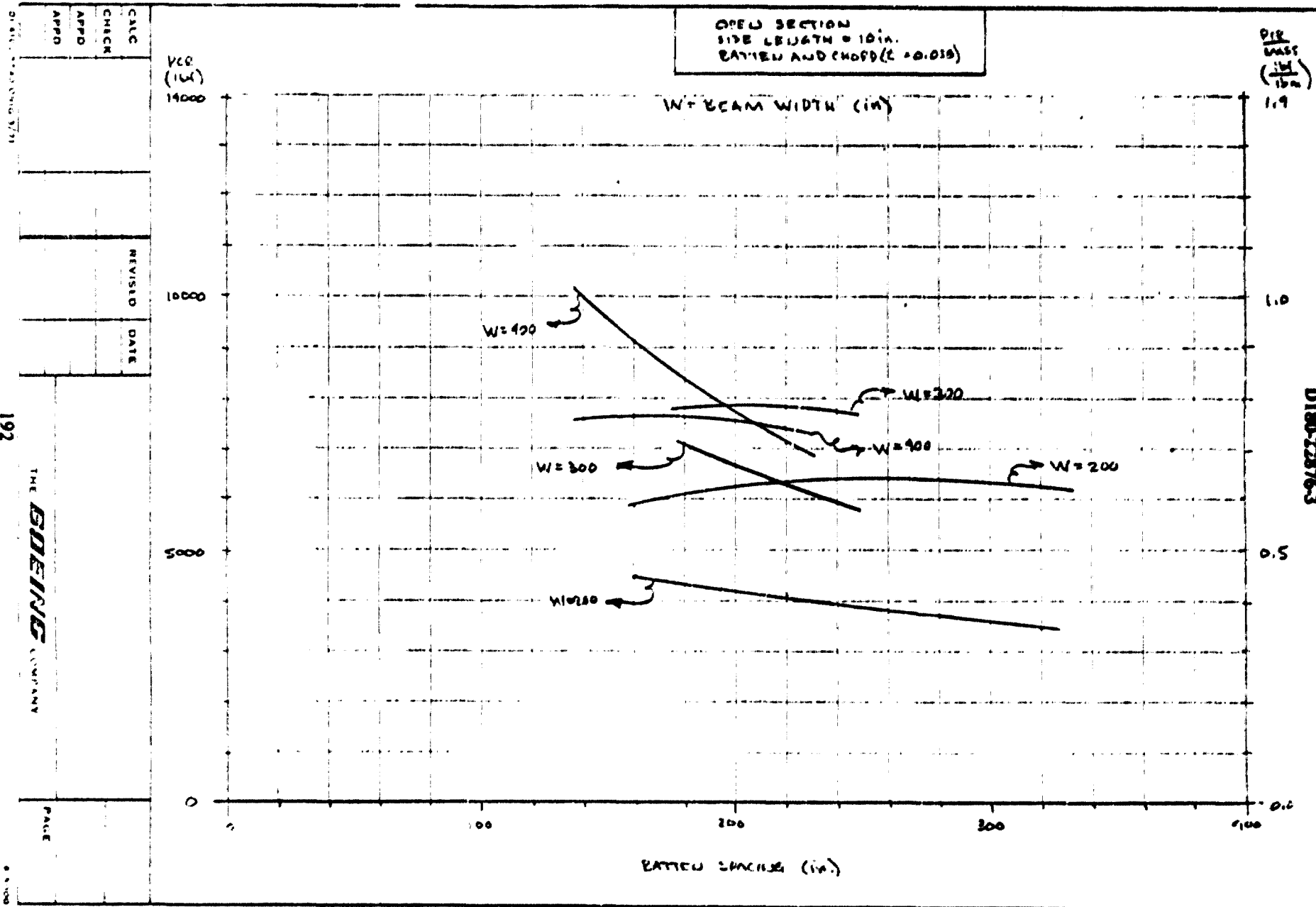
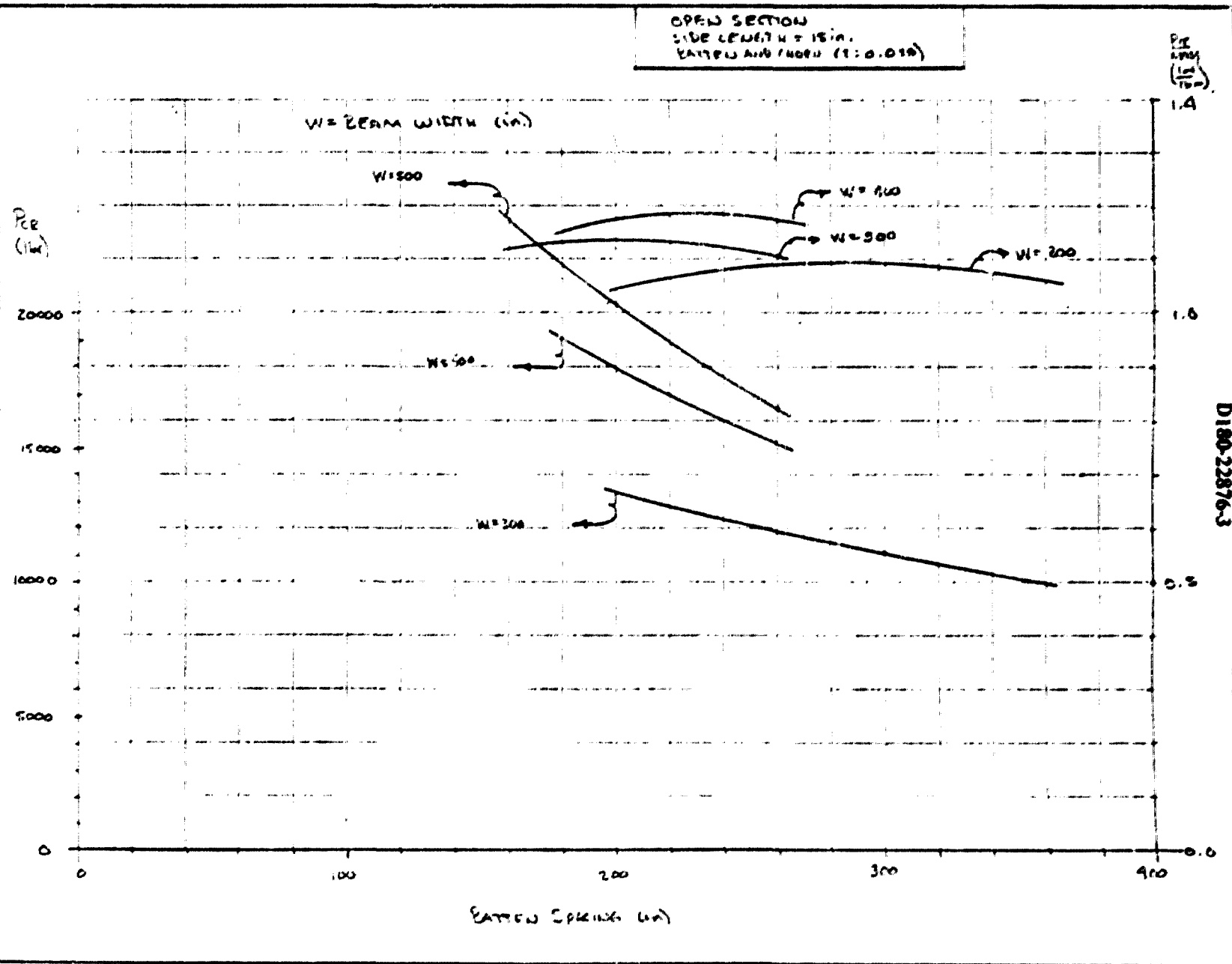


# FIGURE 9



D18022876-3

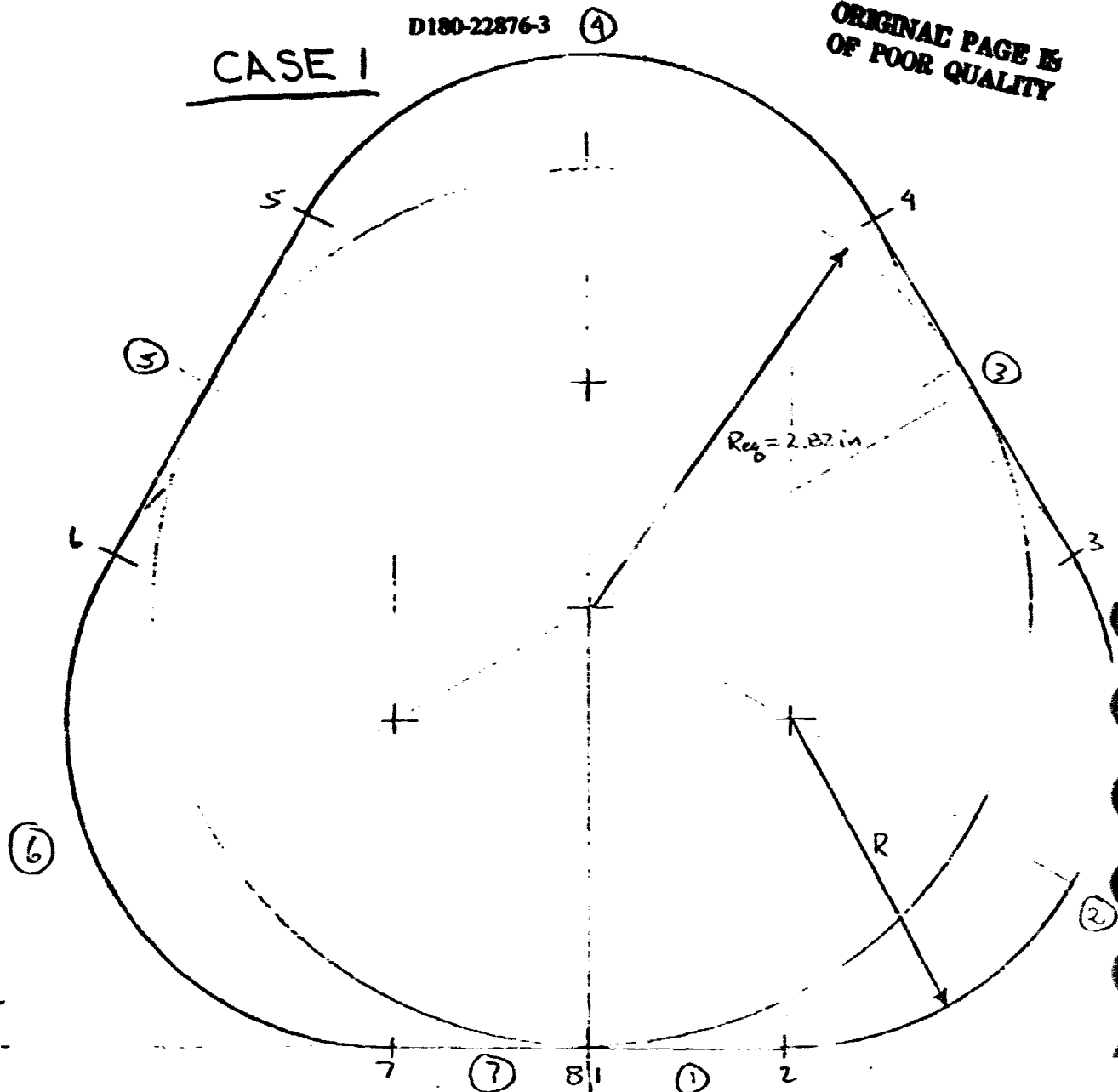
CALC  
INCH  
APPD  
APPD

REVISIONS  
DATE

ORIGINAL PAGE IS  
OF POOR QUALITY

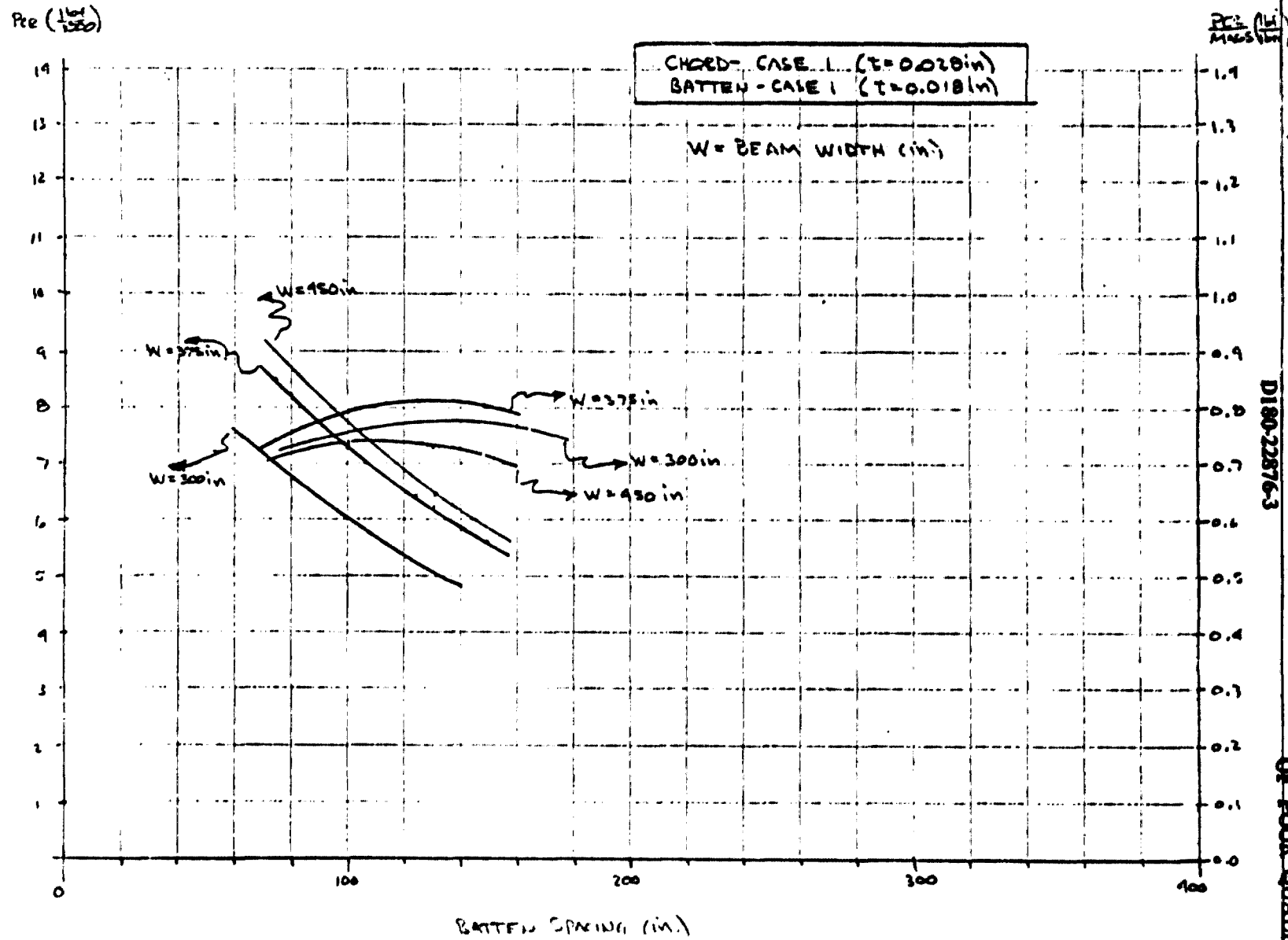
CASE 1

FIGURE 10



SEGMENT	WIDTH	THICKNESS (0.010, 0.020)	RADIUS	NODE	X	Y
(1)	1.240	t		1	0.010	0.0
(2)	4.398	t	2.10	2	1.250	0.0
(3)	2.50	t		3	3.066	3.144
(4)	4.398	t	2.10	4	1.920	5.320
(5)	2.50	t		5	-1.920	5.320
(6)	4.398	t	2.10	6	-3.066	3.144
(7)	1.240	t		7	-1.250	0.0
				8	-0.010	0.00

FIGURE 11



**ORIGINAL PAGE IS  
OF POOR QUALITY**

**DI 80-22876-3**

			REVISED	DATE	
CALC					
CHECK					
APPD					
APPD					

**THE DOERING COMPANY**

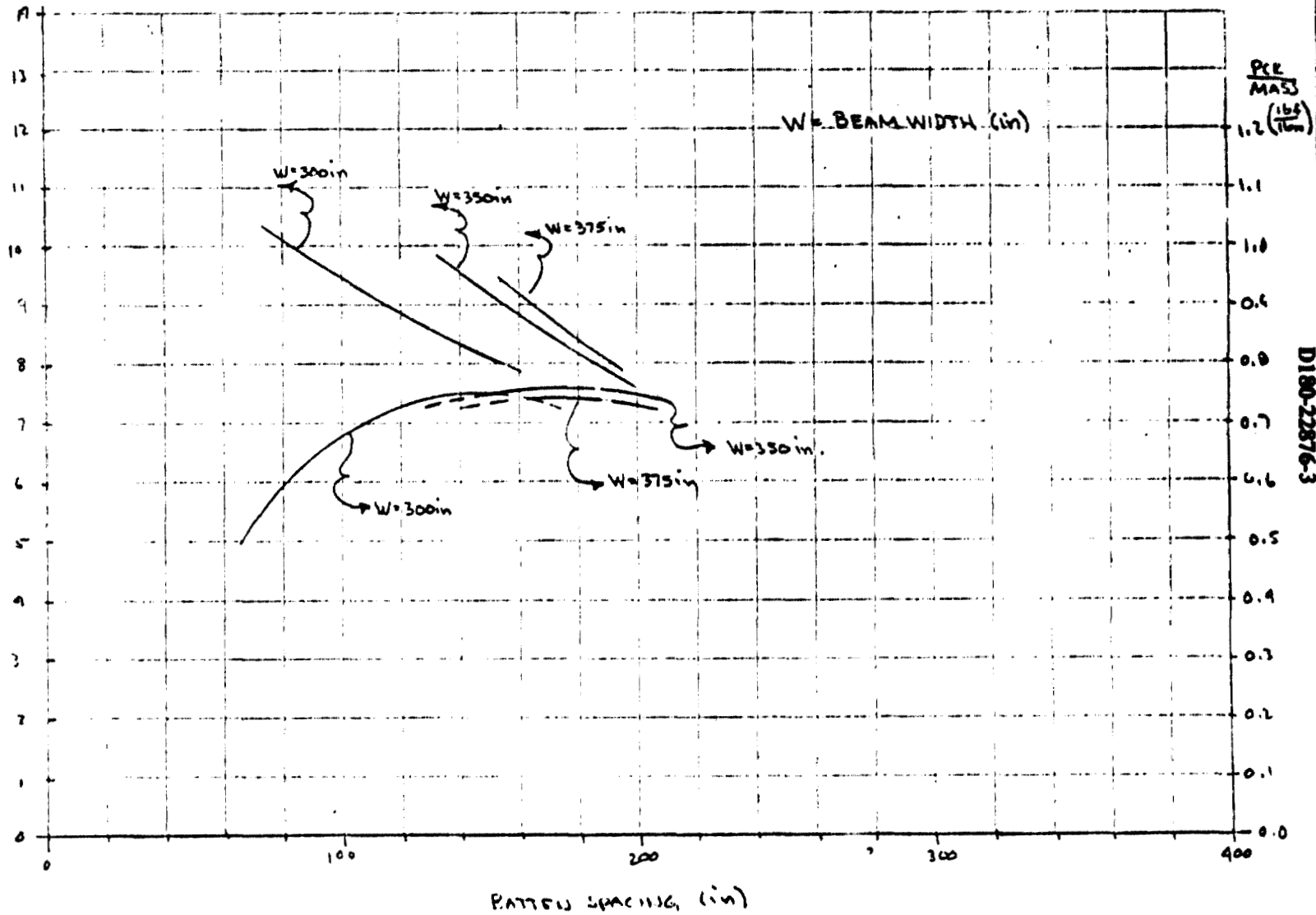
PAGE



FIGURE 12

PER (1/100)

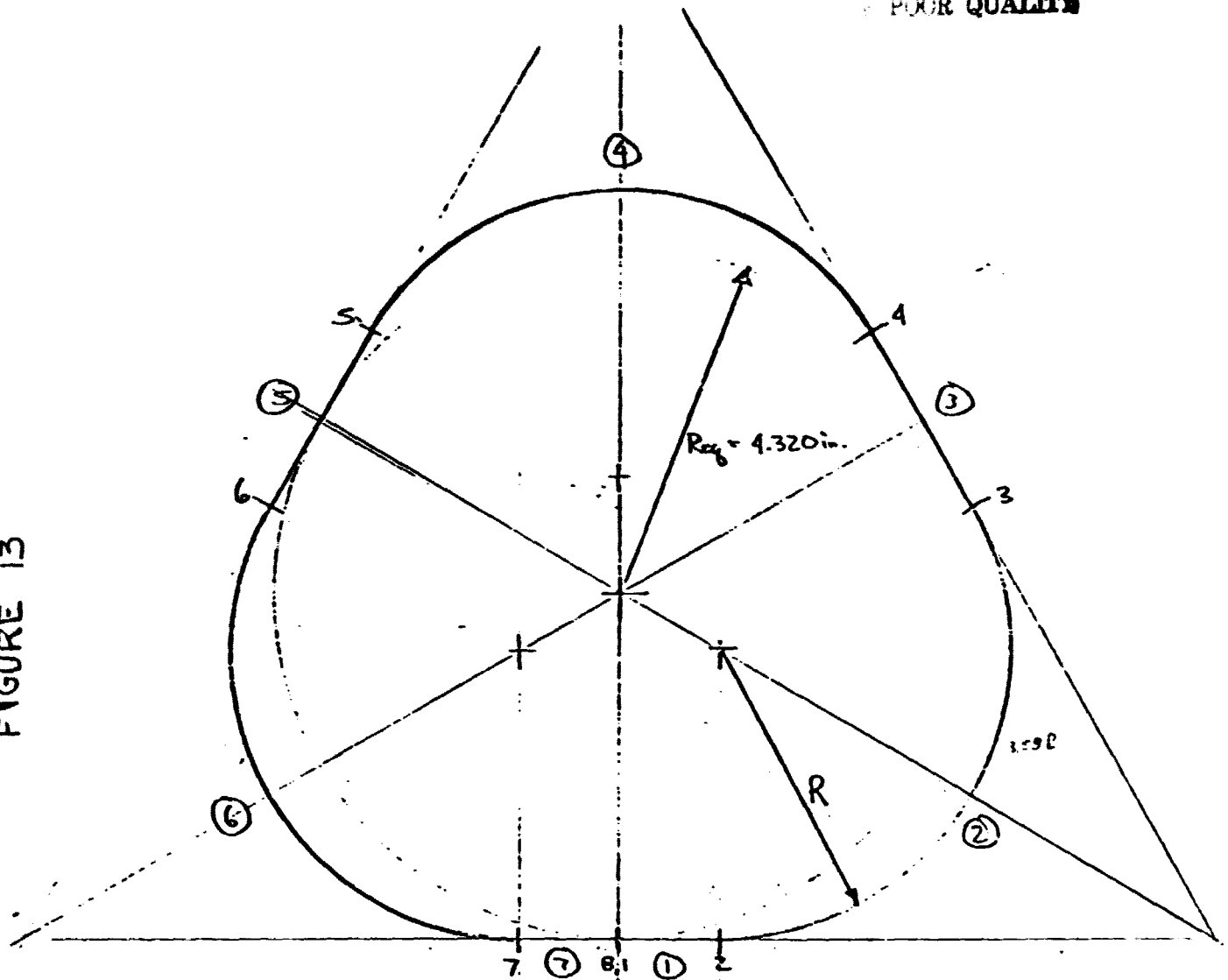
CHORD - CASE 1 ( $\tau = 0.038$ )  
BATTEN - CASE 1 ( $\tau = 0.038$ )



D180-22876-3

CASE 2ORIGINAL PAGE  
POOR QUALITY

FIGURE 13



SEGMENT	WIDTH	THICKNESS (0.019, 0.020)	RADIUS	NODE	X	Y
①	1.240	t		1	0.010	0.0
②	7.498	t	3.580	2	1.250	0.0
③	2.50	t		3	4.328	5.384
④	7.498	t	3.580	4	3.092	7.560
⑤	2.50	t		5	-3.092	7.560
⑥	7.498	t	3.580	6	-4.328	5.384
⑦	1.240	t		7	-1.250	0.0
				8	-0.010	0.0

FIGURE 14

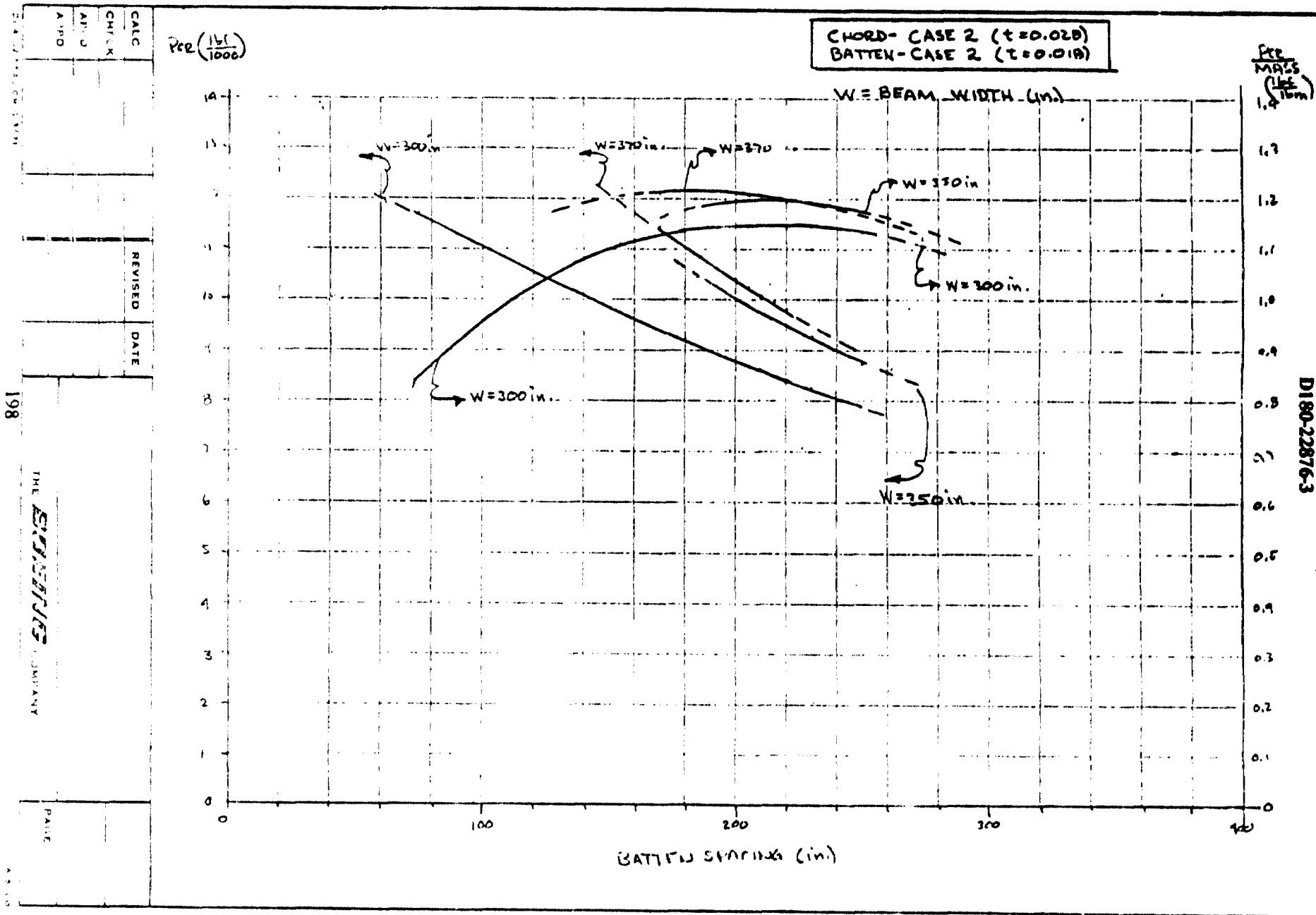
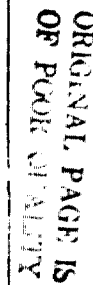


FIGURE 15



# FIGURE 16

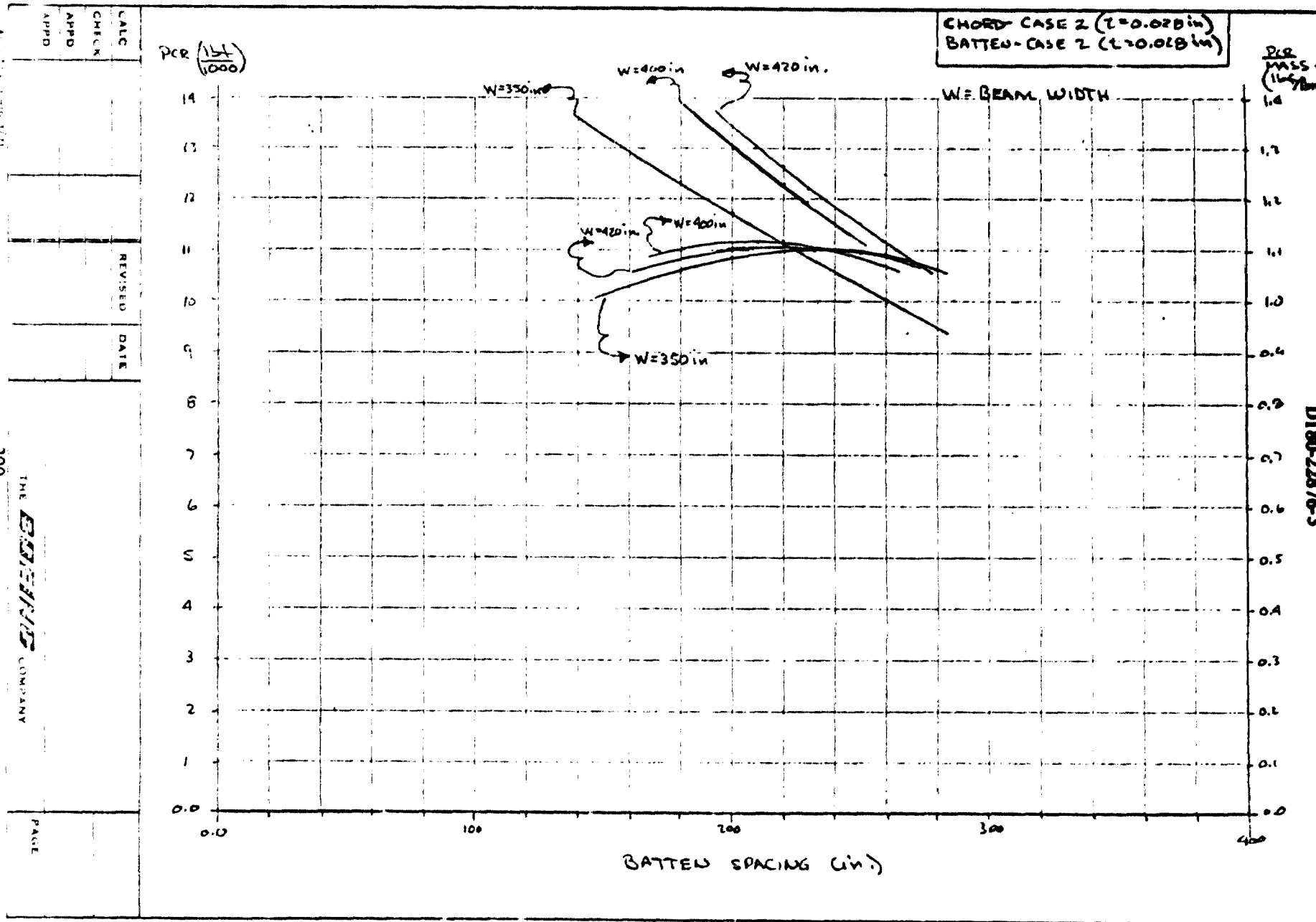


FIGURE 17

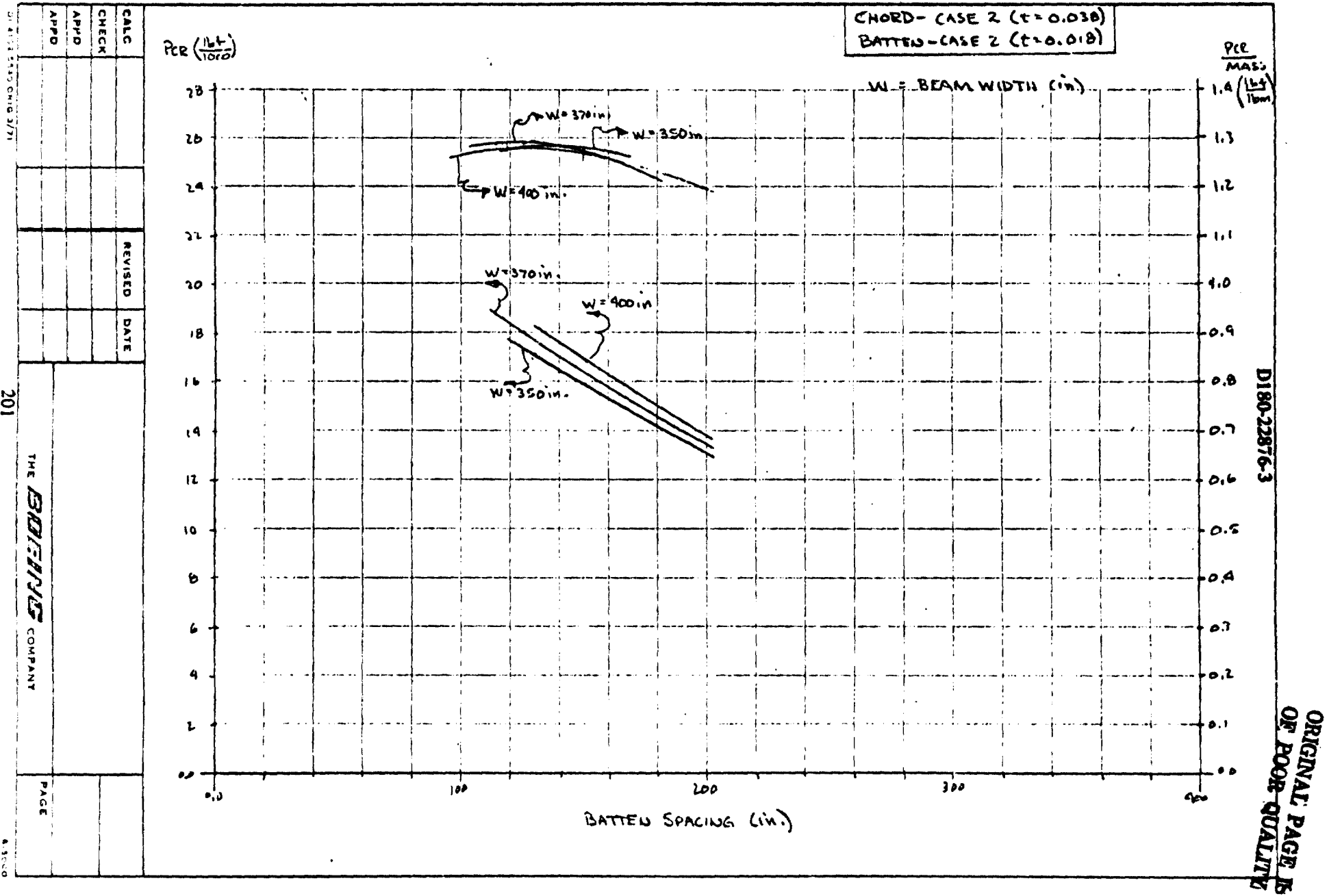
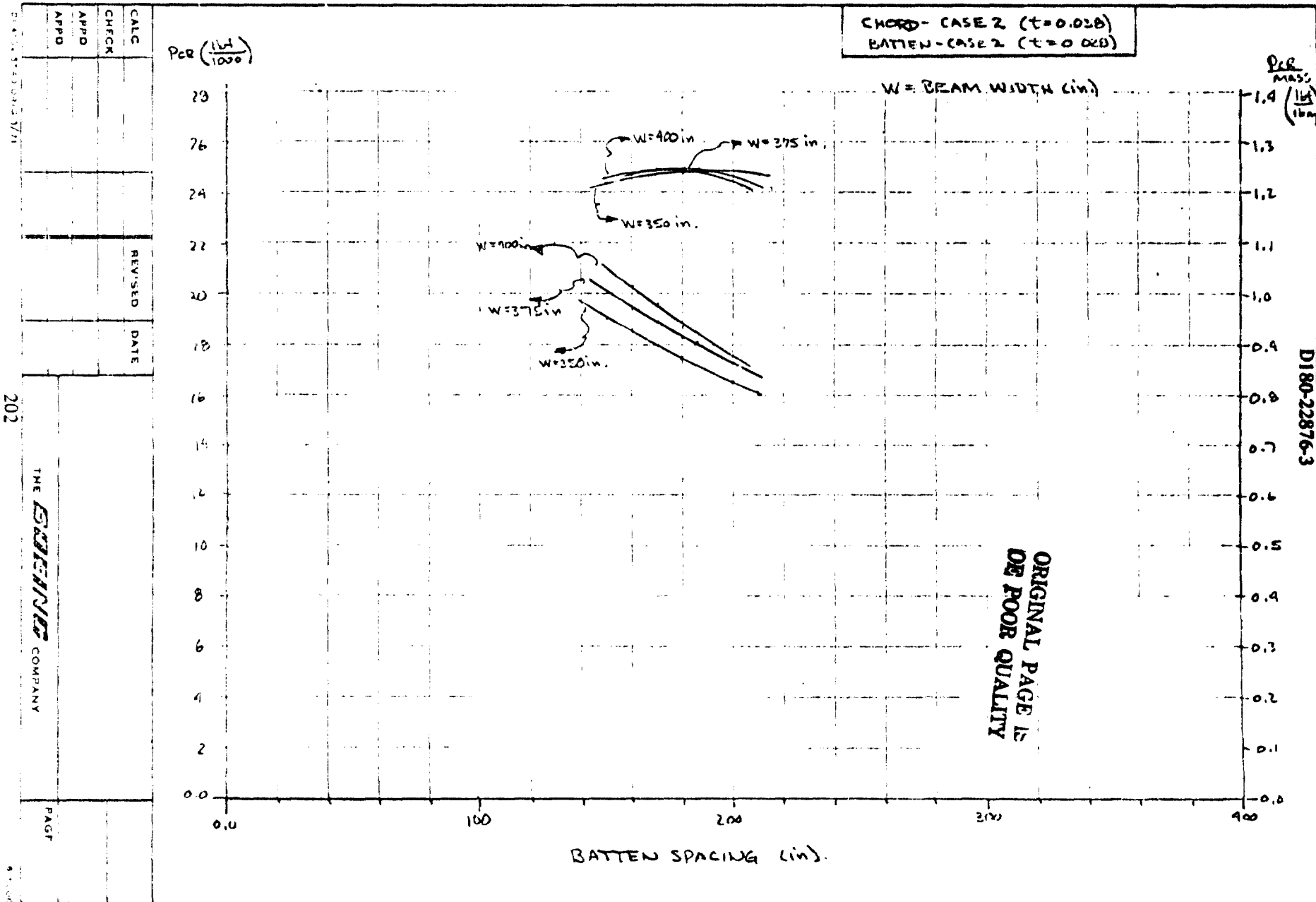
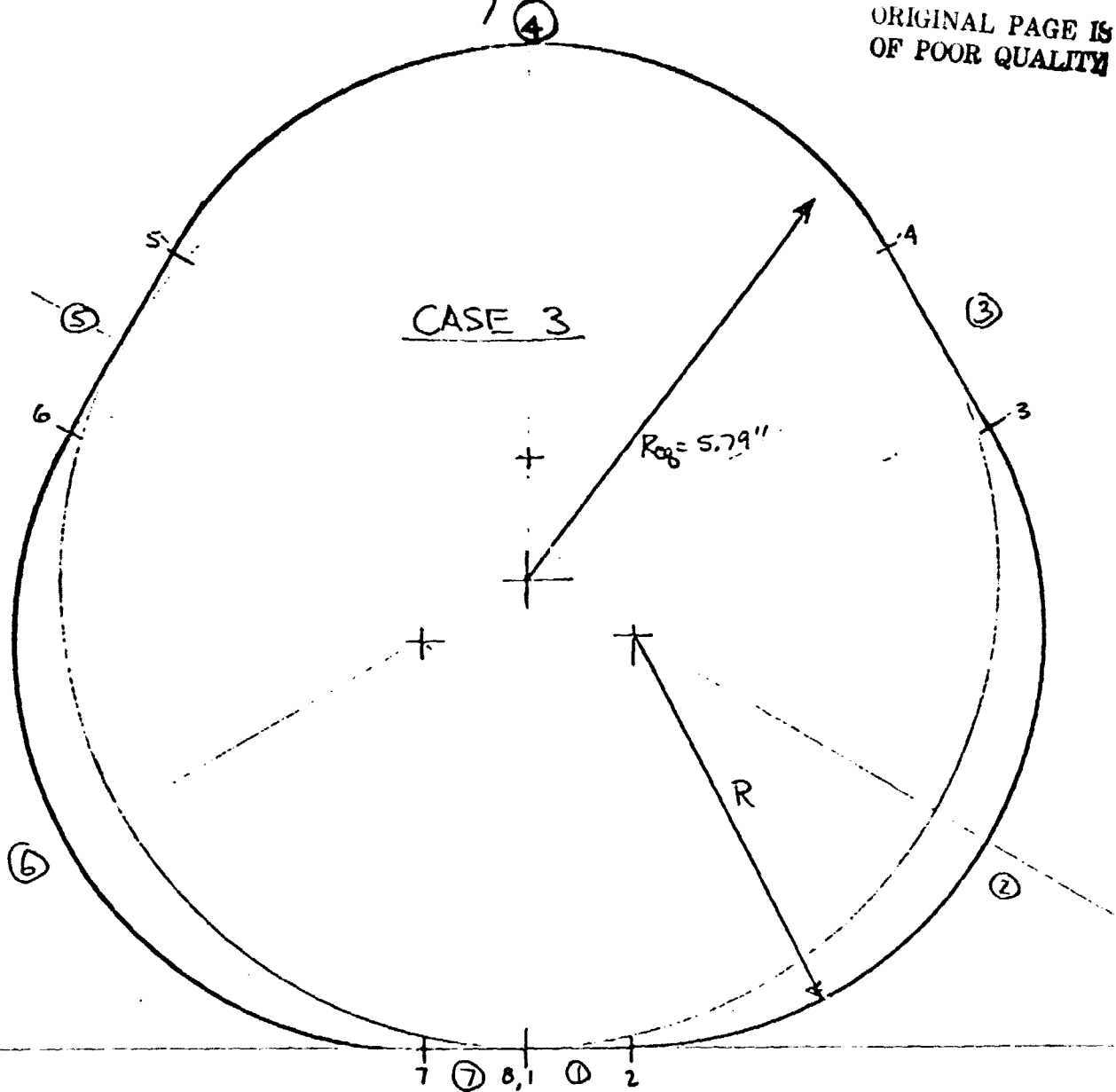


FIGURE 18



D180-22876-3

ORIGINAL PAGE IS  
OF POOR QUALITY



SEGMENT	WIDTH	THICKNESS (0.015, 0.022)	RADIUS	NODE	X	Y
①	1.240	t		1	0.010	0.0
②	10.619	t	5.07	2	1.250	0.0
③	2.500	t		3	5.672	7.592
④	0.619	t	5.07	4	4.408	9.800
⑤	2.500	t		5	-4.408	9.800
⑥	10.619	t	5.07	6	-5.672	7.592
⑦	1.240	t		7	-1.250	0.0
				8	-0.010	0.0





FIGURE 21

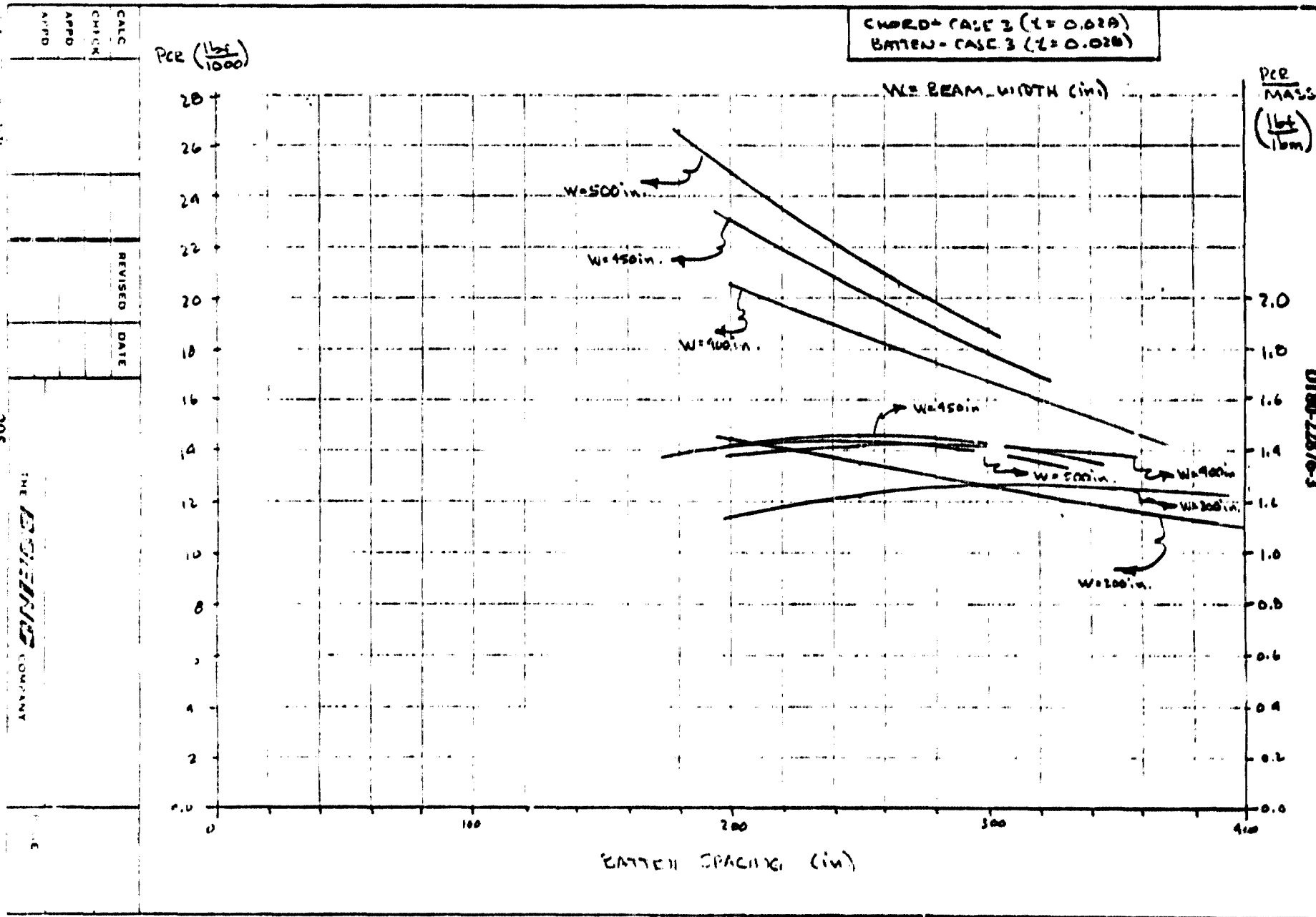


# FIGURE 22

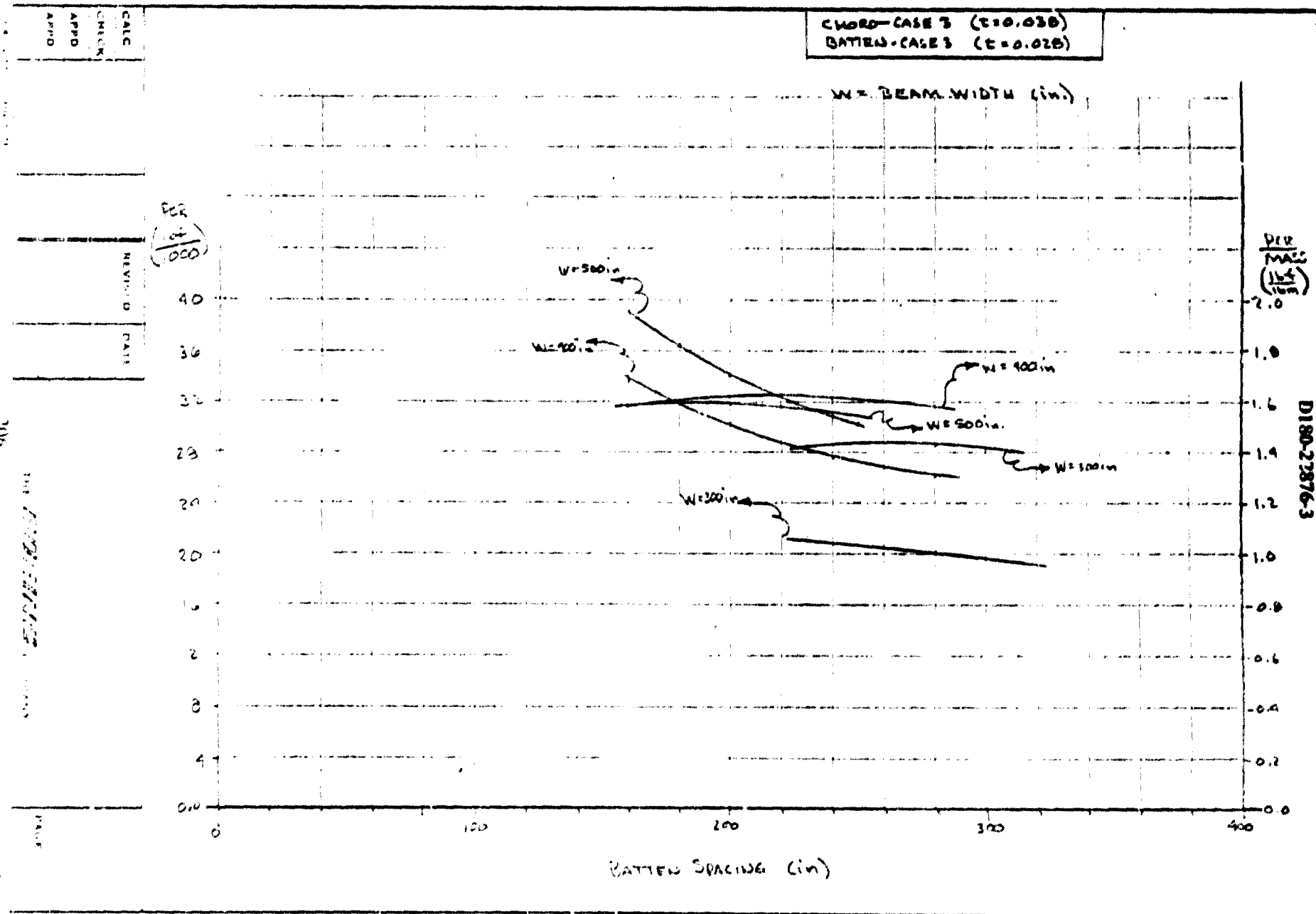
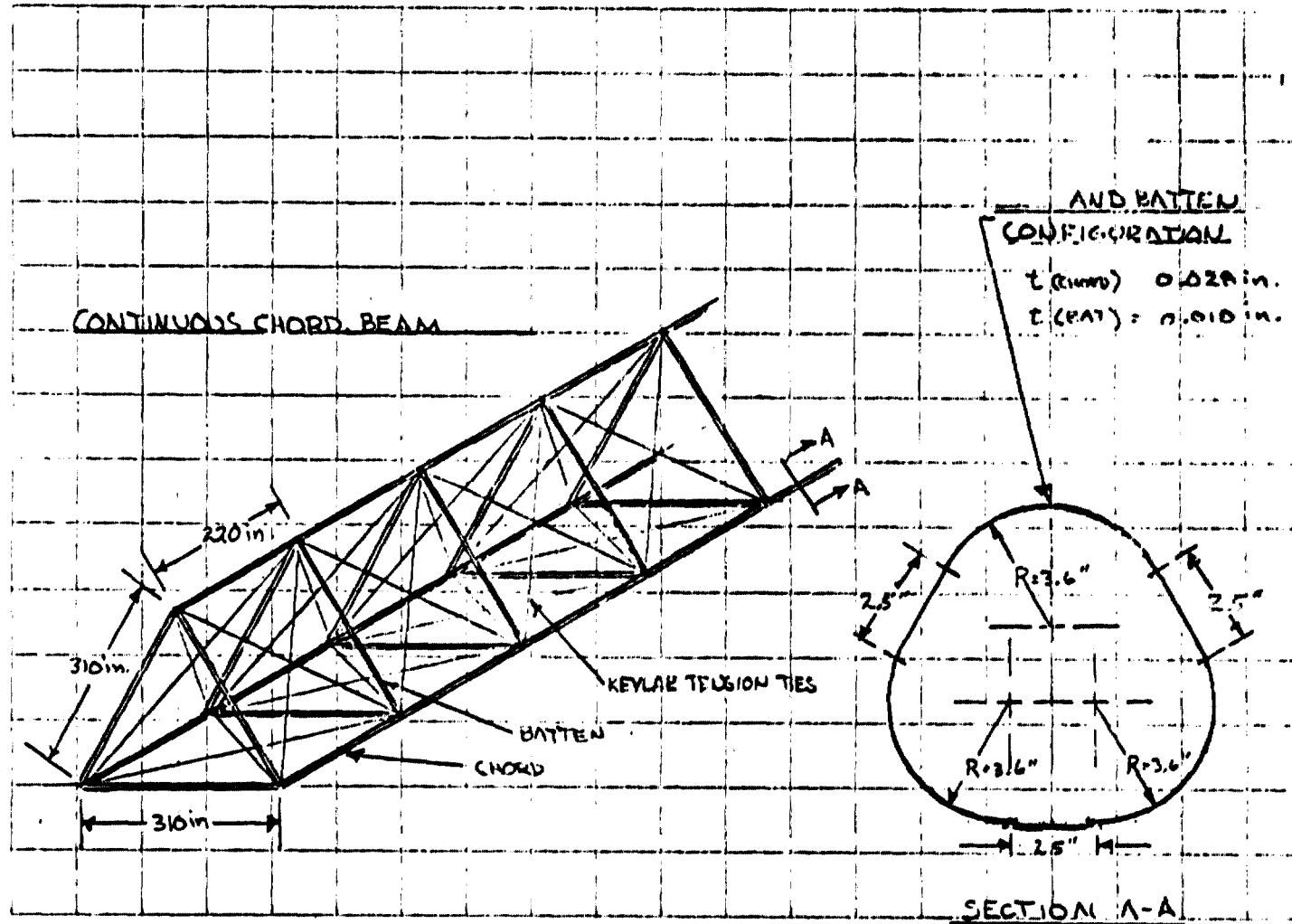


FIGURE 23



DI-80-22876-3

ORIGINAL PAGE  
OF POOR QUALITY

CALC	0. DEWIND	1/12/73	REVISED	DATE
CHECK				
APPD				
APPD				

CLOSED CHORD  
CONTINUOUS BEAM SOLN.

THE EDWARDS COMPANY

PAGE

FIGURE 24

# CLOSED CHORD CONTINUOUS BEAM CHARACTERISTICS

## COMPONENTS :

CHORD -  $EI_x \sim EI_y = 2.398 \text{ E } 8$

THICKNESS - 0.028 in.

0.004 in. FIBER COVER  
0.020 in. HHS-LSY (40-50)  
0.004 in. FIBER COVER

$A_{CHORD} = 0.8386 \text{ in.}$

BATTEN -  $EI_x \sim EI_y = 1.542 \text{ E } 8$

THICKNESS - 0.018 in.

0.004 in. FIBER  
0.010 in. HHS-LSY  
0.004 in. FIBER

TENSION TIES - KEVLAR

DIAMETER - 0.117 in.

## BEAM :

WIDTH - 310 in. (7.87 m)

LENGTH BETWEEN BATTENS - 220 in. (5.59 m)

MASS OF CHORD - 3910 lbm

MASS OF BATTEN - 3553 lbm

MASS OF TENSION TIES - 199 lbm

**TOTAL MASS - 7662 lbm**

**$P_{CR} = 8670 \text{ lbs.}$**

20 M TAPERED TYPE

MASS TOTAL - 6163 lbm

$P_{CR} = 8650 \text{ lbs.}$

DI80-22876-3

ORIGINAL PAGE IS  
OF POOR QUALITY

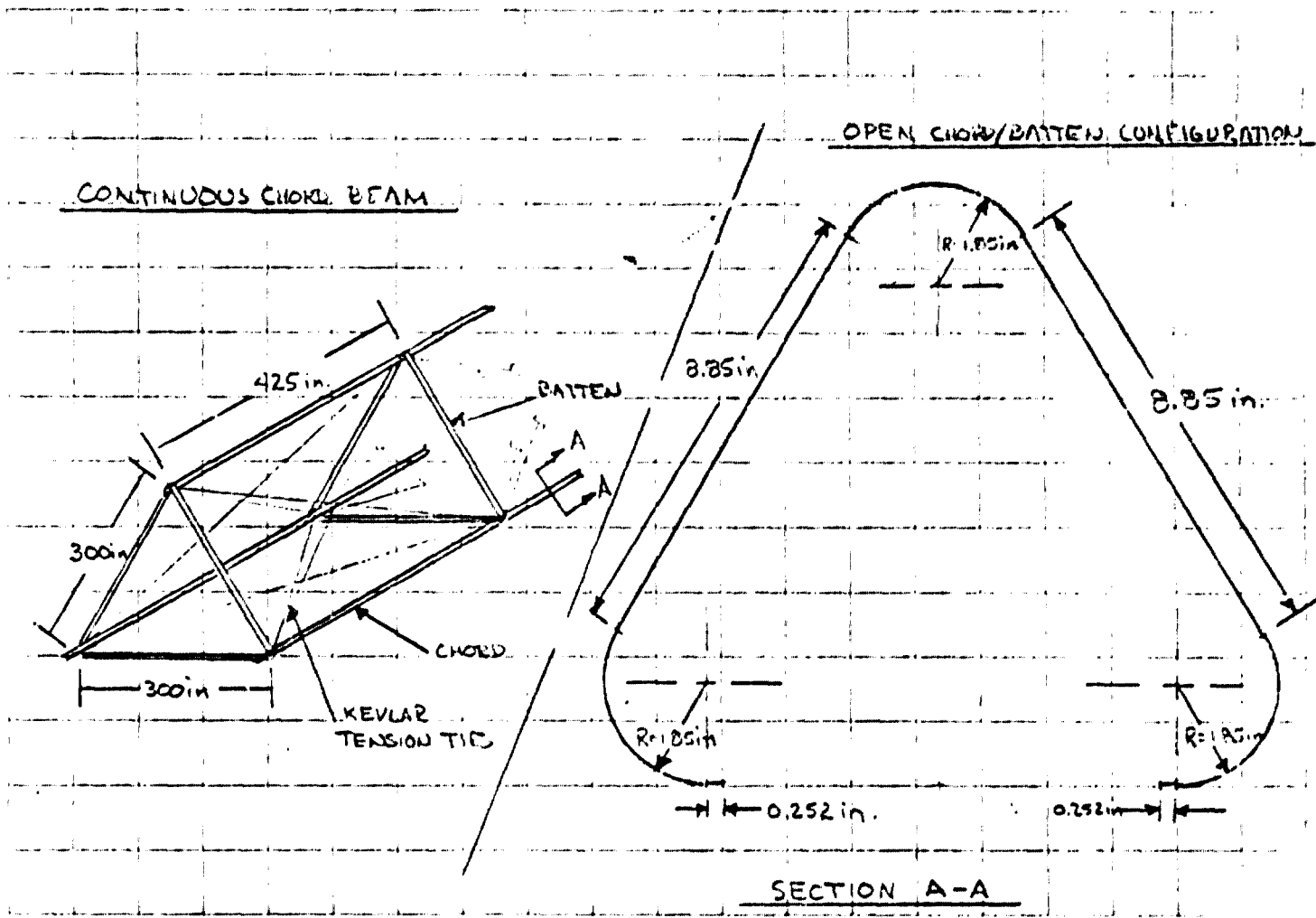
CALC  
CHECK  
APPD  
APPD

REVISED  
DATE

208

THE BOEING COMPANY

PAGE



**D180-22876-3**

ORIGINAL PART IS  
DE POOR QUALITY

התעורר

1121

**REVISED**

DATE

Advised

1/12/71

**REVISED**

DATE \_\_\_\_\_

# OPEN CHORD

RD

\_\_\_\_\_

\_\_\_\_\_

---

1

100

•  
•  
•  
•  
•  
•  
•  
•  
•

THE **STOKES** COMPANY

FIGURE 26

## OPEN CHORD CONTINUOUS BEAM CHARACTERISTICS

## COMPONENTS

CHORD -

$$EI_x = 3.544 \text{ EB } 14\text{f-in}^2$$

Area - 1.090 in<sup>2</sup>

Thickness - 0.038 in.

- 0.004 in

E-1B1 CONF 2

- 0.030 in

NM5-LST (Gr-Fr)

- 0.0041

E-181 62112

BATTEN -

SAME AS CHORD

TENSION TIES -

MATERIAL - KEVLAR

DIAMETER — 0.101 in.

BEAM

WIDTH - 300 in. (7.62 m)

DISTANCE BETWEEN BATTENS - 425 in. (10.80 m)

MASS OF CHORD - 5100.0 lbm.

MASS OF BATTENS - 3600.0 lbm.

MASS OF CEMENTATION - 75.4 lbm

TOTAL MASS - 8775.4 INCH

\_\_\_\_\_

PCR -- 8730 lbs.

20 m TAPERED TUBE

MASS TOTALE 6163 lbm

Per - 8650160

**D180-22876-3**

ORIGINAL PAGE IS  
OF POOR QUALITY